3D electrical resistivity of Gran Canaria Island using magnetotelluric data

J. Ledo[1,2], M. García-Merino[2], H. Larnier[2,3], K. Slezak[2*], P. Piña-Varas[1], A. Marcuello[1], P. Queralt[1], N. M. Pérez[2,3], H.-U. Schmincke[4] and M. Sumita[4].

[1]Departament de Dinàmica de la Terra i dels Oceans, Universitat de Barcelona, Spain.

[2]Instituto Volcanológico de Canarias (INVOLCAN), 38320 La Laguna, Tenerife, Canary Islands, Spain

[3]Instituto Tecnológico y de Energías Renovables (ITER), 38600 Granadilla de Abona, Tenerife, Canary Islands, Spain

[4]GEOMAR Helmholtz Centre for Ocean Research Kiel, Wischhofstr. 1-3, 24148 Kiel, Germany.

[*]now at Department of Geophysics, Universidad de Chile, Blanco Encalada 2002, Santiago, Chile

Keywords:
Geophysics, Magnetotelluric, Volcanic island, Electrical resistivity

Abstract

Gran Canaria, one of the two main islands of the Canary Archipelago of NW Africa, has been volcanically active for at least 15 million years. The island went through several volcanic cycles that varied greatly in composition and extrusive and intrusive activity. The complex orography of the island has excluded extensive land geophysical surveys on the island. A review of the available geophysical information on the island shows that it has been obtained mainly through marine and airborne geophysical surveys. A new dataset comprising 100 magnetotelluric soundings acquired on land has been used to obtain the first 3D electrical resistivity model of the island at crustal scale. The model shows high resistivity values close to the surface in the exposed Tejeda Caldera that extends at depth to the SE cutting the islands in half. Outside the inferred limits of the Tejeda Caldera the 3D model shows low resistivity values that could be explained by hydrothermal alteration at deeper levels and the presence of marine saltwater intrusion at shallower levels near the coast. The presence of unonnected vertical-like structures, with very low resistivity (<10 ohm m) could be associated to small convective cells is confirmed by the sensitivity analysis carried out in the present study. Those structures are the most likely candidates for a detailed analysis in order to determine their geothermal economic potential. A comprehensive review of existing geophysical data and with the new 3D electrical resistivity model is presented.

1. Introduction

Gran Canaria island is part of the Canary Archipelago (Spain), a large intraplate volcanic oceanic island chain forming a 450 km long east-west volcanic belt some 200 km off the northwestern African coast (Fig. 1). Intraplate volcanic islands are systems in which its growth, a result of mantle processes, and degradation by mass wasting could be related among the different intraplate volcanic islands (Schmincke and Sumita, 2014). Thus, the evolution of the long-lived older Canary Islands compared to the relatively short-lived Hawaiian Islands has been discussed in detail by (Schmincke and Sumita, 2011). The Canary Islands rest on top of a rigid and thick oceanic lithosphere of Jurassic age (Schmincke et al., 1998) that has limited the amount of subsidence of the archipelago compared to the Hawaiian Islands.

Gran Canaria is nearly circular, has a diameter of about 45 km and rises to 1956 m above sea level (m.a.s.l.) in Pico de las Nieves, in the central part of the island. Gran Canaria is likely one of the most intensely studied oceanic islands in the world (see review in Schmincke and Sumita, 2011). The geological map of the island (Fig. 1) shows a complex multi-stage basaltic shield cut by a ca. 20-km collapse caldera, the source of several tens of rhyolitic to later phonolitic ignimbrites, dominating a broad belt inside the marginal basaltic shield lava formations. The well-exposed center of the island is made-up of a huge trachytic-phonolitic cone sheet swarm cut by local syenite intrusions. A clear NW-SE lineation that divides the island into two parts (Fig. 1A), is basically a boundary between a stable southwest and a northeastern half highly susceptible to mass wasting since the basaltic shield stages. The geological and morphological contrasts between the SW and NE parts of the island have been noted for almost 100 years and were commonly interpreted as due to major faulting. Schmincke (1968) interpreted this boundary zone as basically due to mass wasting largely controlled by climate, north/northeast trade winds having been constant during the evolution of the island since the Miocene. Thus, instability and repeated flank collapses have dominated the evolution of the NE part of Gran Canaria. This lineament has been confirmed by gravity and aeromagnetic data (Blanco-Montenegro et al., 2003; Camacho et al., 2000), although its depth extent is unknown. The intra caldera margin rocks show evidence of hydrothermal alteration at surface (Donoghue et al., 2008), however controversy exists in respect to the exact timing and spatial extent of the hydrothermal activity (Pérez Torrado et al., 2004). The number of geophysical studies on land at crustal scale of the island is reduced to the 3D gravity model of Camacho et al. (2000) that was based on a limited number of measurements that did not cover the whole island uniformly. Moreover, the steep morphology of the island prevents the application of other land high-resolution geophysical methods (i.e. active seismic methods).

Magnetotelluric surveys (MT) have been used extensively to unravel the electrical resistivity distribution and the geothermal potential in different environments (Abdelfettah et al., 2018; Ars et al., 2019; Lee et al., 2019; Maithya and Fujimitsu, 2019; Mun˜oz et al., 2010; Yoshimura et al., 2018). On neighboring islands, magnetotelluric data have been acquired (Coppo et al., 2008; García-Yeguas et al., 2017; Garcia and Jones, 2010; Piña-Varas et al., 2014, 2015, 2018; Pous et al., 2002) and in combination with other geophysical and geochemical datasets (García-Yeguas et al., 2017; Rodríguez et al., 2015) has allow to characterize the main volcano structures and their geothermal capabilities. In this paper, we provide a comprehensive review of existing geophysical data and models of Gran Canaria Island and their comparison with new magnetotelluric data and the first 3D electrical resistivity model of the island that allows to determine not only the deep structure of the main NW-SE lineation but also the spatial extent of hydrothermal alteration at depth.

The energy budget of the Canary archipelago, and the Gran Canaria Island, has an important deficit from a renewable point of view. Only a 2% of the required energy is generated by renewable sources (solar, hydraulic, wind power, biomass) as describes in the Anuario Energético de Canarias (2018). The amount of geothermal energy produced is negligible and related to private installations and neither district heating nor high enthalpy geothermal projects have been yet developed despite the geothermal potential of this volcanic island. This study is a required step toward the future development of the geothermal potential of the island that will allow to become more carbon-neutral in the future.

2. Geological setting

The Canary Islands are located within the African plate very close to its Atlantic continental passive margin. In fact, the distance between Fuerteventura and Juby Cape (in the African continent) is about 100 km (Fig. 1). The Jurassic crust (formed between 165–176 Ma) in which the Canary Islands were constructed, is considered one of the oldest, coldest and thickest oceanic crusts of the planet. It is characterized by a very high rigidity that allows sustaining the different Canarian edifices over million years without evident signs of subsidence. This feature contrasts with other well-known archipelagos, especially those in the Pacific plate like the Hawaiian Islands, where the lithosphere is young, thin and flexible allowing rapid subsidence of the volcanic edifices and formation of atolls and guyots (Schmincke and Sumita, 2011).

The geological evolution of Gran Canaria has been separated into three main evolutionary stages: the Miocene stage consisting of several overlapping basaltic shield volcanoes. The center of the island was cut by a 20 km diameter collapse caldera, source of several tens of rhyolitic to later phonolitic ignimbrites covering much of the basaltic shield and ending at ca 8 Ma, followed by an intense period of erosion and slope collapses during which the height of the islands was reduced by possibly as much as 2000 m or more. A large composite volcanic structure (Roque Nublo stage) grew between ca 5 and 3.3 Ma. The

Roque Nublo phase was followed by massive basaltic and minor phonolitic volcanism in the central part of the island, and the Pliocene basaltic and later Pleistocene to Holocene alkaline volcanic activity in the northern to northeastern part of the island.

The chronostratigraphic division of Gran Canaria included three magmatic cycles separated by erosional intervals (Van den Bogaard and Schmincke, 1998; Hoernle and Schmincke, 1993; Lietz and Schmincke, 1975; Schmincke, 1976): Cycle I (from 15 to 8.0 Ma), an erosional interval of about 3 Ma; Cycle II (the Roque Nublo Group); and Cycle III (Post-Roque Nublo Group), see Fig. 1B. For simplicity, we here consider two main phases of the subaerial construction of the island: a shield stage (ca. 15-8.0 Ma) and a rejuvenated or post-erosive stage (ca. 5 Ma to present), both separated by a period of volcanic inactivity of ca. 3 Ma.

The subaerial Miocene phase started with the rapid formation of the exposed mildly alkalic shield basalts with a decrease in age from west to east, it constitutes, by large, the most abundant material on the island. The shield basalts are covered by a thick pile (up to 500 m) of ignimbrite sheets and minor lavas of predominantly rhyolitic composition forming the Mogan Group. The Mogan Group ignimbrites in turn are overlain by a pile (>300 m) of trachyphonolitic lava flows and ignimbrites forming the Fataga group (Fig. 1B). Volcanic activity was practically absent on the islands between 8 to 5 Ma. During this time the island became deeply eroded. The Pliocene phase began with minor nephelinites at 5 Ma. Subsequently Pliocene Roque Nublo volcanism formed a stratocone, possibly as high as 3000 m.a.s.l. while its lavas filled the deep canyons carved into Tejeda caldera. The southern and northern sectors of the Roque Nublo complex collapsed at 3.5 Ma. Following a possible brief gap in volcanism, highly undersaturated mafic lavas erupted. Quaternary volcanism is restricted to the northern half of the island.

Tejeda Caldera was formed synchronously with the eruption of the Mogan ignimbrites (Fig. 1B). It must have been underlain by a high-level magmatic reservoir, source area for some 15 large-volume ignimbrites and minor early lava flow. The eruption of massive ignimbrite which emptied this reservoir initiated a complex interplay of repeated inflation and deflation cycles (Troll et al., 2002). The gravitational and vertical collapse of the reservoir roof opened ring fractures at the caldera perimeter (Troll and Schmincke, 2002). Surface mapped major ring fractures are located on the southern part of the island, in agreement with the largest outcrop of hydrothermally altered rocks of the island

(Fig. 2A). This elliptical caldera (20 × 17 km wide; Fig.1A) has a vertical displacement of its interior of more than 1000 m (Schmincke and Sumita, 2011).

3. Review of previous geophysical studies

The volcanic, structural, and petrological evolution of Gran Canaria has been studied in extraordinary detail (see summary in Schmincke and Sumita, 2011). However, geophysical studies of the whole island at crustal scale are sparse. In the following we review the previous geophysical surveys carried out to study the upper crust of Gran Canaria Island. The number of geophysical surveys made on land to characterize the upper part of the crust of Gran Canaria is scarce due in part to the complex orography. Bosshard and Macfarlane (1970) report on a previous on land gravity survey in 1965 in Gran Canaria, although given the rough topography and the lack of good elevation models at that time, not terrain correction was applied on this land data to obtain the bouguer anomaly map of the Gran Canaria Island. The anomaly map presented two maximum values in the NW and SE of the island with a minimum value in the center of the island. A NW-SE data transect crossing the island was used to create a 2D density model of the island showing two high density structures in the upper crust associated to the data maxima. The last on land geophysical survey reported on the island was the regional component of the gravity survey (Camacho et al., 2000), using 98 measurement points irregularly distributed, leaving some areas of the island without coverage. Given the suspected high observational noise and the very rugged topography of the island the final bouguer map has up to 3 mGal of uncertainty that corresponds to a more than 10 % error in the final map of the observed Bouguer anomaly. The Bouguer map shows an anomaly with a NW-SE trend associated with the main structural directions of the island. Their final 3D density model also shows this trend, although is not as clear as in the data (Fig. 4C). Bosshard and Macfarlane (1970) were the first ones to study the deep crustal structure of the Canary Islands using marine seismic refraction data. Another deep seismic refraction experiment to study the whole crustal structure of the Canary archipelago was conducted in the late 70’s (Banda et al., 1981). In Gran Canaria Island twelve seismic station were installed along a NW-SE profile crossing the island and two off-shore shots were fired at each extreme of the profile side. The data was interpreted using a three-layer model with velocities of 3.3, 6.3 and 8 km/s respectively and the contact of the layers was located at 1-2 km (b.s.l) and 14 km (b.s.l) (Banda et al., 1981; Suriñach, 1986). Given the design of the experiment and the reduced number of stations on land, no lateral velocity variations were observed. The drillings in the framework of IODP program around the island in the 90's (Schmincke and Sumita, 1998) were accompanied by the acquisition of seismic data mainly in the northern part of the island (Funck et al., 1996; Funck and Schmincke, 1998).

Krastel and Schmincke (2002) derived a 3D model of the P-wave velocity structure of the northern part of the island using both, land and ocean bottom receivers (Ye et al., 1999). All the shots were done offshore and only eight seismic stations were located on the island, manly in its northern part. Ye et al. (1999), using the same data, obtained 2D seismic velocity models along three radial profiles from the center to the island up to more than 60 km form the coast to the N and NE from wide-angle reflection and refraction seismic data. Beneath the island the velocities in the upper part of the volcanic edifice show strong lateral changes at different depths from the surface up to 10 km depth. In order to determine the lateral velocity variation within the volcanic edifice, Krastel and Schmincke (2002) invert the travel times obtained in the same experiment to image the three-dimensional P-wave velocity structure of the central and northern part of the island. The island is characterized by a heterogeneous structure with large lateral velocity variations, especially in the upper part of the volcanic edifice. The depth slices of the 3D inversion model of Krastel and Schmincke (2002) show an NW-SE orientation of the high Vp structures (Fig. 4B, Krastel and Schmincke, 2002). A fast velocity anomaly (> 5.5 km/s) which extends from the lower crust into the volcanic edifice is interpreted as dense intrusions and cumulates formed during the major volcanic cycles. Slow velocities (< 5.0 km/s) may correspond to weaker, porous, subaerial lava or an area with large fractures are observed at shallower levels of the model near the coastline. When compared with the previous 2D seismic refraction experiment (Banda et al., 1981) the 3D seismic velocity model shows higher velocity values and a NW-SE increase of the velocity values with depth.

In 1993 the Spanish National Geographical Institute carried out an aeromagnetic survey of the Canary Islands. The data above Gran Canaria, Fig. 4D, was reprocessed, modelled and interpreted by Blanco-Montenegro et al. (2003). The main result of their work is the magnetic anomaly map of Gran Canaria and surrounding oceanic region at 3800 m a.s.l. that was reduced-to-the-pole (RTP) in order to obtain a crustal model of Gran Canaria. Two transects, NW-SE and SW-NE, were interpreted using a 2.75D forward modelling trial and error approach, The 2.75 D model represents the geology as polygonal prisms with horizontal axes and either finite or infinite extent in the strike direction. However, given that their main purpose was to model the deeper part of the island they approximated the shallower part of the island by a homogeneous body. The most important lateral magnetization structures are located beneath the island between 4 and 15 km depth (b.s.l.) where a mafic core with different values for the module of the total magnetization vector is observed. Moreover, a body with null magnetization, located between 4–7 km depth (b.s.l.), is present in their model and is associated to a shallow syenitic plutonic body. Moreover, the authors identify that the main positive magnetic anomalies displayed over Gran Canaria follow three directions, red discontinuous lines in Fig. 4.

In summary, the geophysical data acquired in Gran Canaria to date was addressed to study the deeper structure of the island (aeromagnetic data, seismic and gravity) and except for the aeromagnetic data the coverage of the seismic and gravity experiments on land were neither uniform nor complete and their results could be constrained by the geometry of the experiments. To gain insight into the upper crust of Gran Canaria we present the results obtained from the 3D inversion of new magnetotelluric data, that represent the first comprehensive geophysical survey at crustal scale acquired on land covering the whole island that will play a key role in the exploitation of geothermal resources.

4. Magnetotelluric data

The magnetotelluric method involves measuring the temporal fluctuations of the horizontal components of the natural electromagnetic field at the Earth's surface to infer the lateral and vertical variations of electrical conductivity of the Earth's interior (Chave et al., 2012, and references therein). We acquired a dataset of 100 new magnetotelluric soundings distributed around the island (Fig. 1A) from July 2017 to September 2017. Instrumentation consisted of three Metronix ADU-07 and two ADU-06, along with EPF06 electrodes and MFS06/07 magnetic coils. Only horizontal electric and magnetic fields were recorded for at least 48 h in NS and EW directions. We used standard multi-site remote reference processing methodology based on Fourier transform (Chave and Thomson, 2004) and wavelet-based methodology for high frequencies (Larnier et al., 2018) to obtain the magnetotelluric response functions for the period range 0.001–1000

s. The main electromagnetic noise sources are associated to small population nuclei in the interior of the island, while industrial areas are located near the coast, except in the western side due to the morphology. In general, data quality is good up to 256 s, at longer periods the data quality decreases and were not considered during the 3D inversion procedure. Given the complex volcanic evolution of the island and the periods of the impedance tensor considered a 3D inversion of the data is mandatory. However, a dimensionality analysis was performed based on the phase tensor (Booker, 2014; Caldwell et al., 2004; Krieger and Peacock, 2014) and the WALDIM (Martí et al., 2005, 2009) decomposition. This analysis is required not only to confirm the 3D behavior of the resistivity distribution over the island (see figures S1 and S2 supplementary material) but also to determine if there are any structural lineaments. For Gran Canaria, neither phase tensor nor WAL invariants results show any special feature that can be associated with the main geological structures outcropping on the island. This lack of strong relationship between the surface geology and the magnetotelluric data could be associate to the complex structure at crustal scale of the island.

5. 3D magnetotelluric data inversion

The 3D electrical resistivity model of the island has been obtained from the full impedance tensor inversion using ModEM code (Egbert and Kelbert, 2012; Kelbert et al., 2014). The initial model consisted of 77 × 73 × 98 layer grid in which the topography and the surrounding bathymetry of the island were fixed, and the land resistivity was 100 ohm m. The horizontal mesh size in the island was 968 m, increasing outside of the island by a factor 1.3. Given that the average distance between the MT sites recorded is 4 km the number of horizontal cells between each MT site, in average, was 4. In the vertical direction the initial mesh size was 5 m increasing by a factor 1.2 with depth till a maximum size of around 100 m up to 1.5 km b.s.l. in order to capture the orography of the island. Thus, 45 vertical layers were used for the topography and the bathymetry close to the island. The covariance (between 0 and 1) controls the behavior of the model norm, a higher covariance results in a smoother overall model with fewer small-scale and rough features which are more heavily penalized (Robertson et al., 2020). In our case we choose a value of 0.2 for the horizontal and vertical directions that is a tradeoff between fitting the data and obtaining a geologically plausible model. To obtain the final inversion model, the four components of the impedance tensor of 100 MT sites were considered using 19 periods in the 0.001–256 s range. The error floor for the off-diagonal impedance components was 5% of each component and for the diagonal components 10 %. The final RMS was 1.70, after 109 iterations, for all the periods and stations considered. Figure S3 in the supplementary material shows a map of RMS distribution for the full tensor and for the different components. Figure S7 in the supplementary material shows the comparison between the measured apparent resistivities and phases of the four tensor components, and model responses for all the sites.

5.1. 3D resistivity model

The final 3D resistivity inversion model is shown in Fig. 2 as six horizontal depth slices and 2 vertical cross-sections. The upper part of the model (-500 m.a.s.l.), is very heterogeneous and shows major resistivity contrasts that can be associated to the presence of highly porous materials and fractures with or without meteoritic water and clays that can produce the observed resistivity contrast. However, at depth, the most obvious feature is the high resistivity (> 500 ohm m) (label R1 in Fig. 2) central region surrounded by a less resistive structure (20-50 ohm.m), label C1 in Fig. 2. This high resistivity structure seems to be delimited by the walls of the Tejeda Caldera up to depths of -2000 m.a.s.l. With increasing depth, the high resistivity structure elongates in SE direction and at -5000 m.a.s.l. is cutting in two the island. In the vertical cross-sections (Fig. 2b), also the most obvious feature is the presence of a high resistivity anomaly (R1) associated with the Tejeda Caldera. It shows a near vertical contact with the surrounding materials. Inside the Tejeda caldera the presence of an intrusive complex of cone sheet swarm surrounding a central core of hypabyssal syenite stocks (Schmincke and Sumita, 2011; Fig. 1A) as well as the fluid-rock interaction sealing the fractures will reduce the permeability of the central part of the island drastically and produce the observed high resistivity in the 3D model.

The low resistivity values found in the caldera rim can be associated with the presence of hydrothermal alteration especially along the major caldera boundary fault (Schmincke, 1976; Schmincke and Sumita, 1998). Another striking result is the pervasive low resistivity (20-50 ohm.m) observed around the Tejeda caldera that covers practically all the island at depth. Moreover, there are a few near-vertical low resistivity structures (<10 ohm m) (label C2 in Fig. 2) in the south and in the eastern part of the island.

Given the geological evolution of the island with Miocene shield basalts forming the core of the island and probably saturated in fresh water a resistivity value of a few hundred ohm.m or higher was expected (Drury, 1979; Flóvenz et al., 2005). To explain these observed values, we can consider two end members: hydrothermal alteration or presence of saline fluids. Hydrothermal alteration has been observed in the Tejeda Caldera rim (Fig. 1A) and it is invoked in many cases to explain the low resistivity cap observed in many volcanic areas (Aizawa et al., 2009; Flóvenz et al., 2005; Komori et al., 2013; Piña-Varas et al., 2014). Geothermal fields in volcanic areas usually present a low resistivity structure (smectite) above a resistive core, the bottom of the low resistivity structure is usually associated to the change from smectite to chlorite at around 230 ◦C. The resistivity value of smectite in geothermal reservoirs is reported to have values between 1-10 ohm m (Gunderson et al., 2000; Ussher et al., 2000a), and in our 3D electrical resistivity model the zones that present this range of values are small with a vertical-like structure and do not show connections among them (see figure S4 in the supplementary material). In comparison with neighboring Tenerife where a thick and continuous low resistivity structure was associated to the clay cap (Piña-Varas et al., 2014) Gran Canaria lacks this regional clay cap with low electrical resistivity. High temperature hydrothermal alteration processes may increase the resistivity of some rocks by converting smectite clays to illitic or chloritic clays (Ussher et al., 2000b), but this increase is frozen in and does not change when the system cools down. Thus, we can interpret that most of the deep island rocks have been exposed to a pervasive high temperature hydrothermal alteration (>230 ◦C) due to the longevity of the overall Tejeda caldera structure cooling, roughly between the start of the P1 Ignimbrite eruptions (14 Ma) and the late Fataga period (8 Ma).

The observed vertical-like structures (label C2 in Fig. 2) could be associated to hydrothermal alteration, smectite clays, produced by small isolated convective cells. Their size and distribution is similar to that observed in geothermal fields (i.e. Taupo Volcanic Zone, Bibby et al., 1995; Masaya hydrothermal system, Pearson et al., 2012). The number of convection cells and their dimensions are dependent primarily on rock permeability and heat or fluid injection rate for a given geometry (Pearson et al., 2012). In Gran Canaria the top of all these structures is located around 660 m.b.s.l. implying that at this depth a regional, more impermeable layer, within the shield basalts, must be present to stop the progression of the convection cell to the surface. A sensitivity analysis of these structures was carried removing each of them individually from the final model and calculating the 3D MT forward problem (Fig. 3). The presence of all these structures is justified by the misfit in the apparent resistivity and phases curves of the MT sites located close to each structure. The misfit is mainly observed in the off-diagonal components but can also be observed in the diagonal ones. The sites located in the southern part of the island (sites 11, 27, 40 and 86) are more affected by the removal of this structures than the sites located in the eastern part of the island (sites 79 and 92).

Saline water intrusion (SWI) occurs in the island due to the overexploitation for agricultural and touristic developments (Cabrera and Custodio, 2004). Figure S5 (supplementary material) shows the map of Cl- (ppm) obtained from the data available at the control network of Consejo Insular de Aguas de Gran Canaria (CIAGC, 2007–2015). Near the cost the SWI can reach up to 10 km inland in the SE of the island with chloride content reaching up to 2000 ppm. In the 80's the Spanish Geological Survey (IGME) carried out two boreholes in the SE of the island for geothermal purposes (IGME, 1981) see Fig. 1 for location. The two boreholes, located inland more than 7 km from the coast, reached 600 m depth trough the basaltic shield. The average temperature gradient of both drillholes was 6.5 ◦C/100 m reaching more than 65 ◦C at their bottom. The analysis of the different geophysical logs reports a medium porosity of 22 % and 5000 Cl- ppm that corresponds to a water salinity of 1 ohm m. Those porosity values agree with the ones found for the interbedded rhyolitic-trachypohonolitic volcaniclastic sediments correlated with the Miocene Fataga and Mogán Groups in the borehole logs of site 953C of the Ocean Drilling Program (Weaver et al., 1998). Using these values of porosity and water salinity in Archie's law gives a bulk resistivity between 20 ohm·m and 60 ohm m, that agree with the observed resistivity values in the 3D model. Outside the Tejeda Caldera the chloride content of the water is, on average, 100 ppm and 200 ppm for the northern and southern part of the island respectively, and the associated bulk electrical resistivity derived from Archie's law gives values of thousands of ohm.m. In these areas electrolytic conduction is ruled out to explain the observed resistivity.

The presence of water, with different chloride composition, and the observed porosity values might explain the low resistivity values observed in the shallower to intermediate, z > -500 m.a.s.l. parts of the 3D electrical resistivity model near the coast but is unlikely to explain both, the deeper low resistivity values observed in all the model and the near surface value around the Tejeda Caldera. Saline magmatic fluids also can decrease the resistivity, but they are not expected to be found at present time at the depths imaged by our resistivity model. The study of Plio-Quaternary volcanic activity in the northeastern part of the island (Aulinas et al., 2010) and their thermobarometric studies suggest a multistage magma ascent with evident signals of magma mixing between hot basic pristine magmas (mantle origin) and more evolved magmas at crustal levels. Their analysis of clinopyroxenes found in recent volcanic deposits indicate that its crustal crystallization happened between 7-15 km depth with a notable increase in depth of the eruptions occurring in the last 10 ka, ruling out the presence of shallow magmatic fluids at present.

A combination of both, hydrothermal alteration for the deeper parts of the island and the presence of mixed waters with a moderate amount of salinity within medium-high porosity and highly fractured Miocene shield basaltic rocks in the shallow parts near the coast are considered as the most likely explanations of the observed resistivity values.

6. Discussion and conclusions

In this section, we will compare the electrical resistivity model with the seismic velocity model of Krastel and Schmincke (2002), the density model of Camacho et al. (2000) and the magnetic anomalies of the island (Blanco-Montenegro et al., 2003). Although the degree of resolution of each of the three models (p-wave velocity, density and electrical resistivity) are different, and the data of the seismic and density models do not uniformly cover the island, it is still possible to compare the models at depth. Vp-seismic velocity and density models are not digitally available. We only have the published images, so the comparison has only been possible with the images published in plan view at 5 km depth (b.s.l) for the Vp-seismic velocity and 6 km depth (b.s.l) for the density model as well as the magnetic anomalies map (Fig. 4).

It can be observed (Fig. 4) that velocities inside the island are generally high ($Vp > 5.5$ km/s) with an increase towards the center of the island (up to 7 km/s). This increase in velocity in the central part of the island was interpreted as dense intrusions (Krastel and Schmincke, 2002). At 5 km depth, the zone with a maximum horizontal gradient of the velocity model (white line) delineates a NW-SE limit that coincides with the northern limit between the more resistive island center and the less resistive northern part of the island. A velocity of 5.5 km/s can be considered high for a basalt (Christensen and

Salisbury, 1973) suggesting that the pores may be fully saturated with water that will agree with the possible explanation of the low resistivity observed. The 3D density model of Camacho et al. (2000) was obtained using only 98 gravity measurements mainly covering the N-NE part of the island. The data show a NW to SE trend that is reflected in the final inversion model. In their inversion procedure they assume that the subsurface anomalous structures may be described by a fixed positive or negative density contrast. Thus, positive-density structures with a NW-SE alignment (white discontinuous line) are present in the northwest and in the southeast sectors of the island. Those bodies roughly agree with the high resistivity structures crossing the island. The scarcity of gravimetric data and the inversion procedure followed do not allow a more detailed comparison with the other geophysical observables. The main positive magnetic anomalies over Gran Canaria (Blanco-Montenegro et al., 2003) can be clearly correlated with the NW-SE structural trend dividing the island in two. The ENE-WSE magnetic trend (red discontinuous line) that is evident in the NW part of the island is also present in the density and electrical resistivity models. The available regional geophysical data and models show that the deeper structure of the island is mainly controlled by NW-SE structural trends.

The main electrical resistivity distribution observed in the 3D model can be correlated with previous geological interpretations. Thus, using previous geological interpretations by several authors (Donoghue et al., 2010; Schmincke and Sumita, 1998) we constructed a SE-NW geological cross-section (Fig. 5) on top of the electrical resistivity model. The lateral limits of the Tejeda Caldera at depth (black solid line on Fig. 5) coincide with the highest gradient zones. Inside the Tejeda Caldera the white discontinuous line shows the possible location of the Fataga and Mogán crystallized magma chambers that are no longer actives (Carracedo and Troll, 2016). Their resistivity is around 100 ohm m and roughly coincide with a body with null magnetization located between 2 and 5 km depth (Blanco-Montenegro et al., 2003), in contrast with more resistive syenitic intrusions located on top near the surface. The low resistivity observed at shallow levels in the caldera can be due to meteoritic water circulation. Outside the Tejeda Caldera the prevalent low resistivity observed is concurrent with the low velocity observed in the 3D velocity model (Krastel and Schmincke, 2002). Those electrical resistivity and velocity values are likely due to the combination of hydrothermal alteration and fractures originated during all the eruptive episodes on the island.

We have obtained the first 3D regional geophysical model of the whole island using 100 broadband MT stations regularly distributed along the island. The final 3D electrical resistivity model shows a shallower depth, a high resistivity structure in the center of the island that coincides with the surface trace of the Tejeda Caldera. This high resistivity structure grows to the SE with increasing depth and correlates with the seismic and gravity anomalies previously found by other geophysical models as well as with magnetic data. Outside the Tejeda Caldera, a prevalent low resistivity structure is imaged with resistivity values in the range 20-50 ohm.m. The origin of this low resistivity values can be caused by several factors but a combination of hydrothermal alteration and the presence of mixed waters with a moderate amount of salinity within medium-high porosity Miocene shield basaltic rocks are considered as the most likely explanations. From a geothermal point of view further and detailed studies of those anomalies are required in order to determine their economic potential.

Acknowledgments

This research was supported by the project GC_geotermia_01, cofinanced by the Consejo Insular de la Energía de Gran Canaria (Cabildo Insular de Gran Canaria) and Instituto Volcanológico de Canarias (INVOLCAN). The data discussion on this work was also supported by the projects RTC-2017-6627-3 and DI-16-08959, co-financed by the Spanish National Plan for Scientific-Technical Research and Innovation 2013-2016, INVOLCAN and Instituto Tecnológico y de Energías Renovables (ITER). Gary Egbert, Naser Meqbel and Anna Kelbert are thanked for providing the ModEM code. H-U Schmincke acknowledges Deutsche Forschungsgemeinschaft Grant SCHM 250/94-1. Editor in Chief Christopher Bromley, Martyn Unsworth and two more anonymous reviewers helped to improve and clarify this manuscript.

References

Abdelfettah, Y., Saisha, P., Larnier, H., Matthey, P.D., Schill, E., 2018. Continuous and time-lapse magnetotelluric monitoring of low volume injection at Rittershoffen geothermal project, northern Alsace – France. Geothermics 71 (April 2017), 1–11. https://doi.org/10.1016/j.geothermics.2017.08.004.

Aizawa, K., Ogawa, Y., Ishido, T., 2009. Groundwater flow and hydrothermal systems within volcanic edifices: delineation by electric self-potential and magnetotellurics. J. Geophys. Res. Solid Earth. https://doi.org/10.1029/2008JB005910.

Anuario Energético de Canarias. http://www.gobiernodeca-narias.org/istac/jaxiistac/descarga.do?uripx=urn:uuid:e0affad3-8530-433b-a6cd-d86cbe258944.

Ars, J.-M., Tarits, P., Hautot, S., Bellanger, M., Coutant, O., Maia, M., 2019. Joint inversion of gravity and surface wave data constrained by magnetotelluric: application to deep geothermal exploration of crustal fault zone in felsic basement. Geothermics 80, 56–68. https://doi.org/10.1016/j.geothermics.2019.02.006.

Aulinas, M., Gimeno, D., Fernandez-Turiel, J.L., Perez-Torrado, F.J., Rodriguez-Gonzalez, A., Gasperini, D., 2010. The Plio-Quaternary magmatic feeding system beneath Gran Canaria (Canary Islands, Spain): constraints from thermobarometric studies. J. Geol. Soc. 167, 785–801. https://doi.org/10.1144/0016-76492009-184.

Banda, E., Dañobeitia, J.J., Suriñach, E., Ansorge, J., 1981. Features of crustal structure under the Canary Islands. Earth Planet. Sci. Lett. 55, 11–24.

Bibby, H.M., Caldwell, T.G., Davey, F.J., Webb, T.H., 1995. Geophysical evidence on the structure of the Taupo Volcanic Zone and its hydrothermal circulation. J. Volcanol. Geotherm. Res. 68, 29–58.

Blanco-Montenegro, I., Torta, J.M., García, A., Arana, V., 2003. Analysis and modelling of the aeromagnetic anomalies of Gran Canaria (Canary Islands). Earth Planet. Sci. Lett. https://doi.org/10.1016/S0012-821X(02)01129-9.

Booker, J.R., 2014. The magnetotelluric phase tensor: a critical review. Surv. Geophys. https://doi.org/10.1007/s10712-013-9234-2.

Bosshard, E., Macfarlane, D.J., 1970. Journal of geophysical research. Journal of Geophysical Research 75 (26), 4901–4917.

Cabrera, M.C., Custodio, E., 2004. Groundwater flow in a volcanic-sedimentary coastal aquifer: Telde area, Gran Canaria, Canary Islands, Spain. Hydrogeol. J. 12 (3), 305–320. https://doi.org/10.1007/s10040-003-0316-y.

Caldwell, T.G., Bibby, H.M., Brown, C., 2004. The magnetotelluric phase tensor. Geophys. J. Int. https://doi.org/10.1111/j.1365-246X.2004.02281.x.

Camacho, A.G., Montesinos, F.G., Vieira, R., 2000. Gravity inversion by means of growing bodies. Geophysics 65 (1), 95–101. https://doi.org/10.1190/1.1444729.

Carracedo, J.C., Troll, V.R., 2016. The Geology of the Canary Islands. The Geology of the Canary Islands.

Chave, A.D., Thomson, D.J., 2004. Bounded influence magnetotelluric response function estimation. Geophys. J. Int. 157 (3), 988–1006. https://doi.org/10.1111/j.1365-246X.2004.02203.x.

Chave, A.D., Jones, A.G., Mackie, R., Rodi, W., 2012. The Magnetotelluric Method. Cambridge University Press, Cambridge. https://doi.org/10.1017/ CBO9781139020138.

Christensen, N.I., Salisbury, M.H., 1973. Velocities, elastic moduli and weathering-age relations for pacific layer 2 basalts. Earth Planet. Sci. Lett. 19 (4), 461–470. doi.org/10.1016/0012-821X(73)90190-8.

Coppo, N., Schnegg, P.A., Heise, W., Falco, P., Costa, R., 2008. Multiple caldera collapses inferred from the shallow electrical resistivity signature of the Las Cañaadas caldera, Tenerife, Canary Islands. J. Volcanol. Geotherm. Res. 170 (3–4), 153–166. https:// doi.org/10.1016/j.jvolgeores.2007.09.013.

Donoghue, E., Troll, V.R., Harris, C., O'Halloran, A., Walter, T.R., Pérez Torrado, F.J., 2008. Low-temperature hydrothermal alteration of intra-caldera tuffs, Miocene Tejeda caldera, Gran Canaria, Canary Islands. J. Volcanol. Geotherm. Res. 176 (4), 551–564. https://doi.org/10.1016/J.JVOLGEORES.2008.05.002.

Donoghue, E., Troll, V.R., Harris, C., 2010. Fluid-rock interaction in the miocene, postcaldera, Tejeda Intrusive Complex, Gran Canaria (Canary Islands): insights from mineralogy, and O- and H-isotope geochemistry. J. Petrol. 51 (10), 2149–2176. doi.org/10.1093/petrology/egq052.

Drury, M.J., 1979. On laboratory measurements on basalts and gabbros. Geophys. J.R. Astr. Soc 56, 241–253.

Egbert, G.D., Kelbert, A., 2012. Computational recipes for electromagnetic inverse problems. Geophys. J. Int. https://doi.org/10.1111/j.1365-246X.2011.05347.x.

Flóvenz, Ó.G., Spangenberg, E., Kulenkampff, J., Árnason, K., Karlsdóttir, R., Huenges, E., 2005. The Role of Electrical Interface Conduction in Geothermal Exploration. Proceedings World Geothermal Congress.

Funck, T., Schmincke, H.-U., 1998. Growth and destruction of Gran Canaria deduced from seismic reflection and bathymetric data. J. Geophys. Res. Solid Earth 103 (7), 15393–15407.

Funck, T., Dickmann, T., Rihm, R., Krastel, S., Lykke-Andersen, H., Schmincke, H.-U., 1996. Reflection seismic investigations in the volcaniclastic apron of Gran Canaria and implications for its volcanic evolution. Geophys. J. Int. 125 (2), 519–536. https://doi.org/10.1111/j.1365-246X.1996.tb00015.x.

Garcia, X., Jones, A.G., 2010. Internal structure of the western flank of the Cumbre Vieja volcano, la Palma, Canary Islands, from land magnetotelluric imaging. J. Geophys. Res. Solid Earth 115 (7), 1–12. https://doi.org/10.1029/2009JB006445.

García-Yeguas, Araceli, Ledo, J., Pin˜a-Varas, P., Prudencio, J., Queralt, P., Marcuello, A., et al., 2017. A 3D joint interpretation of magnetotelluric and seismic tomographic models: the case of the volcanic island of Tenerife. Comput. Geosci. https://doi.org/ 10.1016/j.cageo.2017.08.003.

Gunderson, R., Cumming, W., Astra, D., Harvey, C., Ussher, G., Harvey, C., et al., 2000. Analysis of smectite clays in geothermal drill cuttings by the methylene blue method: for well site geothermometry and resistivity sounding correlation. Proceedings World Geothermal Congress 1175–1181.

Hoernle, K., Schmincke, H.-U., 1993. The petrology of the tholeiites through melilite nephelinites on Gran Canaria, Canary Islands: crystal fractionation, accumulation, and depths of melting. J. Petrol. 34 (3), 573–597. https://doi.org/10.1093/ petrology/34.3.573.

IGME, 1981. Estudio Del Gradiente Geotermico En Zonas Anomalas De Gran Canaria. Informe IGME.

Kelbert, A., Meqbel, N., Egbert, G.D., Tandon, K., 2014. ModEM: a modular system for inversion of electromagnetic geophysical data. Comput. Geosci. https://doi.org/ 10.1016/j.cageo.2014.01.010.

Komori, S., Kagiyama, T., Takakura, S., Ohsawa, S., Mimura, M., Mogi, T., 2013. Effect of the hydrothermal alteration on the surface conductivity of rock matrix: comparative study between relatively high and low temperature hydrothermal systems. J. Volcanol. Geotherm. Res. https://doi.org/10.1016/j.jvolgeores.2013.08.009.

Krastel, S., Schmincke, H.U., 2002. Crustal structure of northern Gran Canaria, Canary Islands, deduced from active seismic tomography. J. Volcanol. Geotherm. Res. 115 (1–2), 153–177. https://doi.org/10.1016/S0377-0273(01)00313-4.

Krieger, L., Peacock, J.R., 2014. MTpy: a Python toolbox for magnetotellurics. Comput. Geosci. https://doi.org/10.1016/j.cageo.2014.07.013.

Larnier, H., Sailhac, P., Chambodut, A., 2018. Detection and characterization of lightning-based sources using continuous wavelet transform: application to audiomagnetotellurics. Geophys. J. Int. https://doi.org/10.1093/gji/ggx418.

Lee, B., Unsworth, M., A´rnason, K., Cordell, D., 2019. Imaging the magmatic system beneath the Krafla geothermal field, Iceland: a new 3-D electrical resistivity model from inversion of magnetotelluric data. Geophys. J. Int. 220 (1), 541–567. https://doi.org/10.1093/gji/ggz427.

Lietz, J., Schmincke, H.-U., 1975. Miocene-pliocene sea-level changes and volcanic phases on gran Canaria (Canary Islands) in the light of new K-Ar ages. Palaeogeogr. Palaeoclimatol. Palaeoecol. 18 (3), 213–239. https://doi.org/10.1016/0031-0182(75)90034-6.

Maithya, J., Fujimitsu, Y., 2019. Analysis and interpretation of magnetotelluric data in characterization of geothermal resource in Eburru geothermal field, Kenya. Geothermics 81, 12–31. https://doi.org/10.1016/j.geothermics.2019.04.003.

Martí, A., Queralt, P., Jones, A.G., Ledo, J., 2005. Improving Bahr's invariant parameters using the WAL approach. Geophys. J. Int. 163 (1) https://doi.org/10.1111/j.1365-246X.2005.02748.x.

Martí, A., Queralt, P., Ledo, J., 2009. WALDIM: a code for the dimensionality analysis of magnetotelluric data using the rotational invariants of the magnetotelluric tensor. Comput. Geosci. 35 (12), 2295–2303. https://doi.org/10.1016/j.cageo.2009.03.004.

Muñoz, G., Bauer, K., Moeck, I., Schulze, A., Ritter, O., 2010. Exploring the Gross Schonebeck (Germany) geothermal site using a statistical joint interpretation of magnetotelluric and seismic tomography models. Geothermics 39, 35. https://doi.org/10.1016/j.geothermics.2009.12.004.

Pérez Torrado, F.J., Cabrera Santana, M.C., Anto´n Gil, A., Muñoz Sanz, F., 2004. Estratigrafía y petrología de los depósitos de 'Azulejos' del borde de la Caldera de Tejeda (Gran Canaria, Islas Canarias). Geotemas 6, 159–162.

Pearson, S.C.P., Kiyosugi, K., Lehto, H.L., Saballos, J.A., Connor, C.B., Sanford, W.E., 2012. Integrated geophysical and hydrothermal models of flank degassing and fluid flow at Masaya volcano, Nicaragua. Geochem. Geophys. Geosyst. 5 (13) https://doi. org/10.1029/2012GC004117.

Piñaa-Varas, P., Ledo, J., Queralt, P., Marcuello, A., Bellmunt, F., Hidalgo, R., Messeiller, M., 2014. 3-d magnetotelluric exploration of Tenerife geothermal system (Canary Islands, Spain). Surv. Geophys. 35 (4) https://doi.org/10.1007/s10712- 014-9280-4.

Piña-Varas, P., Ledo, J., Queralt, P., Marcuello, A., Bellmunt, F., Ogaya, X., et al., 2015. Vertical collapse origin of Las Can˜adas caldera (Tenerife, Canary Islands) revealed by 3-D magnetotelluric inversion. Geophys. Res. Lett. 42 (6) https://doi.org/10.1002/ 2015GL063042.

Piñaa-Varas, P., Ledo, J., Queralt, P., Marcuello, A., Perez, N., 2018. On the detectability of Teide volcano magma chambers (Tenerife, Canary Islands) with magnetotelluric data. Earth Planets Space 70 (1). https://doi.org/10.1186/s40623-018-0783-y.

Pous, J., Heise, W., Schnegg, P.A., Muñoz, G., Martí, J., Soriano, C., 2002. Magnetotelluric study of the Las Canadas caldera (Tenerife, Canary Islands): structural and hydrogeological implications. Earth Planet. Sci. Lett. 204 (1–2), 249–263. https:// doi.org/10.1016/S0012-821X(02)00956-1.

Robertson, K., Thiel, S., Meqbel, N., 2020. Quality over quantity: on workflow and model space exploration of 3D inversion of MT data. Earth Planets Space 72 (1). https:// doi.org/10.1186/s40623-019-1125-4.

Rodríguez, F., Pérez, N.M., Padrón, E., Melián, G., Piña-Varas, P., Dionis, S., et al., 2015. Surface geochemical and geophysical studies for geothermal exploration at the southern volcanic rift zone of Tenerife, Canary Islands, Spain. Geothermics. https:// doi.org/10.1016/j.geothermics.2015.02.007.

Schmincke, H.-U., 1968. Pliozäne, subtropische Vegetation auf Gran Canaria. Die Naturwissenschaften 55 (4), 185–186. https://doi.org/10.1007/BF00591034.

Schmincke, H.-U., 1976. The Geology of the Canary Islands. https://doi.org/10.1007/978-94-010-1566-0_4.

Schmincke, H-U, Sumita, M., 1998. Volcanic evolution of Gran Canaria reconstructed from apron sediments: synthesis of vicap project drilling. Proc. Ocean Drill. Prog. Sci. Results 157 (23), 443–469. https://doi.org/10.2973/odp.proc. sr.157.135.1998.

Schmincke, H.-U., Sumita, M., 2011. The canary archipelago - growth and decline of volcanic islands | Der kanarische archipel vor Nordwest-Afrika: Wachstum und zerfall von vulkaninseln. Geogr. Rundsch. 63 (6), 18–25.

Schmincke, H.-U., Sumita, M., 2014. Instability of oceanic volcanic edifices: examples of sector collapse, debris avalanches, and debris flows from Gran Canaria (Canary Islands). Adv. Nat. Technol. Hazards Res. 37 https://doi.org/10.1007/978-3-319-00972-8_54.

Schmincke, H-U., Klügel, A., Hansteen, T.H., Hoernle, K., van den Bogaard, P., 1998. Samples from the Jurassic ocean crust beneath Gran Canaria, La Palma and

Lanzarote (Canary Islands). Earth Planet. Sci. Lett. 163, 343–360. https://doi.org/ 10.1016/S0012-821X(98)00168-X.

Suriñach, E., 1986. La estructura cortical del archipielago Canario, resultados de la interpretación de perfiles sísmicos profundos. Anales de Física 82, 62–77.

Troll, V.R., Schmincke, H.-U., 2002. Magma mixing and crustal recycling recorded in ternary feldspar from compositionally zoned peralkaline Ignimbrite “A”, Gran Canaria, Canary Islands. J. Petrol. 43 (2), 243–270.

Troll, V.R., Walter, T.R., Schmincke, H.U., 2002. Cyclic caldera collapse: piston or piecemeal subsidence? Field and experimental evidence. Geology 30 (2), 135–138. https://doi.org/10.1130/0091-7613(2002)030<0135:CCCPOP>2.0.CO;2.

Ussher, G., Harvey, C., Johnstone, R., Anderson, E., 2000a. Understanding the resistivities observed in geothermal systems Grenada geothermal View project mariposa geothermal view project understanding the resistivities observed IN geothermal systems. In: Proceedings World Geothermal Congress. May 2000, pp. 1915–1920. Retrieved from. https://www.researchgate.net/publication/ 265468337.

Ussher, Greg, Harvey, C., Johnstone, R., Anderson, E., 2000b. Understanding the resistivities observed in geothermal systems. In: World Geothermal Congress 2000. May, pp. 1915–1920.

Van den Bogaard, P., Schmincke, H.-U., 1998. Chronostratigraphy of Gran Canaria. Proc. Ocean Drill. Prog. Sci. Results 157, 127–140.

Weaver, P.P.E., Schmincke, H.-U., Firth, J.V., Duffield, W. (Eds.), 1998. Proceedings of the Ocean Drilling Program. Vol. 157.

Ye, S., Canales, J.P., Rihm, R., Dañobeitia, J.J., Gallart, J., 1999. A crustal transect through the northern and northeastern part of the volcanic edifice of Gran Canaria, Canary Islands. J. Geodyn. https://doi.org/10.1016/S0264-3707(98)00028-3.

Yoshimura, R., Ogawa, Y., Yukutake, Y., Kanda, W., Komori, S., Hase, H., et al., 2018. Resistivity characterisation of Hakone volcano, Central Japan, by three-dimensional inversion. Earth Planets Space 70 (1), 66. https://doi.org/10.1186/623-018-0848-y

Figure captions.

Figure 1. A. Geological map of Gran Canaria Island. Black points: location of the magnetotelluric stations. B. Eruptive rates and ages of the main Volcano-stratigraphic units of Gran Canaria. Modified from Schmincke and Sumita, 2010.

Figure 2. a): Horizontal cross-sections of the 3D electrical resistivity model. The white continuous line on the top left horizontal cross-section shows the limit of the saltwater intrusion (SWI), see figure S5 from the supplementary material for further details; b): Vertical cross sections SW-NE across the island.

Figure 3. Sensitivity analysis of the low resistivity vertical-like structures of the 3D electrical resistivity model. The data recorded in the southern part of the island (sites 11, 27, 40 and 86) are more affected by the removal of this structures than the sites located in the eastern part of the island (sites 79 and 92).

Figure 4. Comparison of horizontal cross sections of the electrical resistivity model at 5 km b.s.l. (A), seismic velocity model at 5 km b.s.l. (Krastel and Schmincke, 2002) (B), density model from Camacho et al. (2000) at 6 km b.s.l (C). and the magnetic anomaly map from Blanco-Montenegro et al. (2003) (D). Continuous white line corresponds to the limit between low and high velocities; dashed white line: contour of the high-density anomalies; red dashed lines: Magnetic alignments revealed by the aeromagnetic anomaly map of Gran Canaria.

Figure 5. Geological interpretation of the electrical resistivity model. The background model corresponds to the vertical SW-NE cross-section of the 3D electrical resistivity model. The pervasive low resistivity observed outside the Tejeda Caldera is likely due to the combination of hydrothermal alteration and fractures originated during all the eruptive episodes on the island. The Tejeda Caldera is imaged as a resistive structure, the deeper Fataga and Mogan group magmatic chambers are imaged as resistive structures in comparison with the structures outside of the caldera but less resistive than the syenitic cone sheet swarm located on top.

Figures

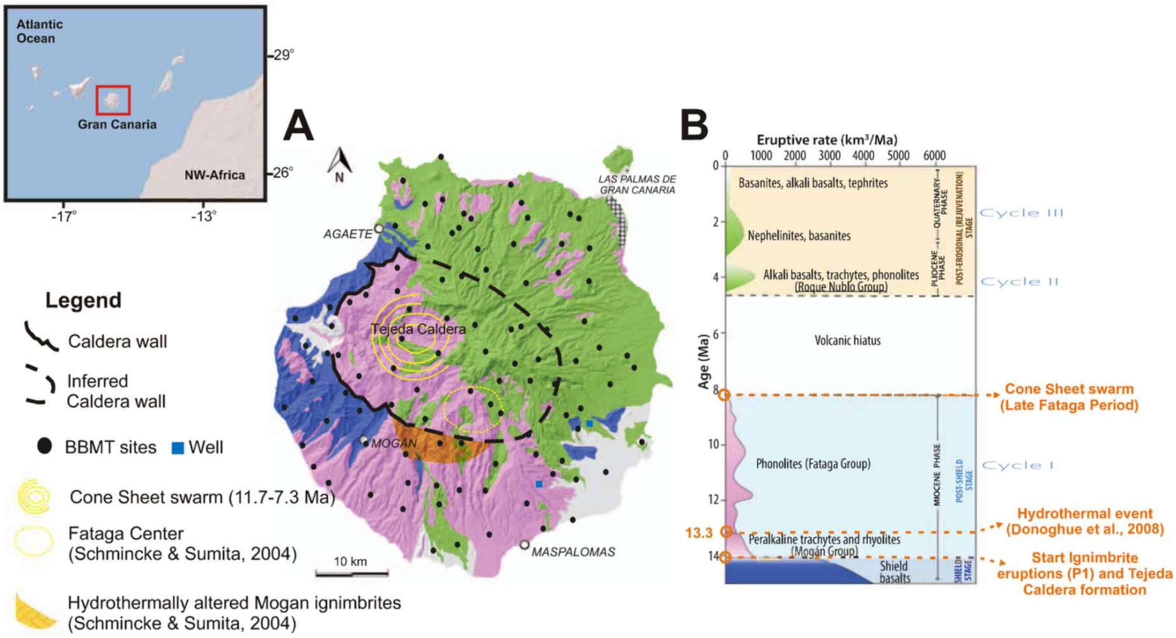

Figure 1

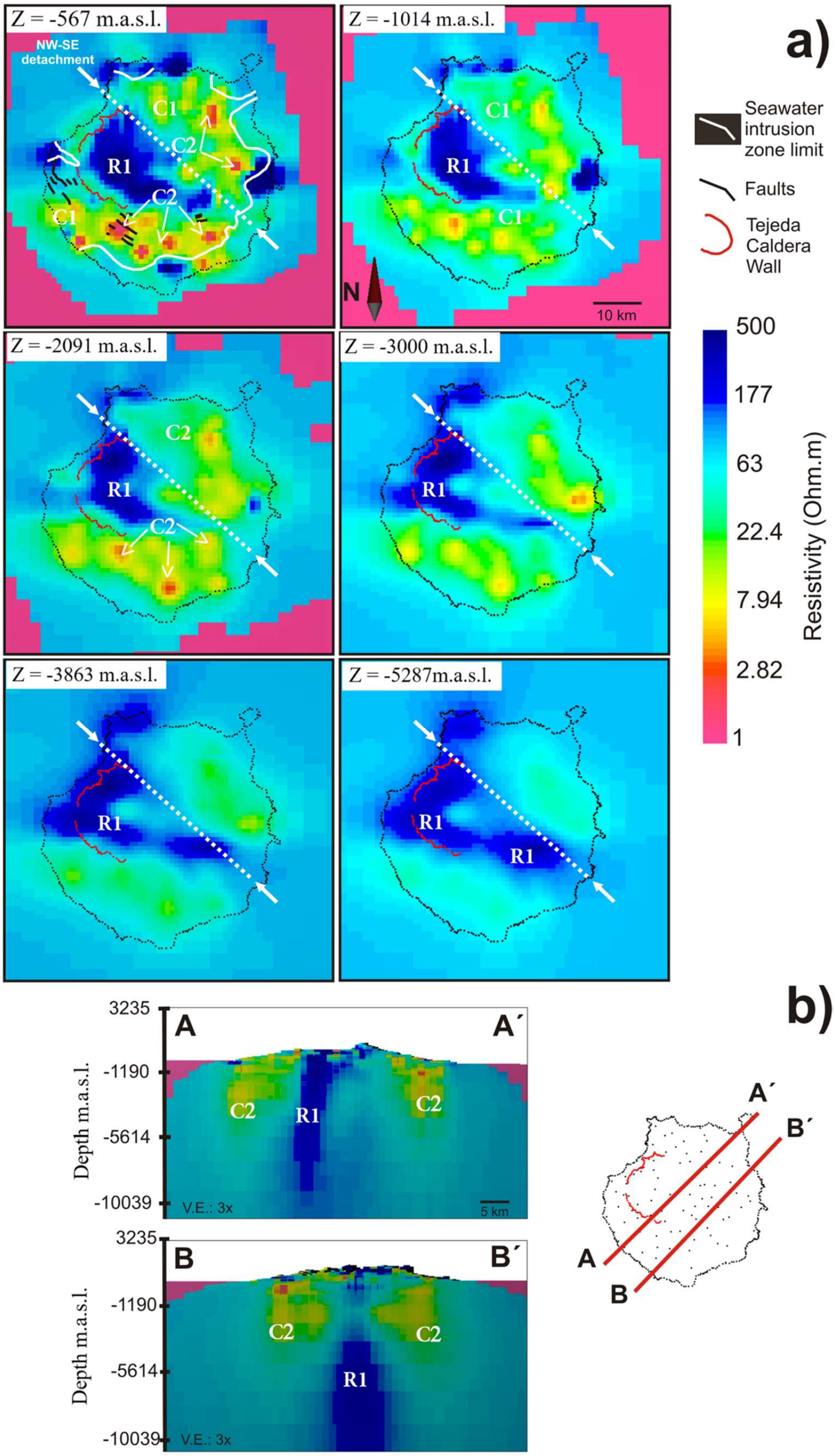

a)
Z = -567 m.a.s.l.
NW-SE detachment
C1
C2
R1
Z = -1014 m.a.s.l.
N
10 km
Seawater intrusion zone limit
Faults
Tejeda Caldera Wall
Z = -2091 m.a.s.l.
Z = -3000 m.a.s.l.
Z = -3863 m.a.s.l.
Z = -5287m.a.s.l.
500
177
63
22.4
7.94
2.82
1
Resistivity (Ohm.m)
b)
A
A´
B
B´
3235
-1190
-5614
-10039
Depth m.a.s.l.
V.E.: 3x
5 km

Figure 2

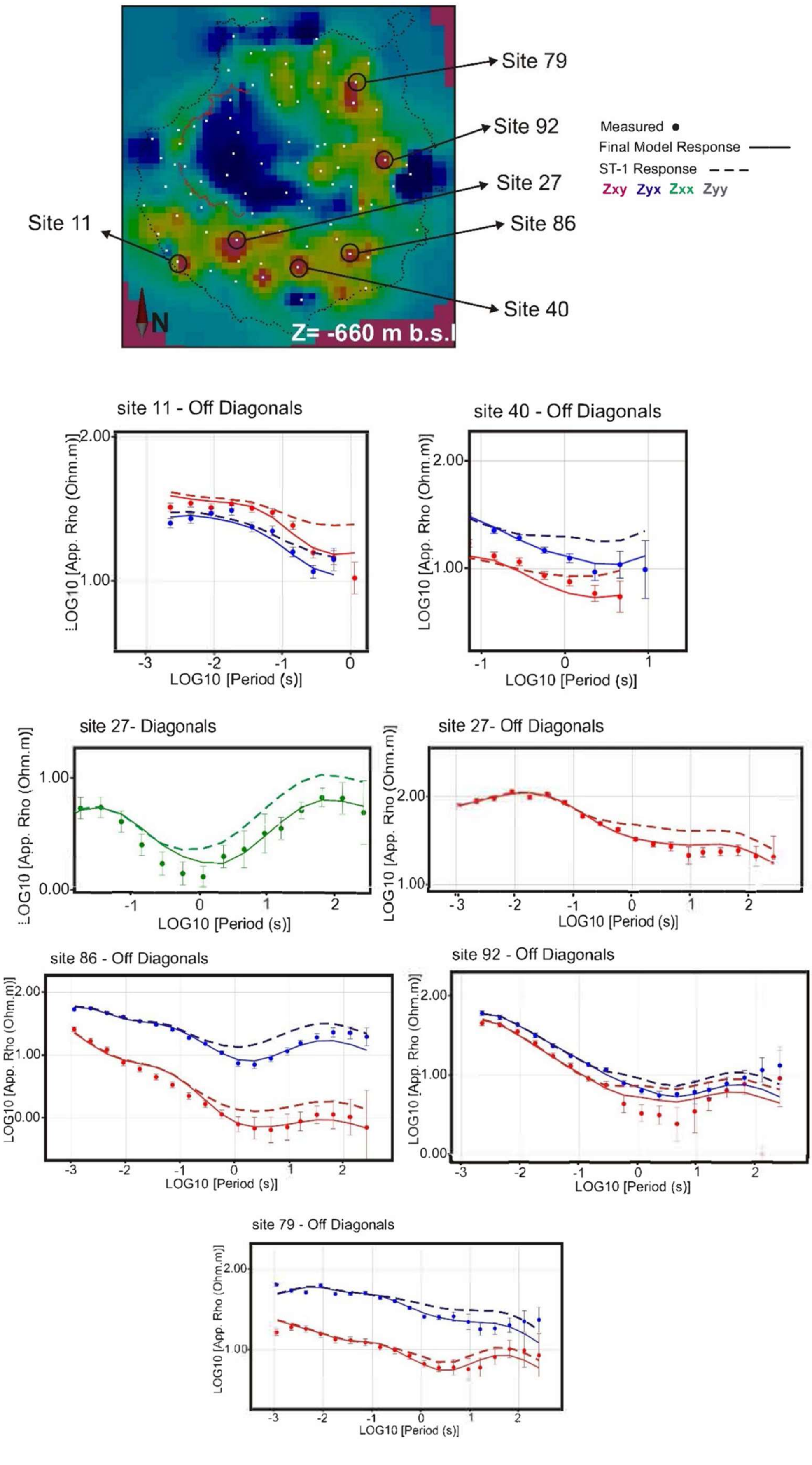
Site 79
Site 92
Site 27
Site 11
Site 86
Site 40
N
Z= -660 m b.s.l
Measured
Final Model Response
ST-1 Response
Zxy Zyx Zxx Zyy
site 11 - Off Diagonals
site 40 - Off Diagonals
site 27- Diagonals
site 27- Off Diagonals
site 86 - Off Diagonals
site 92 - Off Diagonals
site 79 - Off Diagonals
LOG10 [App. Rho (Ohm.m)]
LOG10 [Period (s)]

Figure 3

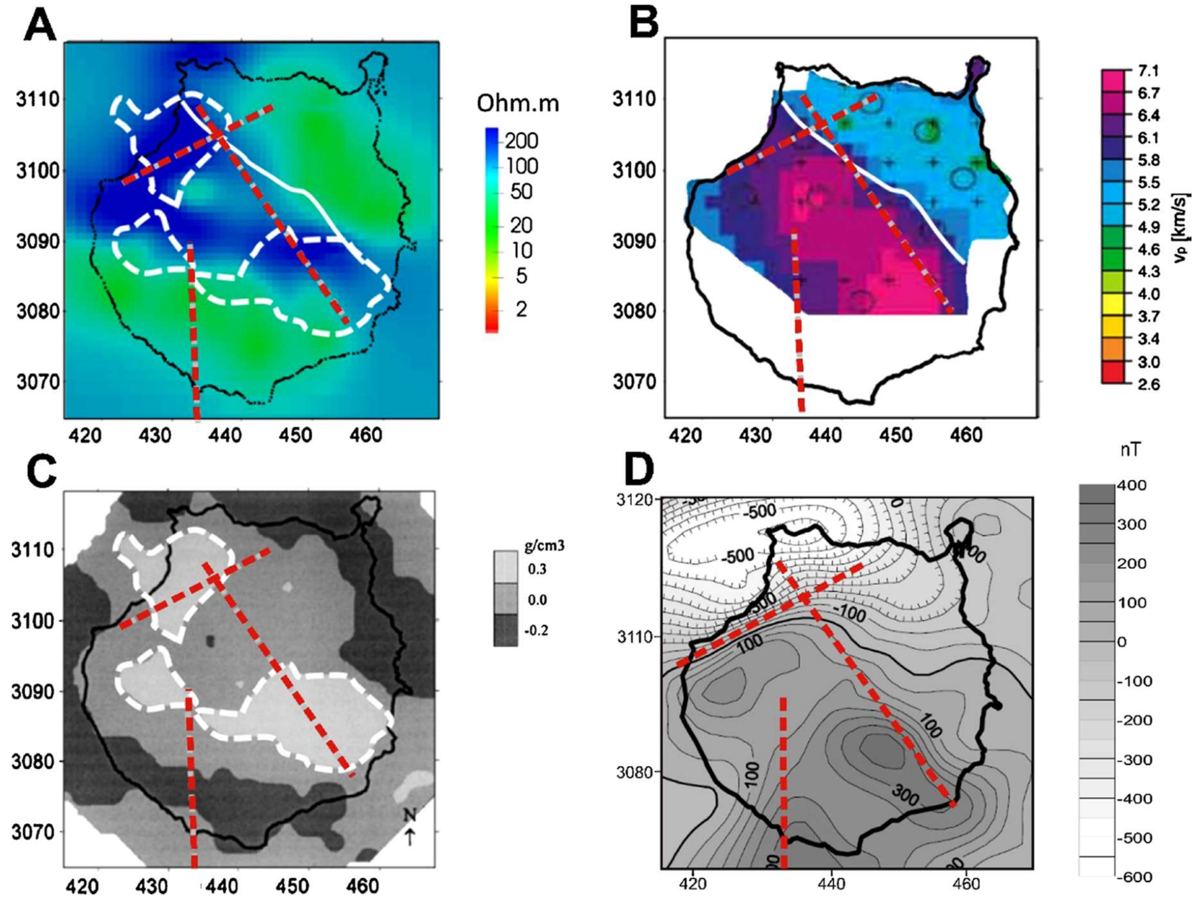

Figure 4

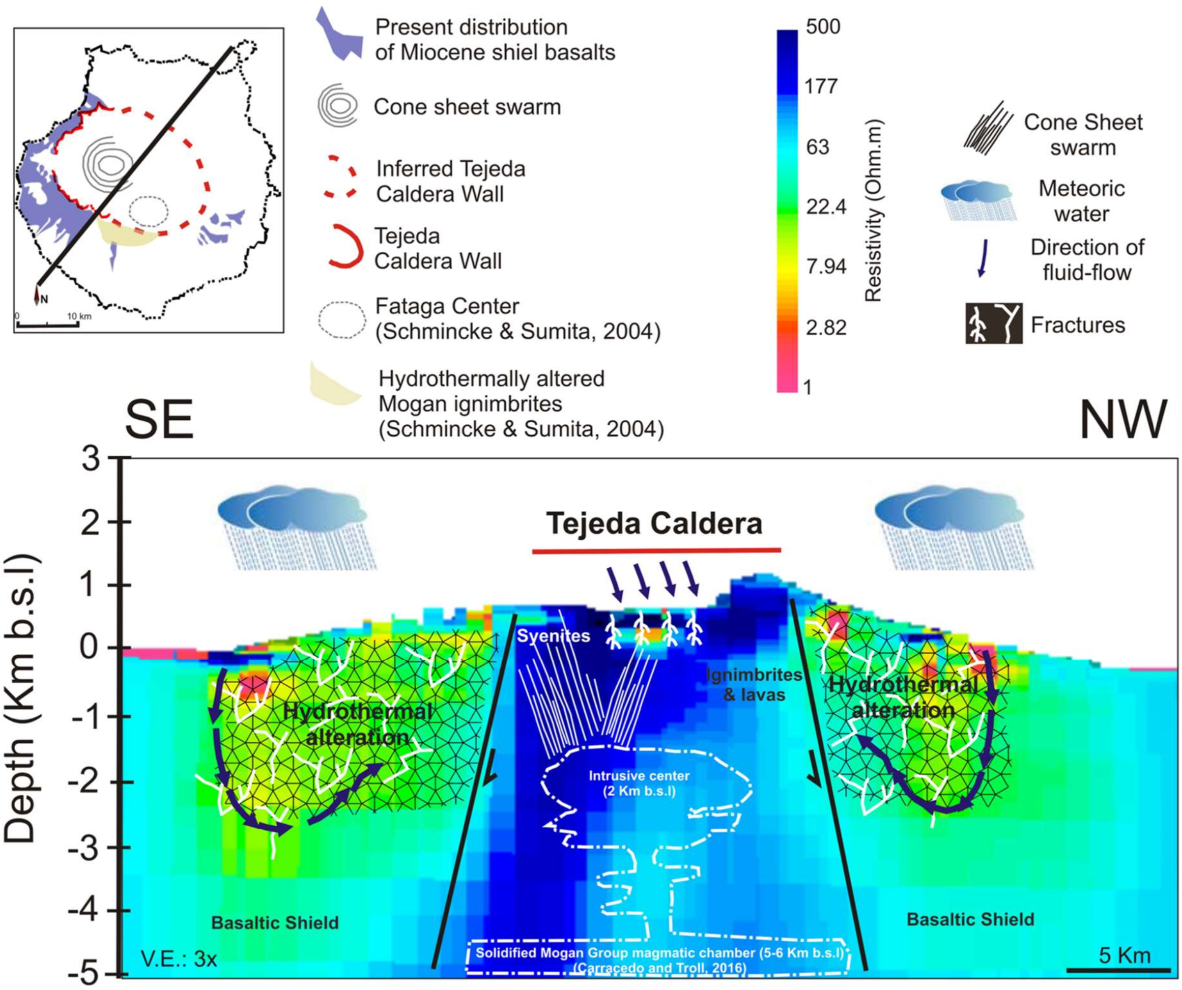

Present distribution of Miocene shiel basalts
Cone sheet swarm
Inferred Tejeda Caldera Wall
Tejeda Caldera Wall
Fataga Center (Schmincke & Sumita, 2004)
Hydrothermally altered Mogan ignimbrites (Schmincke & Sumita, 2004)
500
177
63
22.4
7.94
2.82
1
Resistivity (Ohm.m)
Cone Sheet swarm
Meteoric water
Direction of fluid-flow
Fractures
N
10 km
SE
NW
Depth (Km b.s.l)
3
2
1
0
-1
-2
-3
-4
-5
Tejeda Caldera
Syenites
Ignimbrites & lavas
Hydrothermal alteration
Hydrothermal alteration
Intrusive center (2 Km b.s.l)
Basaltic Shield
Basaltic Shield
V.E.: 3x
Solidified Mogan Group magmatic chamber (5-6 Km b.s.l) (Carracedo and Troll, 2016)
5 Km

Figure 5

Appendix A. Supplementary data (Supporting Information).

Supporting Information for

3D electrical resistivity of Gran Canaria island using magnetotelluric data

J. Ledo[1,2], M. García-Merino[2], H. Larnier[2,3], K. Slezak[2*], P. Piña-Varas[1], A. Marcuello[1], P. Queralt[1], N. M. Pérez[2,3], H.-U. Schmincke[4] and M. Sumita[4].

[1]Departament de Dinàmica de la Terra i dels Oceans, Universitat de Barcelona, Spain.

[2]Instituto Volcanológico de Canarias (INVOLCAN), 38320 La Laguna, Tenerife, Canary Islands, Spain

[3]Instituto Tecnológico y de Energías Renovables (ITER), 38600 Granadilla de Abona, Tenerife, Canary Islands, Spain

[4]GEOMAR Helmholtz Centre for Ocean Research Kiel, Wischhofstr. 1-3, 24148 Kiel, Germany.

[*]now at Department of Geophysics, Universidad de Chile, Blanco Encalada 2002, Santiago, Chile

Corresponding author: Juanjo Ledo (jledo@ub.edu)

Contents of this file

Figures S1 to S7

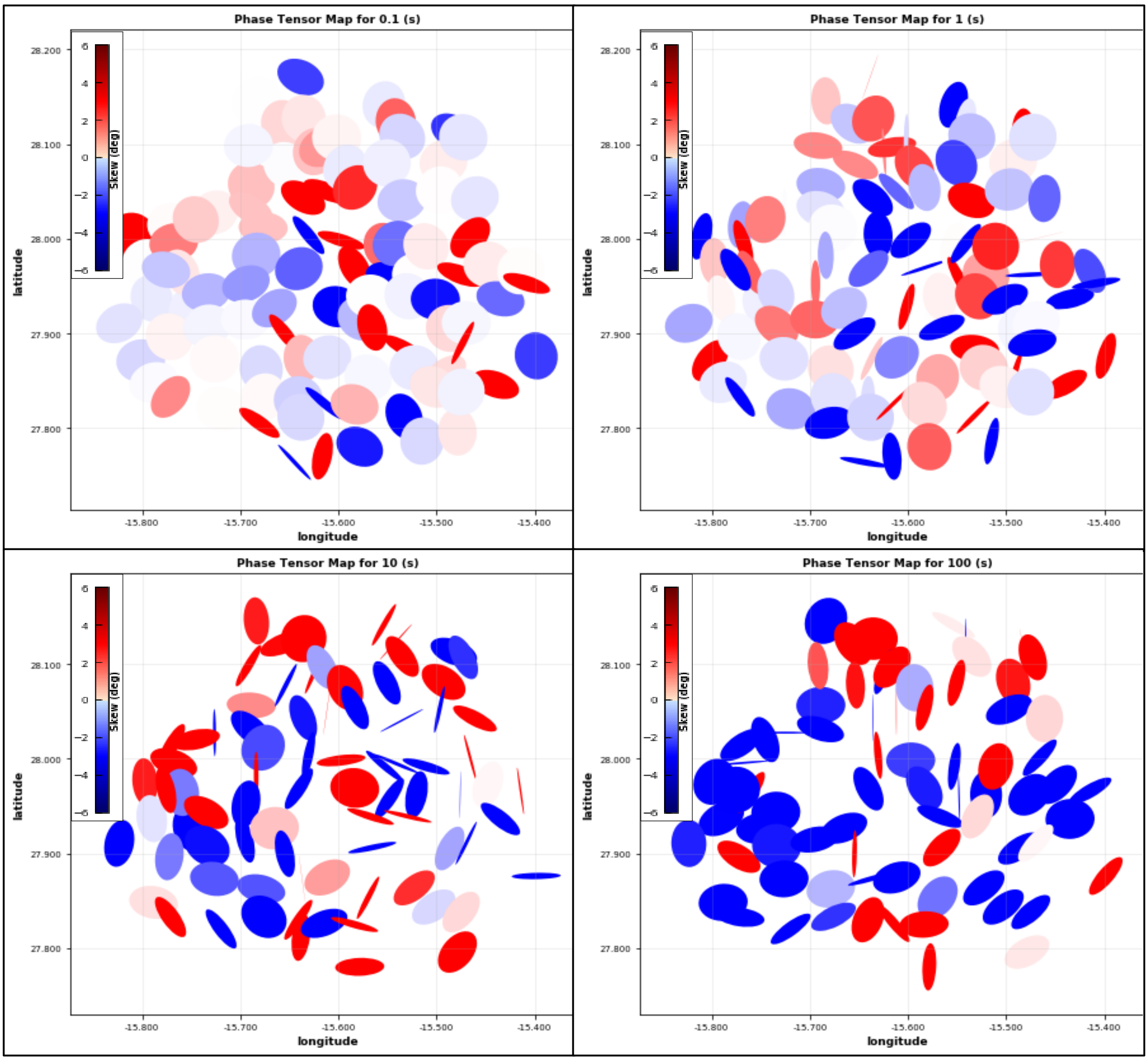

Figure S1. Phase tensor ellipses at four periods for the whole dataset. The color fill of the ellipses is the skew angle. In general, all the data shows a 3D behavior.

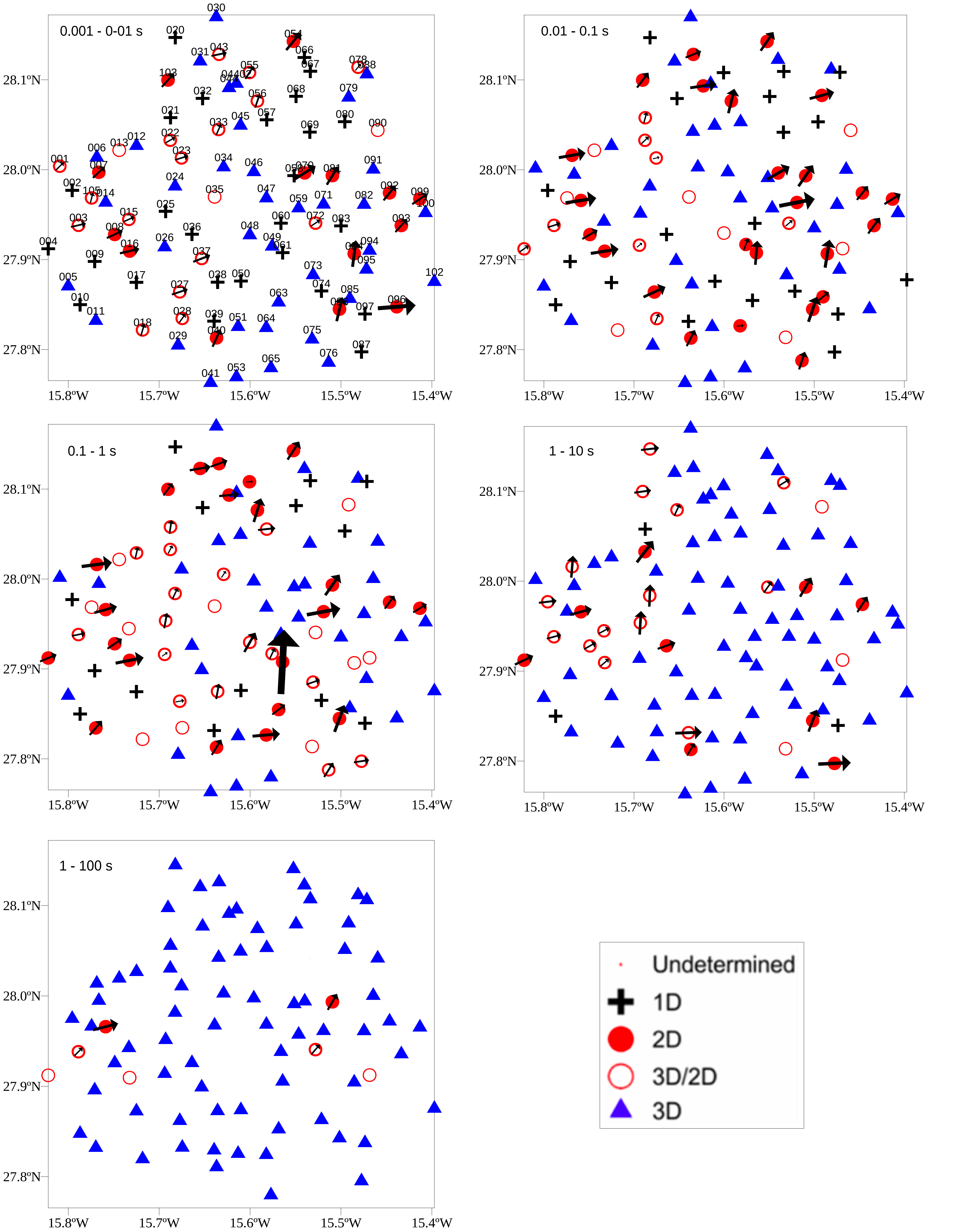

Figure S2. WAL invariants results for different period bands. Black arrows represent the strike direction for the 2D cases. Size of the arrow is inverserly proportional to the error of the strike angle.

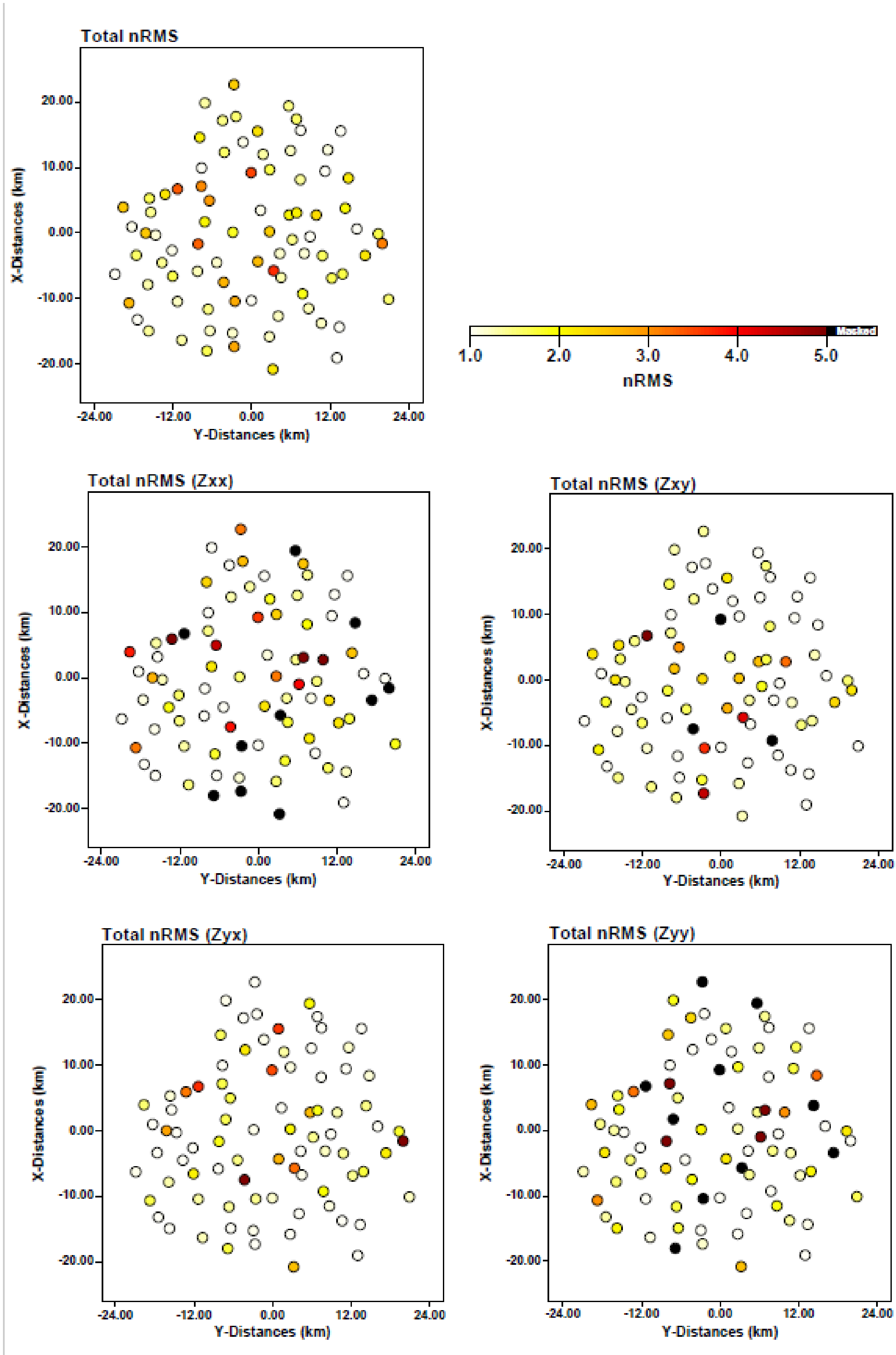

Figure S3. Root mean square (RMS) for the full impedance tensor components and individual components in the period range 0.001 to 256 s between the raw data and the responses of the 3D electrical resistivity of the final model. The average nRMS for all the sites is 1.70.

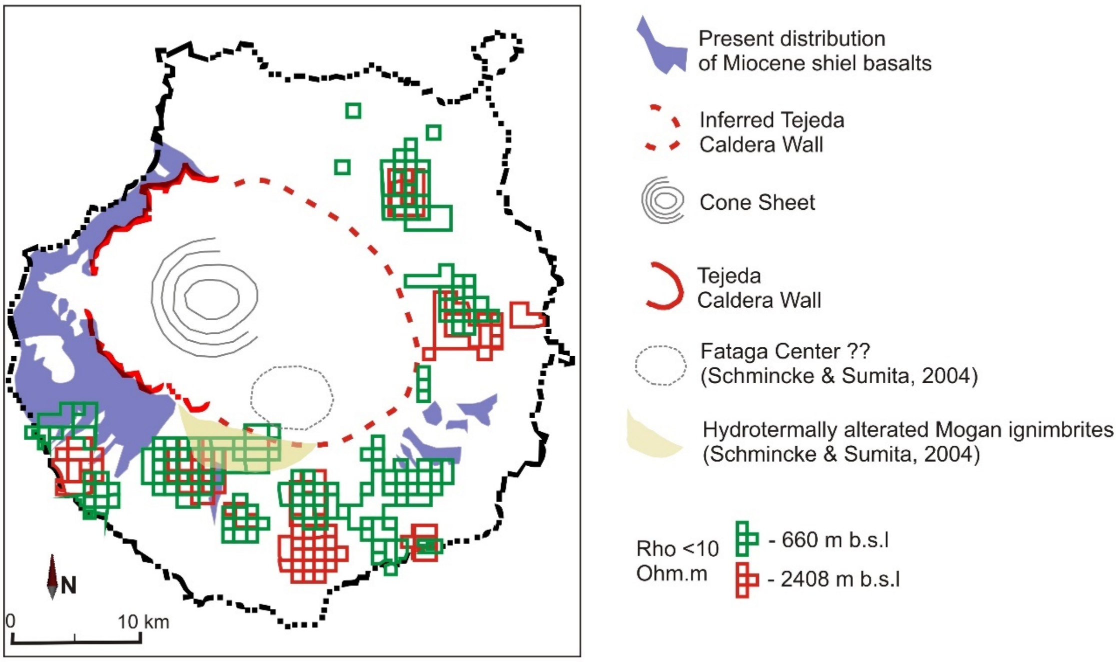

Figure S4. Localization of the near-vertical low resistivity structures of the 3D resistivity model labeled as C2 in figure 2.

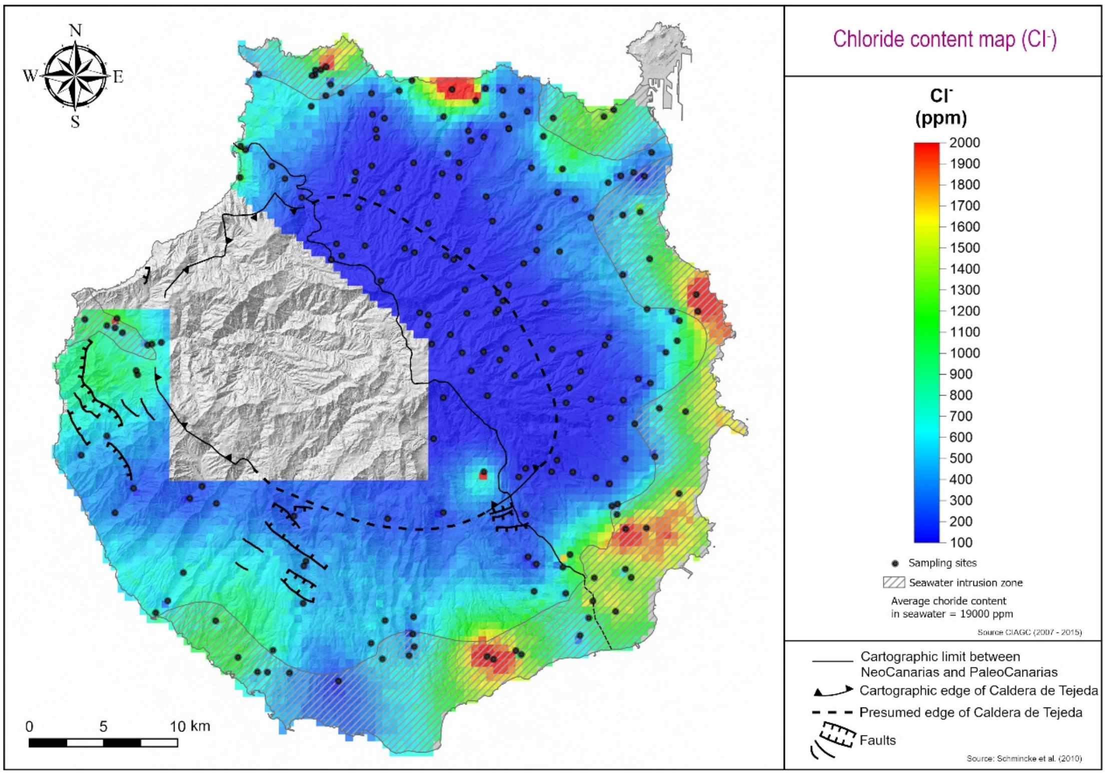

Figure S5. Map of Cl- (ppm) obtained from the database available at the CIAGC (2007-2015).

Figure S6.

Vertical cross sections of the 3D model in NW-SE and perpendicular NE-SW directions.

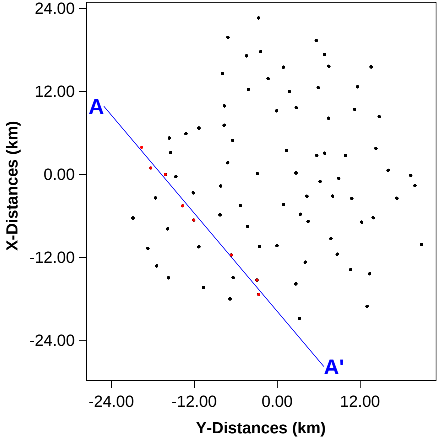

24.00
12.00
0.00
-12.00
-24.00
A
A'
-24.00
-12.00
0.00
12.00
X-Distances (km)
Y-Distances (km)

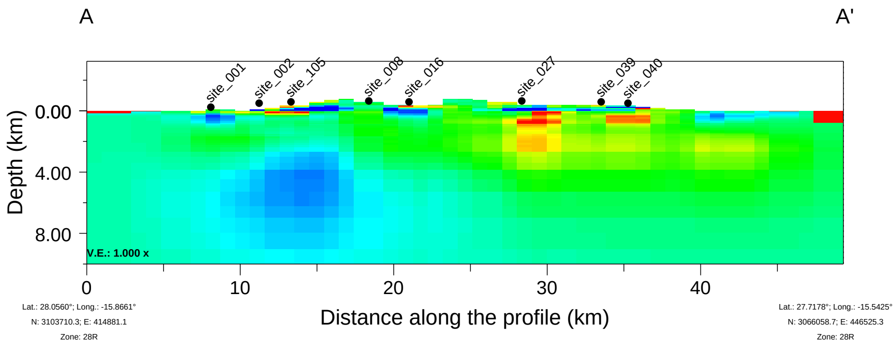

A
A'
site_001
site_002
site_105
site_008
site_016
site_027
site_039
site_040
0.00
4.00
8.00
Depth (km)
V.E.: 1.000 x
0
10
20
30
40
Distance along the profile (km)
Lat.: 28.0560°; Long.: -15.8661°
N: 3103710.3; E: 414881.1
Zone: 28R
Lat.: 27.7178°; Long.: -15.5425°
N: 3066058.7; E: 446525.3
Zone: 28R

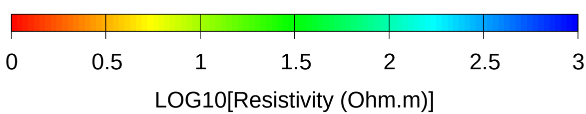

0
0.5
1
1.5
2
2.5
3
LOG10[Resistivity (Ohm.m)]

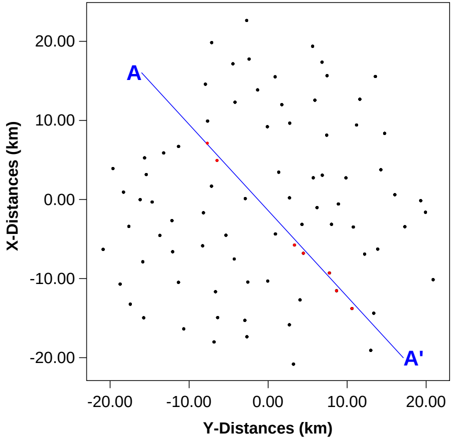
A
A'
X-Distances (km)
Y-Distances (km)
20.00
10.00
0.00
-10.00
-20.00

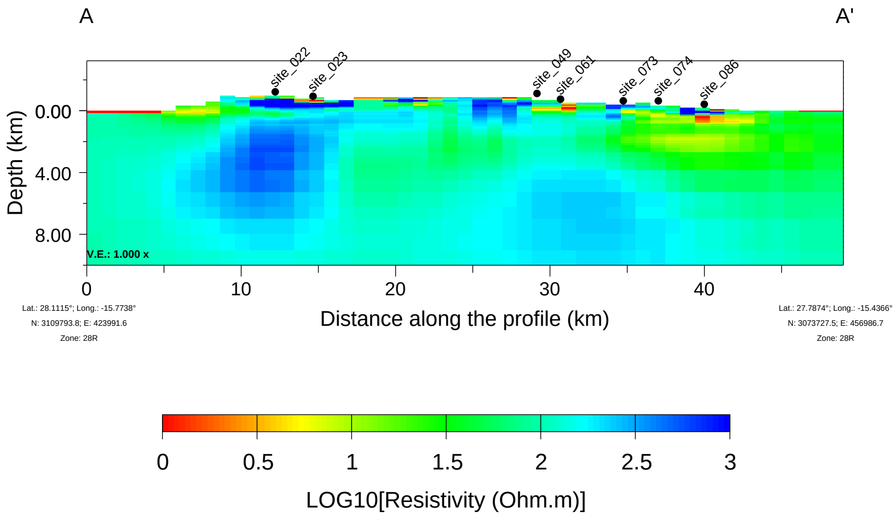
A
A'
site_022
site_023
site_049
site_061
site_073
site_074
site_086
Depth (km)
0.00
4.00
8.00
V.E.: 1.000 x
0
10
20
30
40
Distance along the profile (km)
Lat.: 28.1115°; Long.: -15.7738°
N: 3109793.8; E: 423991.6
Zone: 28R
Lat.: 27.7874°; Long.: -15.4366°
N: 3073727.5; E: 456986.7
Zone: 28R
0
0.5
1
1.5
2
2.5
3
LOG10[Resistivity (Ohm.m)]

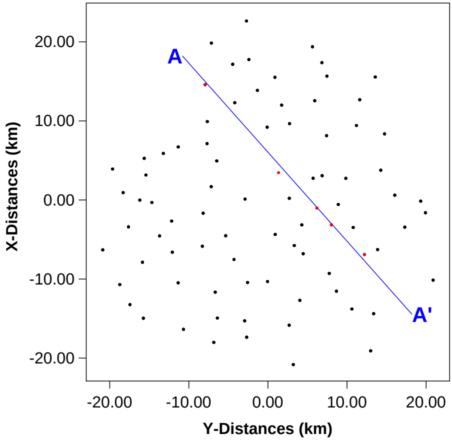
A
A'
20.00
10.00
0.00
-10.00
-20.00
X-Distances (km)
-20.00
-10.00
0.00
10.00
20.00
Y-Distances (km)

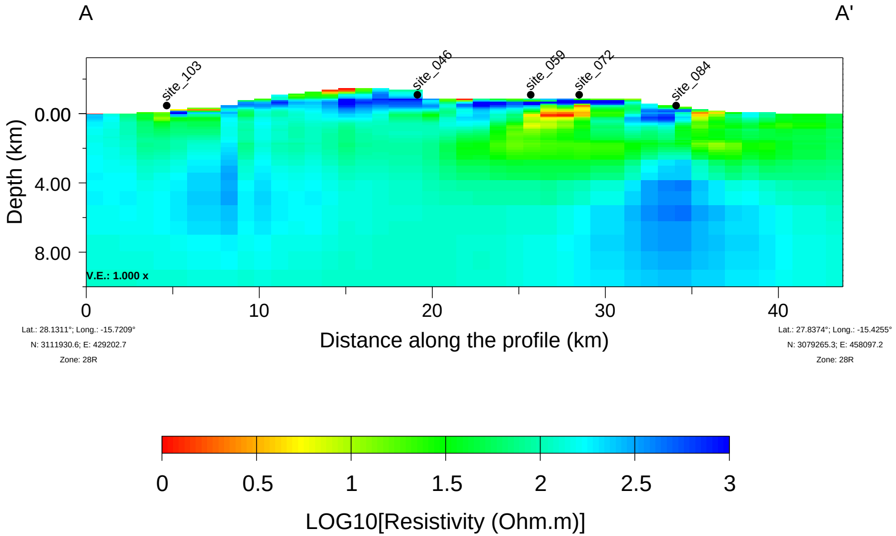
A
A'
site_103
site_046
site_059
site_072
site_084
0.00
4.00
8.00
Depth (km)
V.E.: 1.000 x
0
10
20
30
40
Distance along the profile (km)
Lat.: 28.1311°; Long.: -15.7209°
N: 3111930.6; E: 429202.7
Zone: 28R
Lat.: 27.8374°; Long.: -15.4255°
N: 3079265.3; E: 458097.2
Zone: 28R
0
0.5
1
1.5
2
2.5
3
LOG10[Resistivity (Ohm.m)]

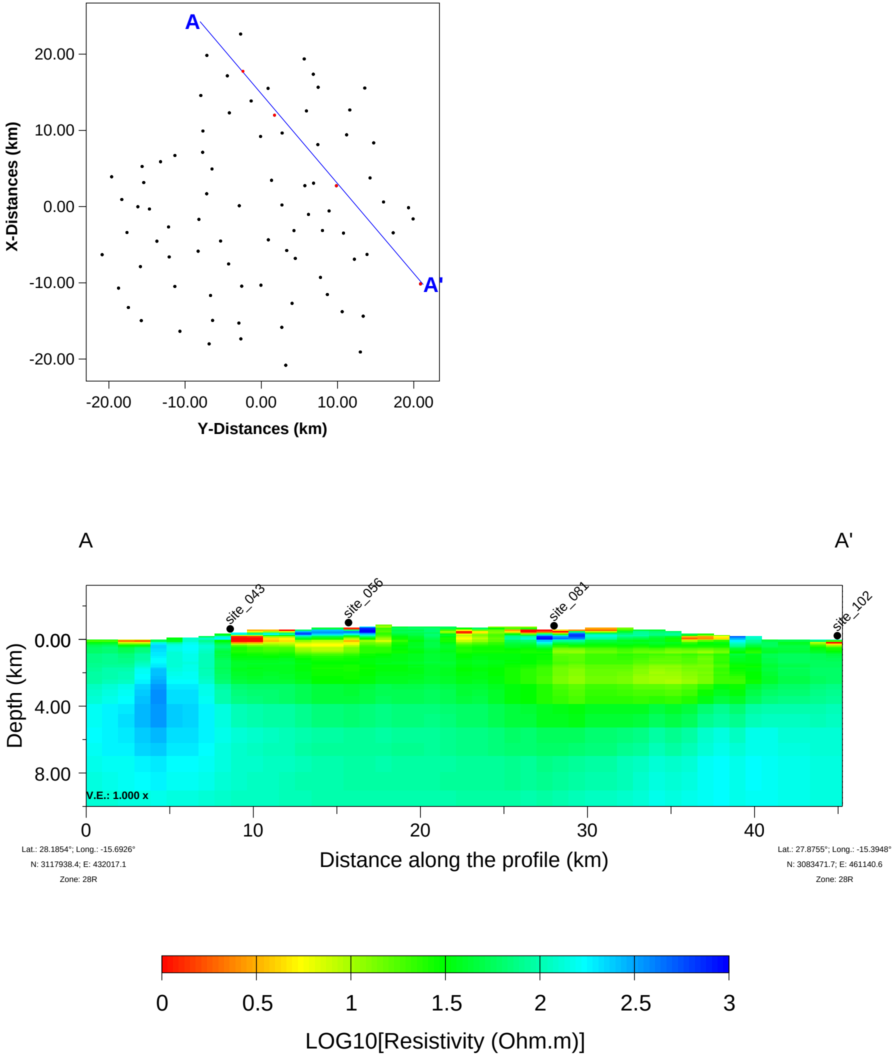
A
A'
20.00
10.00
0.00
-10.00
-20.00
X-Distances (km)
-20.00
-10.00
0.00
10.00
20.00
Y-Distances (km)
A
A'
site_043
site_056
site_081
site_102
0.00
4.00
8.00
Depth (km)
V.E.: 1.000 x
0
10
20
30
40
Distance along the profile (km)
Lat.: 28.1854°; Long.: -15.6926°
N: 3117938.4; E: 432017.1
Zone: 28R
Lat.: 27.8755°; Long.: -15.3948°
N: 3083471.7; E: 461140.6
Zone: 28R
0
0.5
1
1.5
2
2.5
3
LOG10[Resistivity (Ohm.m)]

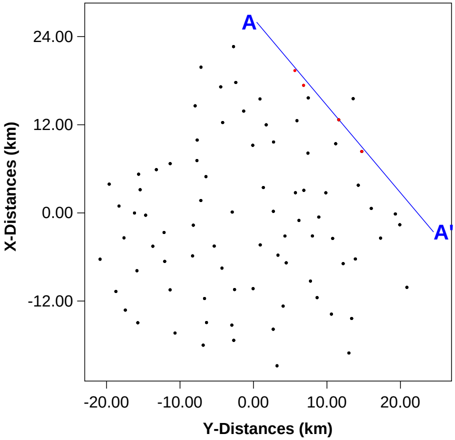
A
A'
24.00
12.00
0.00
-12.00
X-Distances (km)
-20.00
-10.00
0.00
10.00
20.00
Y-Distances (km)

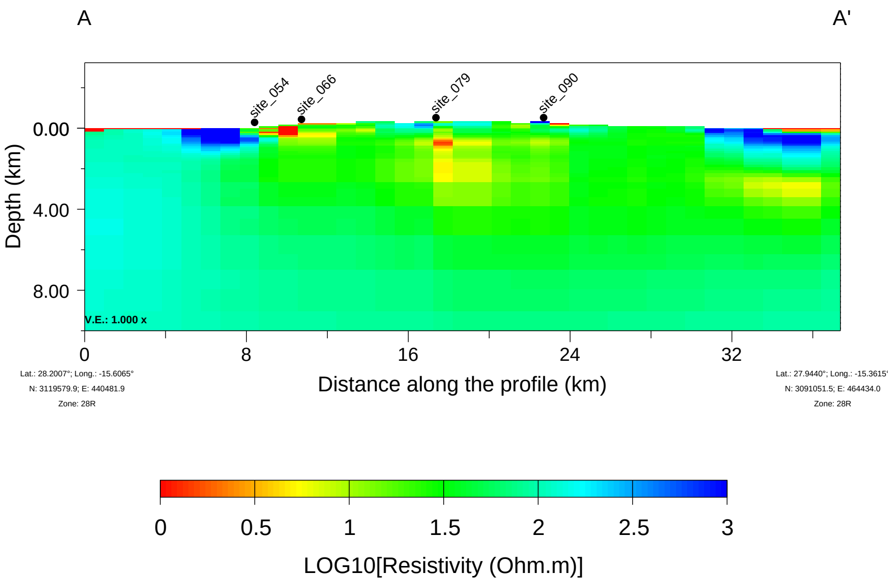
A
A'
site_054
site_066
site_079
site_090
0.00
4.00
8.00
Depth (km)
V.E.: 1.000 x
0
8
16
24
32
Distance along the profile (km)
Lat.: 28.2007°; Long.: -15.6065°
N: 3119579.9; E: 440481.9
Zone: 28R
Lat.: 27.9440°; Long.: -15.3615°
N: 3091051.5; E: 464434.0
Zone: 28R
0
0.5
1
1.5
2
2.5
3
LOG10[Resistivity (Ohm.m)]

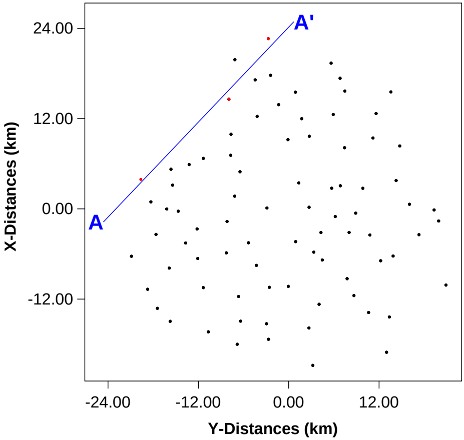
A'
A
24.00
12.00
0.00
-12.00
X-Distances (km)
-24.00
-12.00
0.00
12.00
Y-Distances (km)

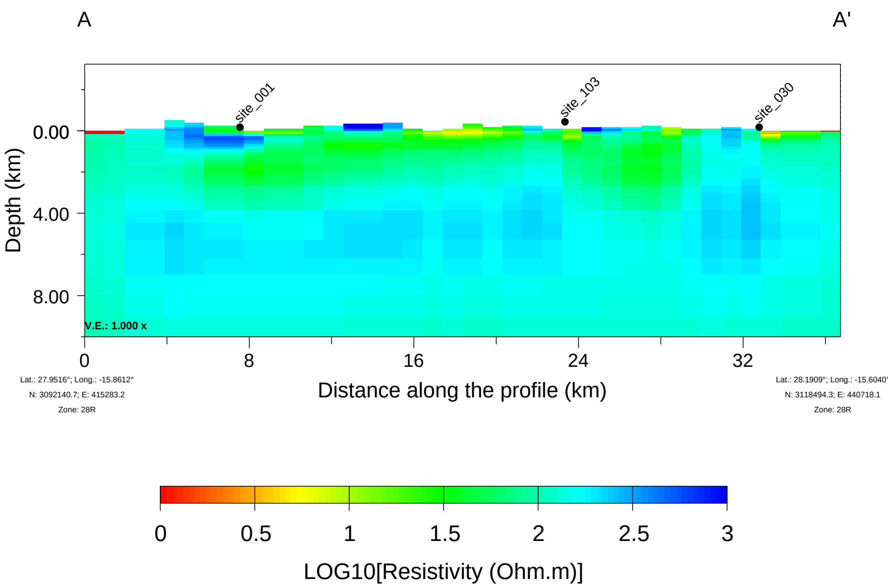
A
A'
site_001
site_103
site_030
0.00
4.00
8.00
Depth (km)
V.E.: 1.000 x
0
8
16
24
32
Distance along the profile (km)
Lat.: 27.9516°; Long.: -15.8612°
N: 3092140.7; E: 415283.2
Zone: 28R
Lat.: 28.1909°; Long.: -15.6040°
N: 3118494.3; E: 440718.1
Zone: 28R
0
0.5
1
1.5
2
2.5
3
LOG10[Resistivity (Ohm.m)]

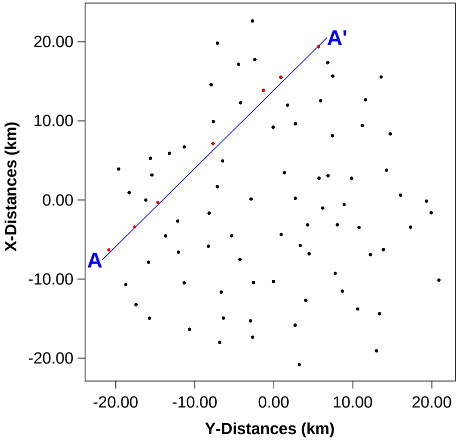

A
A'
X-Distances (km)
Y-Distances (km)
20.00
10.00
0.00
-10.00
-20.00

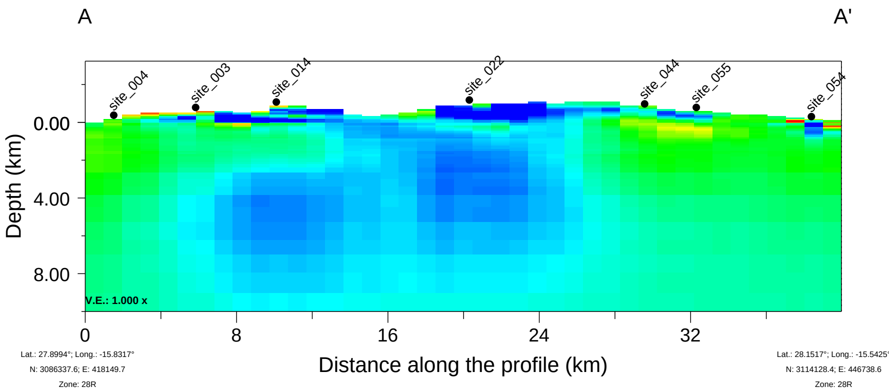

A
A'
site_004
site_003
site_014
site_022
site_044
site_055
site_054
Depth (km)
0.00
4.00
8.00
V.E.: 1.000 x
0
8
16
24
32
Distance along the profile (km)
Lat.: 27.8994°; Long.: -15.8317°
N: 3086337.6; E: 418149.7
Zone: 28R
Lat.: 28.1517°; Long.: -15.5425°
N: 3114128.4; E: 446738.6
Zone: 28R

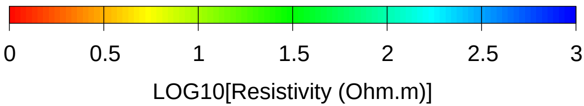

0
0.5
1
1.5
2
2.5
3
LOG10[Resistivity (Ohm.m)]

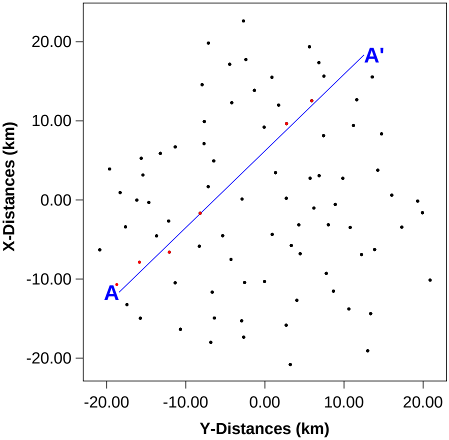
A
A'
X-Distances (km)
Y-Distances (km)
20.00
10.00
0.00
-10.00
-20.00
-20.00
-10.00
0.00
10.00
20.00

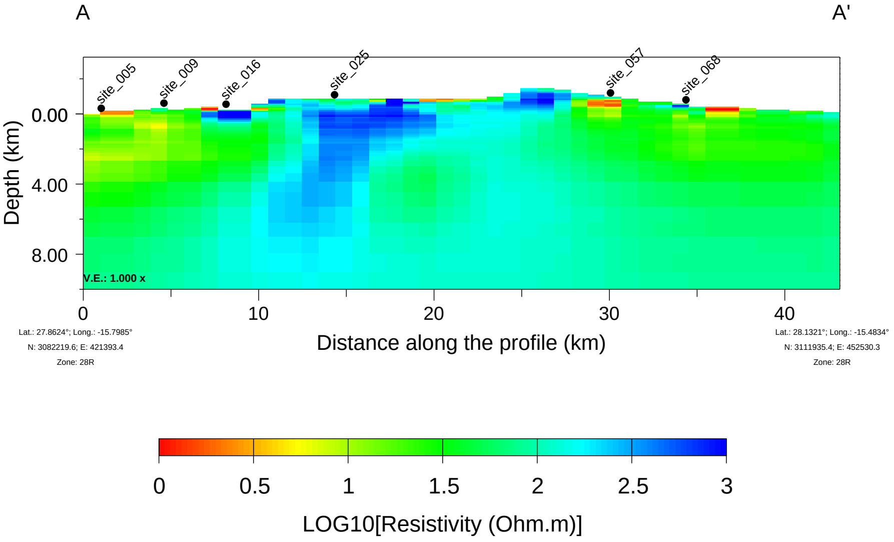
A
A'
site_005
site_009
site_016
site_025
site_057
site_068
Depth (km)
0.00
4.00
8.00
V.E.: 1.000 x
0
10
20
30
40
Distance along the profile (km)
Lat.: 27.8624°; Long.: -15.7985°
N: 3082219.6; E: 421393.4
Zone: 28R
Lat.: 28.1321°; Long.: -15.4834°
N: 3111935.4; E: 452530.3
Zone: 28R
0
0.5
1
1.5
2
2.5
3
LOG10[Resistivity (Ohm.m)]

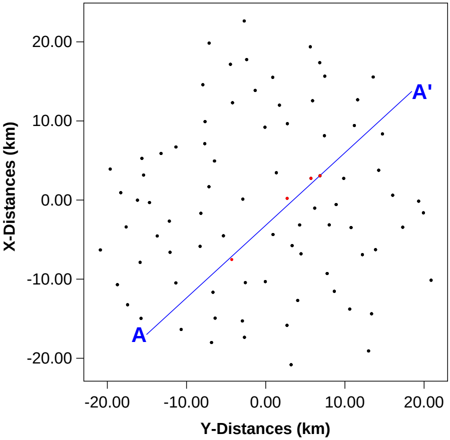

A
A'
20.00
10.00
0.00
-10.00
-20.00
X-Distances (km)
-20.00
-10.00
0.00
10.00
20.00
Y-Distances (km)

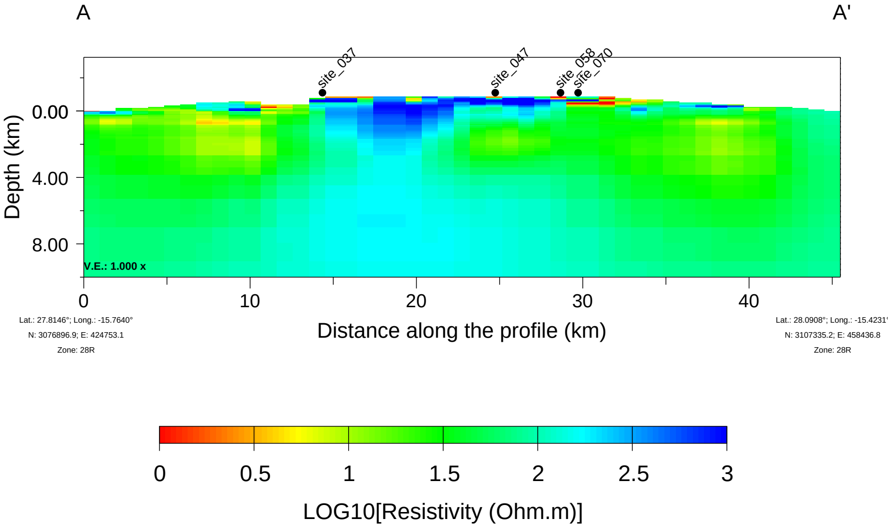

A
A'
site_037
site_047
site_058
site_070
0.00
4.00
8.00
Depth (km)
V.E.: 1.000 x
0
10
20
30
40
Distance along the profile (km)
Lat.: 27.8146°; Long.: -15.7640°
N: 3076896.9; E: 424753.1
Zone: 28R
Lat.: 28.0908°; Long.: -15.4231°
N: 3107335.2; E: 458436.8
Zone: 28R
0
0.5
1
1.5
2
2.5
3
LOG10[Resistivity (Ohm.m)]

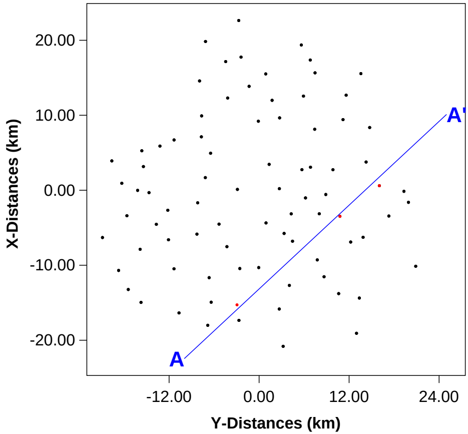
A
A'
20.00
10.00
0.00
-10.00
-20.00
X-Distances (km)
-12.00
0.00
12.00
24.00
Y-Distances (km)

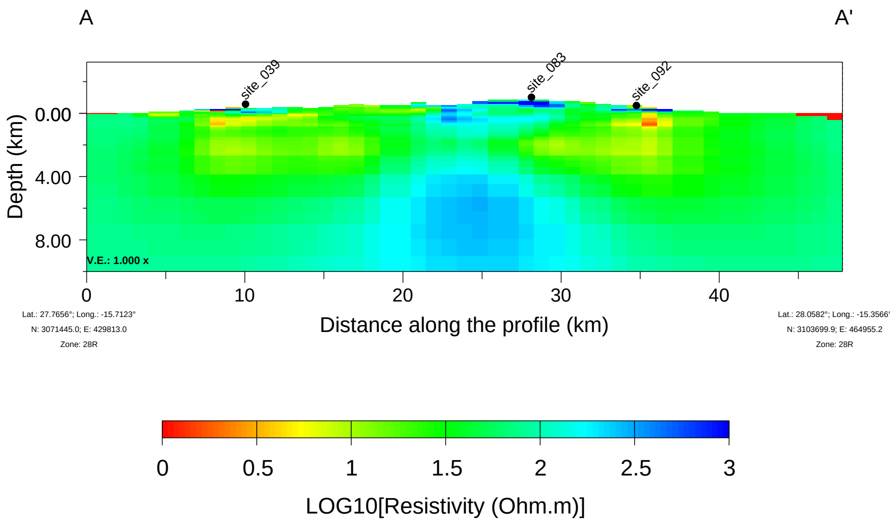
A
A'
site_039
site_083
site_092
0.00
4.00
8.00
Depth (km)
V.E.: 1.000 x
0
10
20
30
40
Distance along the profile (km)
Lat.: 27.7656°; Long.: -15.7123°
N: 3071445.0; E: 429813.0
Zone: 28R
Lat.: 28.0582°; Long.: -15.3566°
N: 3103699.9; E: 464955.2
Zone: 28R
0
0.5
1
1.5
2
2.5
3
LOG10[Resistivity (Ohm.m)]

Figure S7.

Comparison between the four components of the apparent resistivity and phases curves of the model response and the measured data.

Site: site_001

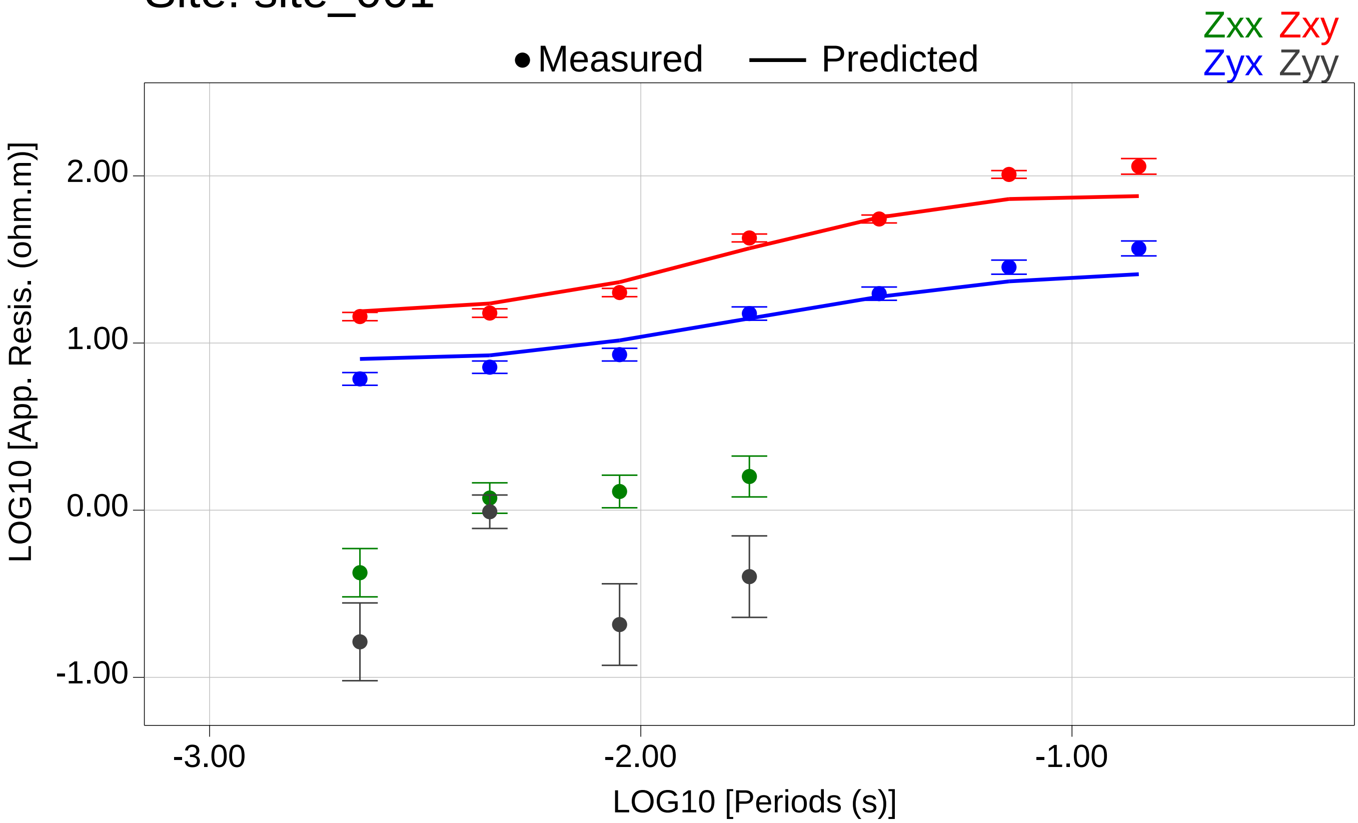

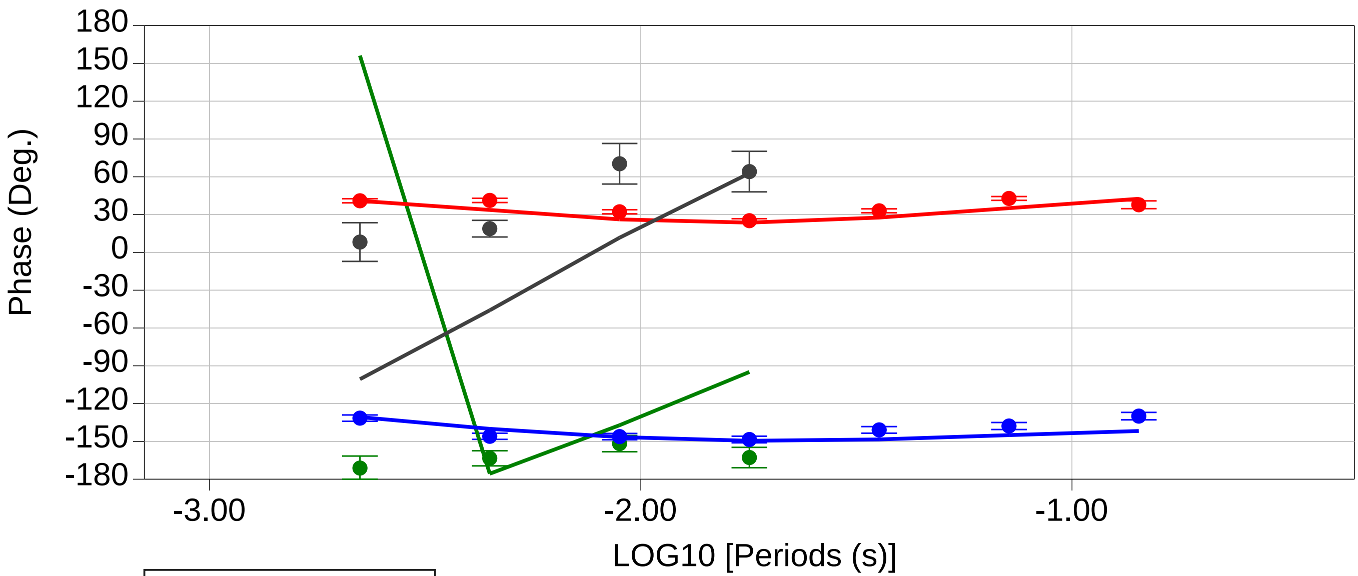

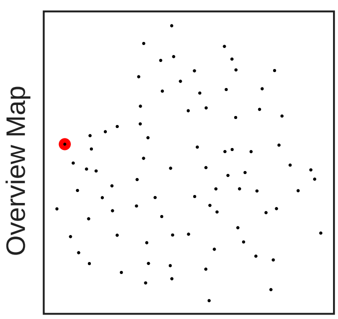

Total RMS = 2.51
Zxx RMS = 3.84
Zxy RMS = 2.23
Zyx RMS = 1.58
Zyy RMS = 2.62

Site: site_002

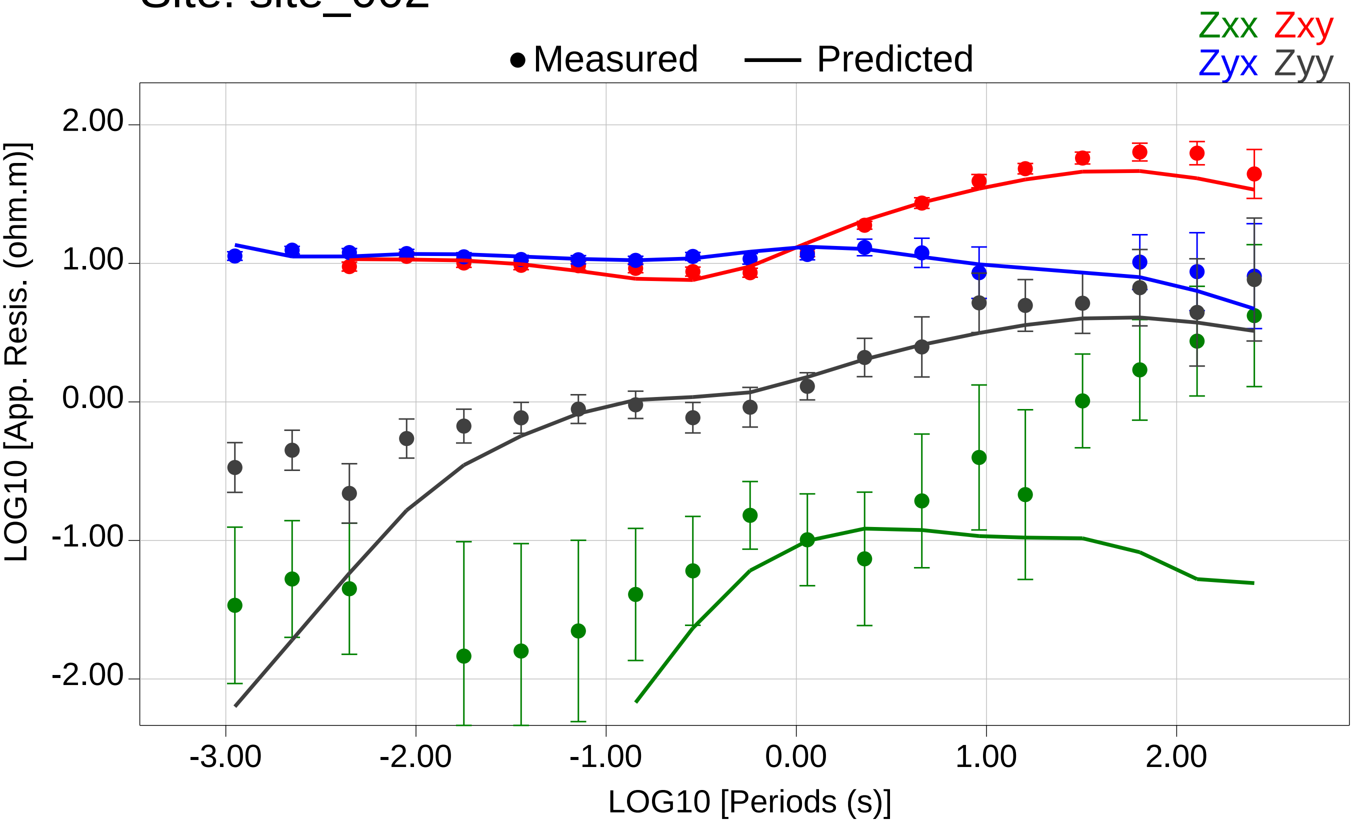

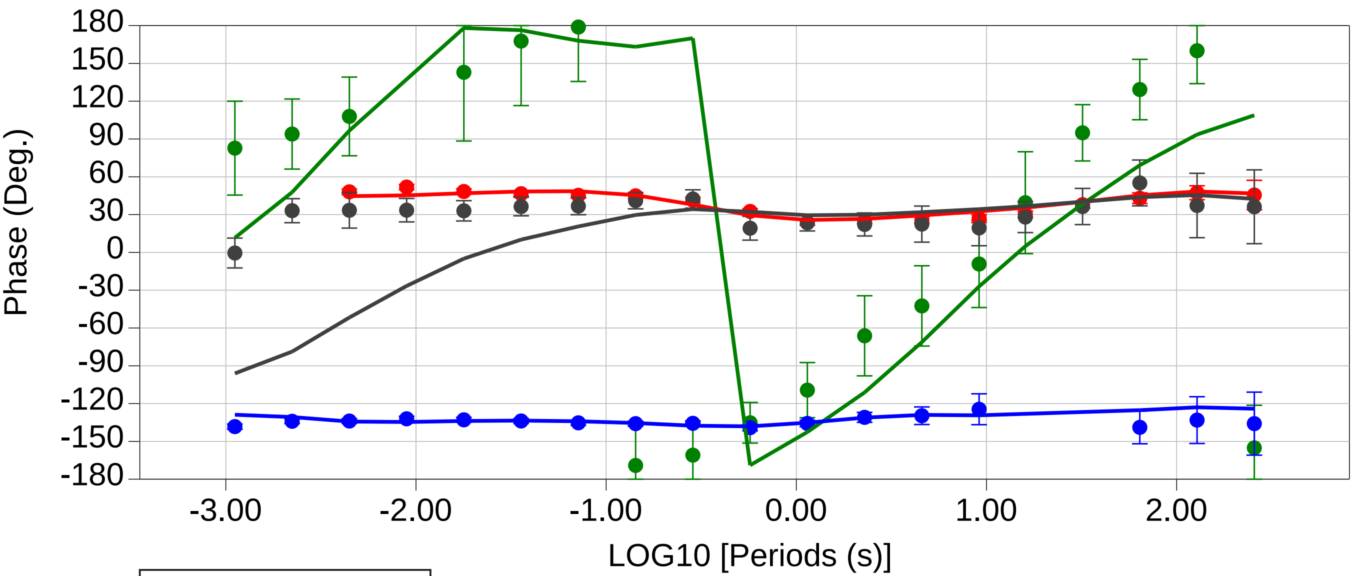

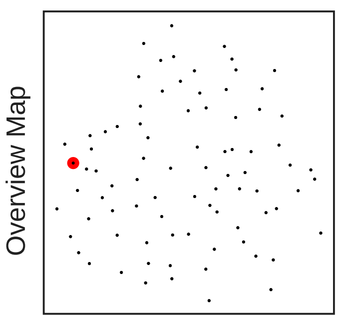

Total RMS = 1.08
Zxx RMS = 0.75
Zxy RMS = 1.04
Zyx RMS = 0.85
Zyy RMS = 1.49

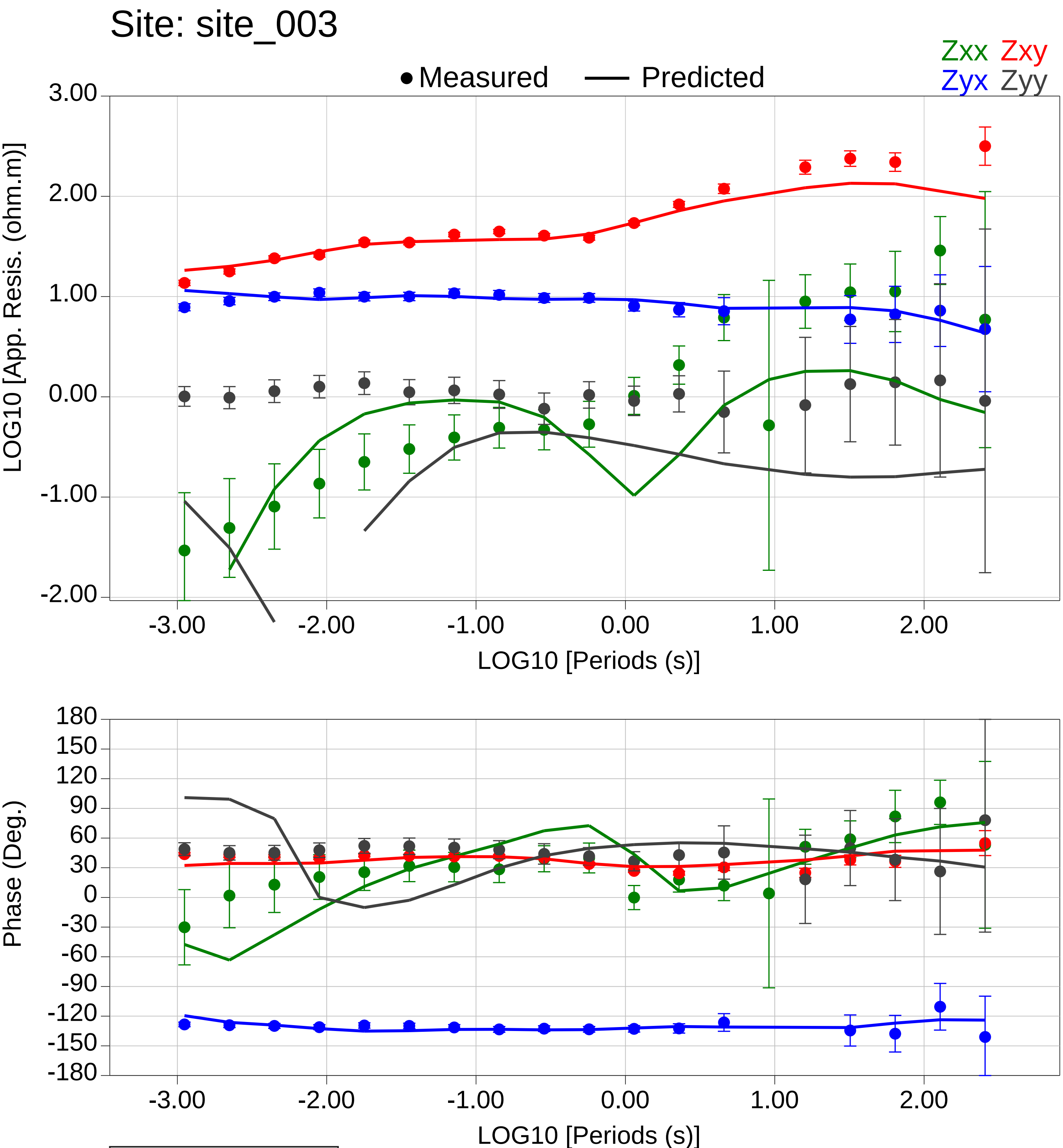

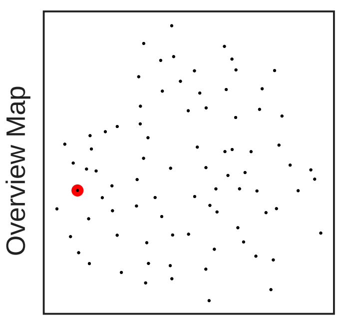

Total RMS = 1.62
Zxx RMS = 1.10
Zxy RMS = 1.84
Zyx RMS = 1.00
Zyy RMS = 2.21

Site: site_004

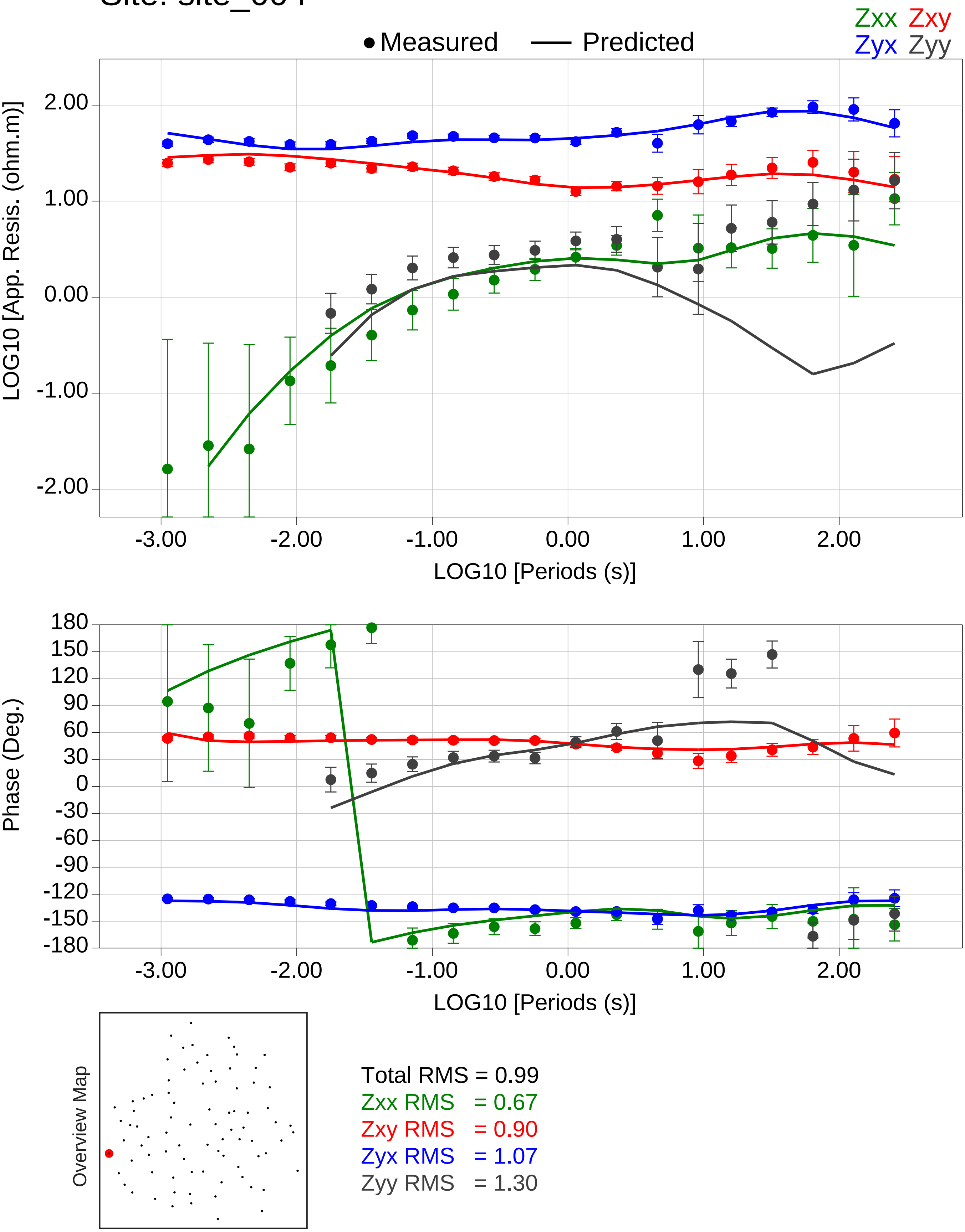

Total RMS = 0.99
Zxx RMS = 0.67
Zxy RMS = 0.90
Zyx RMS = 1.07
Zyy RMS = 1.30

Site: site_005

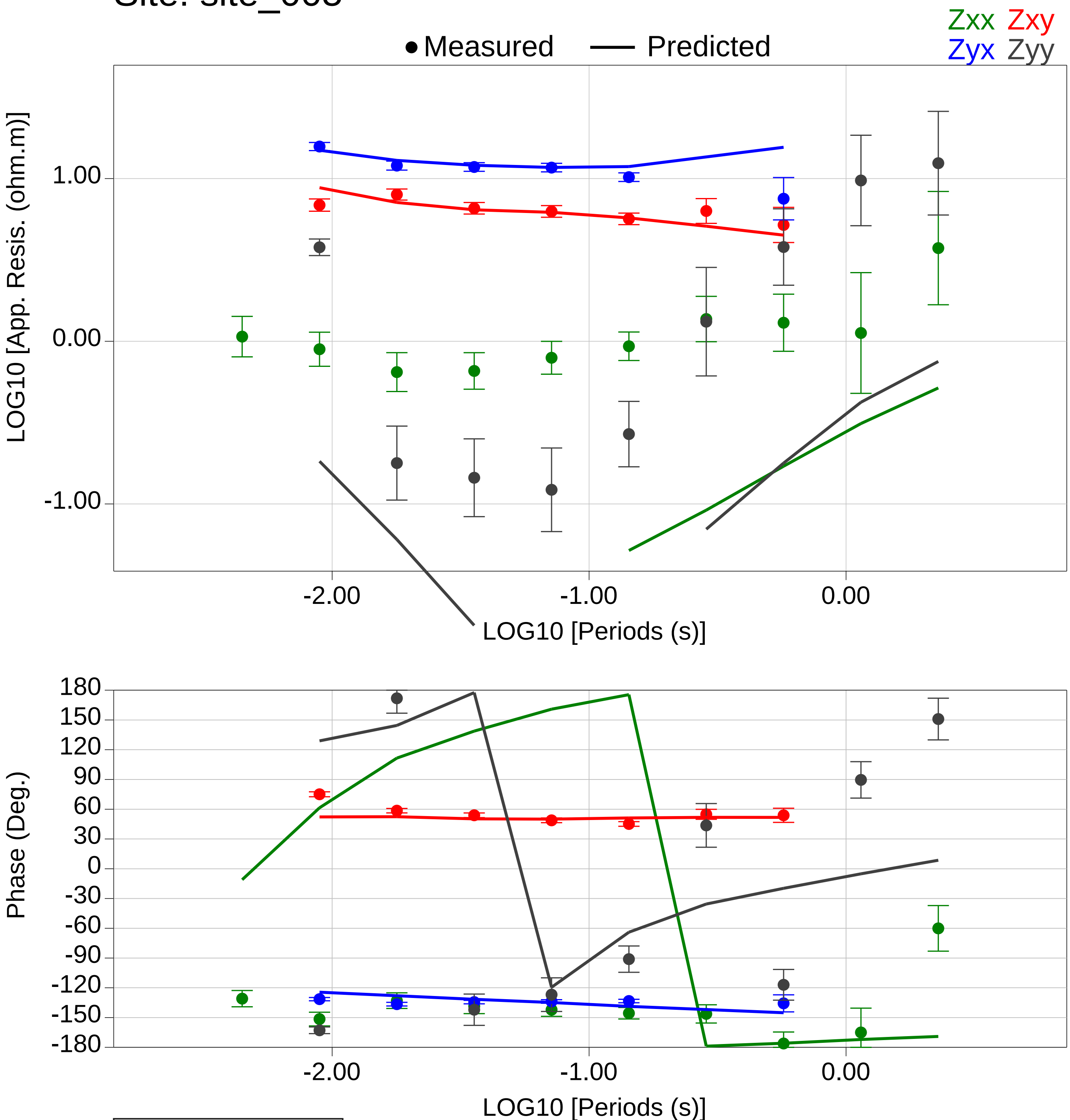

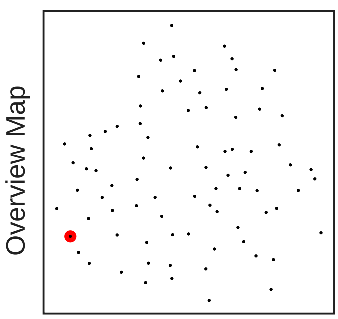

Total RMS = 2.70
Zxx RMS = 3.19
Zxy RMS = 2.10
Zyx RMS = 1.74
Zyy RMS = 3.02

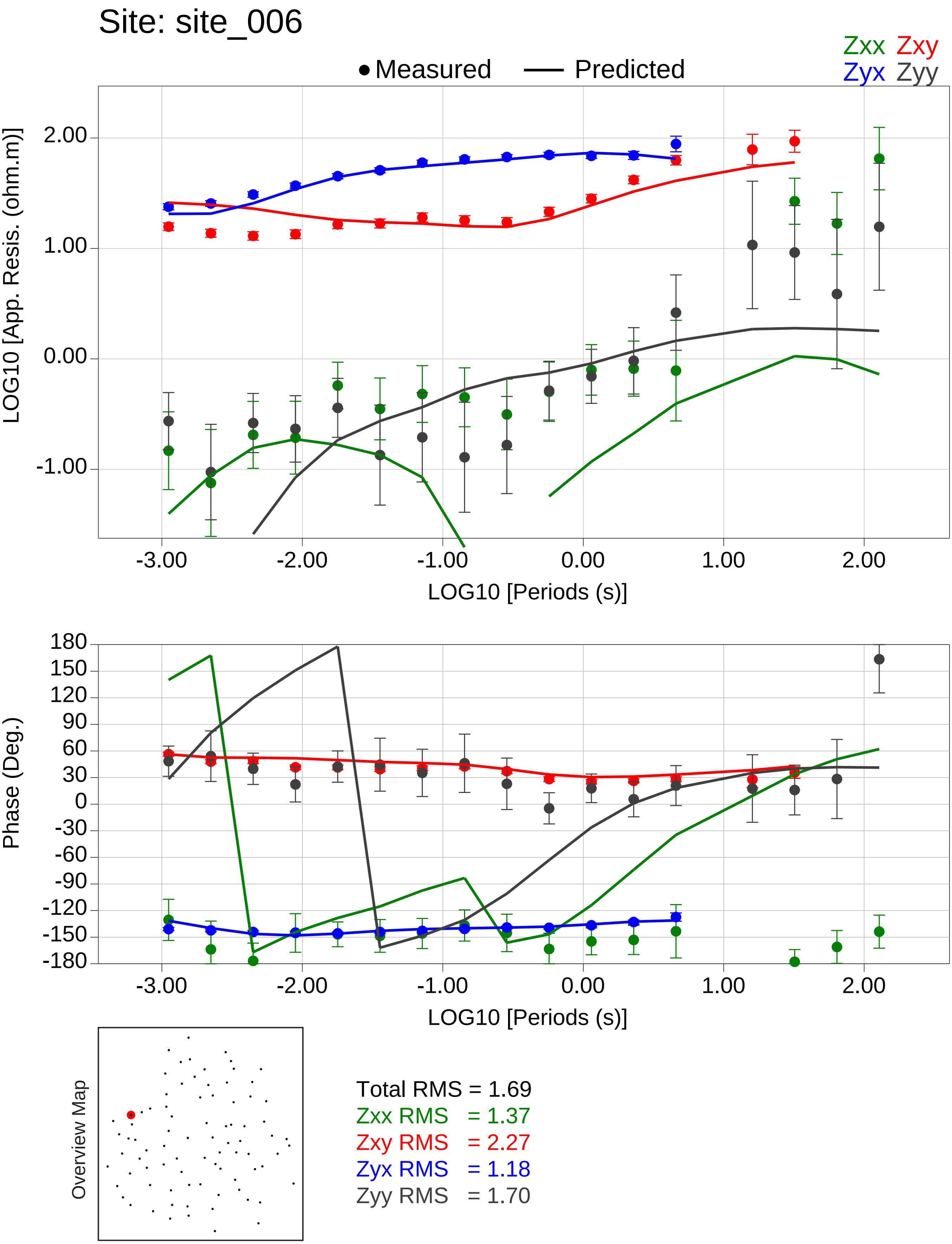

Site: site_006
Measured
Predicted
Zxx Zxy
Zyx Zyy
LOG10 [App. Resis. (ohm.m)]
2.00
1.00
0.00
-1.00
-3.00
-2.00
-1.00
0.00
1.00
2.00
LOG10 [Periods (s)]
Phase (Deg.)
180
150
120
90
60
30
0
-30
-60
-90
-120
-150
-180
-3.00
-2.00
-1.00
0.00
1.00
2.00
LOG10 [Periods (s)]
Overview Map
Total RMS = 1.69
Zxx RMS = 1.37
Zxy RMS = 2.27
Zyx RMS = 1.18
Zyy RMS = 1.70

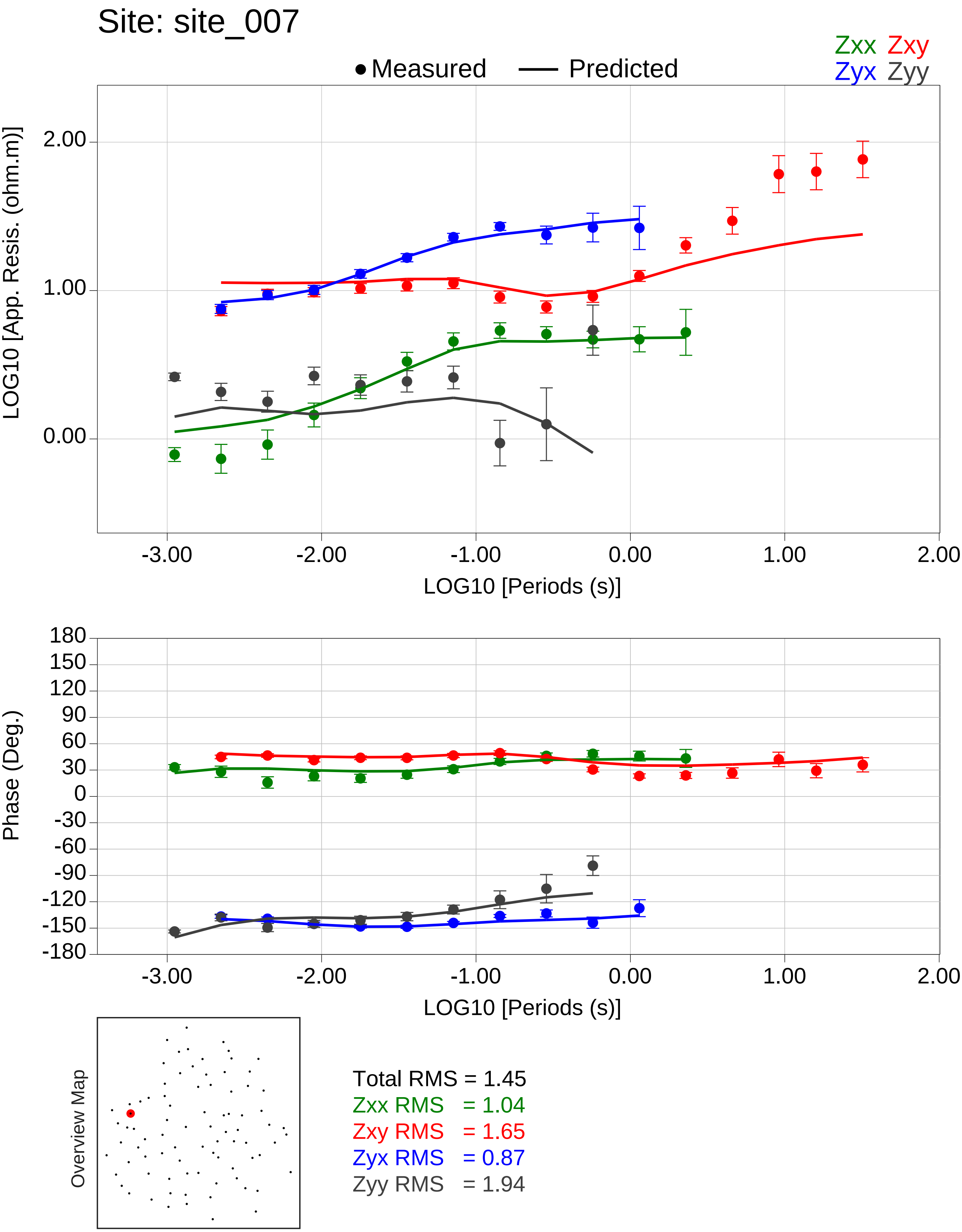

Site: site_007
Measured
Predicted
Zxx Zxy
Zyx Zyy
LOG10 [App. Resis. (ohm.m)]
2.00
1.00
0.00
-3.00
-2.00
-1.00
0.00
1.00
2.00
LOG10 [Periods (s)]
Phase (Deg.)
180
150
120
90
60
30
0
-30
-60
-90
-120
-150
-180
-3.00
-2.00
-1.00
0.00
1.00
2.00
LOG10 [Periods (s)]
Overview Map
Total RMS = 1.45
Zxx RMS = 1.04
Zxy RMS = 1.65
Zyx RMS = 0.87
Zyy RMS = 1.94

Site: site_008

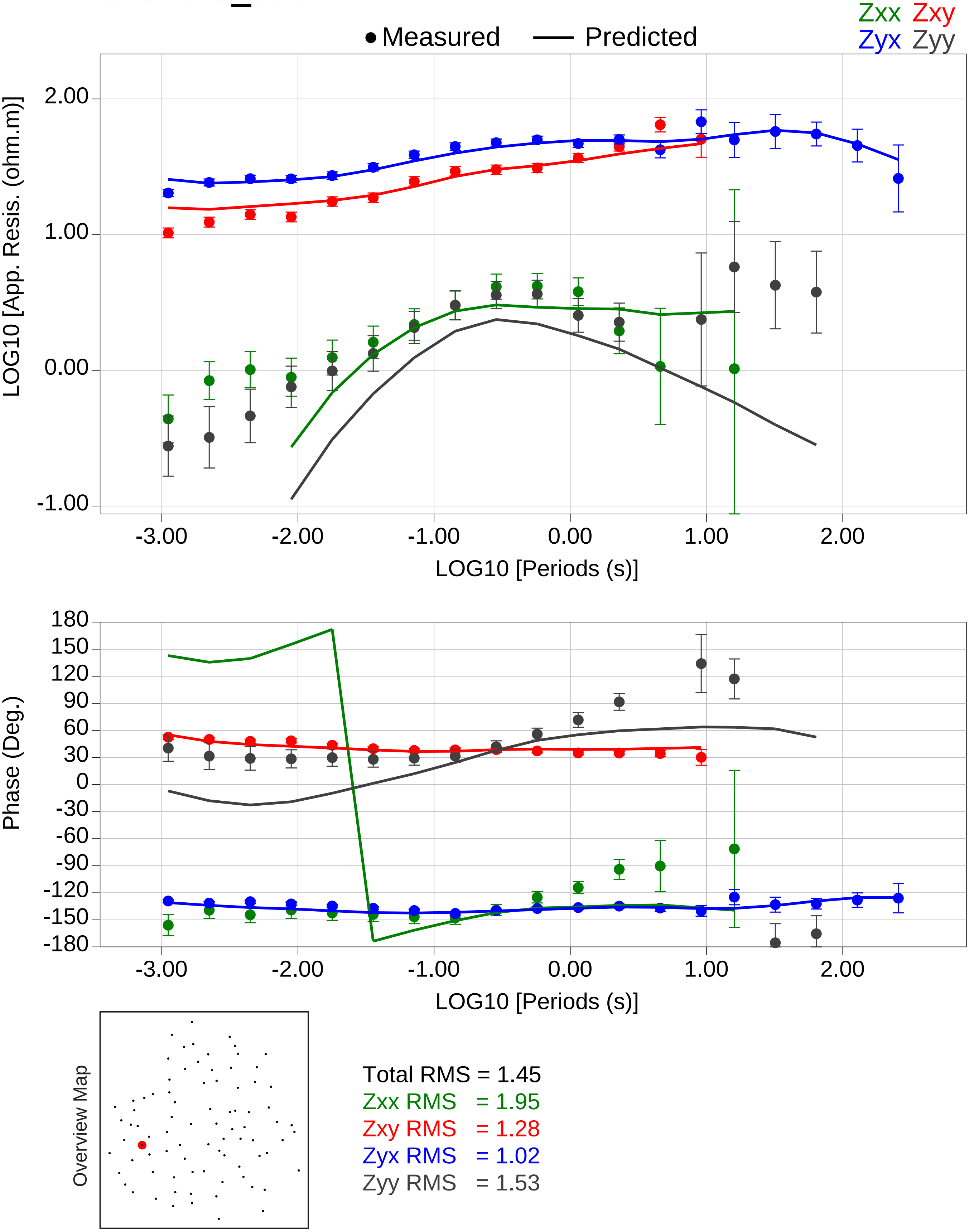

Total RMS = 1.45
Zxx RMS = 1.95
Zxy RMS = 1.28
Zyx RMS = 1.02
Zyy RMS = 1.53

Site: site_009

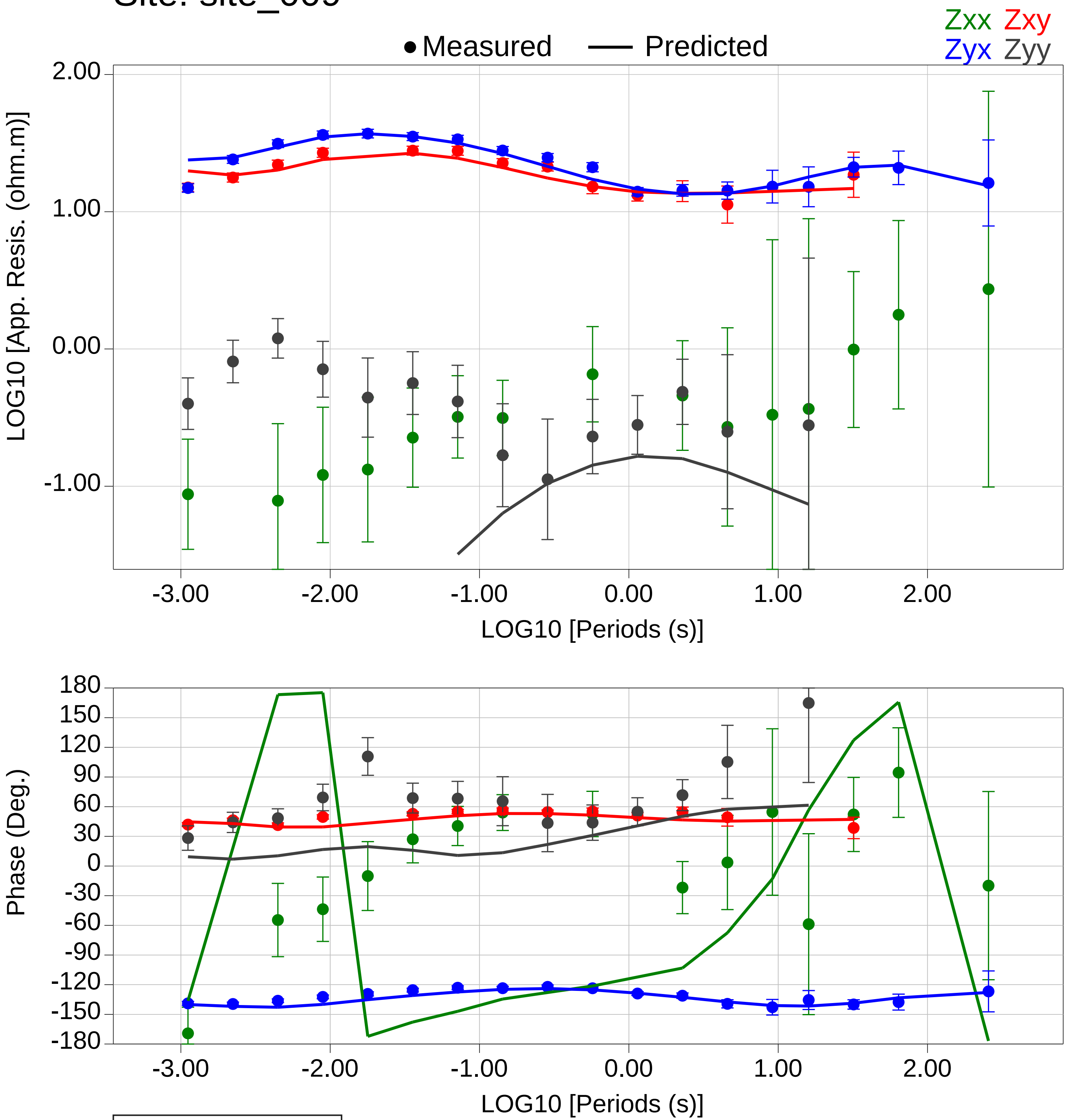

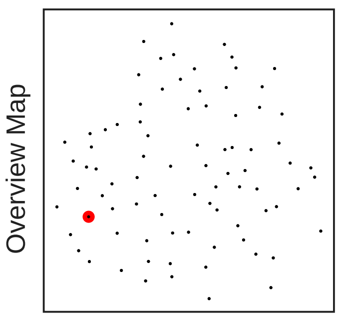

Total RMS = 1.30
Zxx RMS = 1.07
Zxy RMS = 1.21
Zyx RMS = 1.32
Zyy RMS = 1.57

Site: site_010

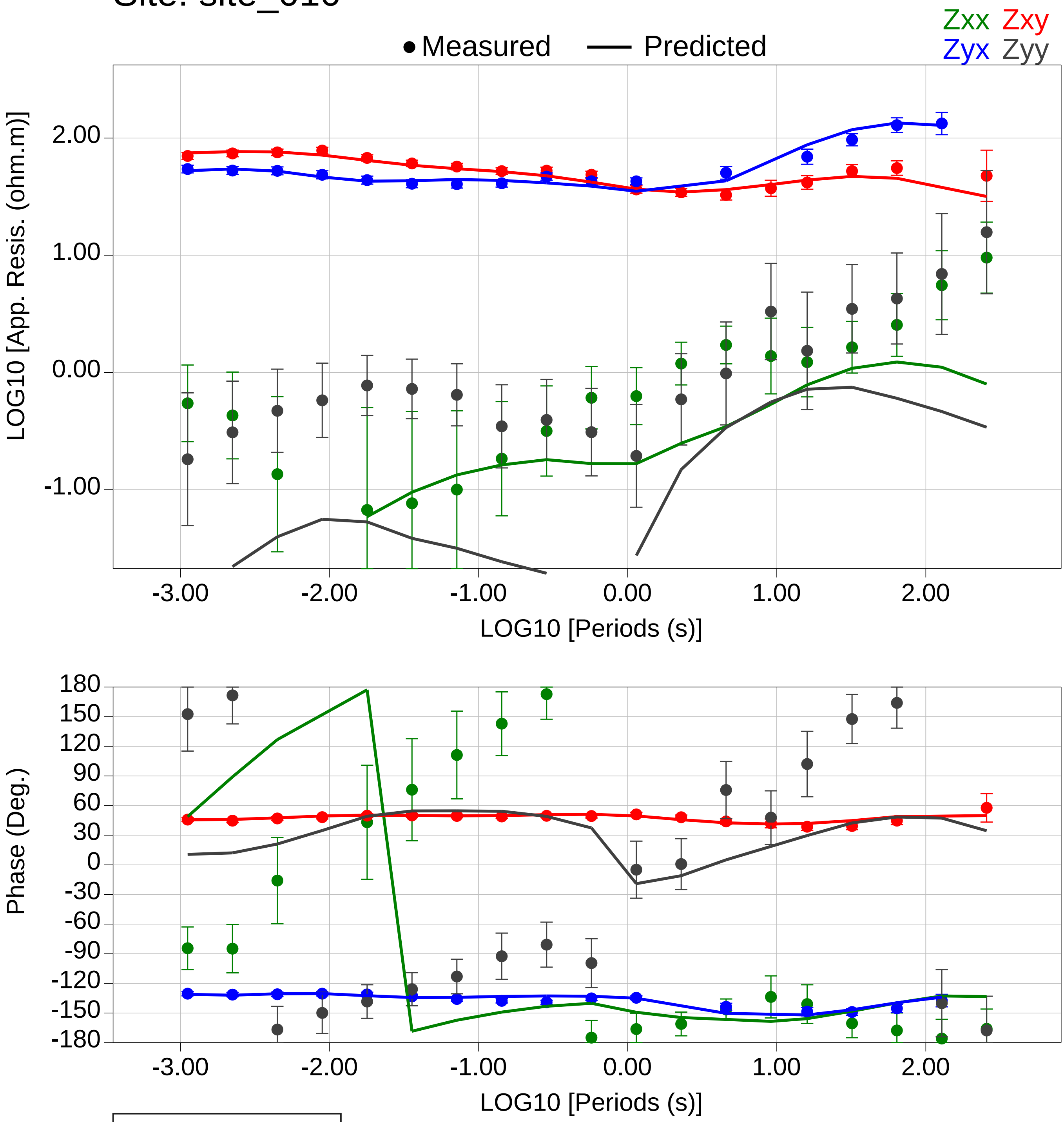

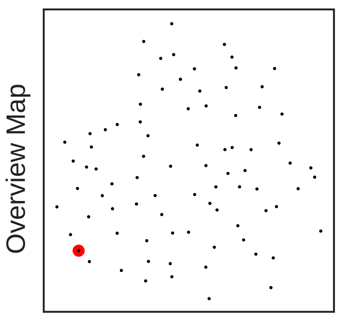

Total RMS = 1.00
Zxx RMS = 1.02
Zxy RMS = 0.57
Zyx RMS = 0.84
Zyy RMS = 1.37

Site: site_011

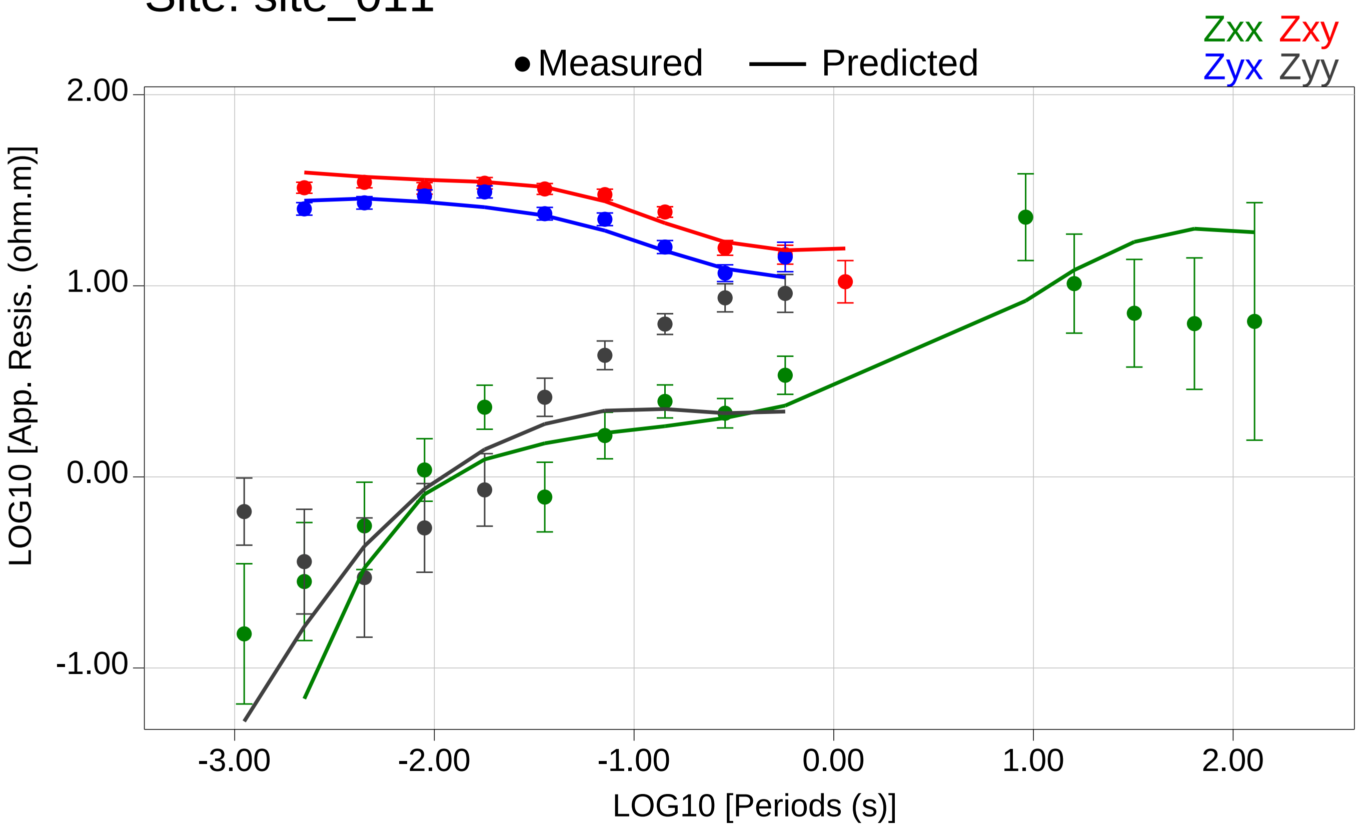

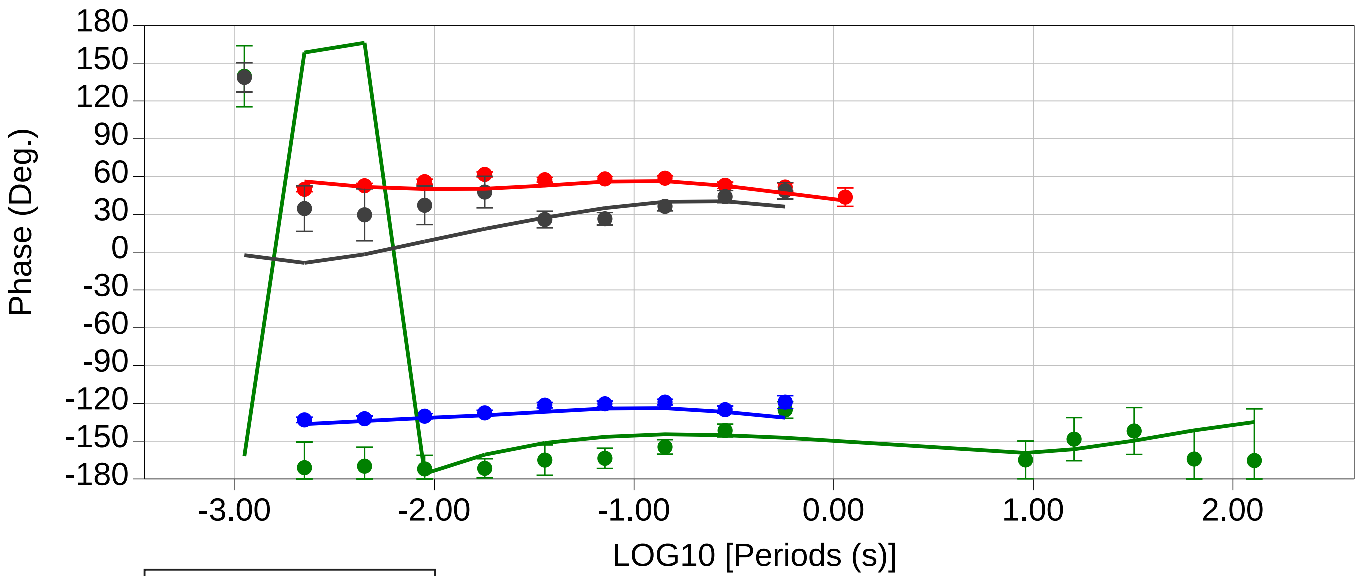

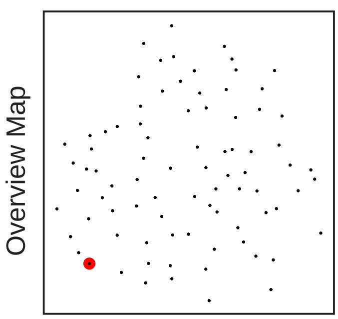

Total RMS = 1.42
Zxx RMS = 0.96
Zxy RMS = 1.48
Zyx RMS = 1.02
Zyy RMS = 2.07

Site: site_012

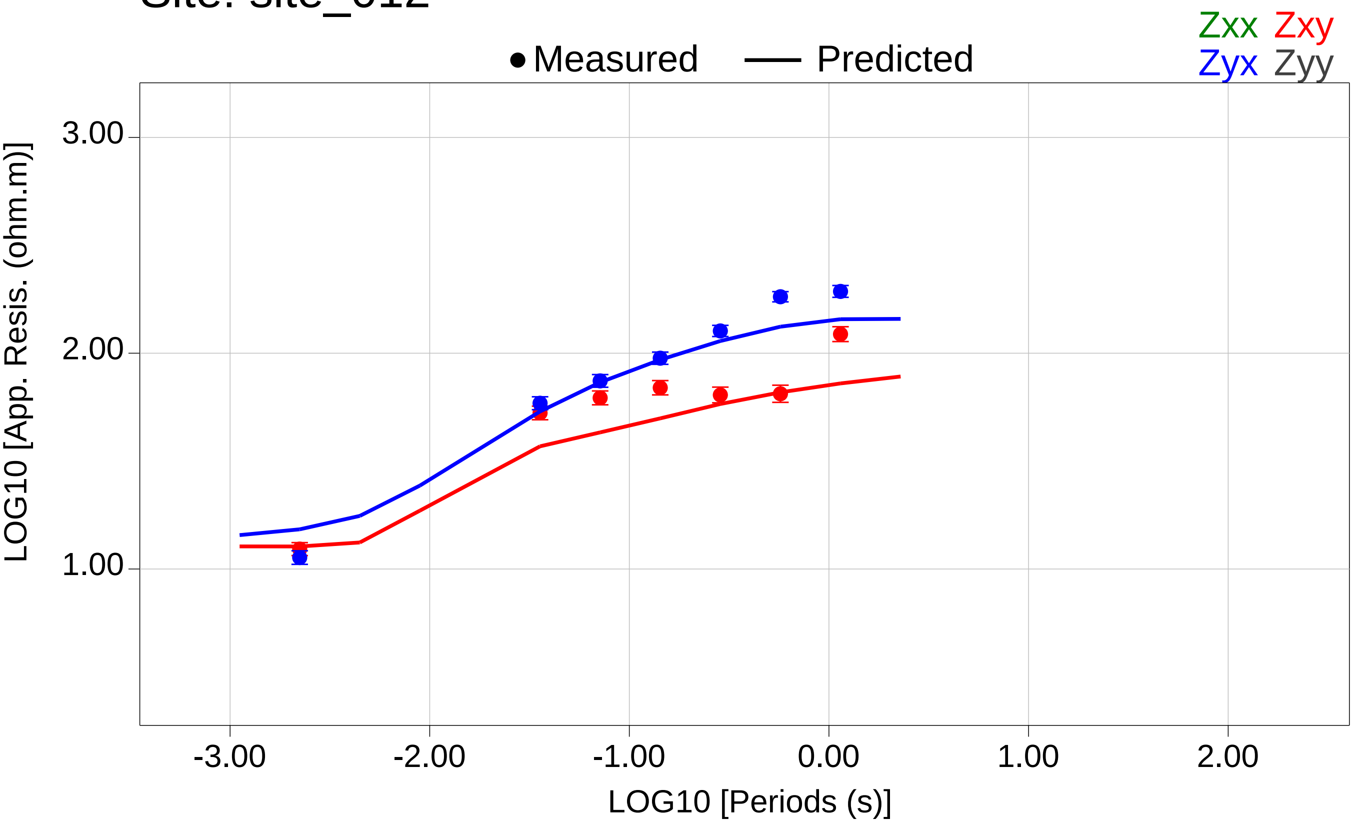

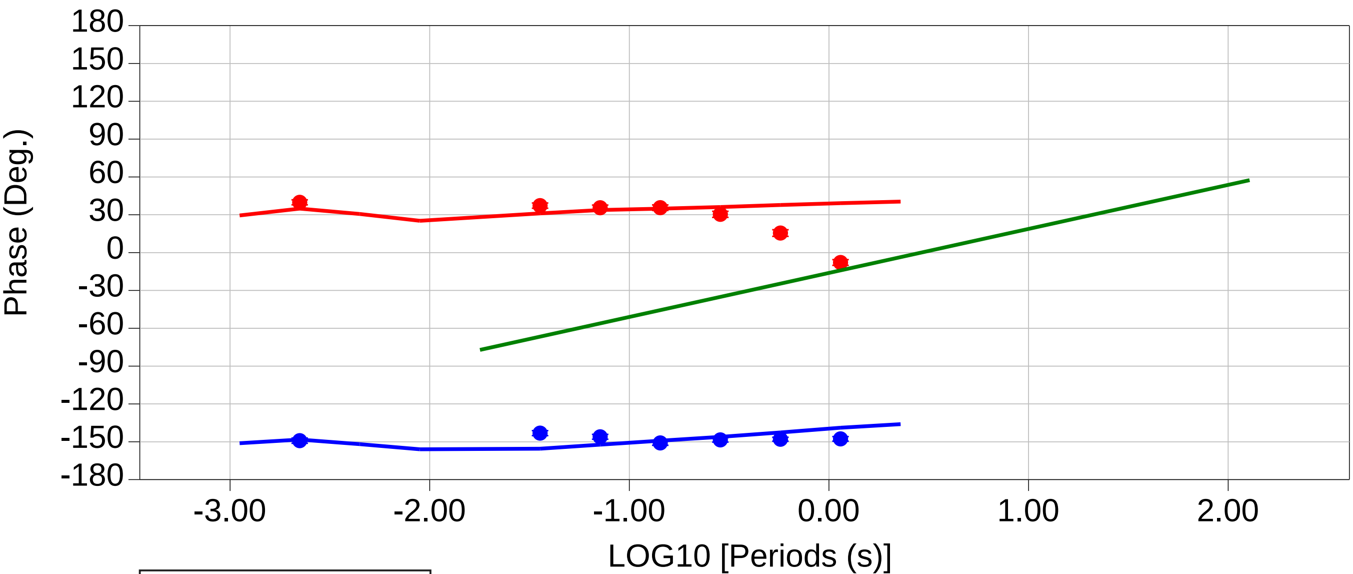

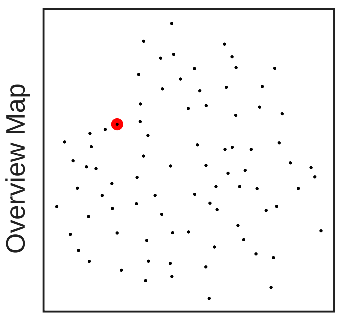

Total RMS = 3.41
Zxx RMS = 0.00
Zxy RMS = 7.05
Zyx RMS = 3.72
Zyy RMS = 0.00

Site: site_013

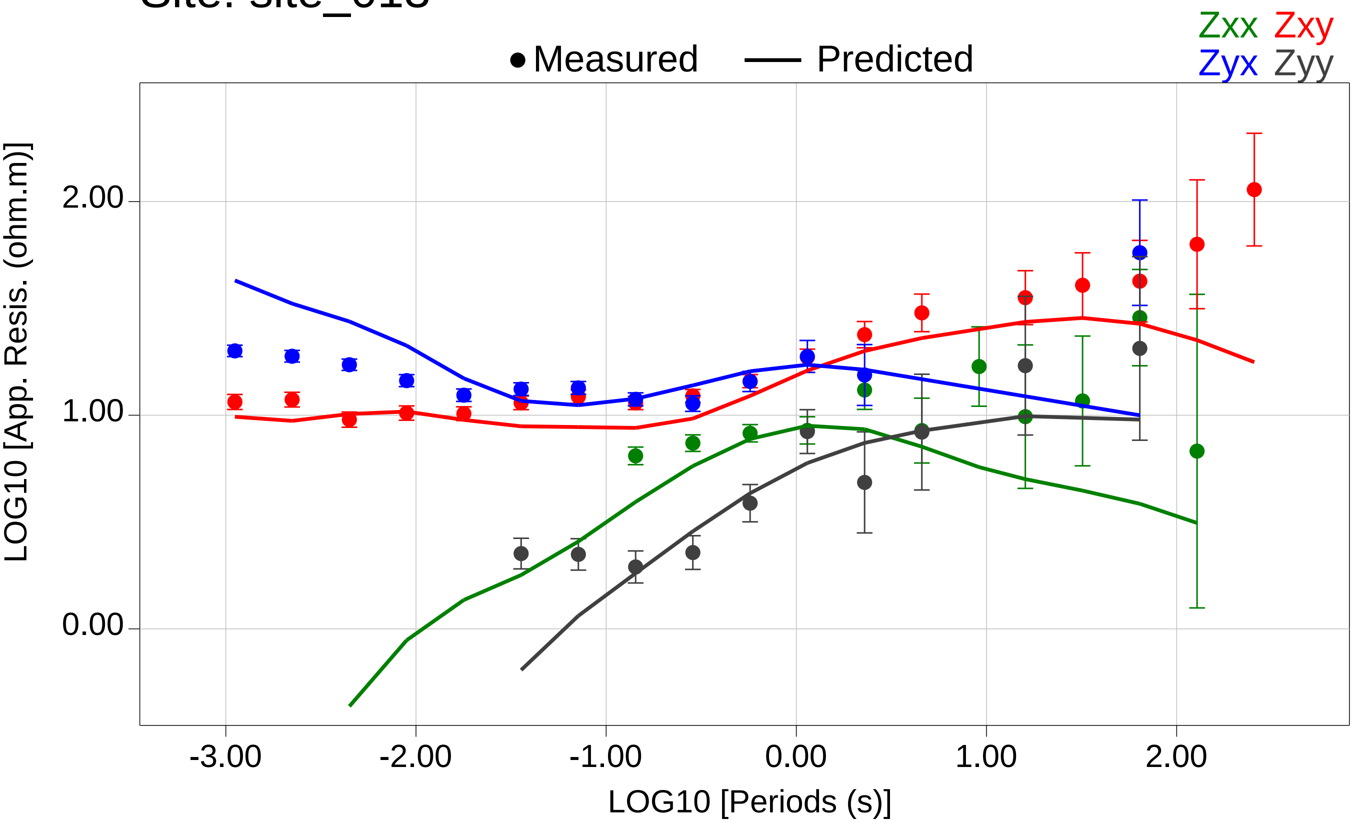

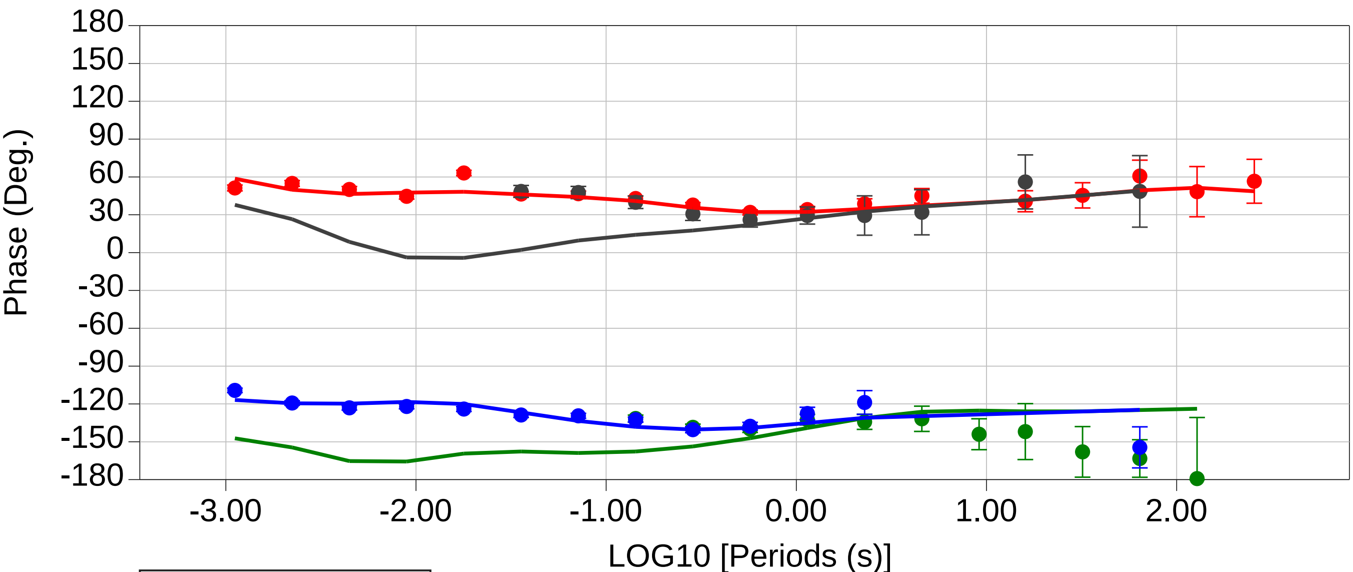

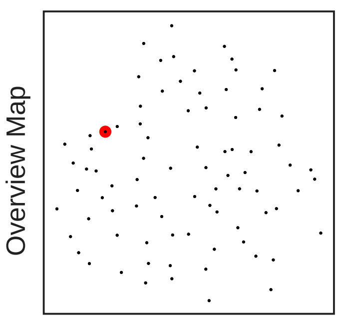

Total RMS = 2.22
Zxx RMS = 5.96
Zxy RMS = 1.46
Zyx RMS = 3.22
Zyy RMS = 3.23

Site: site_014

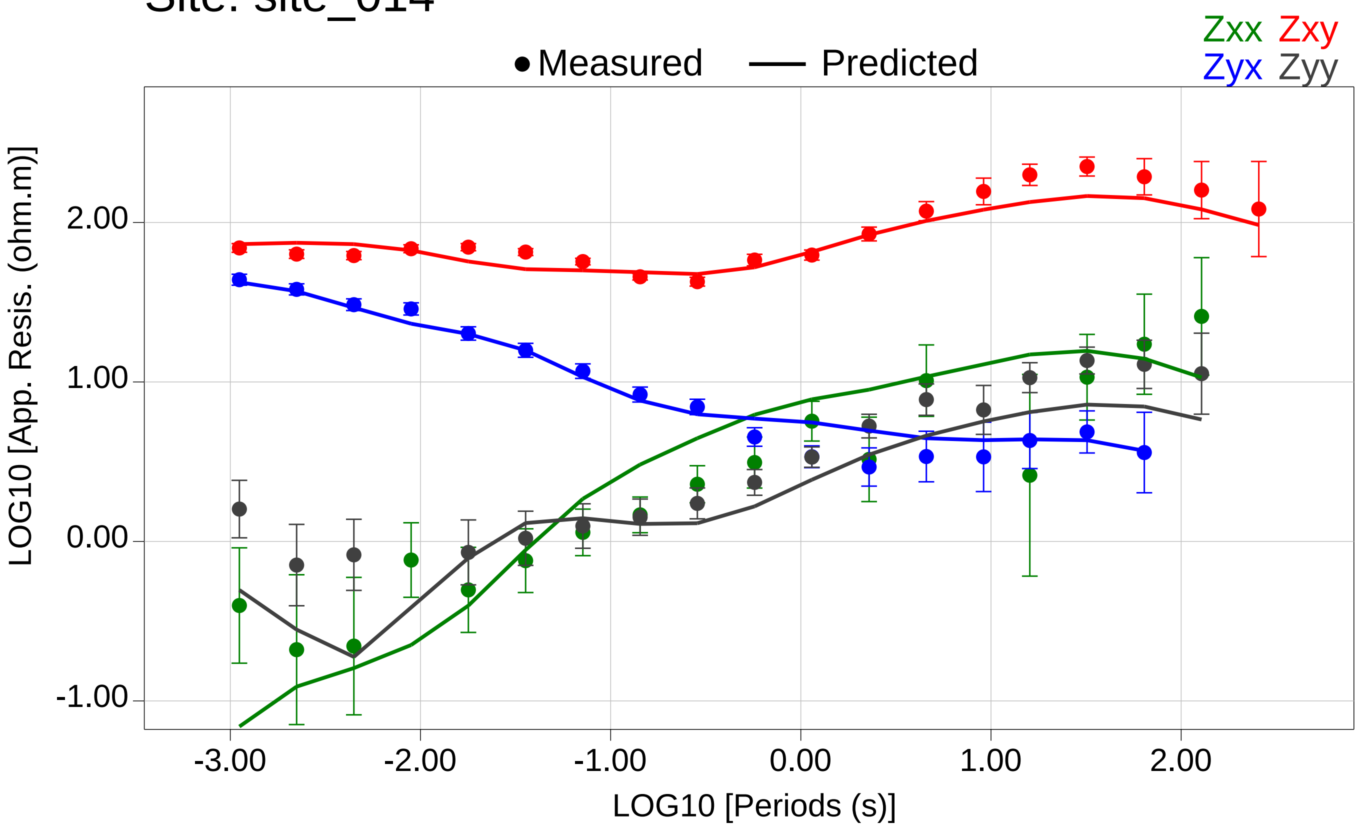

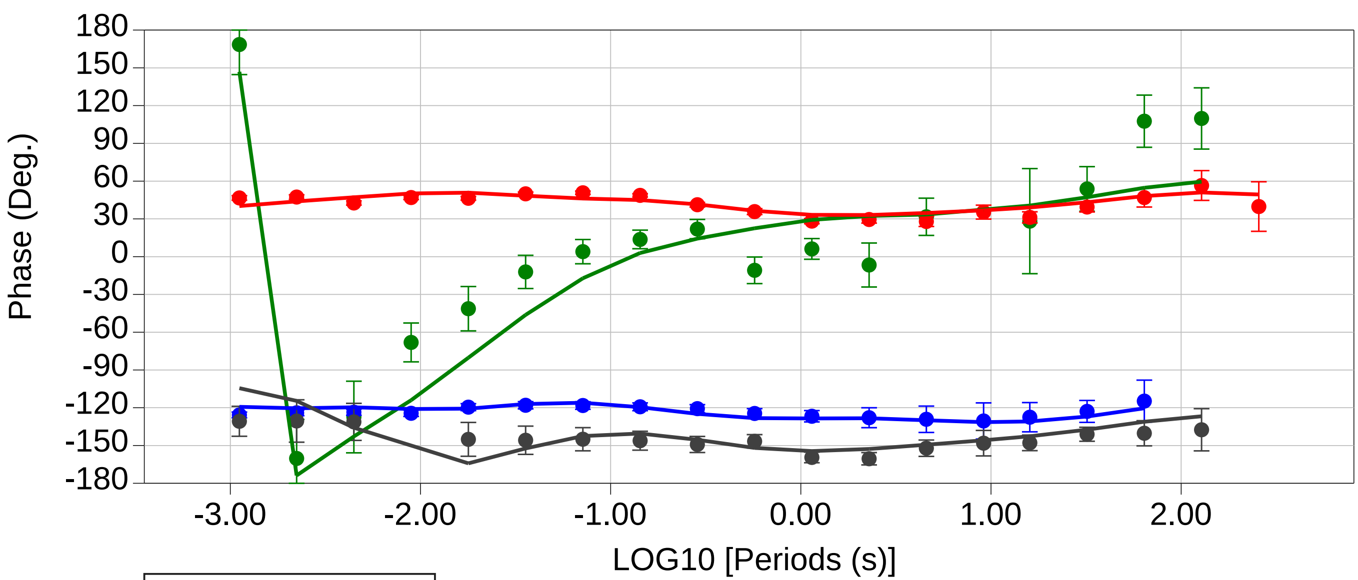

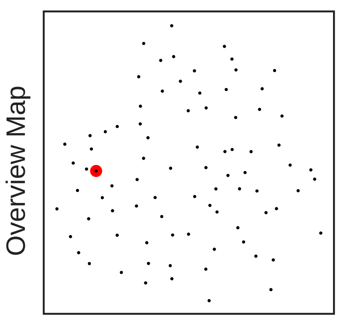

Total RMS = 1.15
Zxx RMS = 1.27
Zxy RMS = 1.43
Zyx RMS = 0.85
Zyy RMS = 0.91

Site: site_015

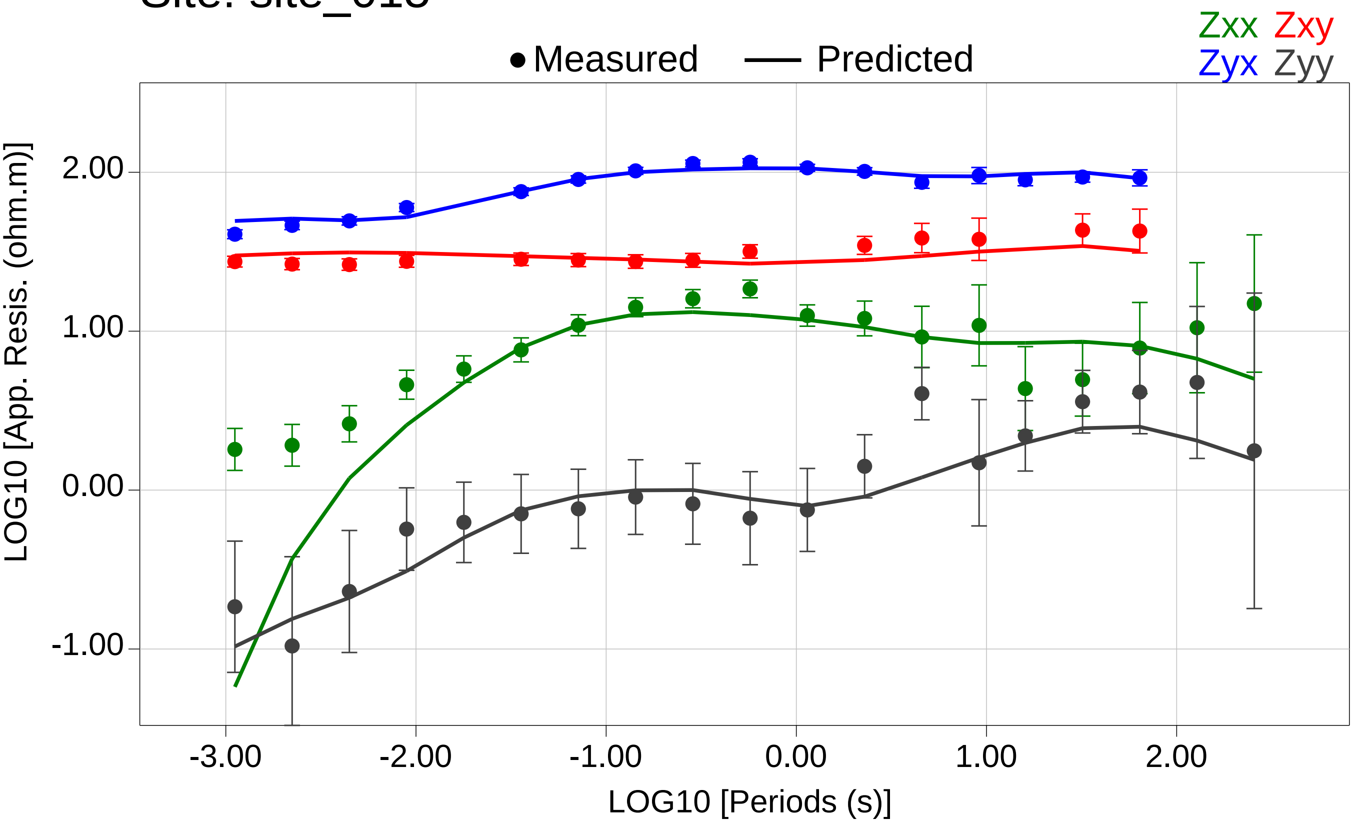

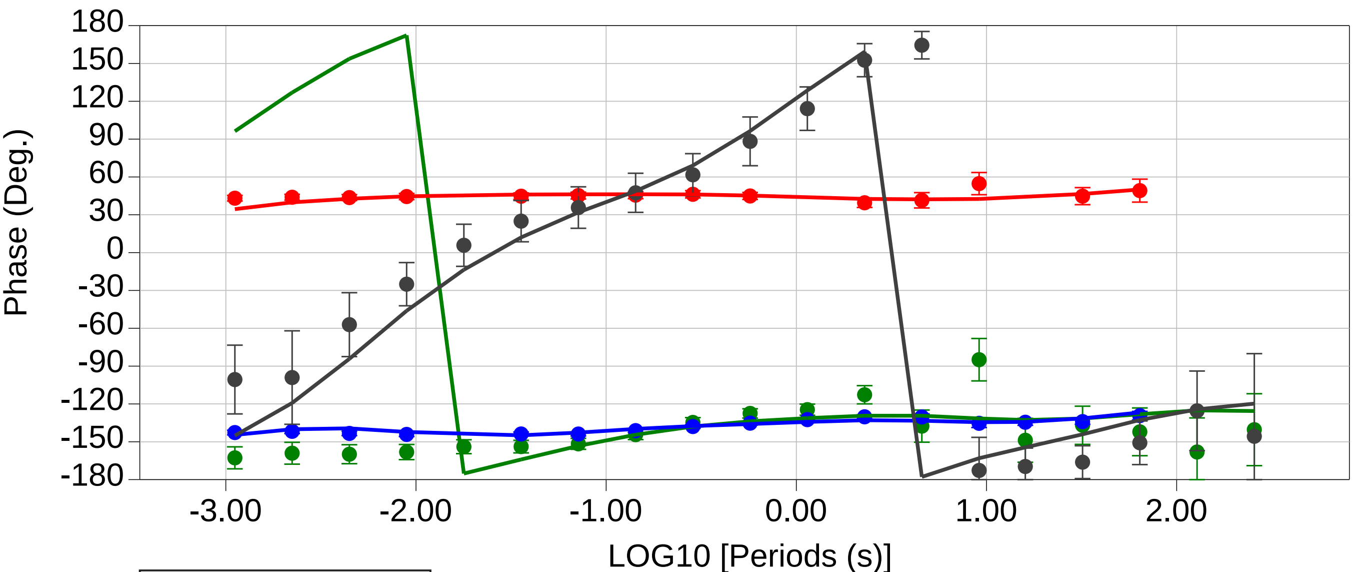

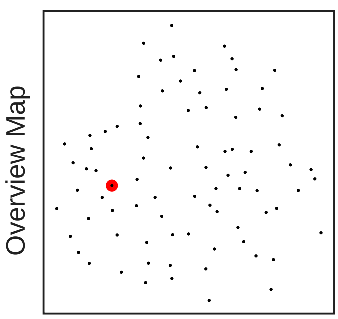

Total RMS = 1.07
Zxx RMS = 1.61
Zxy RMS = 0.88
Zyx RMS = 0.85
Zyy RMS = 0.56

Site: site_016

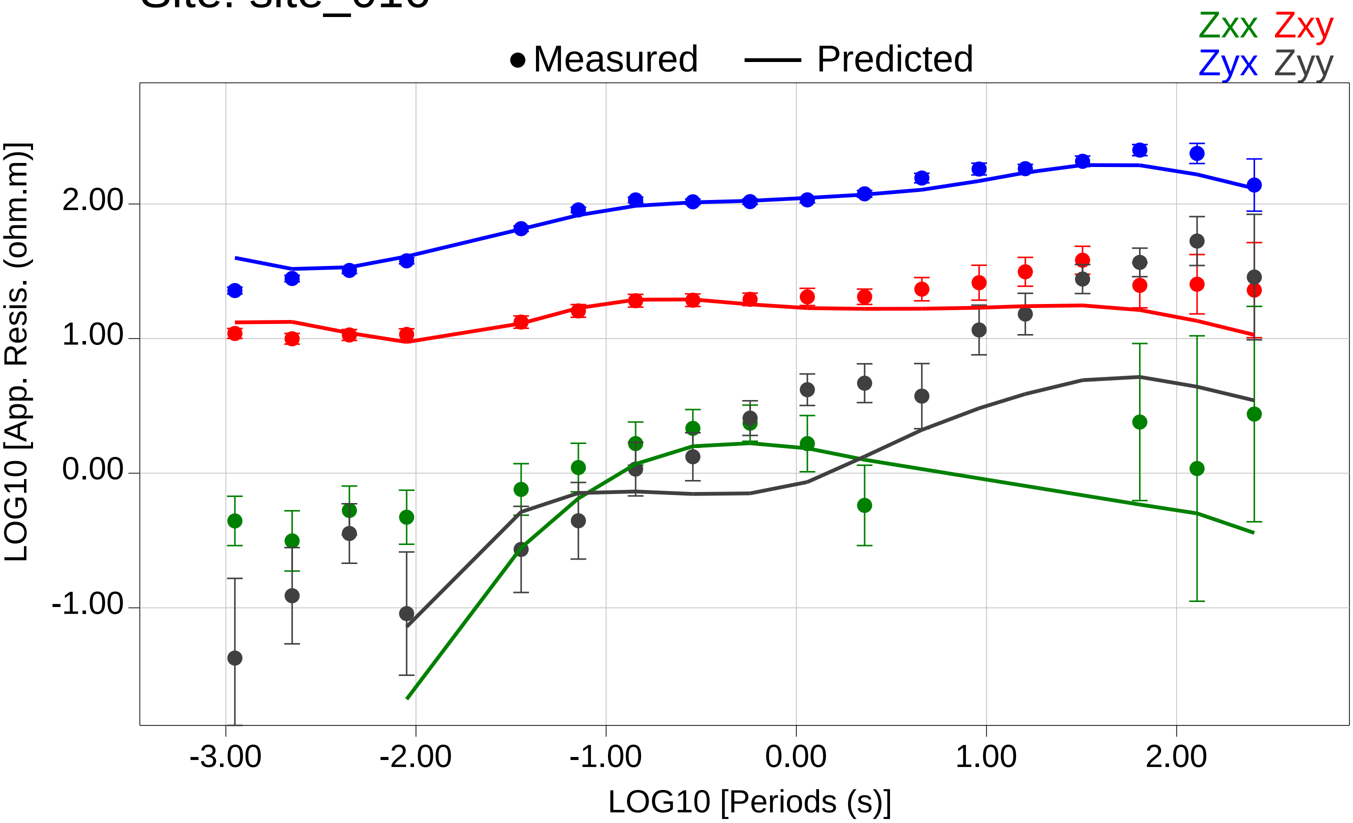

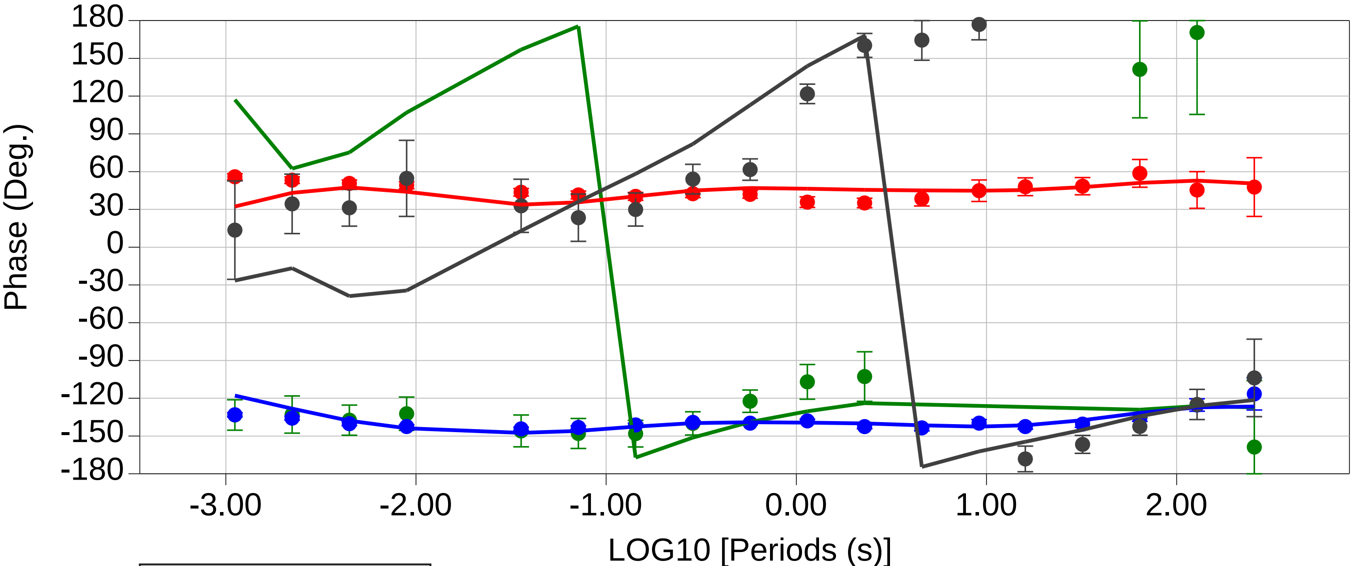

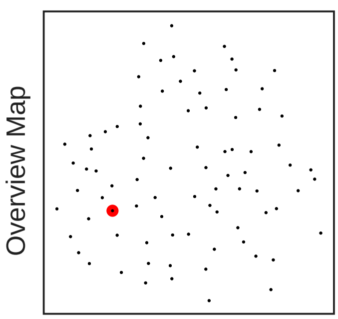

Total RMS = 1.74
Zxx RMS = 1.52
Zxy RMS = 1.66
Zyx RMS = 2.11
Zyy RMS = 1.57

Site: site_017

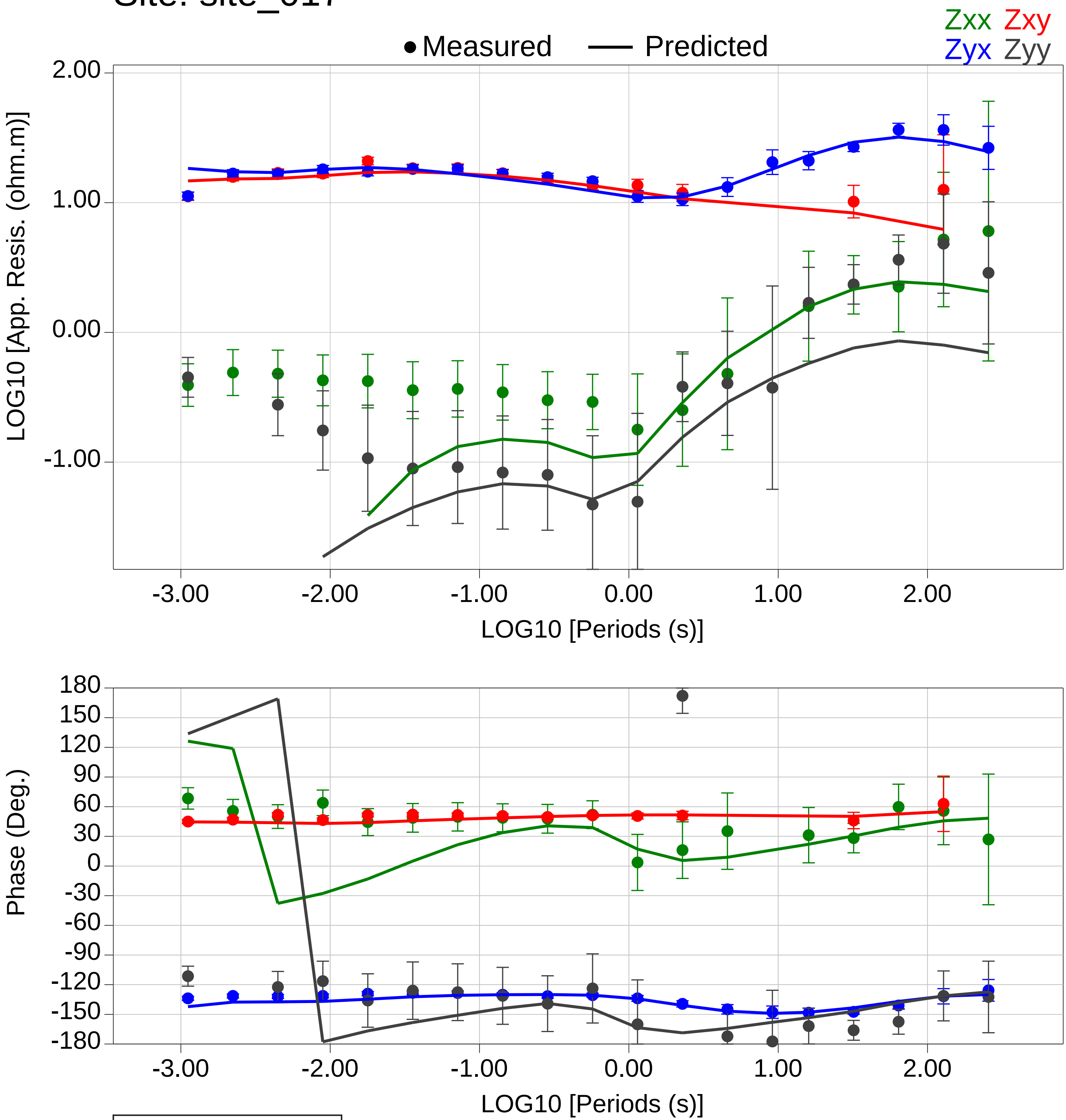

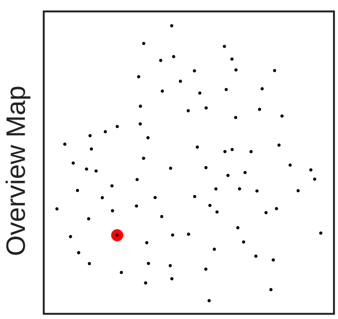

Total RMS = 1.25
Zxx RMS = 1.34
Zxy RMS = 1.21
Zyx RMS = 1.38
Zyy RMS = 1.04

Site: site_018

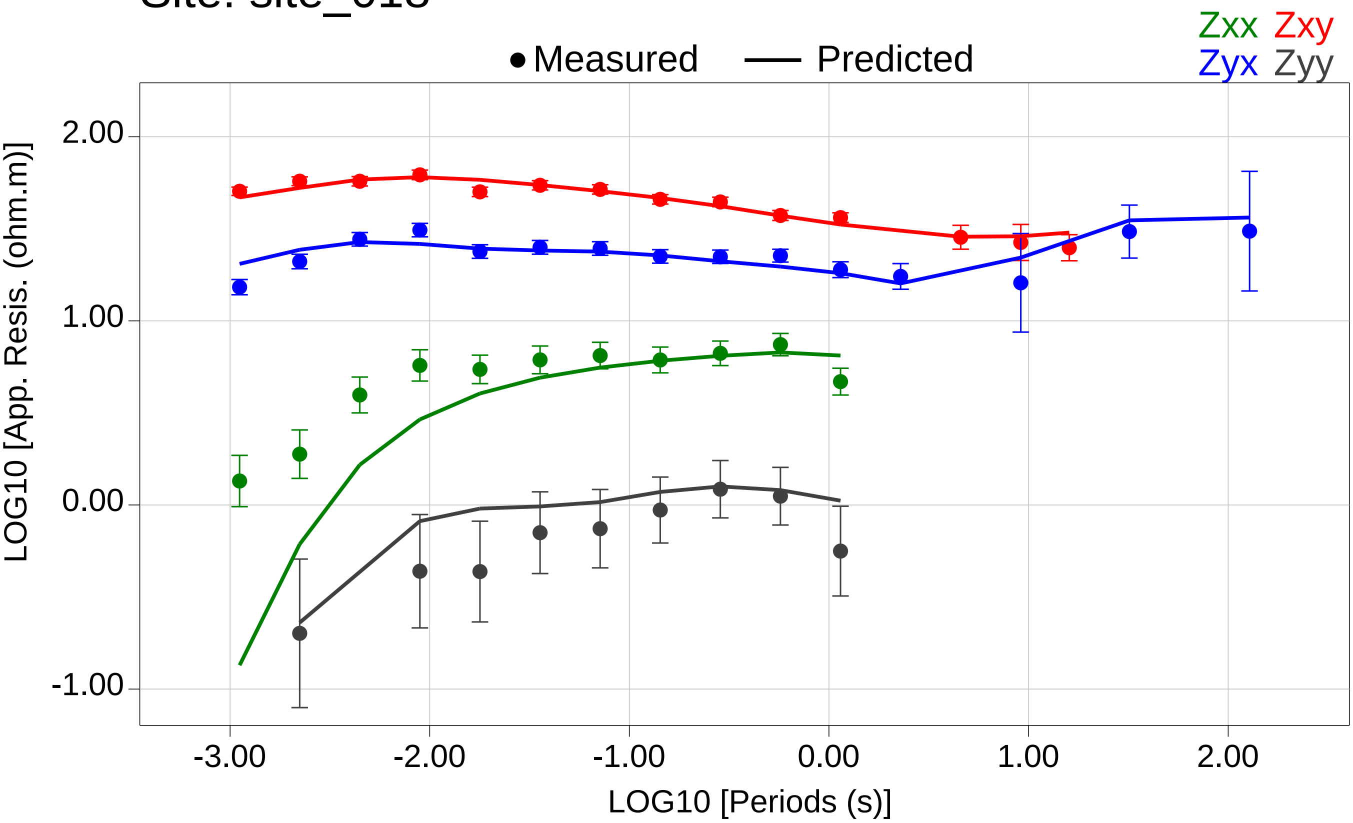

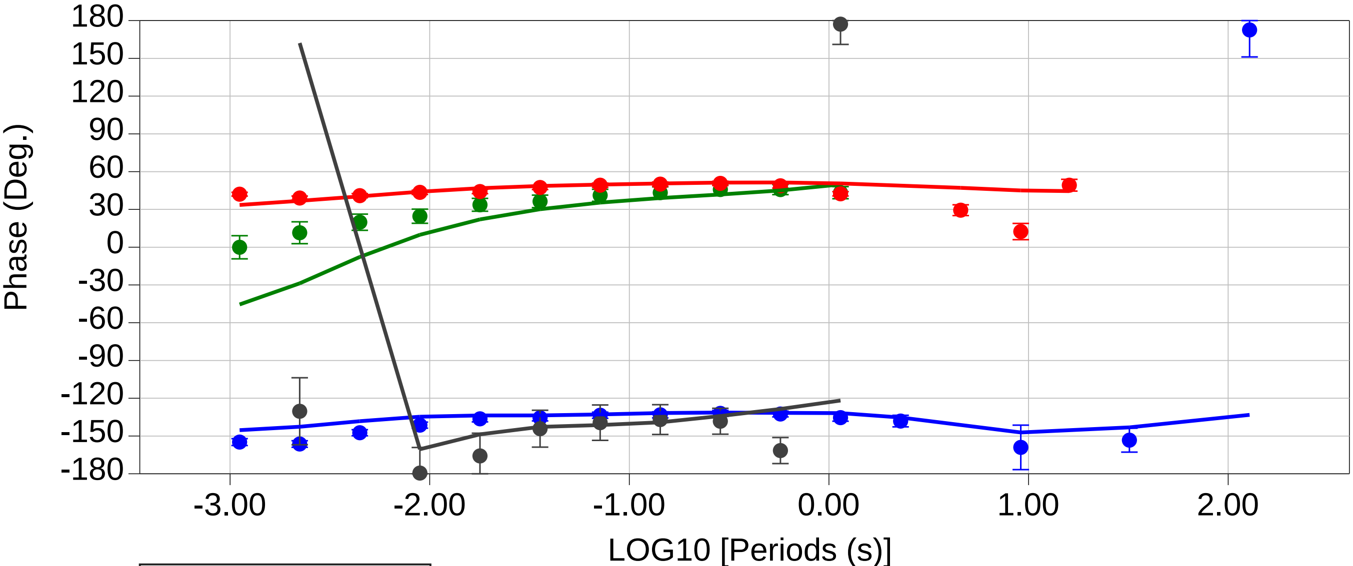

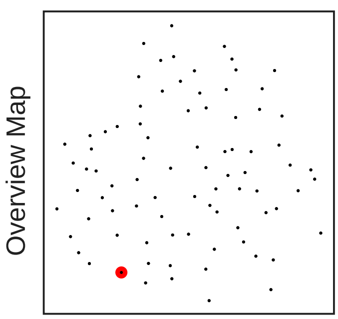

Total RMS = 1.37
Zxx RMS = 1.52
Zxy RMS = 1.47
Zyx RMS = 1.29
Zyy RMS = 1.10

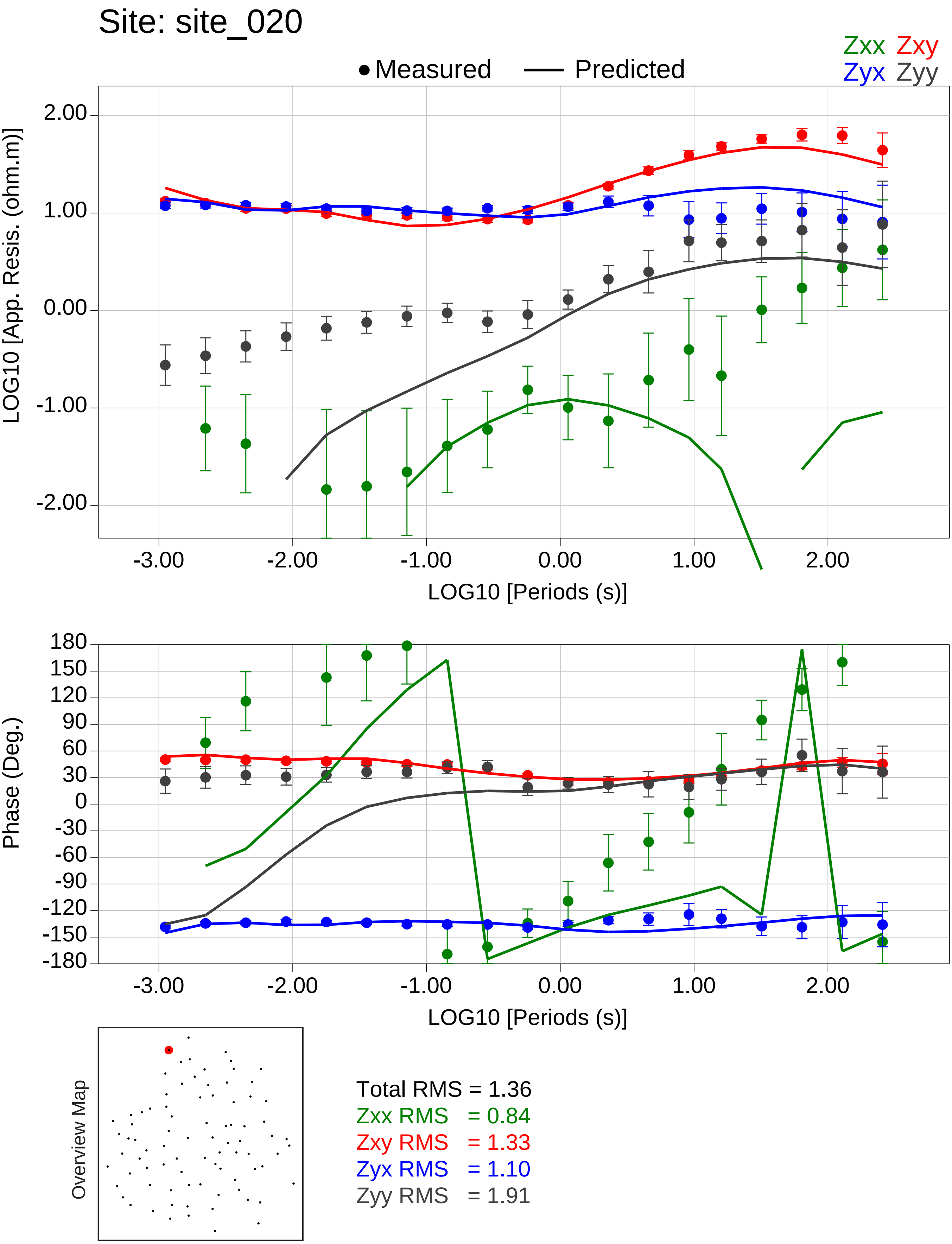

Site: site_020
Measured
Predicted
Zxx Zxy
Zyx Zyy
LOG10 [App. Resis. (ohm.m)]
2.00
1.00
0.00
-1.00
-2.00
-3.00
-2.00
-1.00
0.00
1.00
2.00
LOG10 [Periods (s)]
Phase (Deg.)
180
150
120
90
60
30
0
-30
-60
-90
-120
-150
-180
-3.00
-2.00
-1.00
0.00
1.00
2.00
LOG10 [Periods (s)]
Overview Map
Total RMS = 1.36
Zxx RMS = 0.84
Zxy RMS = 1.33
Zyx RMS = 1.10
Zyy RMS = 1.91

Site: site_021

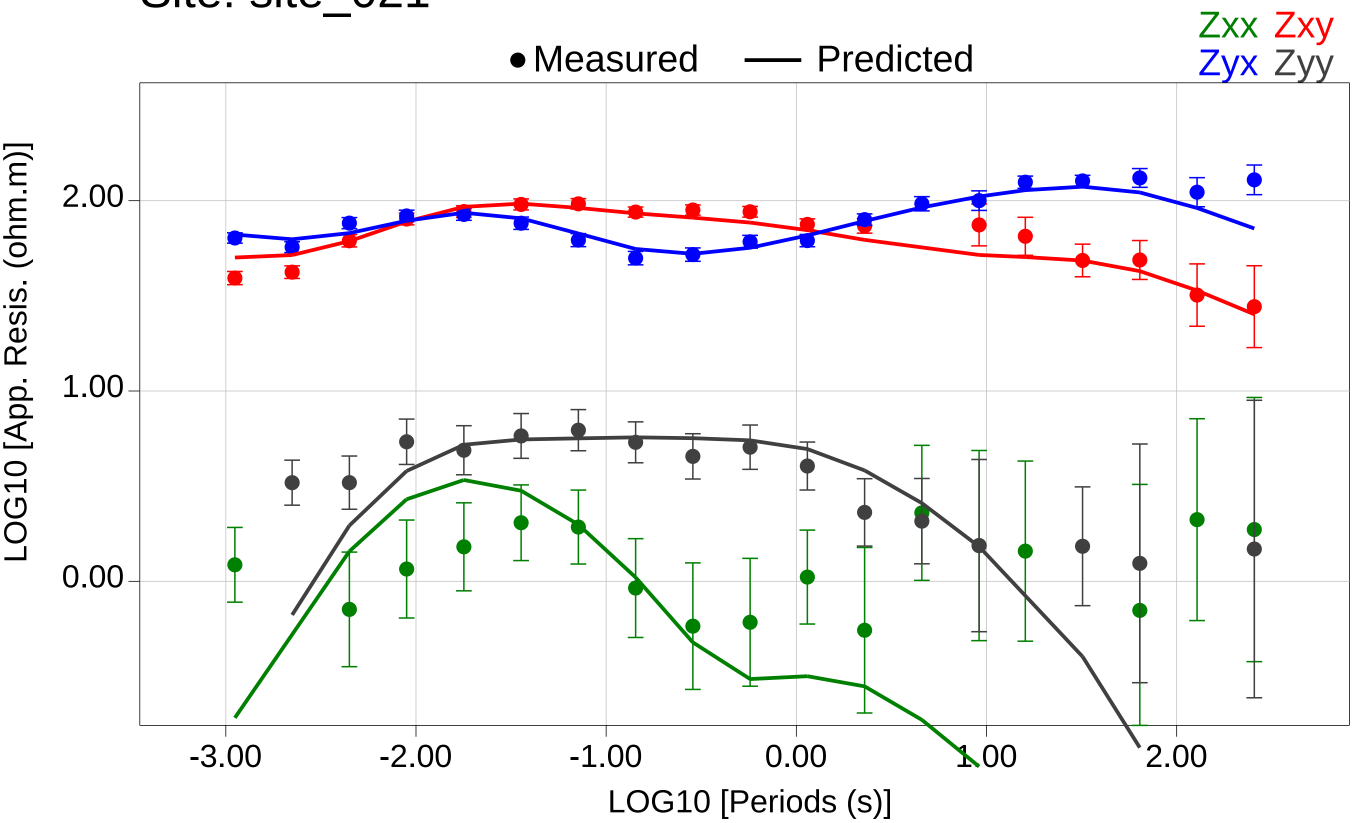

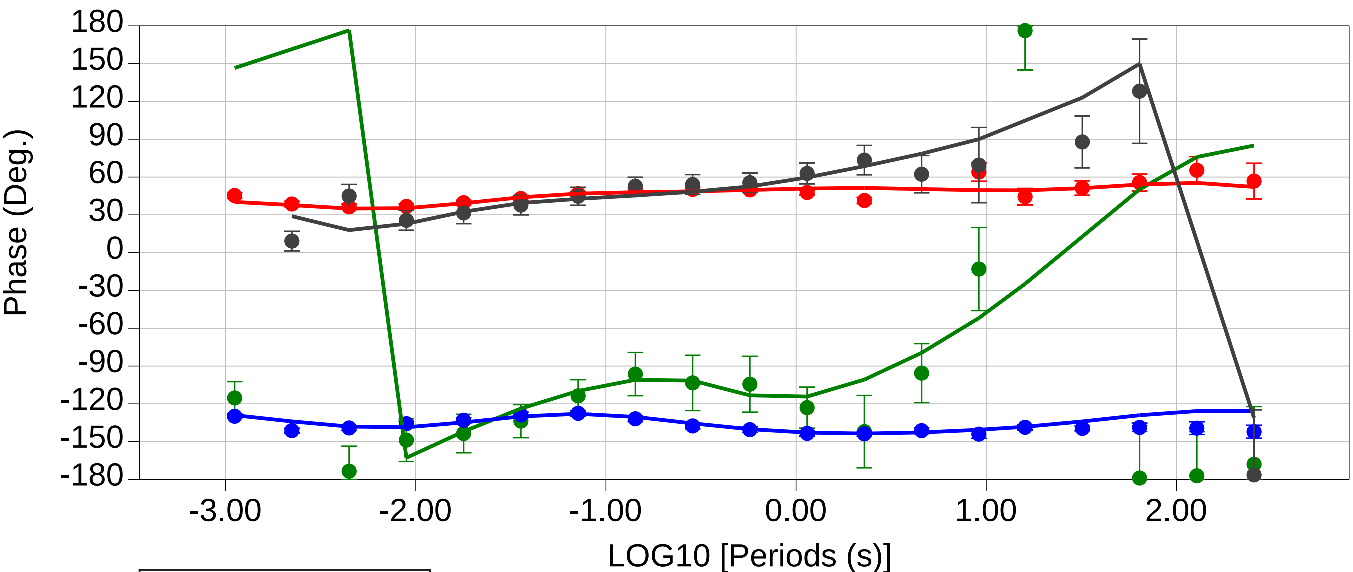

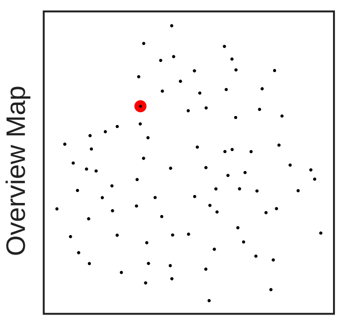

Total RMS = 0.93
Zxx RMS = 0.93
Zxy RMS = 0.95
Zyx RMS = 1.01
Zyy RMS = 0.81

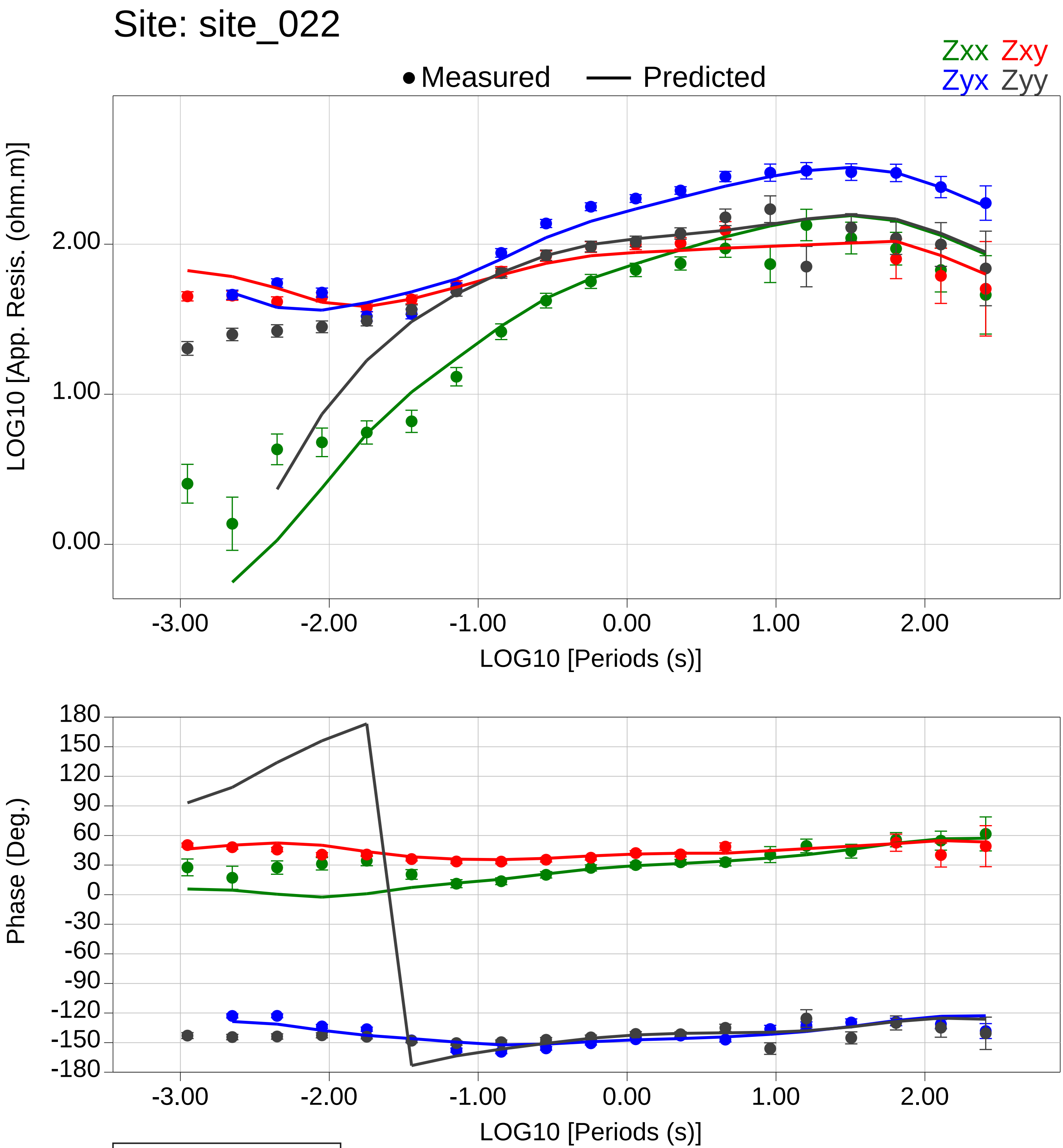

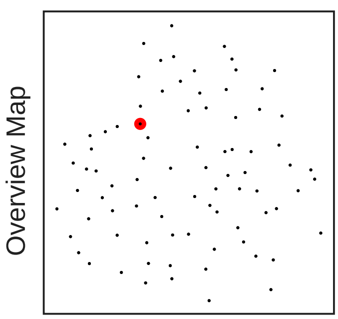

Total RMS = 3.08
Zxx RMS = 1.49
Zxy RMS = 1.43
Zyx RMS = 1.70
Zyy RMS = 5.41

Site: site_023

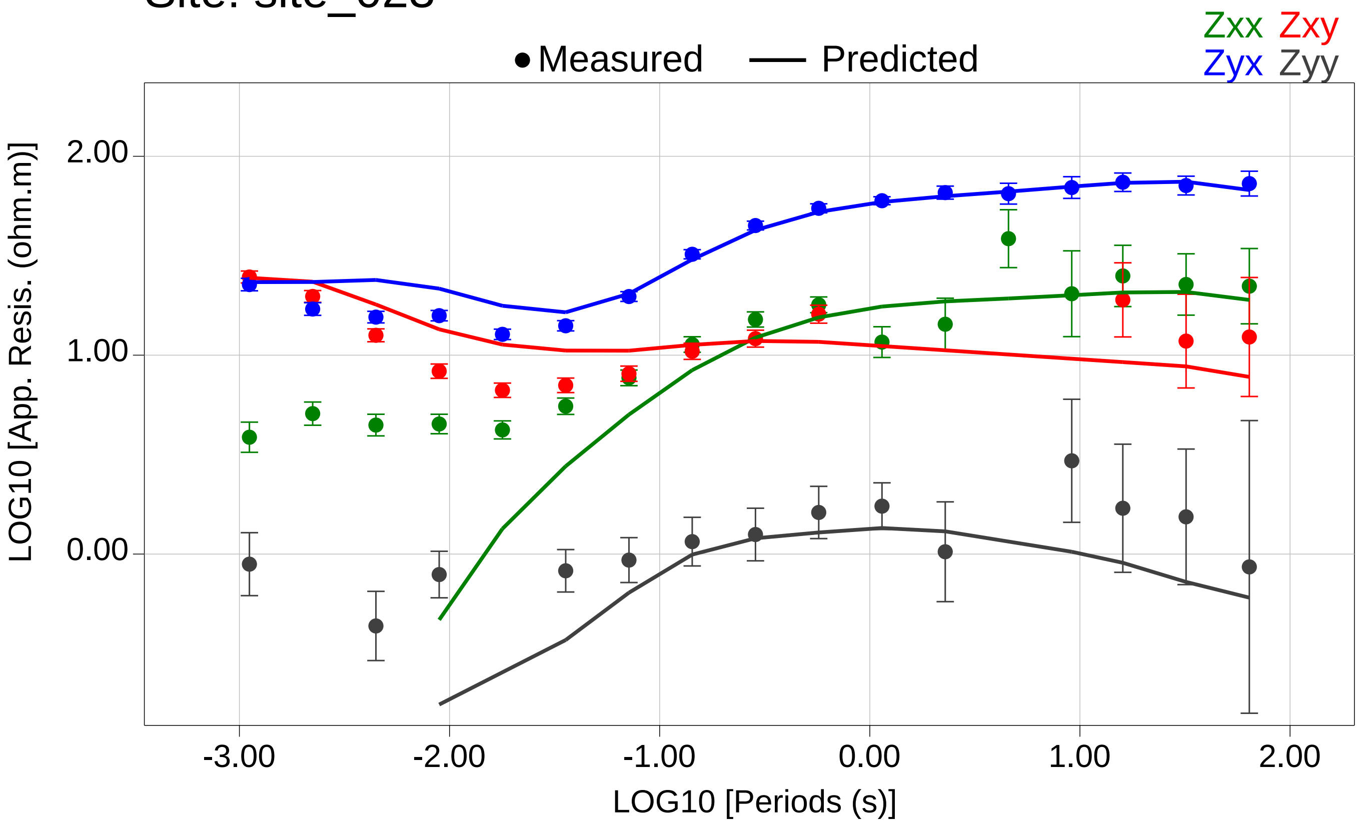

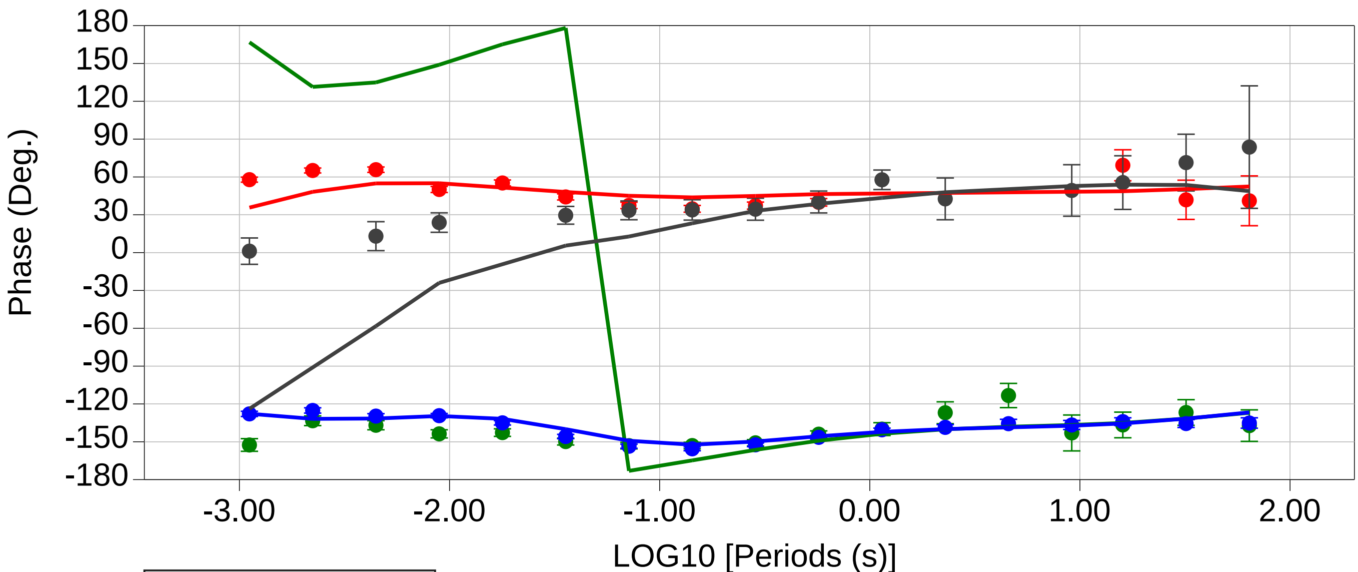

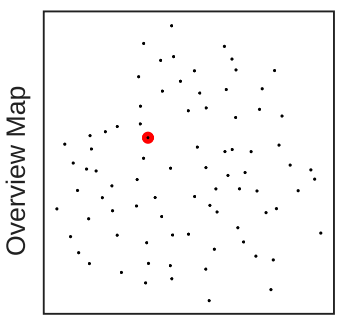

Total RMS = 2.98
Zxx RMS = 4.48
Zxy RMS = 2.99
Zyx RMS = 1.74
Zyy RMS = 1.52

Site: site_024

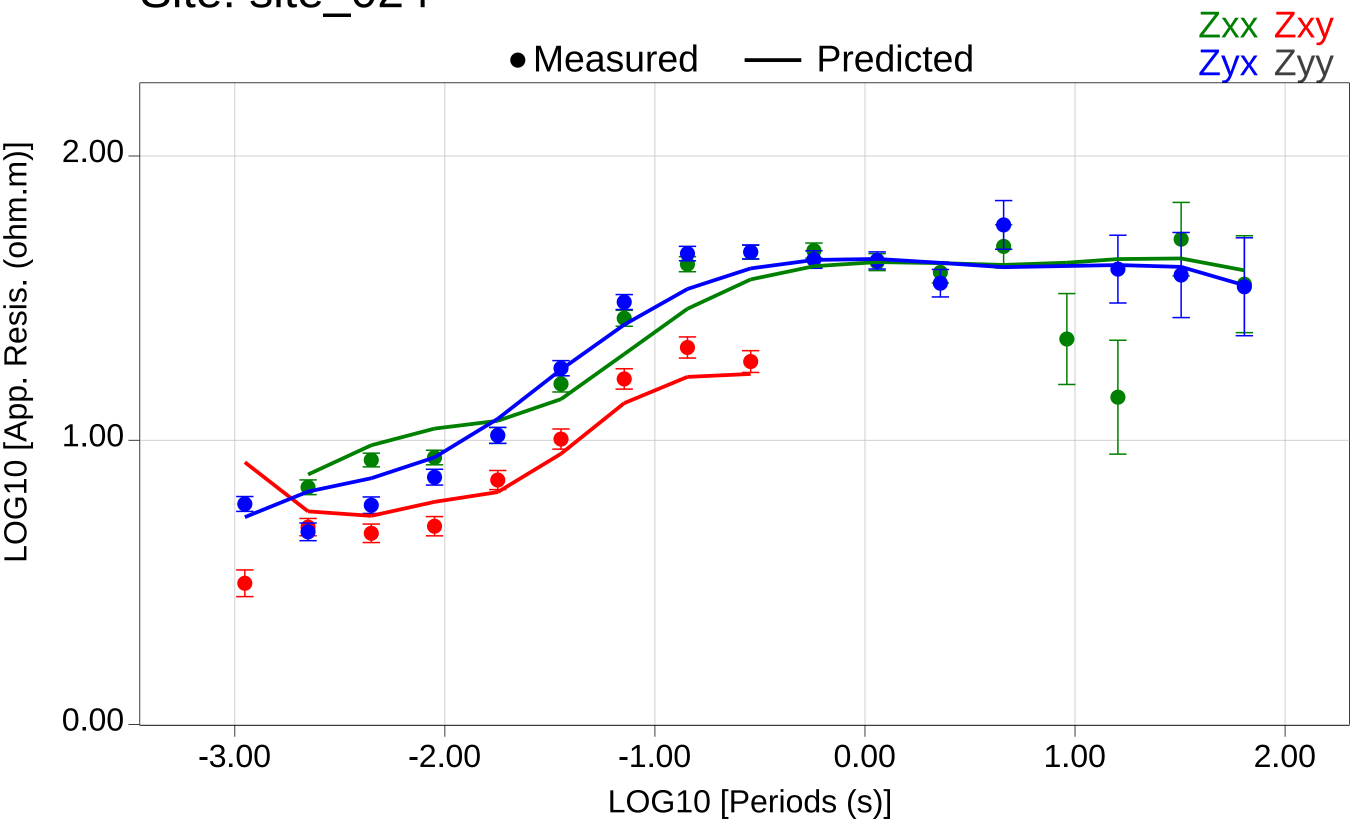

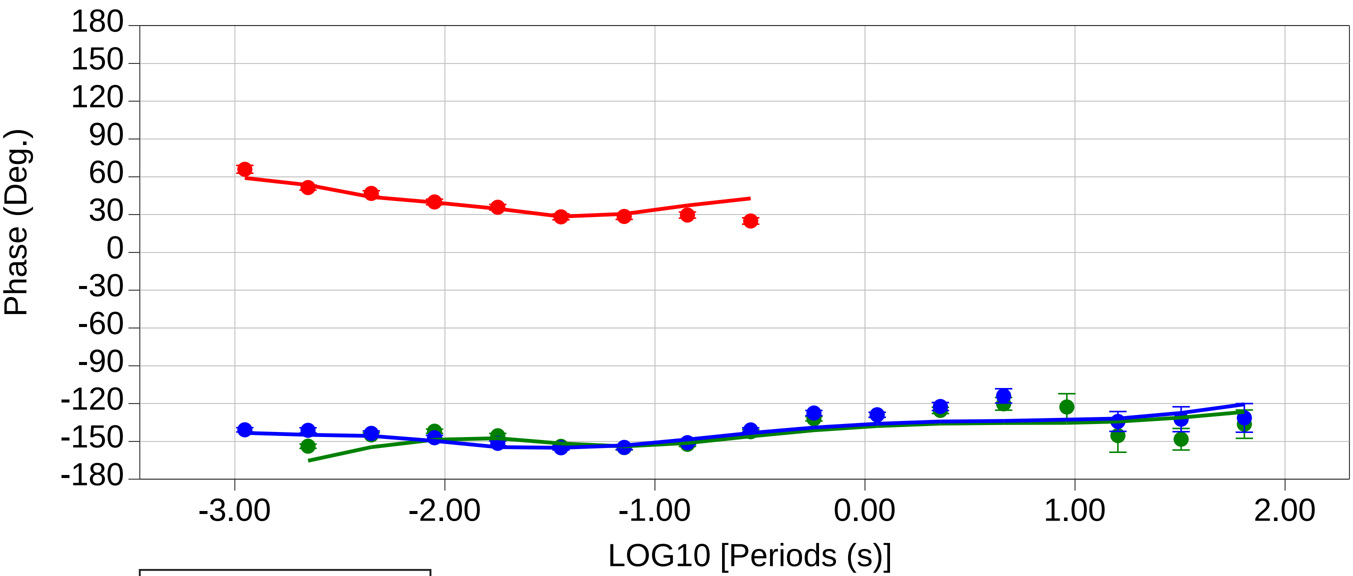

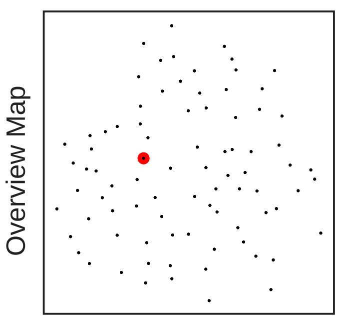

Total RMS = 2.10
Zxx RMS = 2.19
Zxy RMS = 2.56
Zyx RMS = 1.67
Zyy RMS = 0.00

Site: site_025

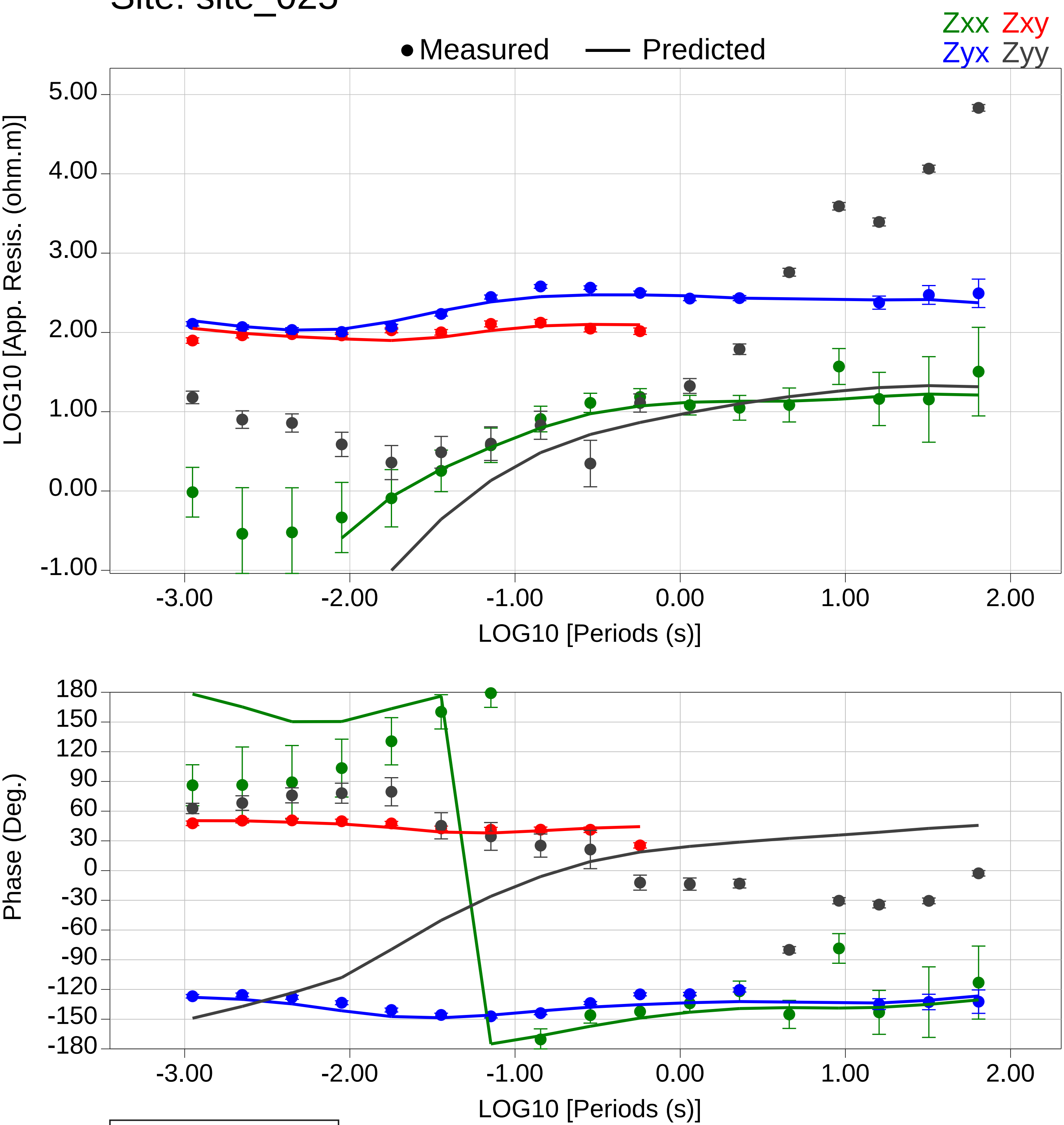

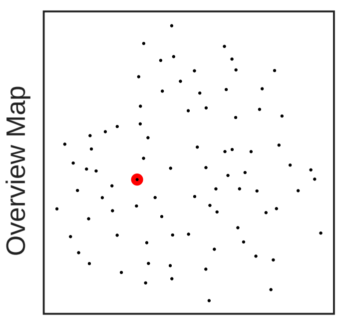

Total RMS = 3.34
Zxx RMS = 0.75
Zxy RMS = 1.75
Zyx RMS = 1.91
Zyy RMS = 5.76

Site: site_026

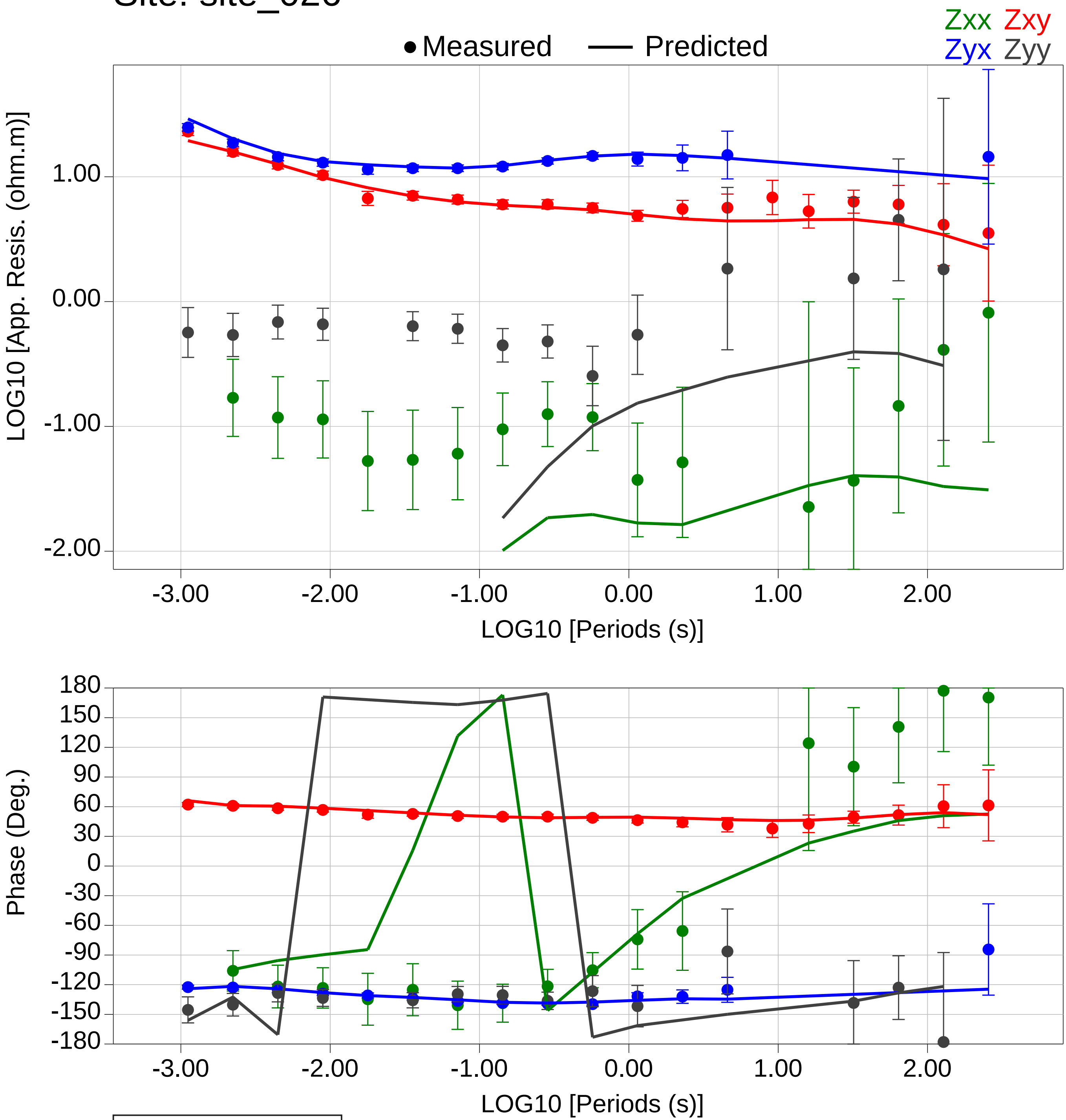

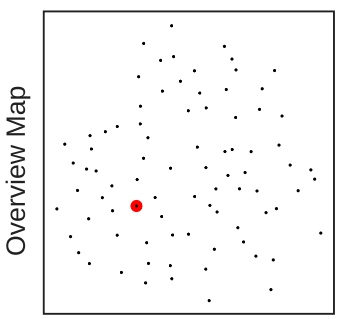

Total RMS = 1.27
Zxx RMS = 0.91
Zxy RMS = 0.58
Zyx RMS = 0.55
Zyy RMS = 2.35

Site: site_027

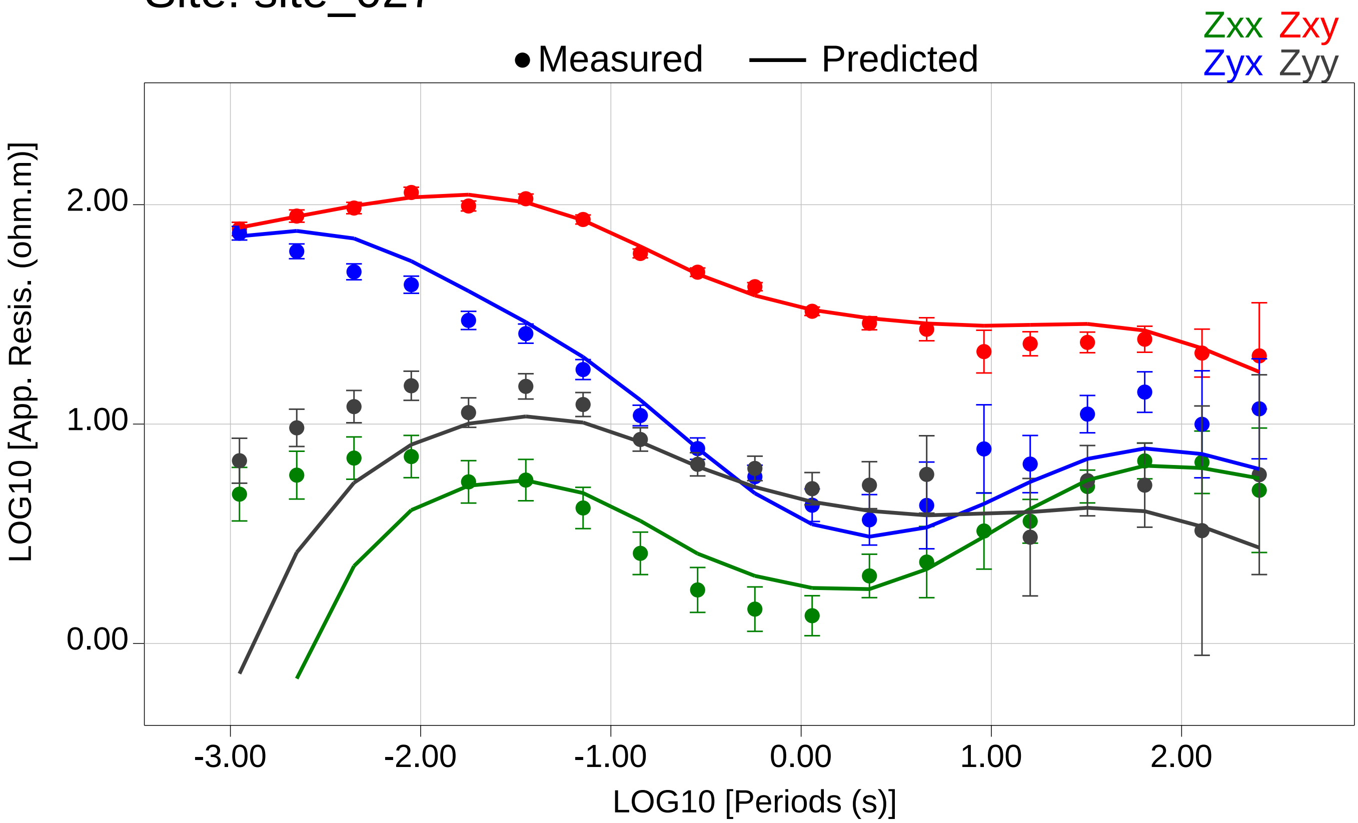

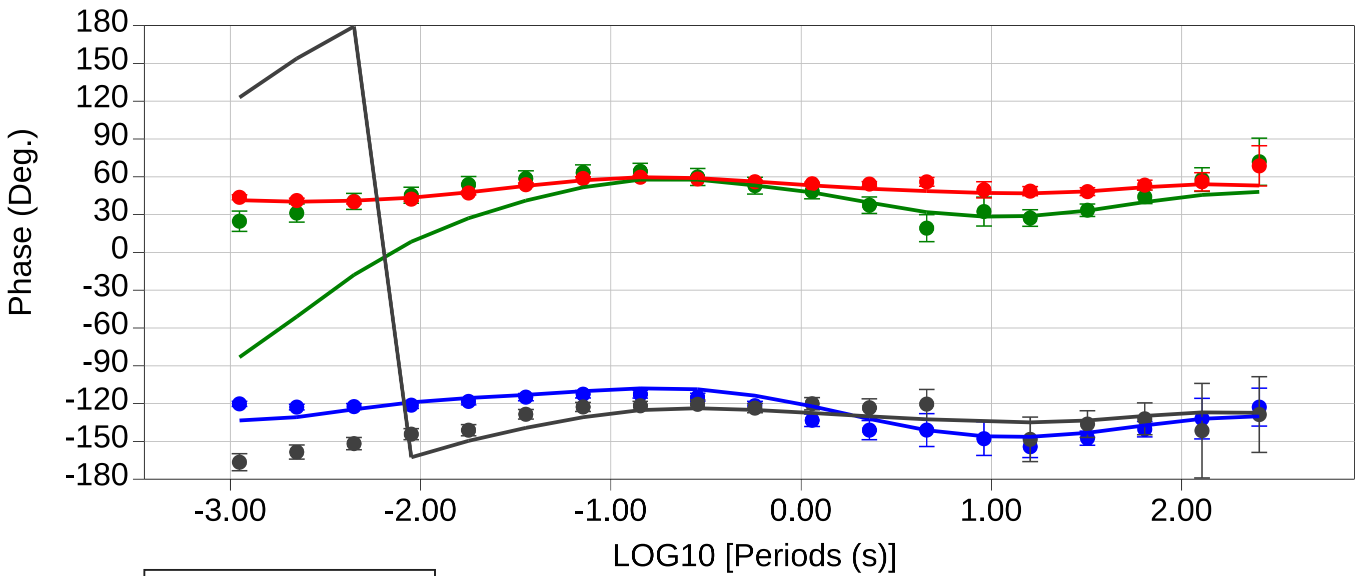

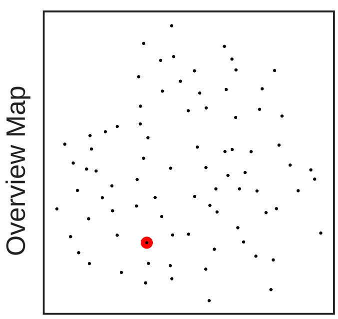

Total RMS = 1.49
Zxx RMS = 1.84
Zxy RMS = 0.72
Zyx RMS = 1.41
Zyy RMS = 1.75

Site: site_028

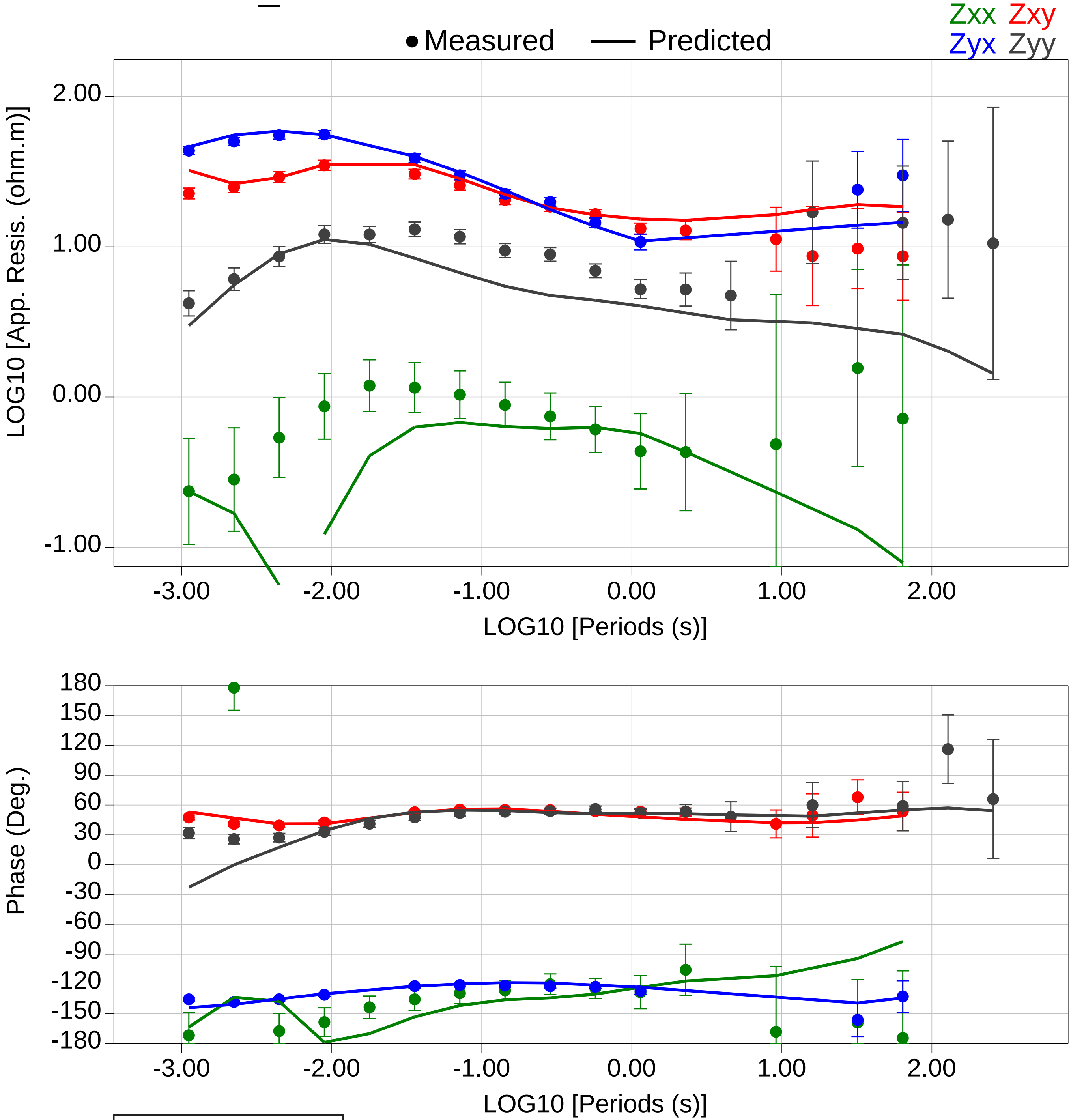

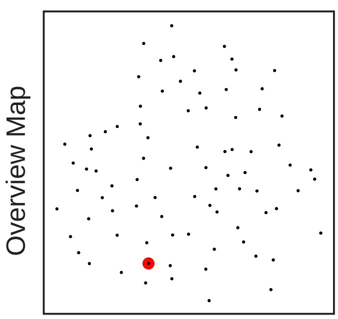

Total RMS = 1.26
Zxx RMS = 0.79
Zxy RMS = 1.06
Zyx RMS = 0.98
Zyy RMS = 1.81

Site: site_029

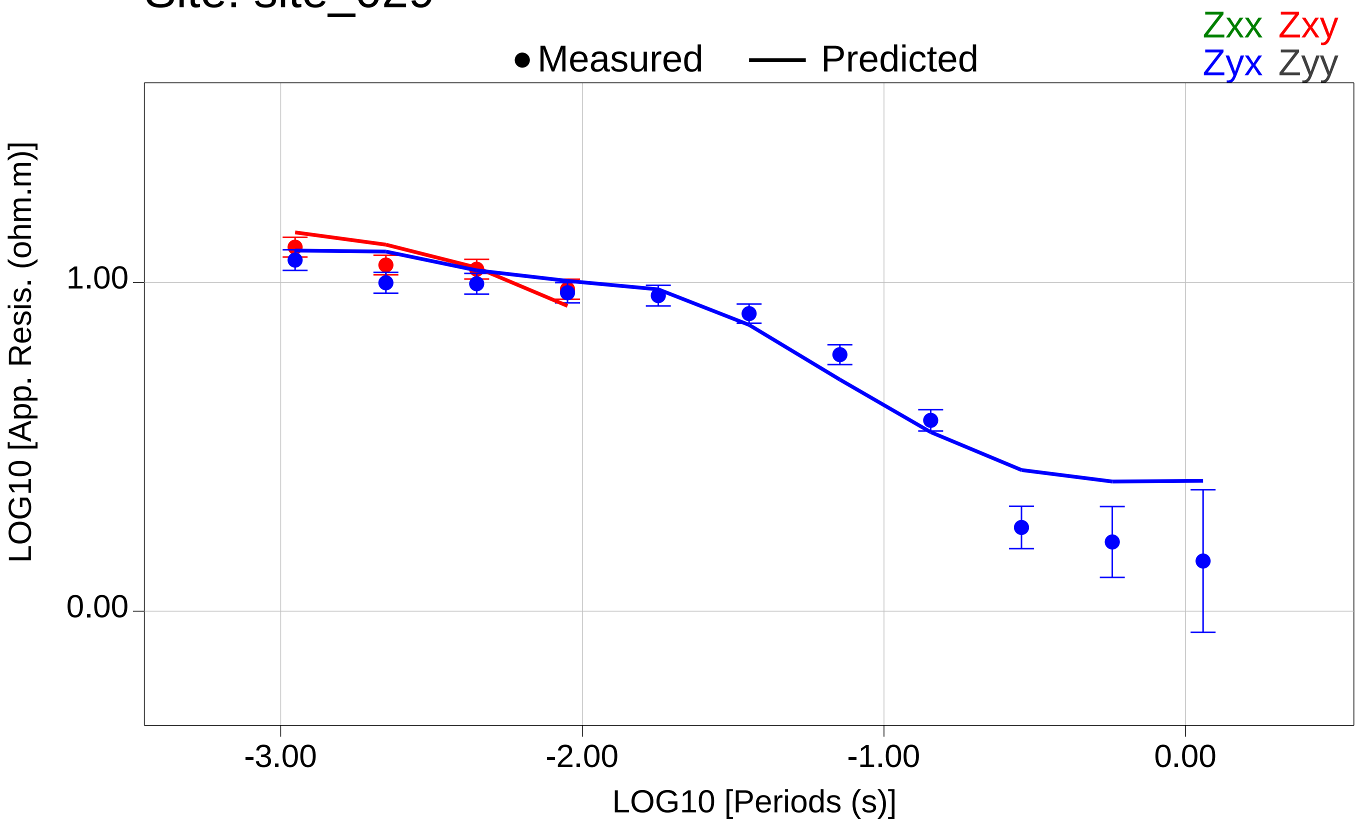

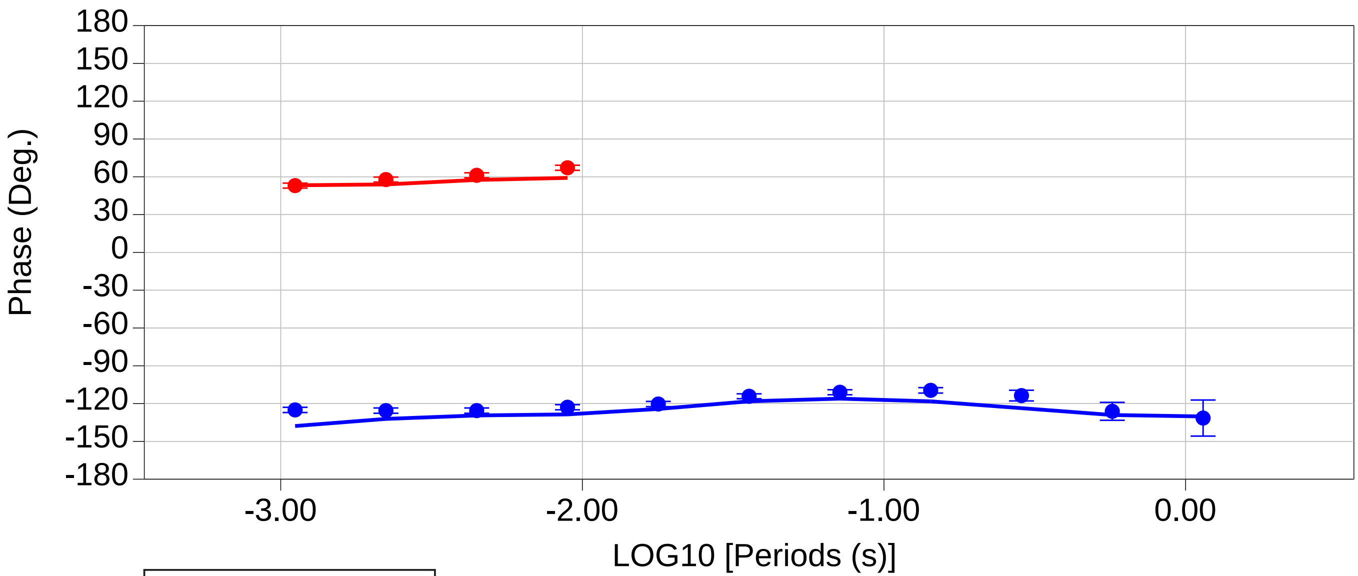

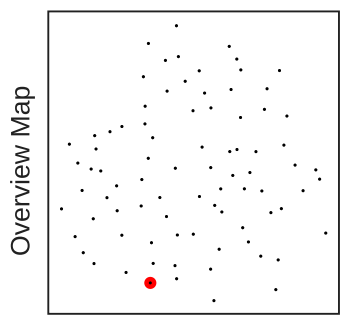

Total RMS = 1.67
Zxx RMS = 0.00
Zxy RMS = 1.42
Zyx RMS = 1.76
Zyy RMS = 0.00

Site: site_030

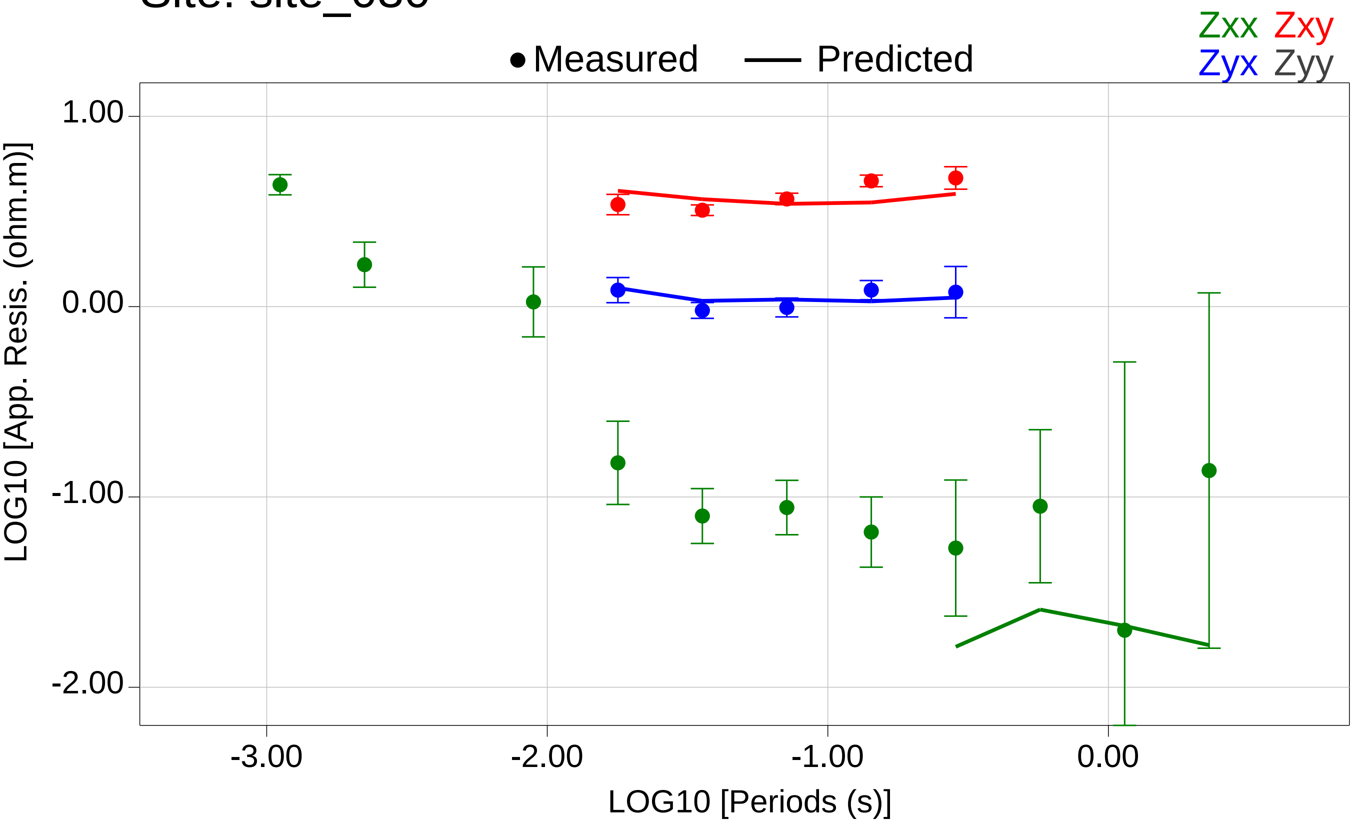

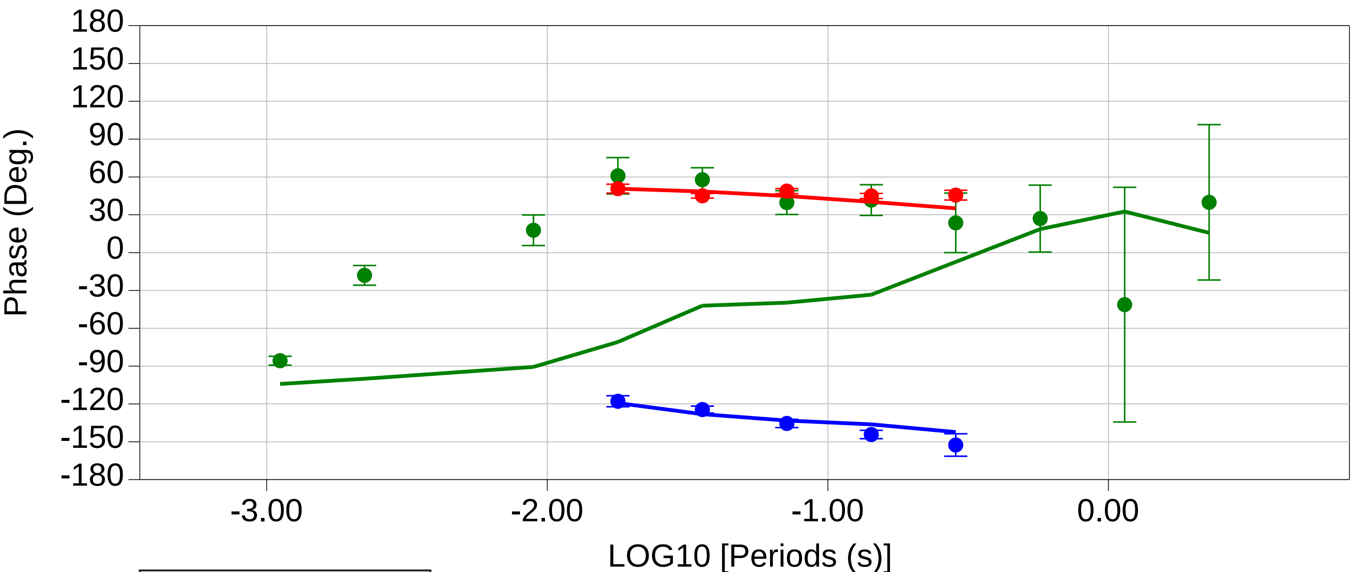

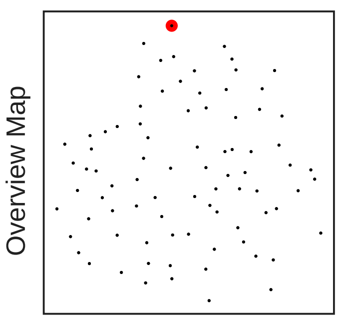

Total RMS = 2.46
Zxx RMS = 3.22
Zxy RMS = 1.41
Zyx RMS = 0.80
Zyy RMS = 0.00

Site: site_031

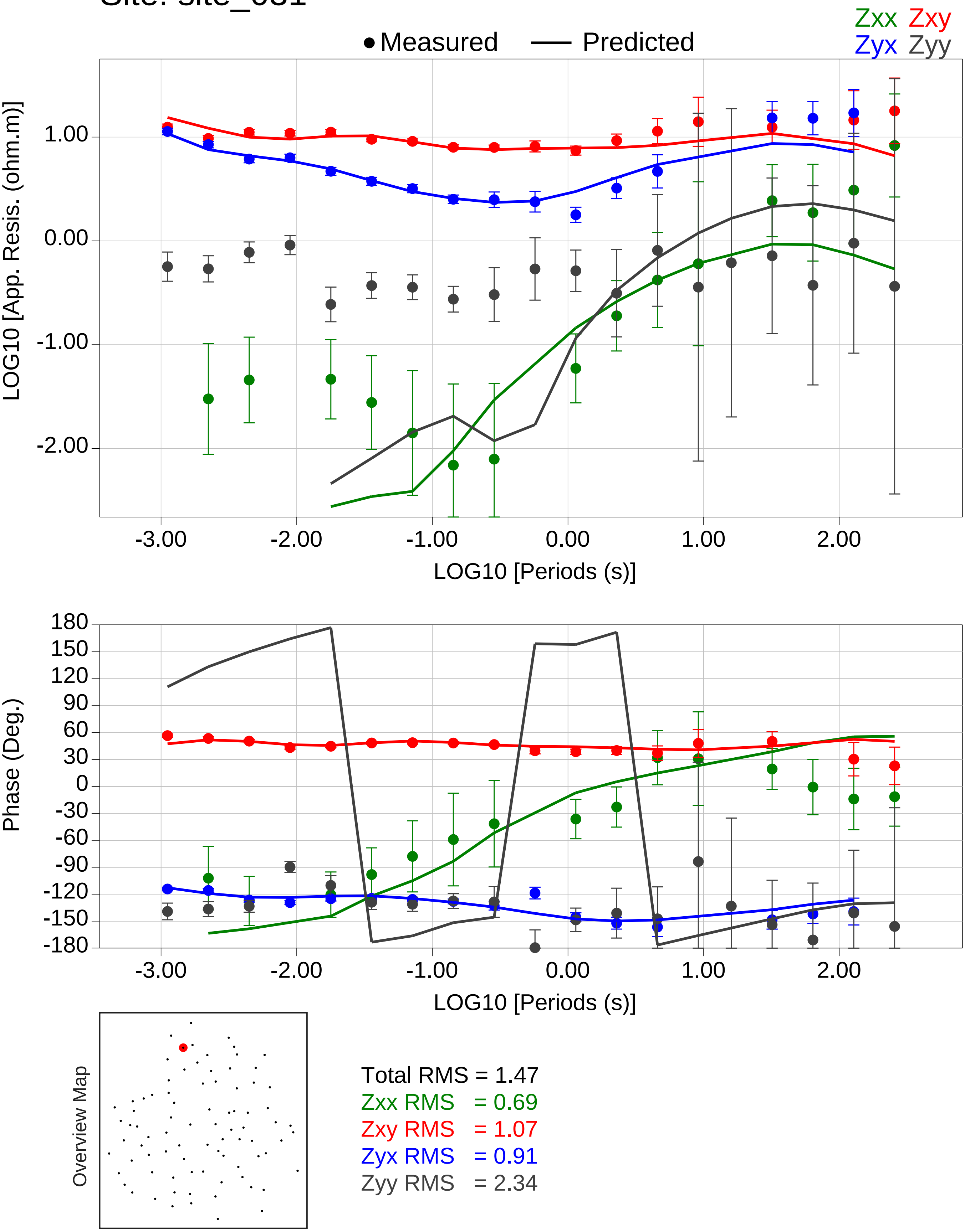

Site: site_032

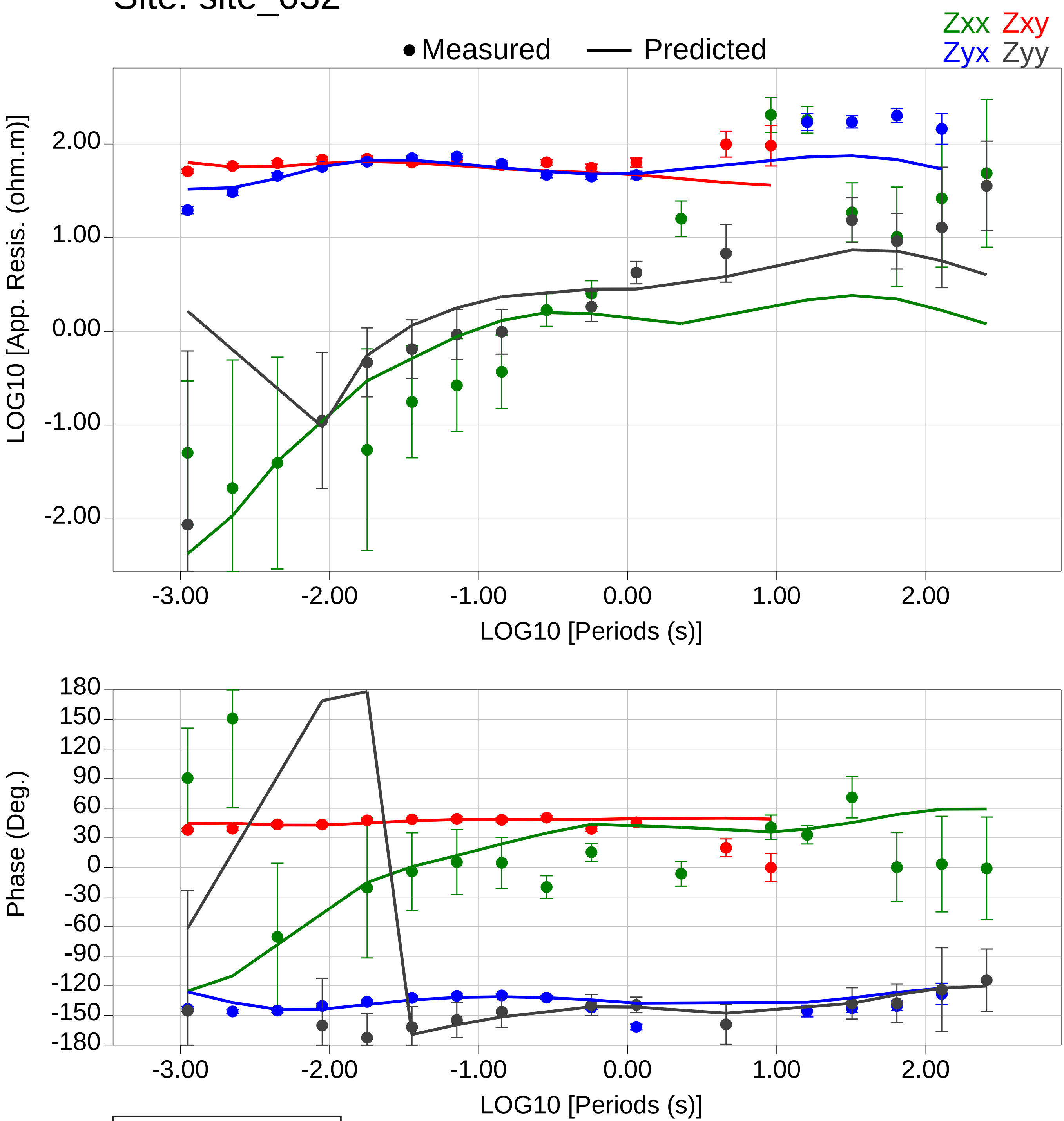

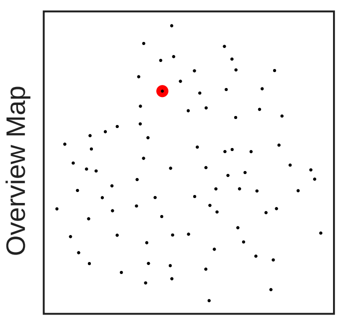

Total RMS = 1.58
Zxx RMS = 1.32
Zxy RMS = 1.44
Zyx RMS = 2.22
Zyy RMS = 1.04

Site: site_035

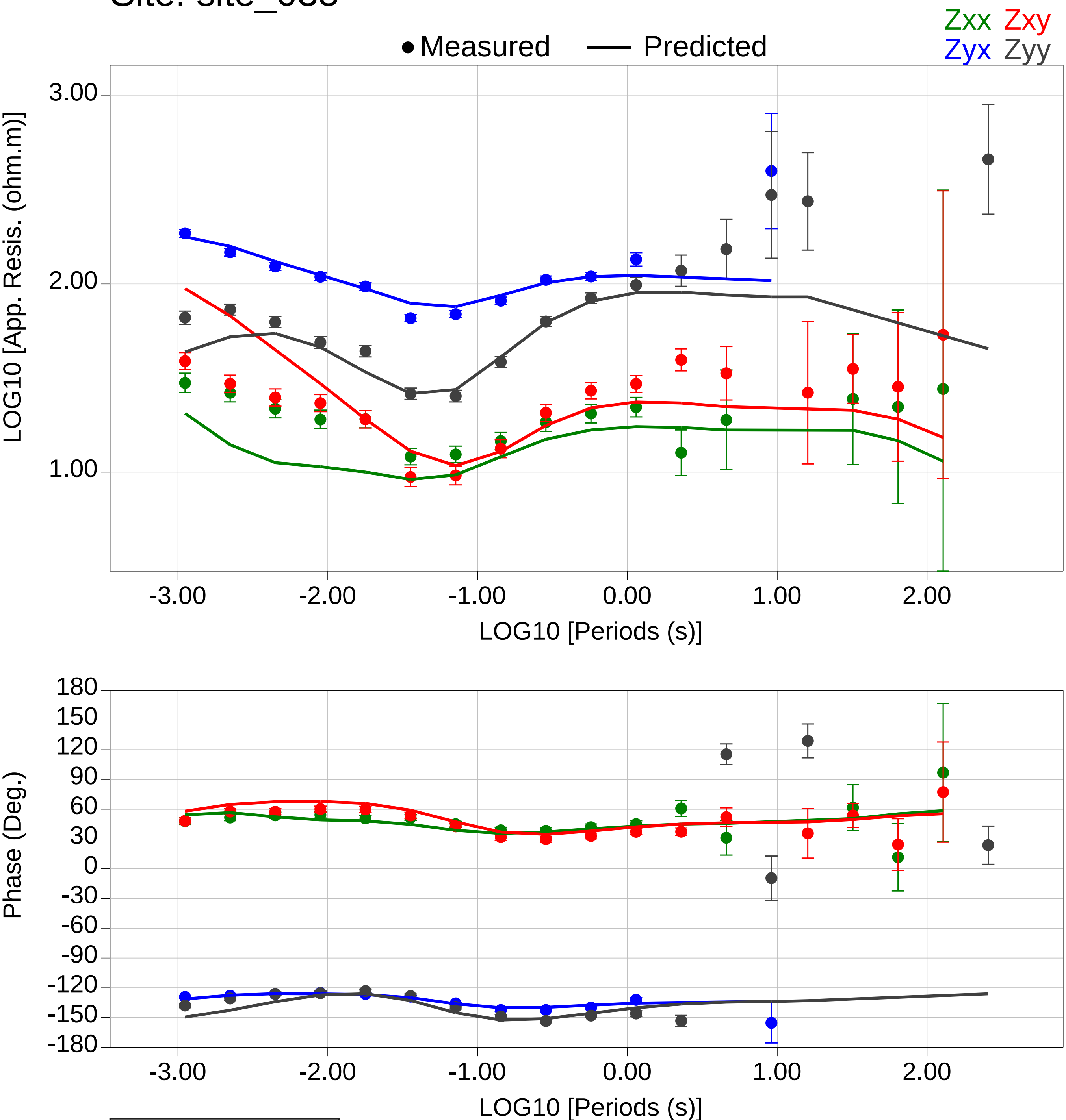

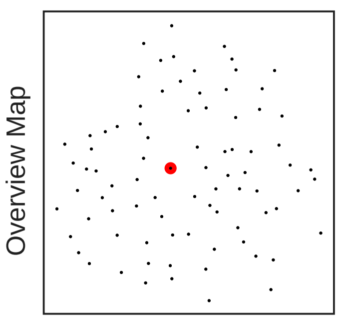

Total RMS = 1.87
Zxx RMS = 1.55
Zxy RMS = 2.31
Zyx RMS = 1.08
Zyy RMS = 2.08

Site: site_036

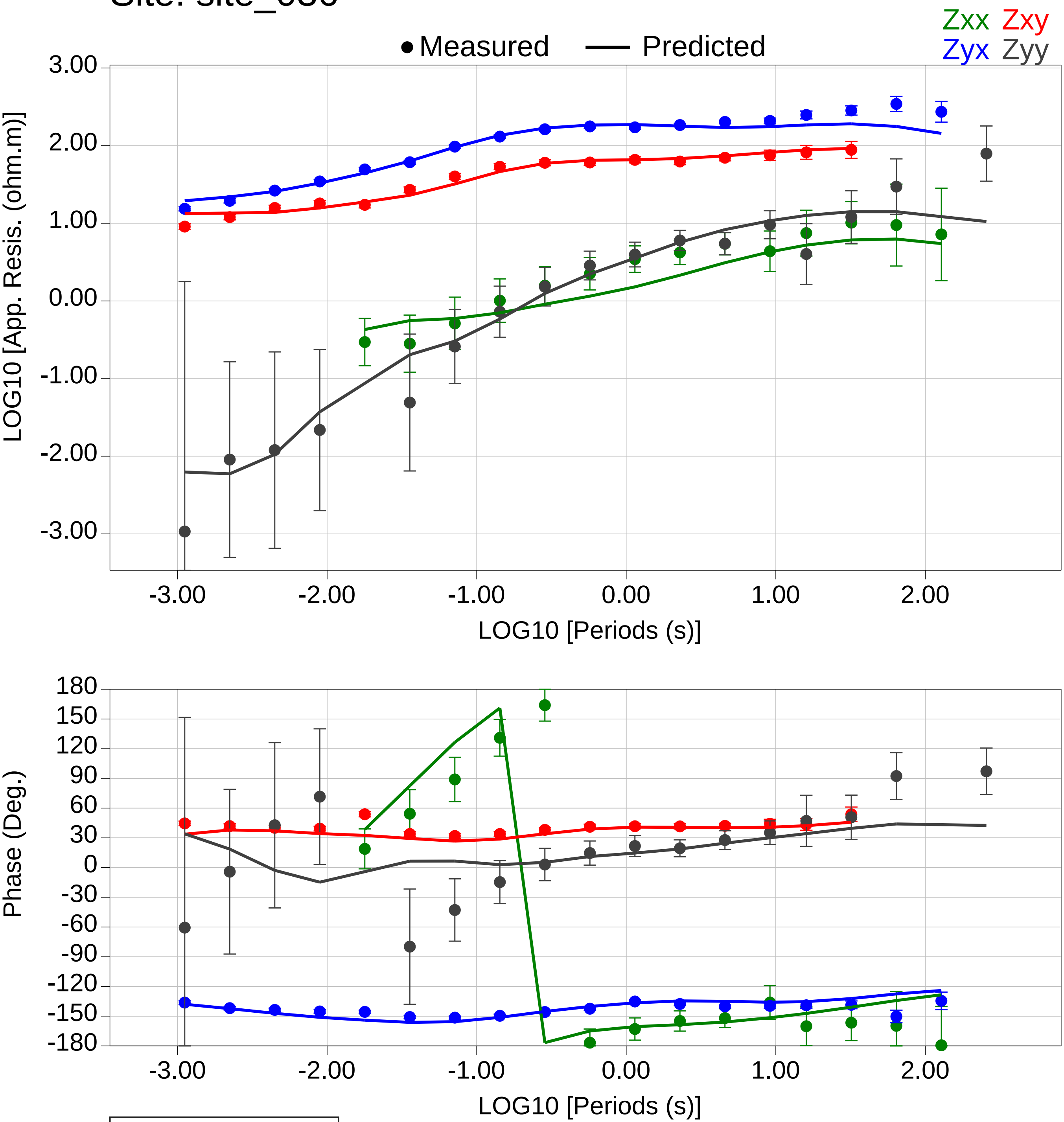

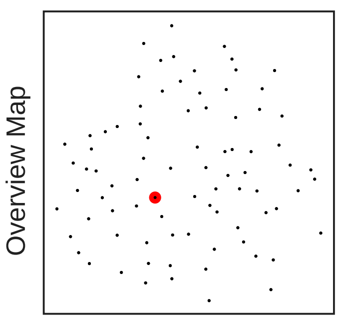

Total RMS = 1.21
Zxx RMS = 0.68
Zxy RMS = 1.63
Zyx RMS = 1.48
Zyy RMS = 0.61

Site: site_037

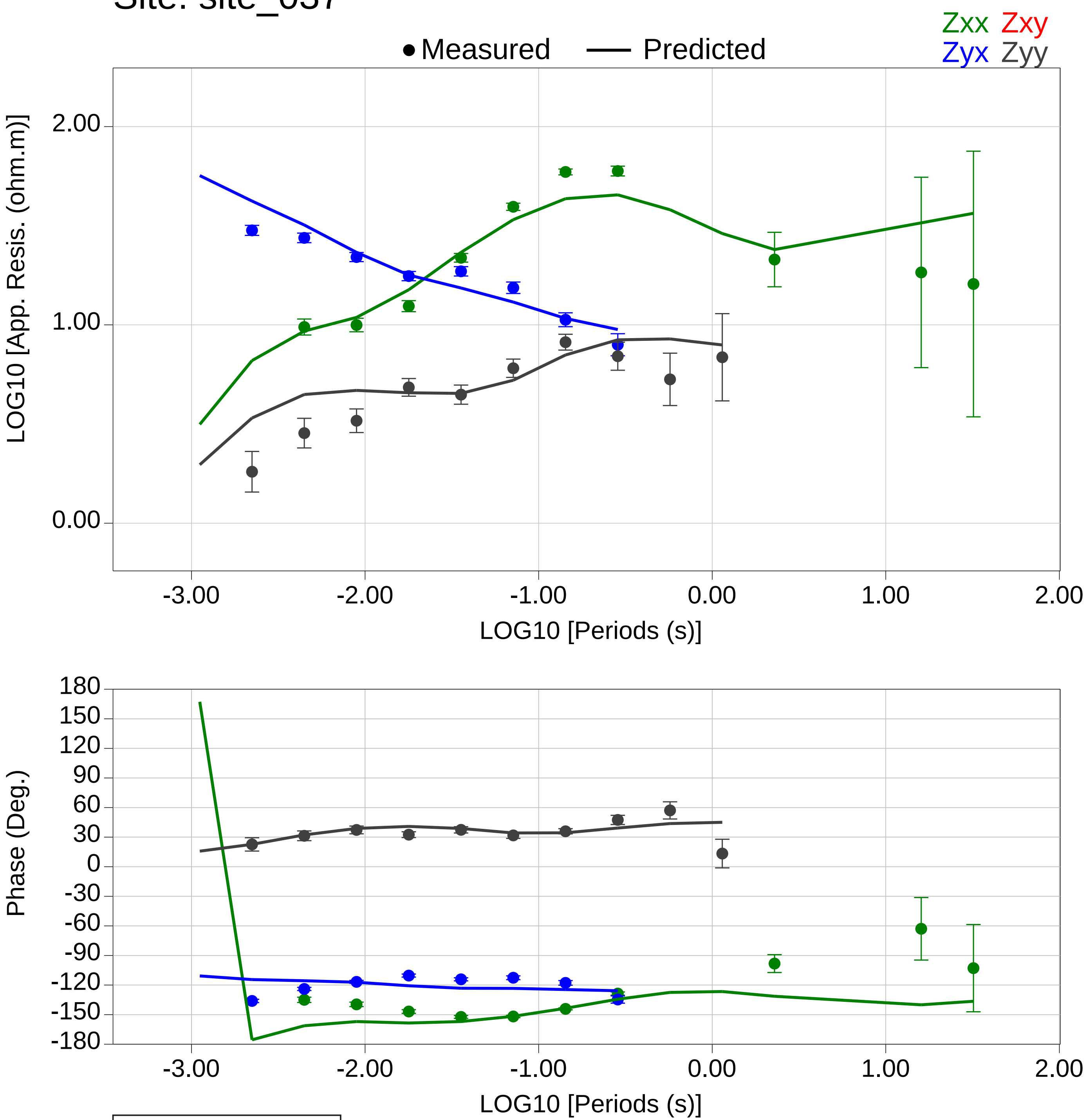

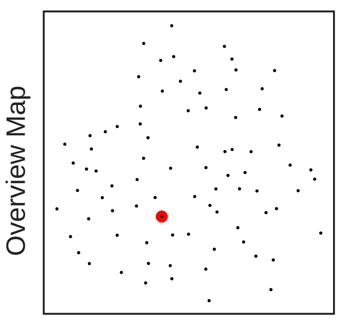

Total RMS = 2.73
Zxx RMS = 3.93
Zxy RMS = 0.00
Zyx RMS = 6.60
Zyy RMS = 2.01

Site: site_038

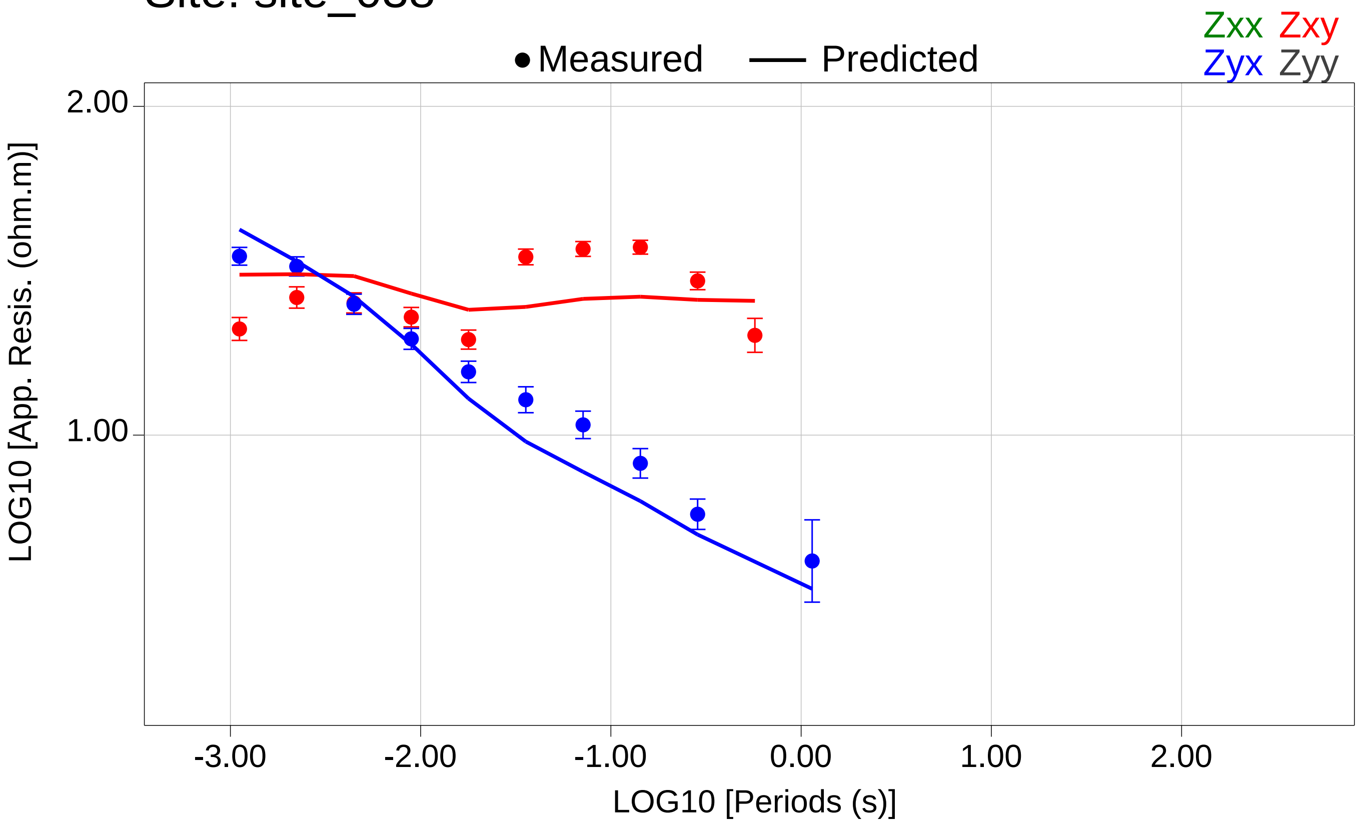

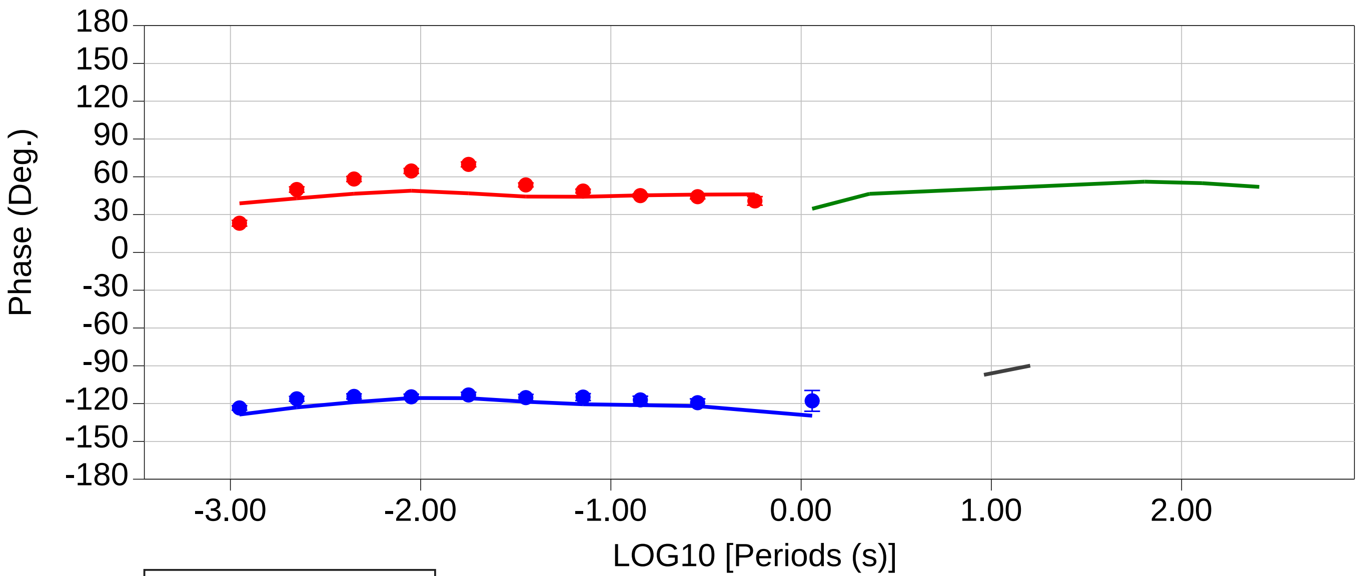

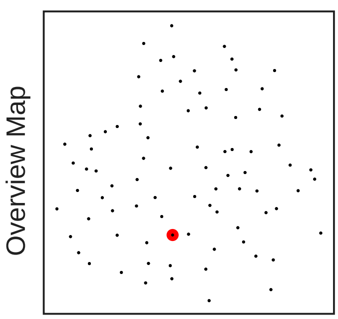

Total RMS = 2.82
Zxx RMS = 0.00
Zxy RMS = 3.72
Zyx RMS = 1.43
Zyy RMS = 0.00

Site: site_039

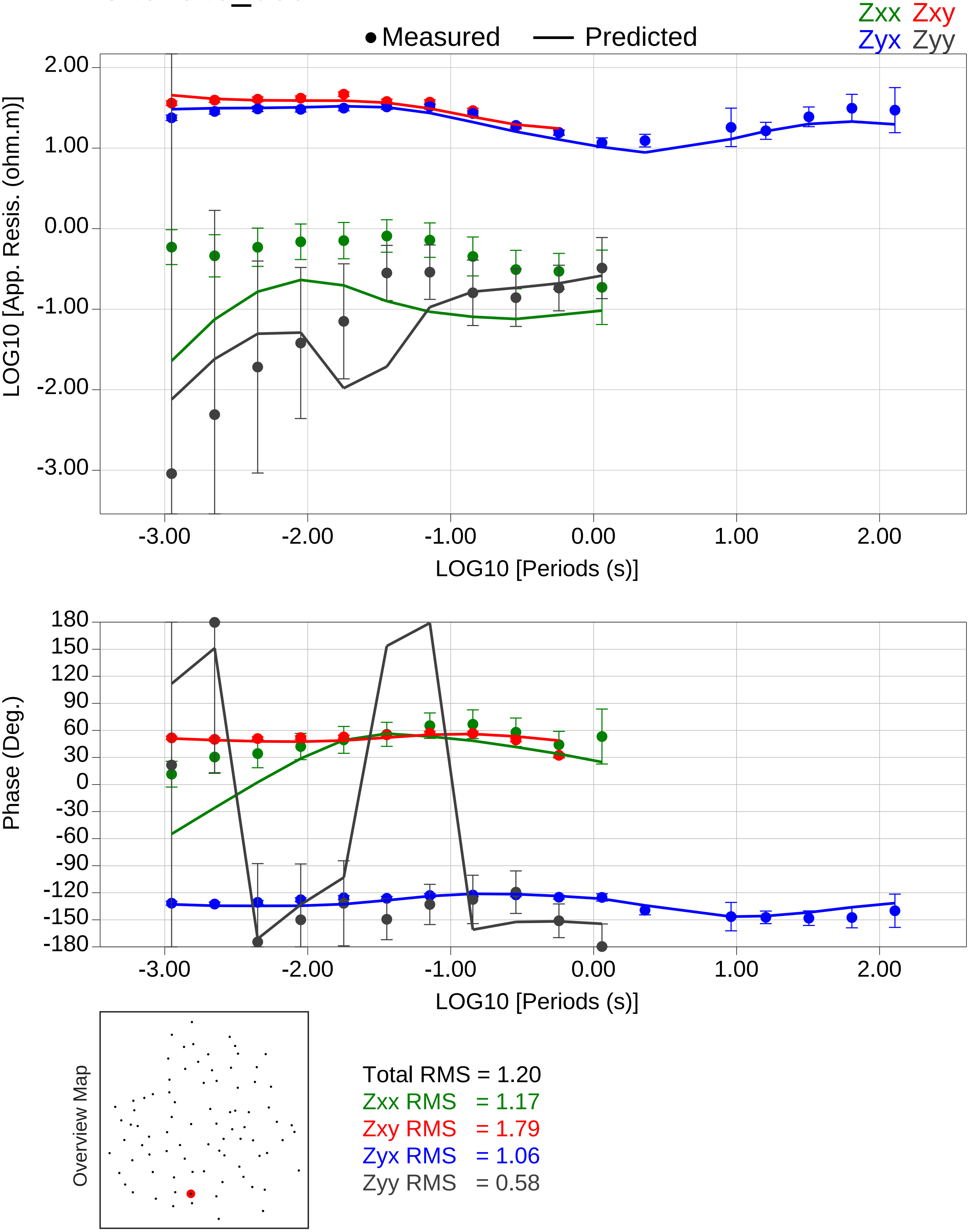

Total RMS = 1.20
Zxx RMS = 1.17
Zxy RMS = 1.79
Zyx RMS = 1.06
Zyy RMS = 0.58

Site: site_040

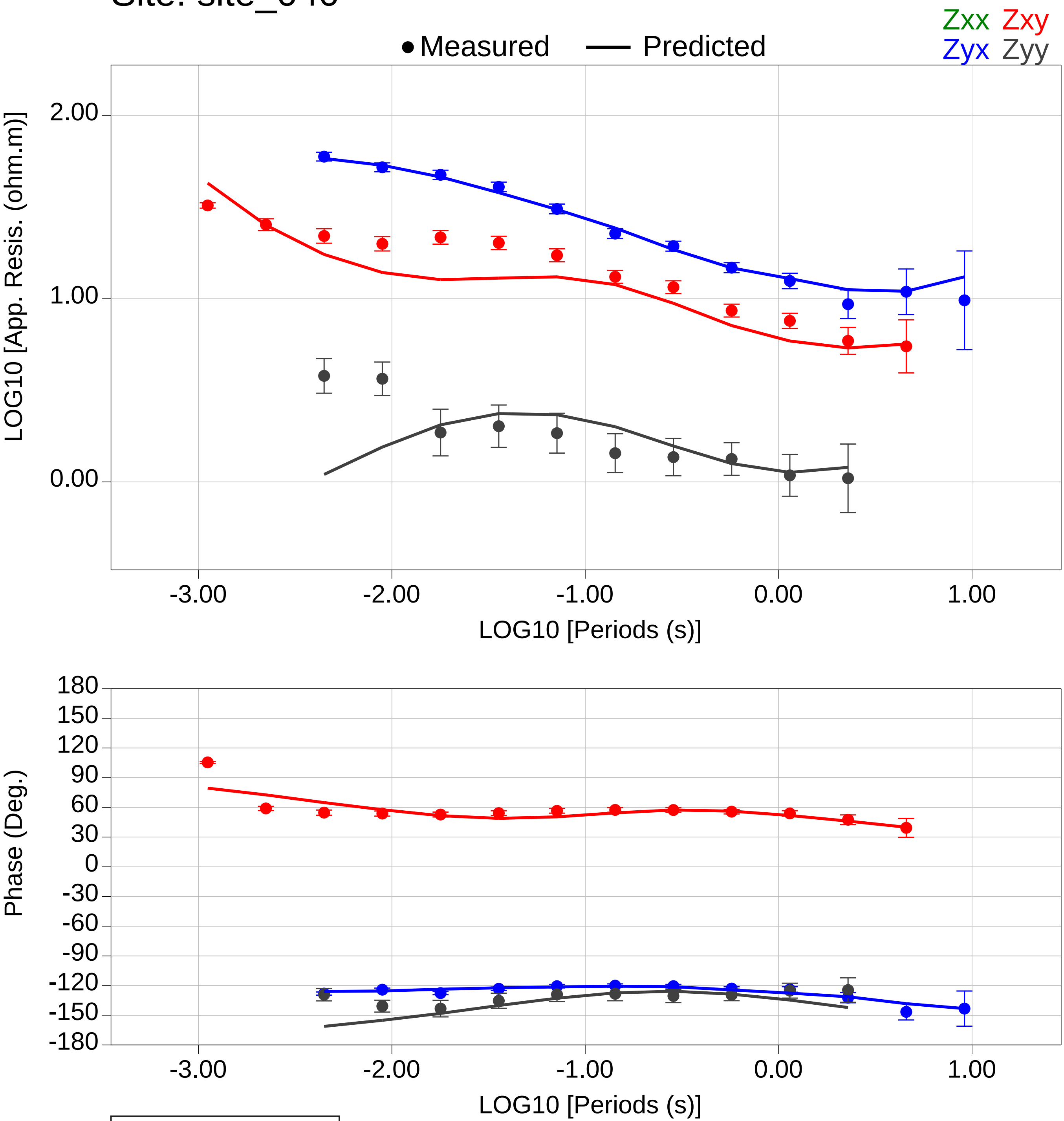

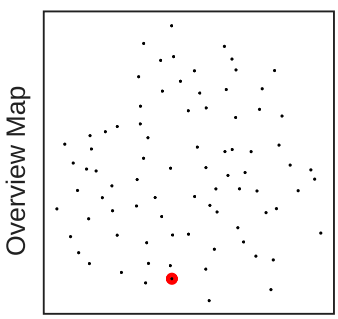

Total RMS = 2.82
Zxx RMS = 0.00
Zxy RMS = 4.48
Zyx RMS = 0.60
Zyy RMS = 1.18

Site: site_043

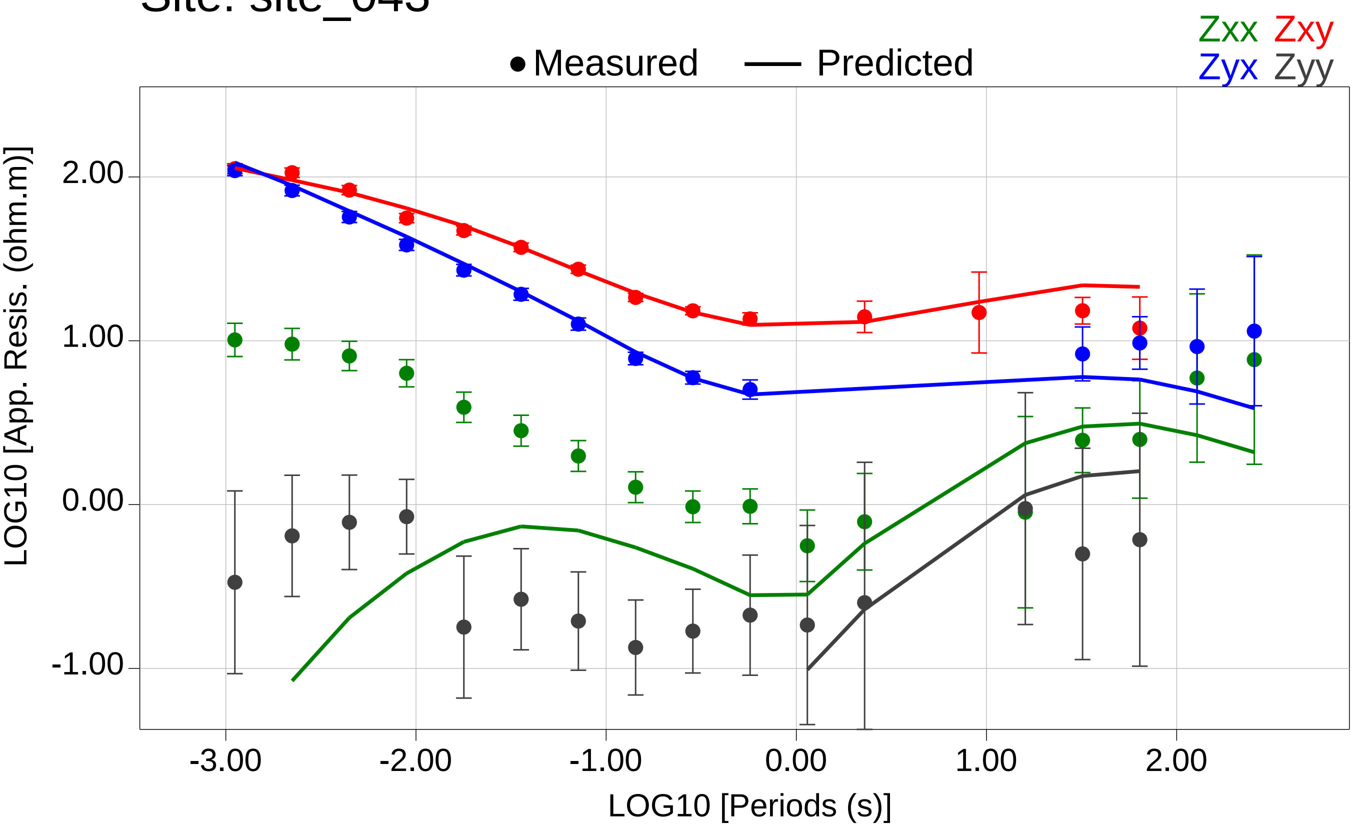

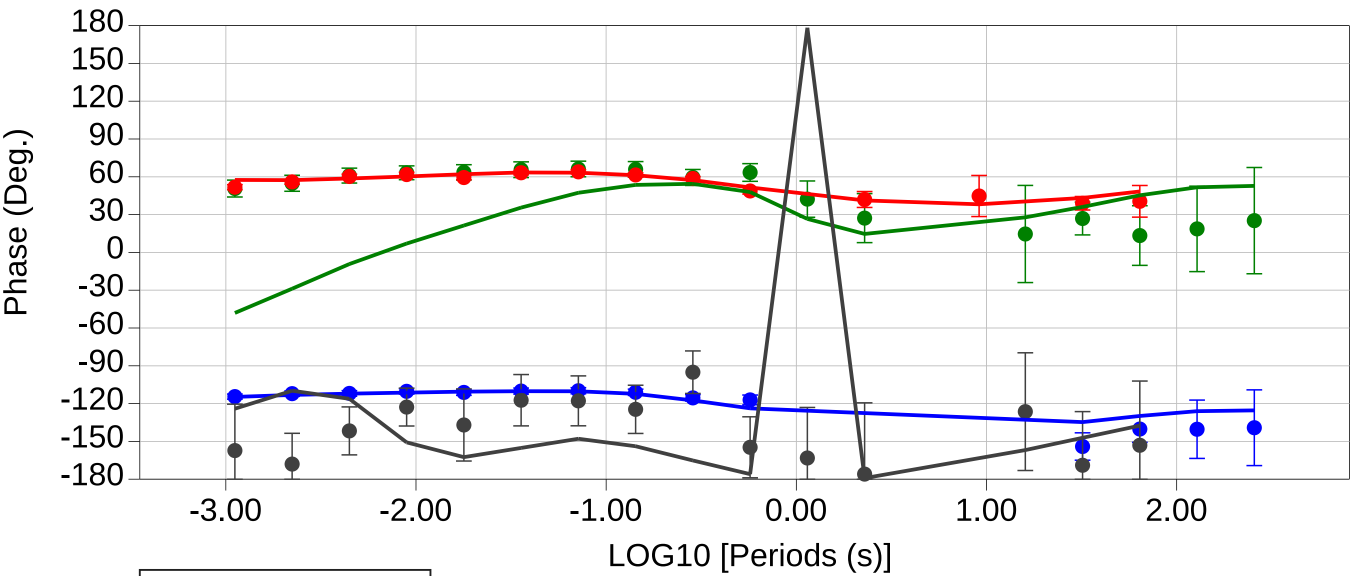

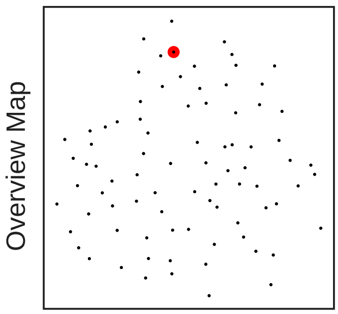

Total RMS = 1.57
Zxx RMS = 2.65
Zxy RMS = 0.78
Zyx RMS = 0.62
Zyy RMS = 1.00

Site: site_044

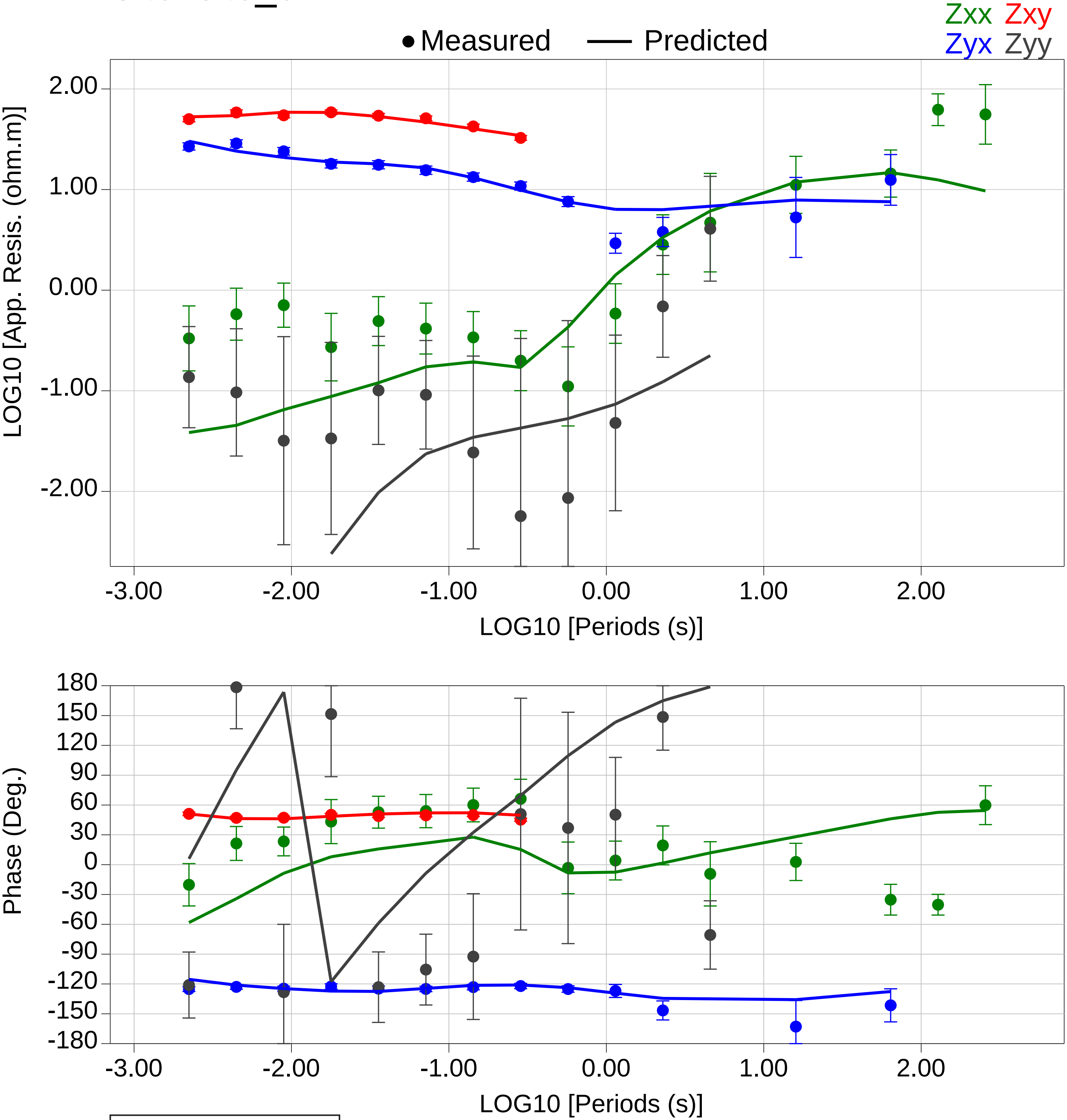

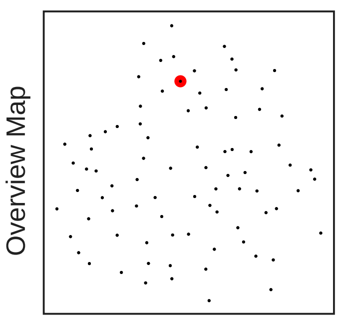

Total RMS = 1.08
Zxx RMS = 1.36
Zxy RMS = 0.89
Zyx RMS = 1.06
Zyy RMS = 0.72

Site: site_045

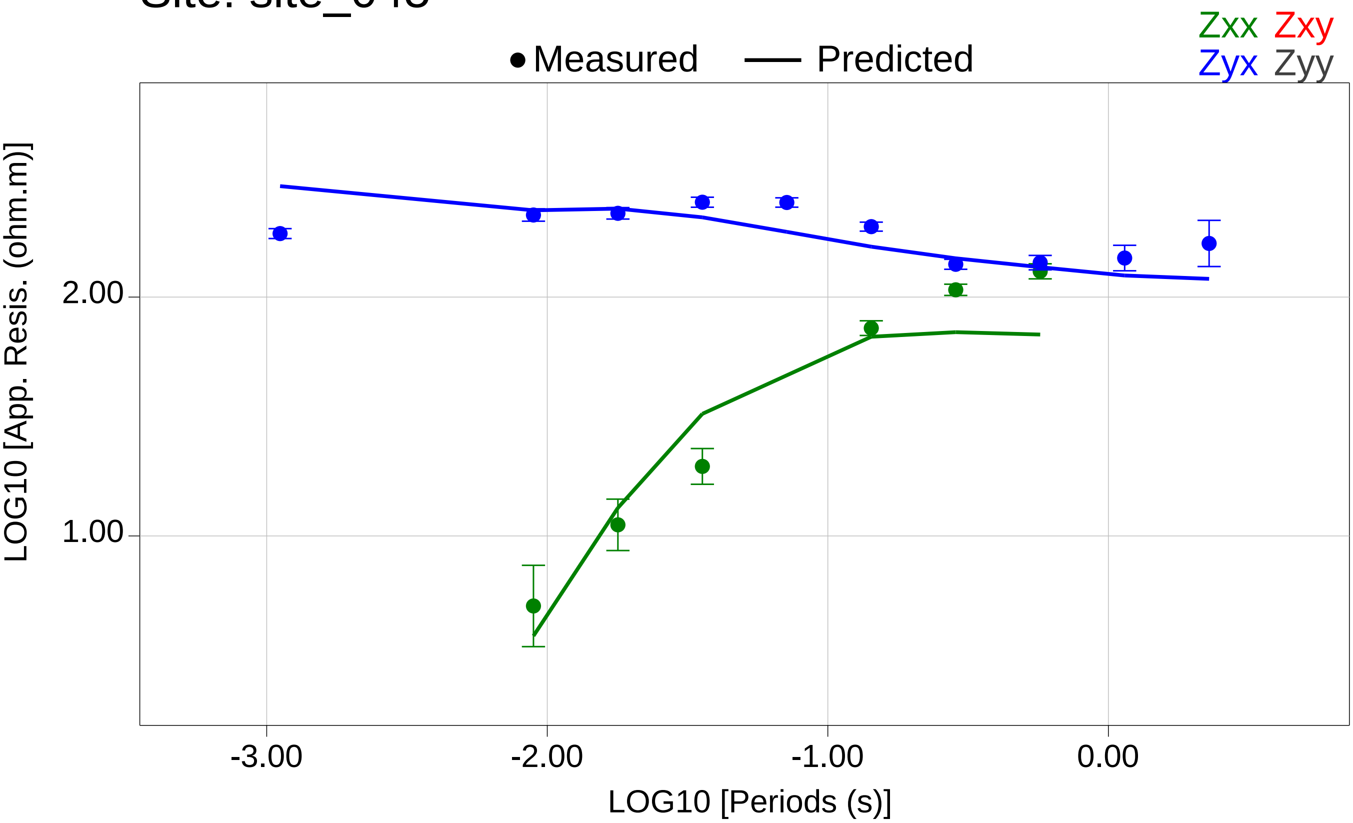

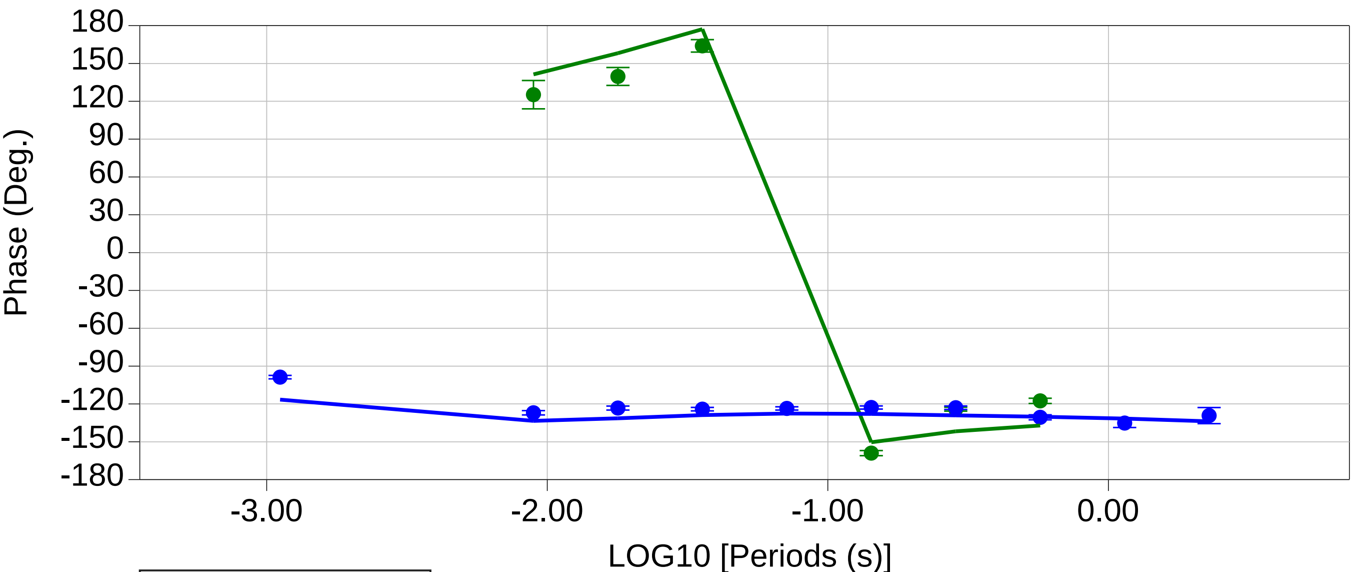

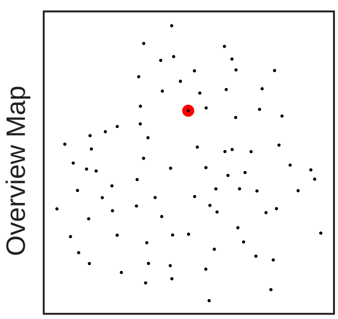

Total RMS = 3.55
Zxx RMS = 3.62
Zxy RMS = 0.00
Zyx RMS = 3.51
Zyy RMS = 0.00

Site: site_046

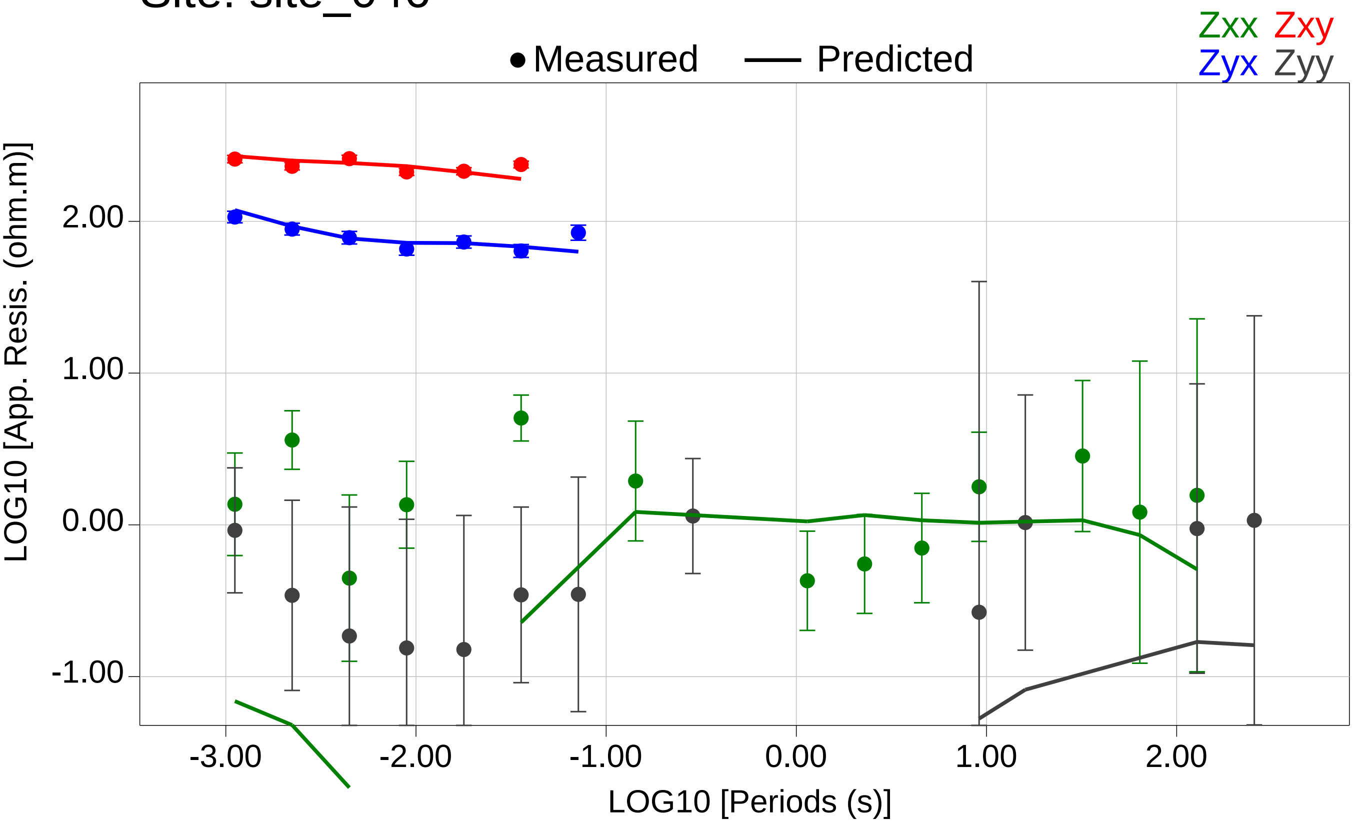

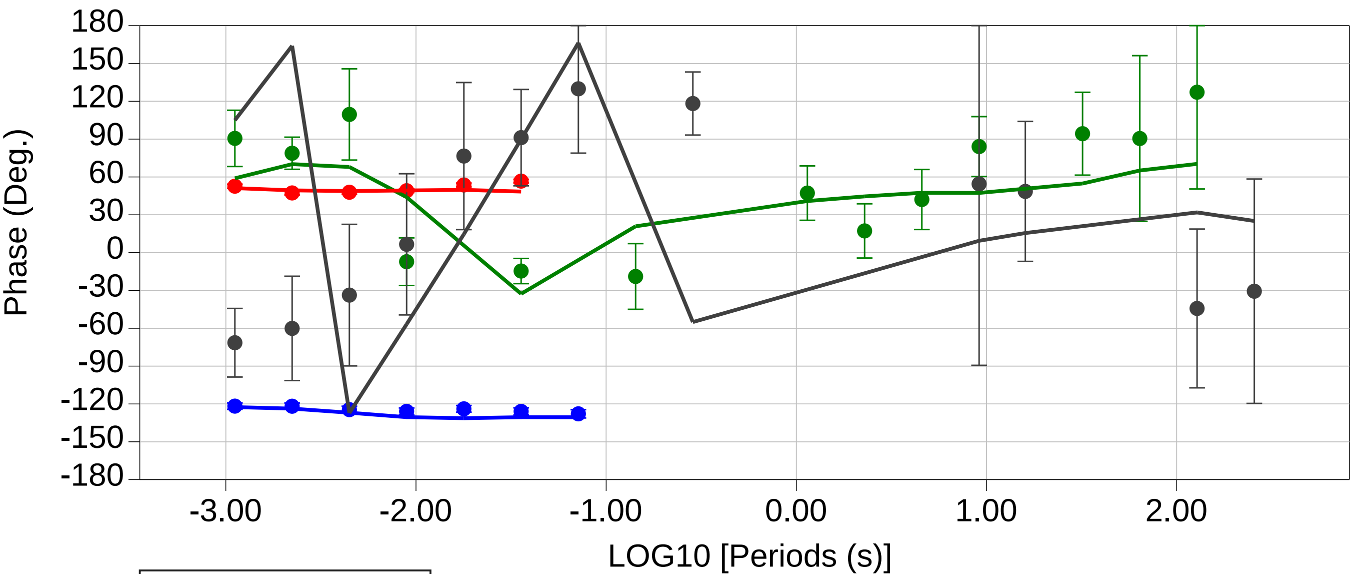

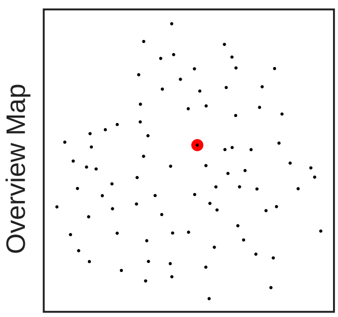

Total RMS = 1.06
Zxx RMS = 1.11
Zxy RMS = 1.61
Zyx RMS = 0.93
Zyy RMS = 0.66

Site: site_047

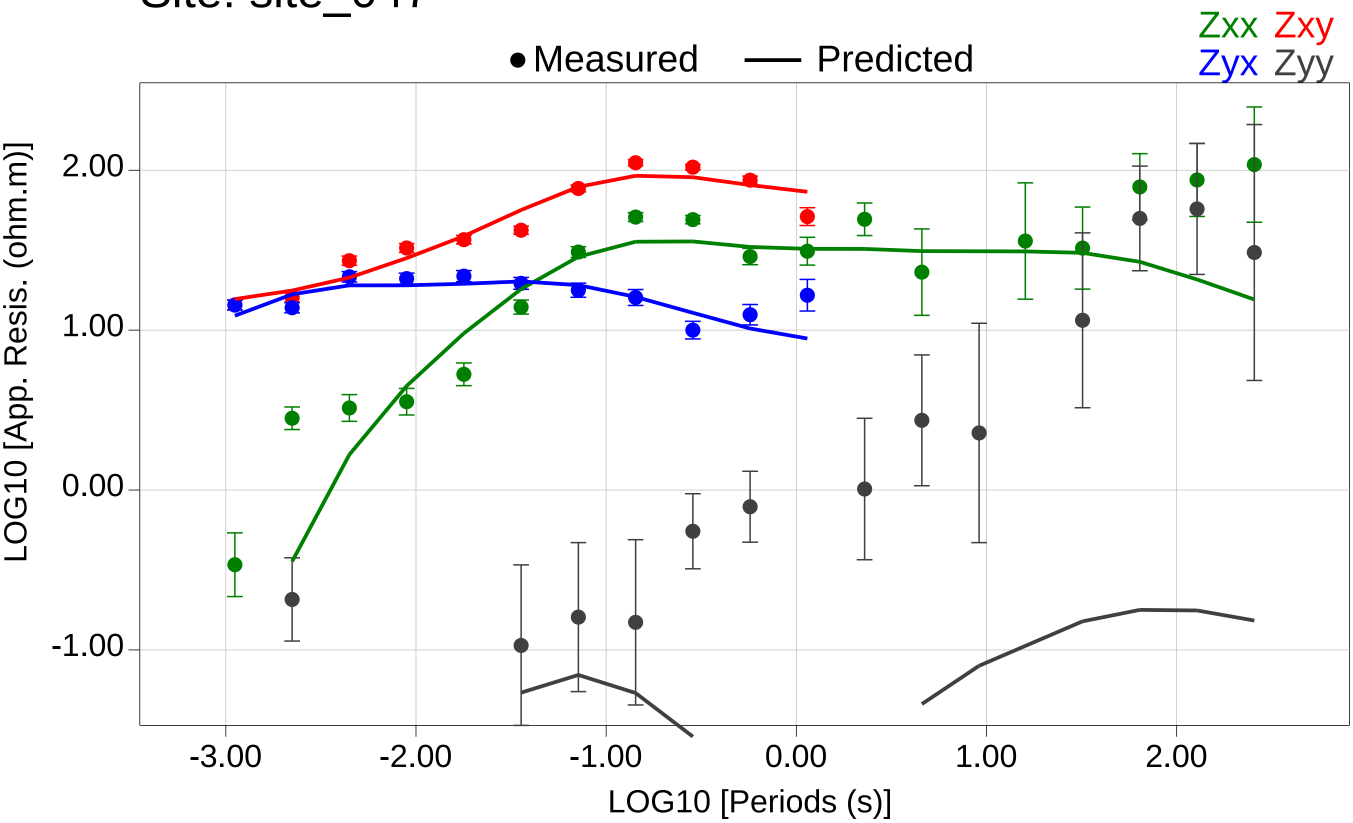

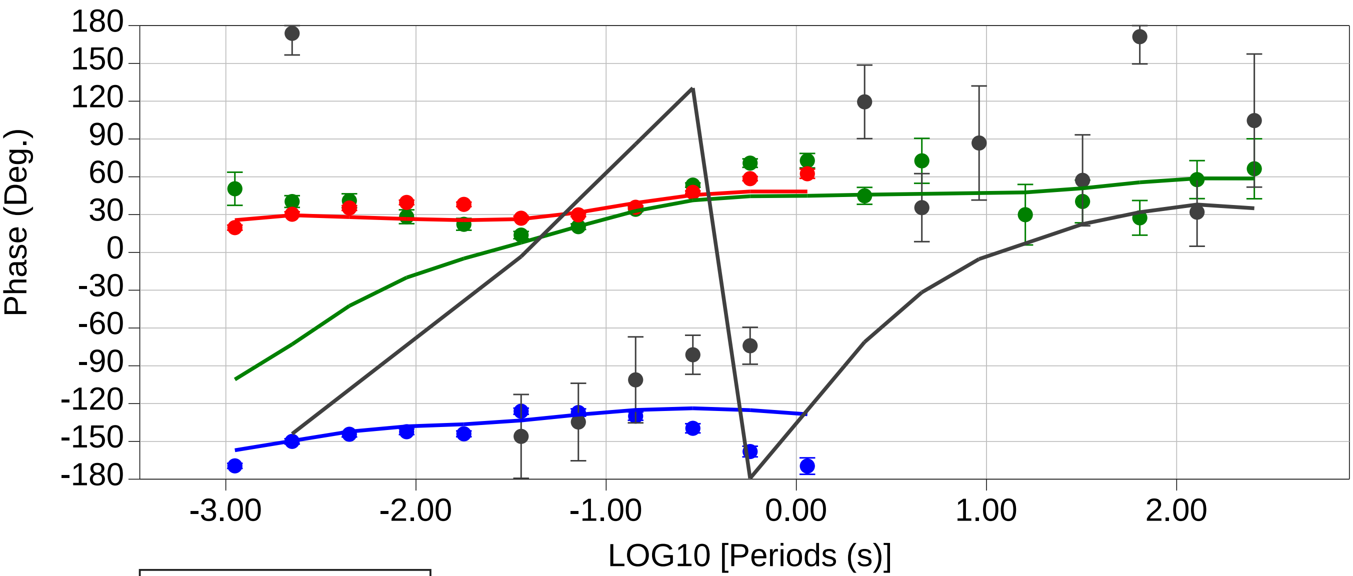

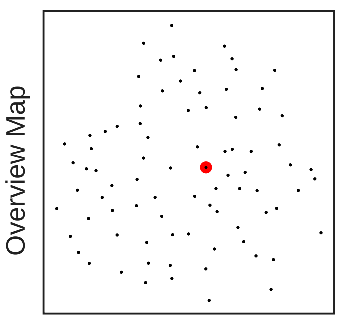

Total RMS = 2.49
Zxx RMS = 3.22
Zxy RMS = 2.51
Zyx RMS = 2.10
Zyy RMS = 1.35

Site: site_048

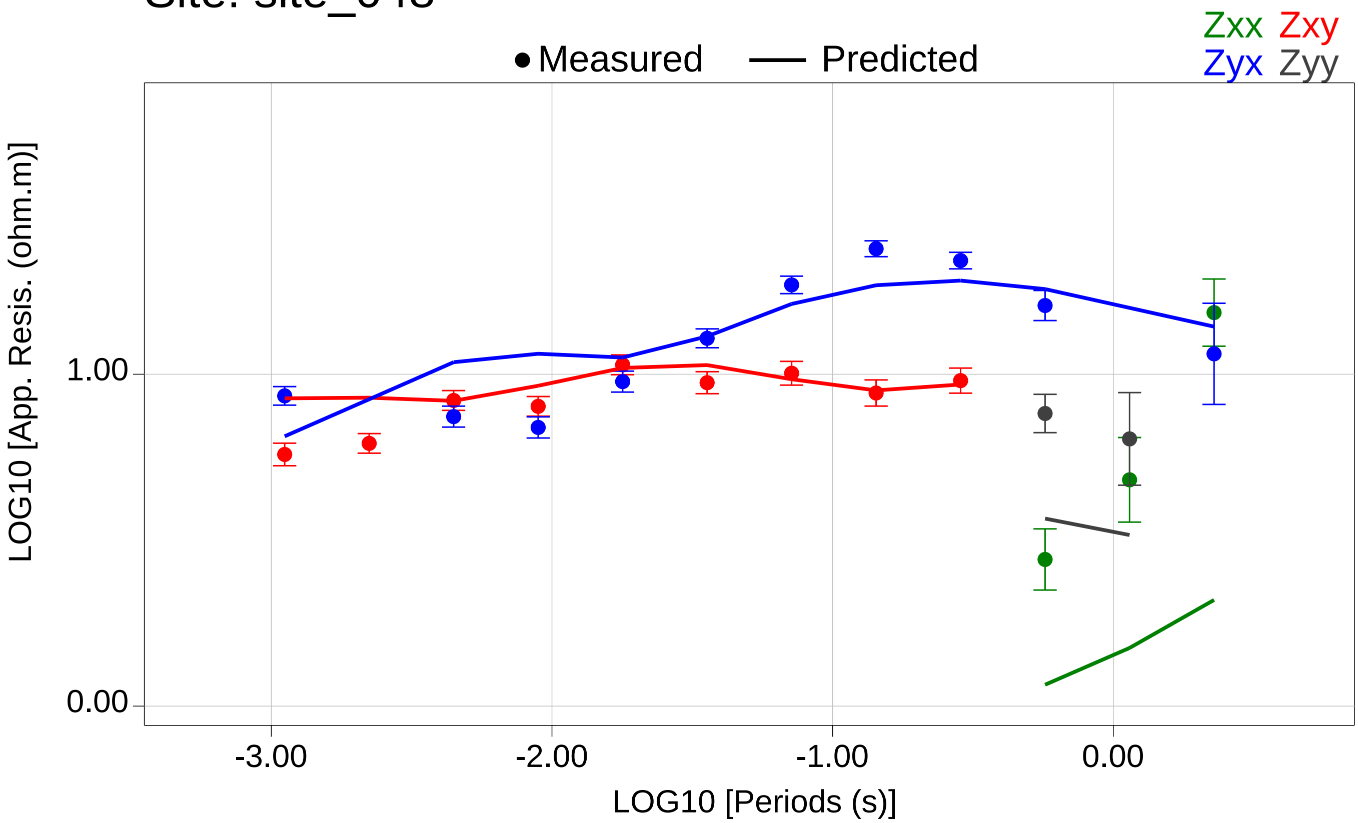

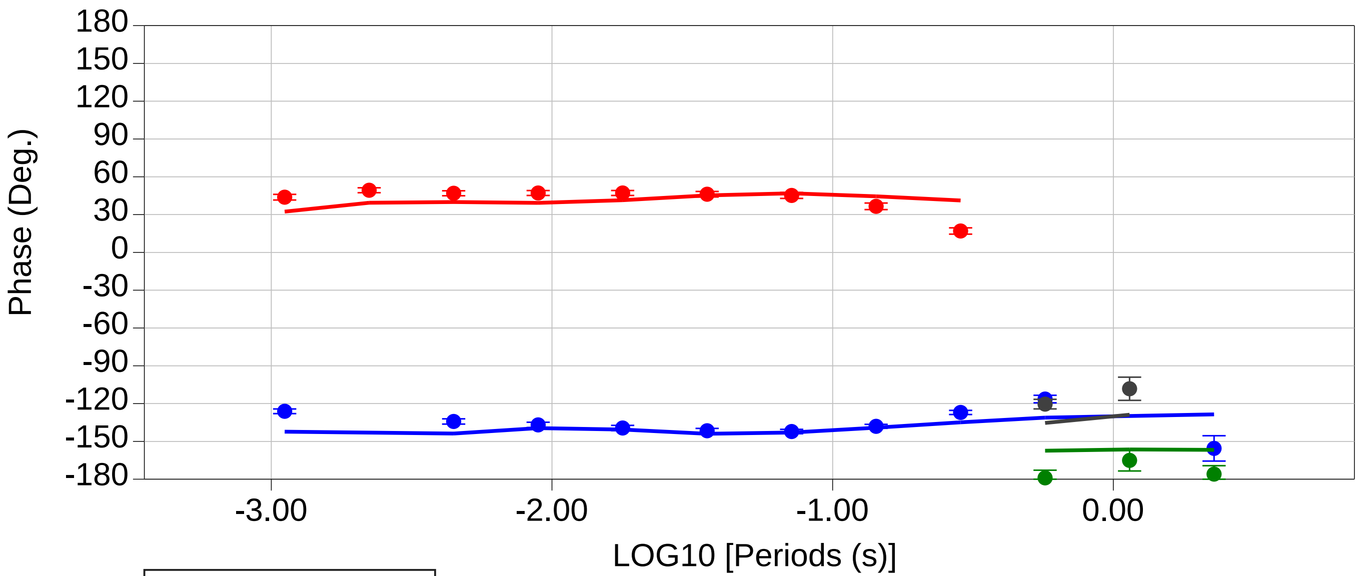

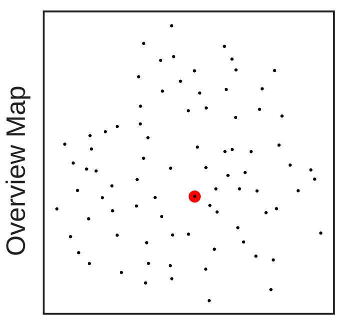

Total RMS = 2.63
Zxx RMS = 2.25
Zxy RMS = 2.71
Zyx RMS = 2.73
Zyy RMS = 2.19

Site: site_049

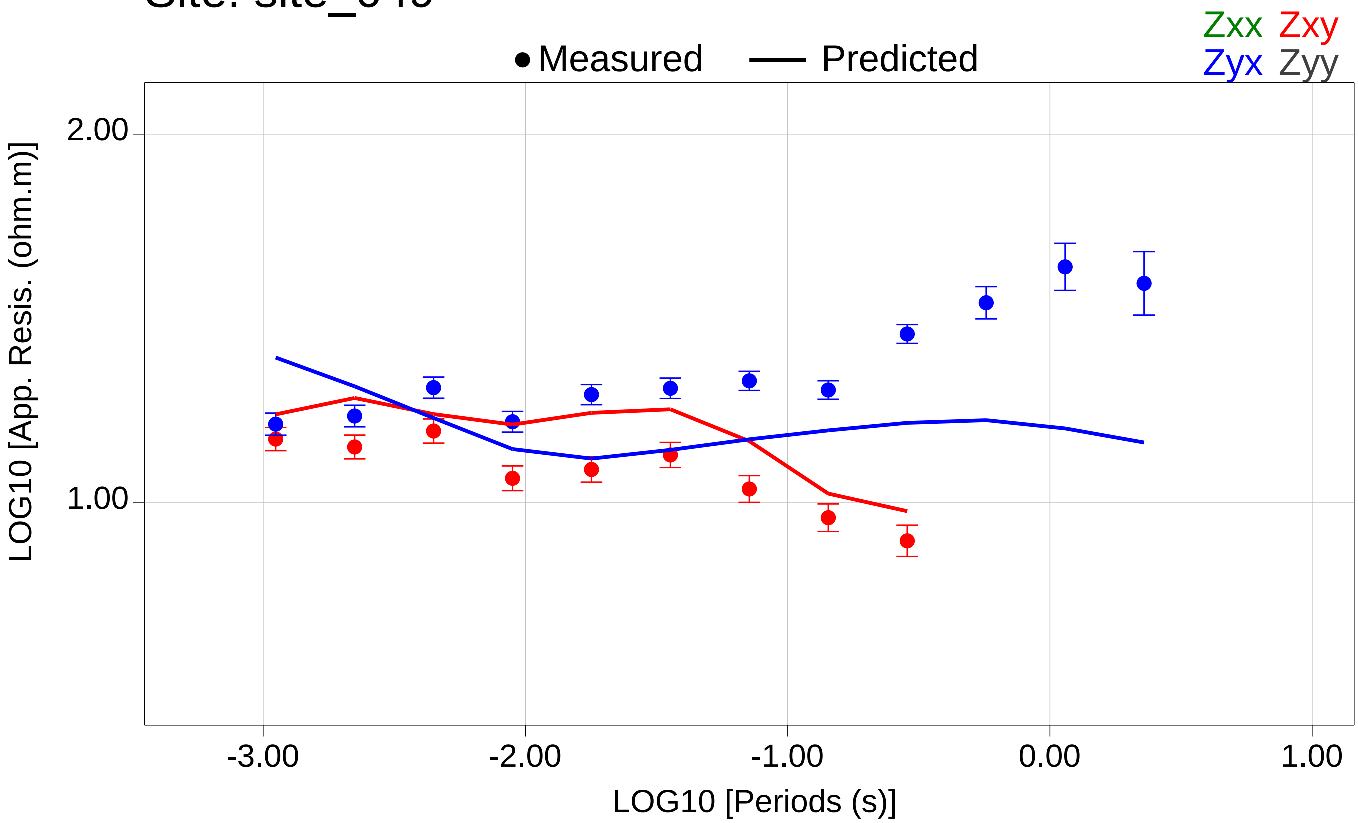

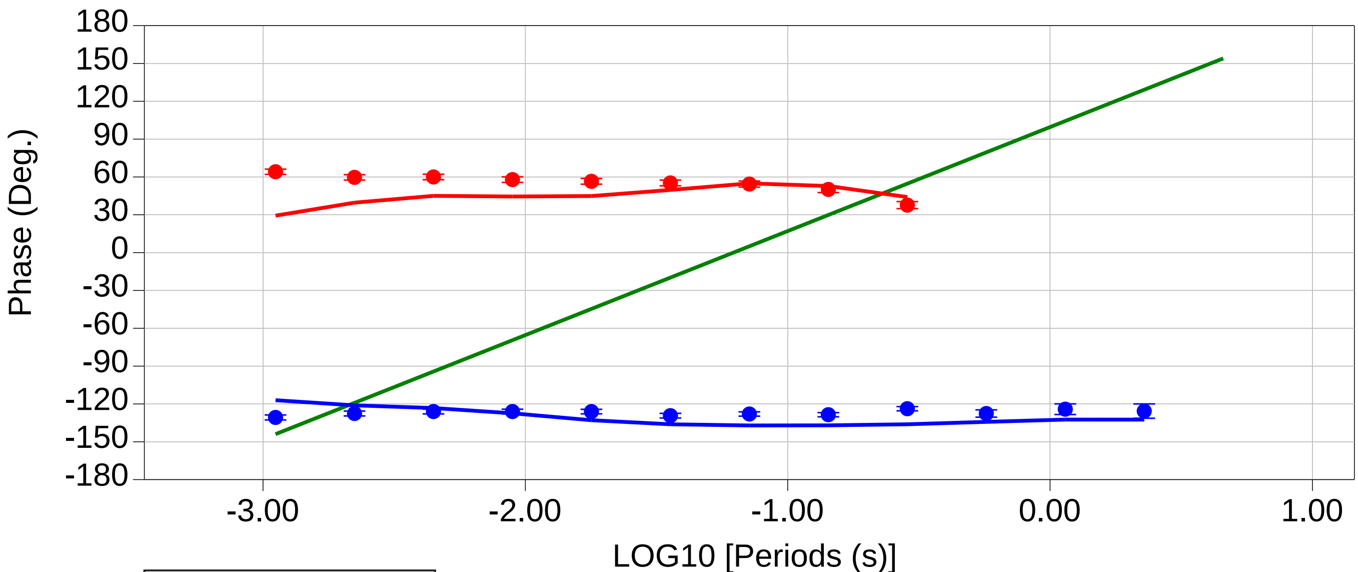

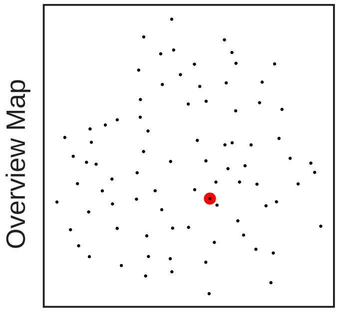

Total RMS = 3.72
Zxx RMS = 0.00
Zxy RMS = 4.24
Zyx RMS = 3.28
Zyy RMS = 0.00

Site: site_050

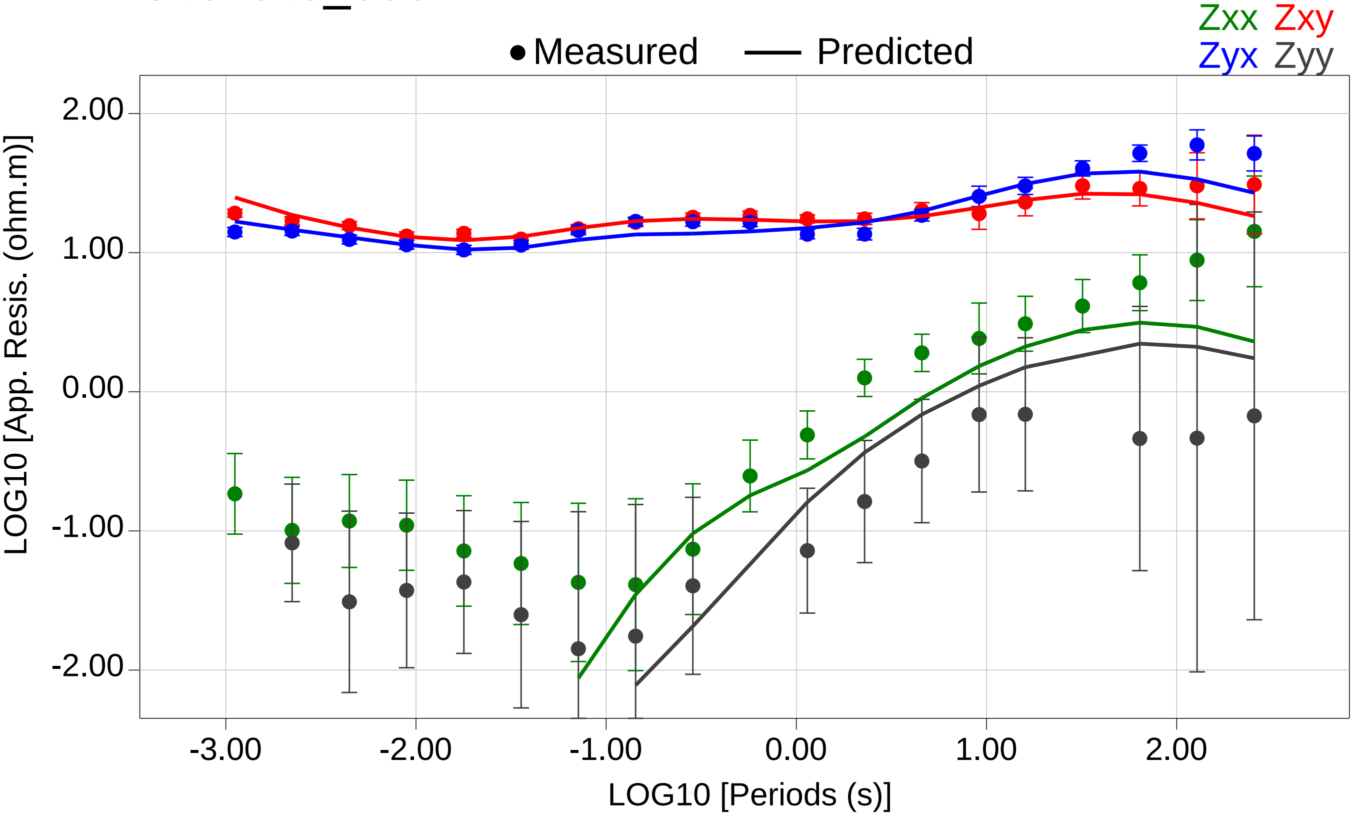

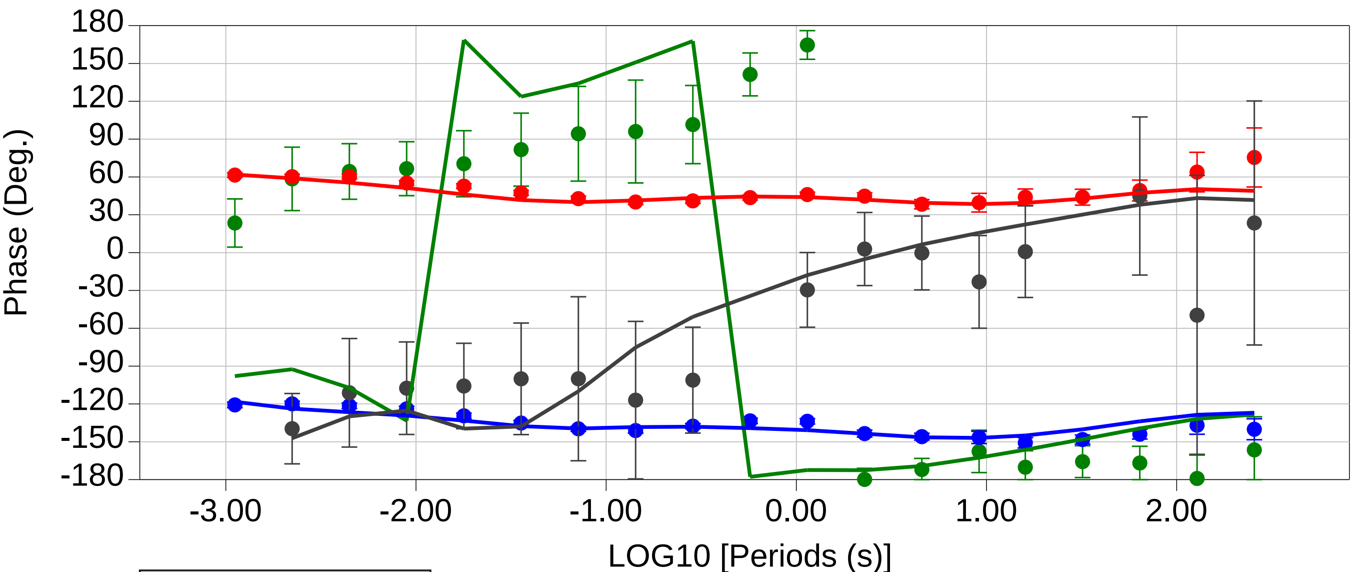

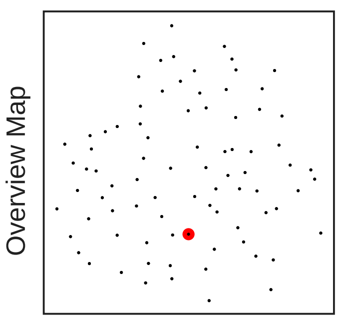

Total RMS = 0.97
Zxx RMS = 1.04
Zxy RMS = 0.94
Zyx RMS = 1.18
Zyy RMS = 0.57

Site: site_054

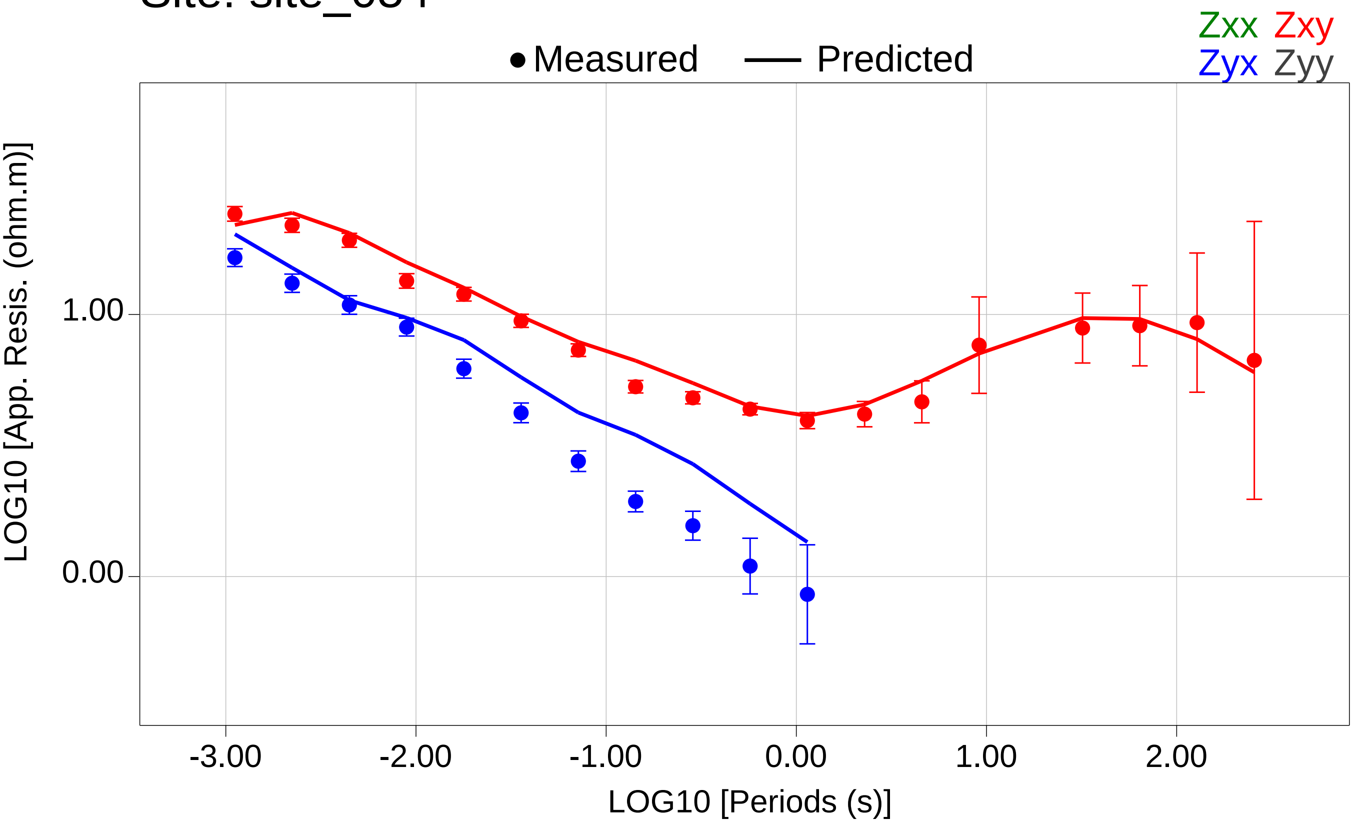

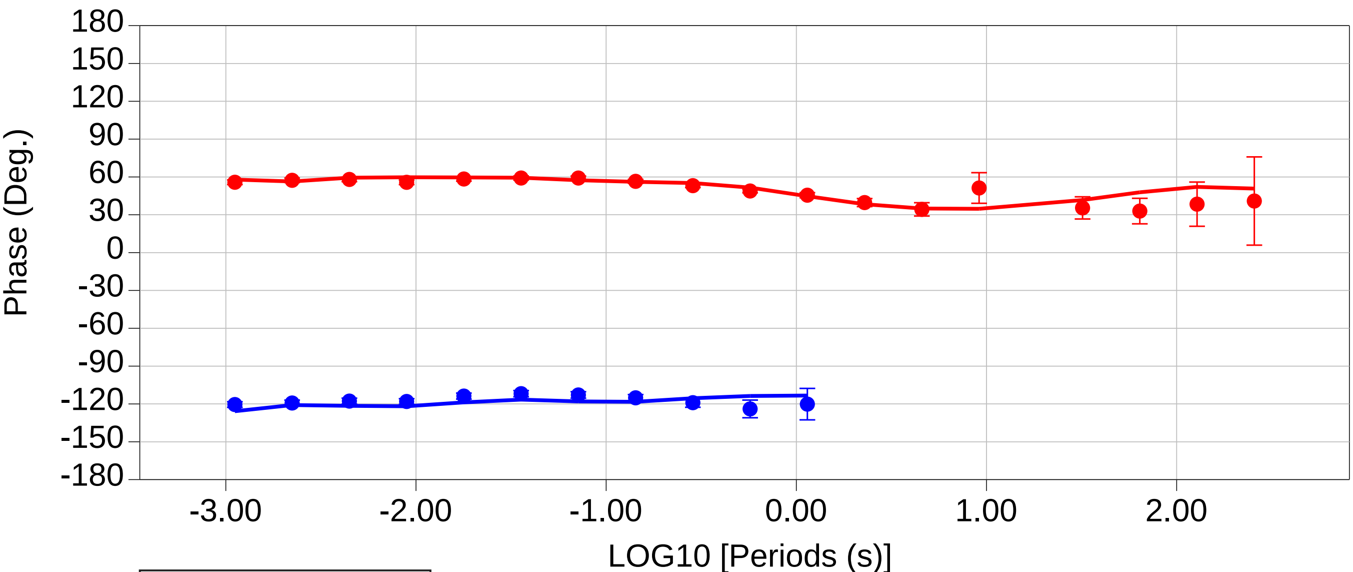

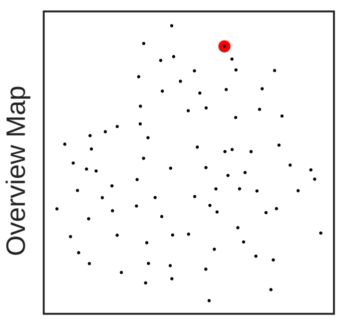

Total RMS = 1.47
Zxx RMS = 0.00
Zxy RMS = 0.95
Zyx RMS = 2.06
Zyy RMS = 0.00

Site: site_055

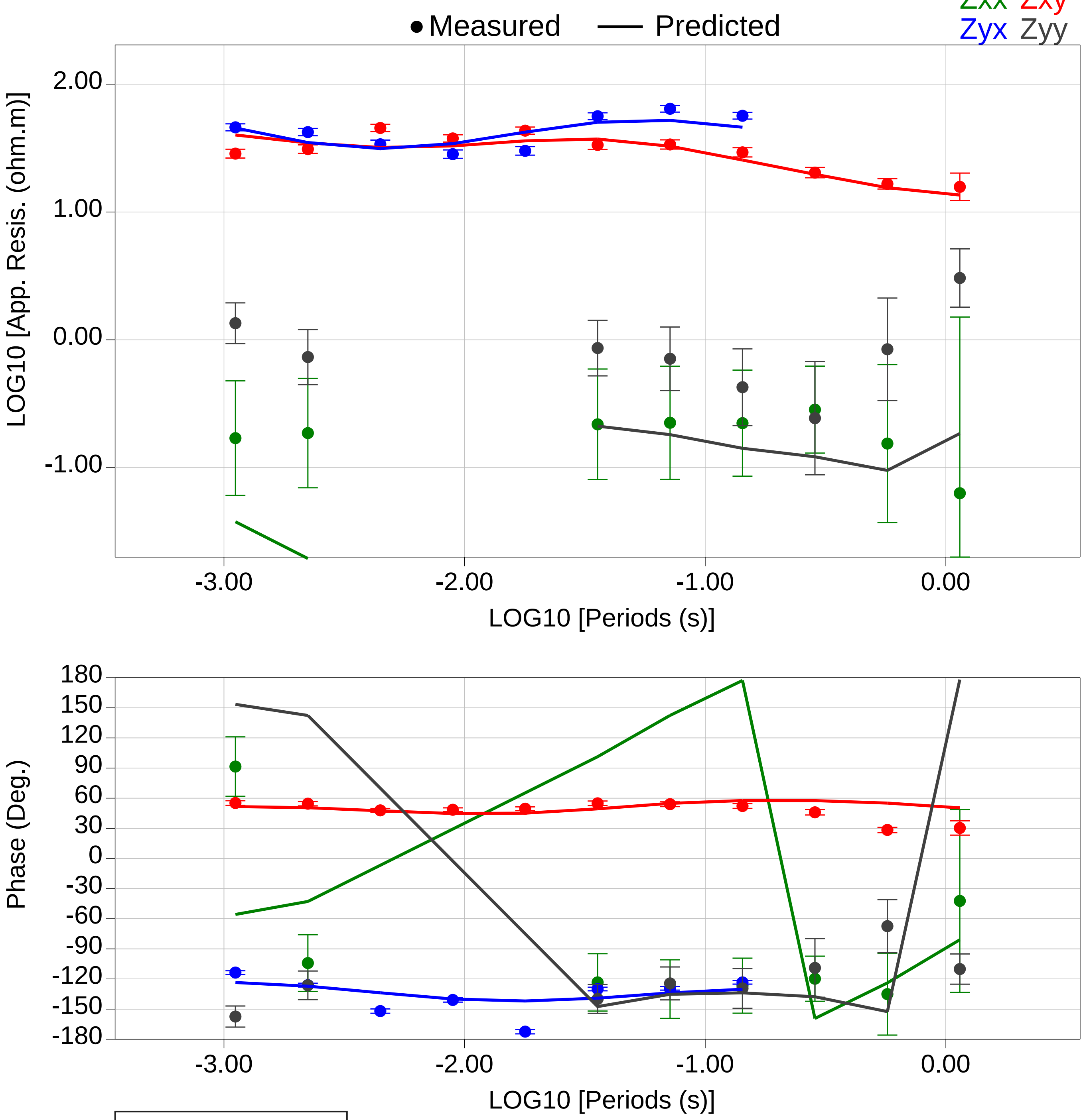

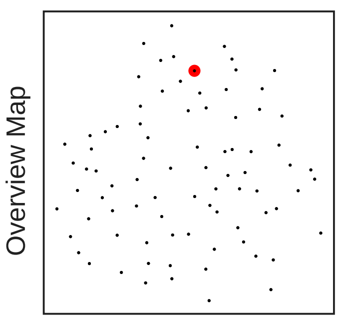

Total RMS = 2.30
Zxx RMS = 0.97
Zxy RMS = 2.20
Zyx RMS = 3.63
Zyy RMS = 1.51

Site: site_056

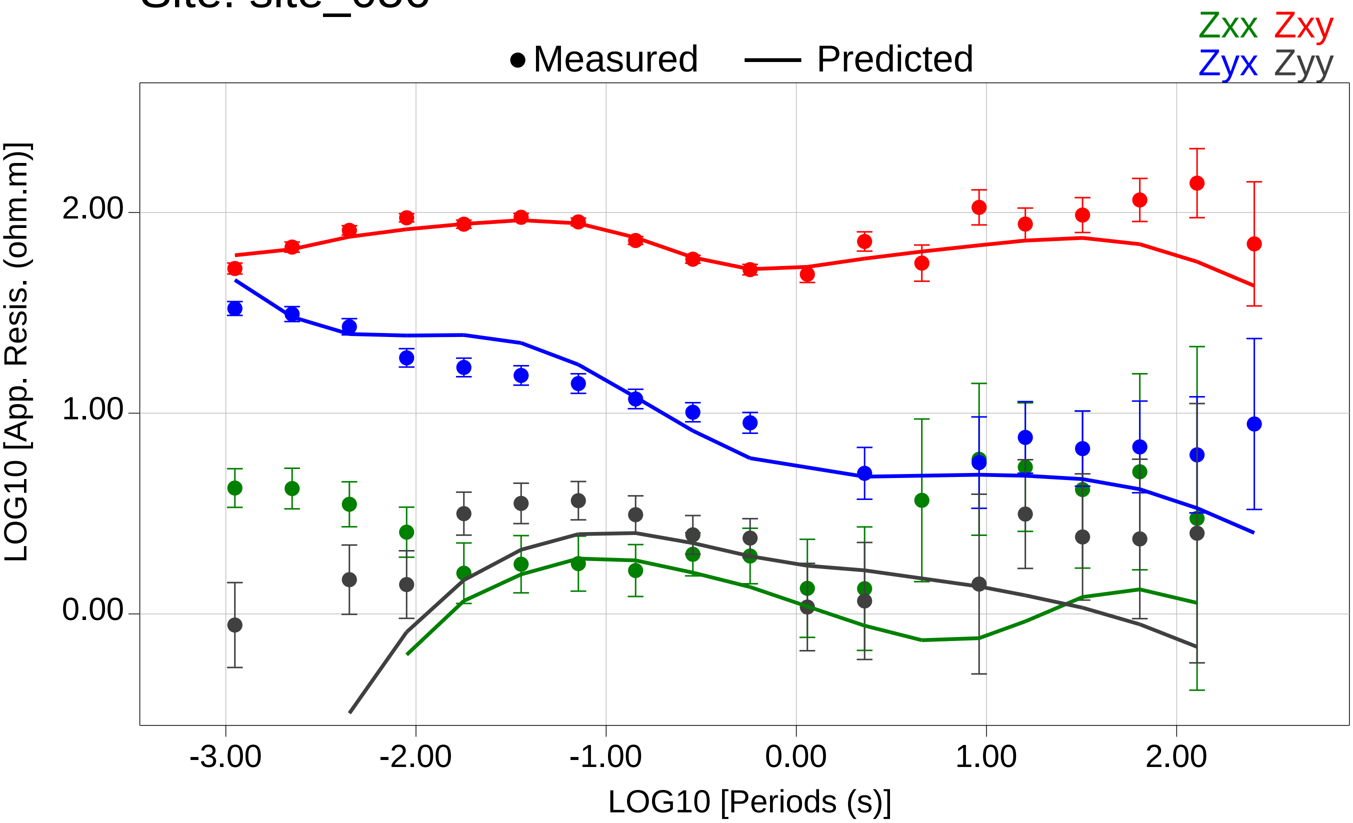

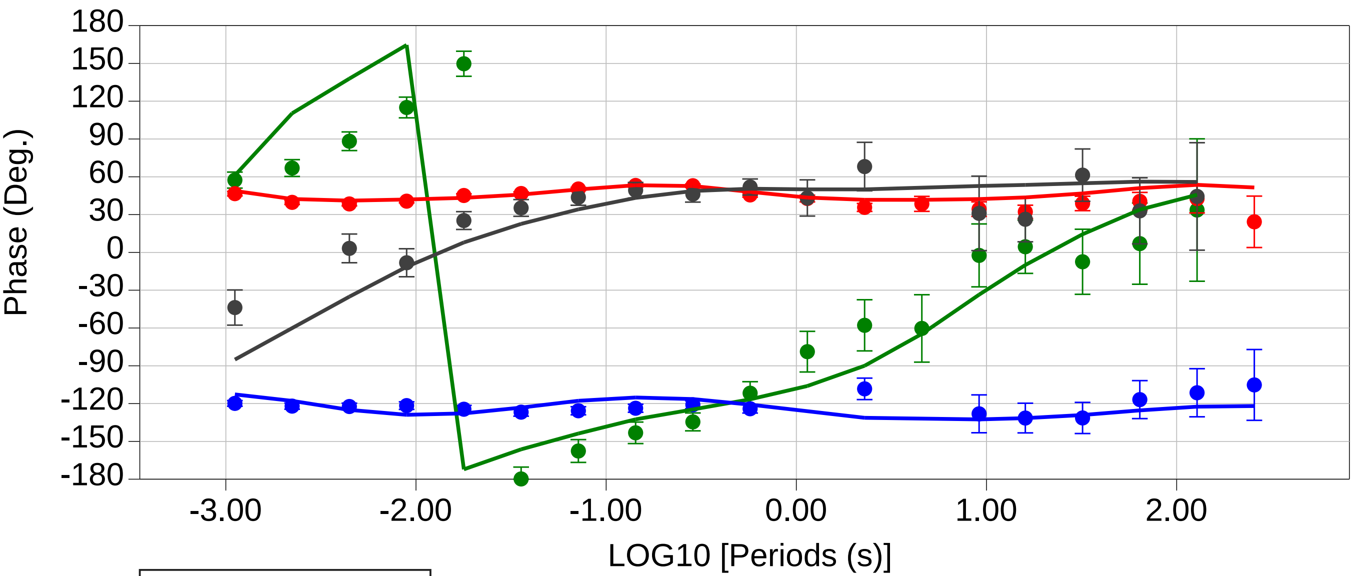

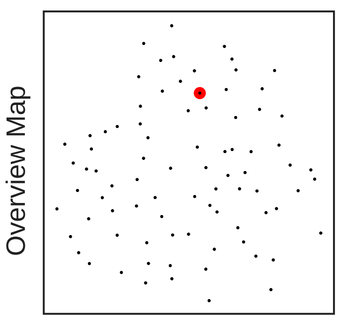

Total RMS = 1.34
Zxx RMS = 1.89
Zxy RMS = 0.90
Zyx RMS = 1.36
Zyy RMS = 0.98

Site: site_057

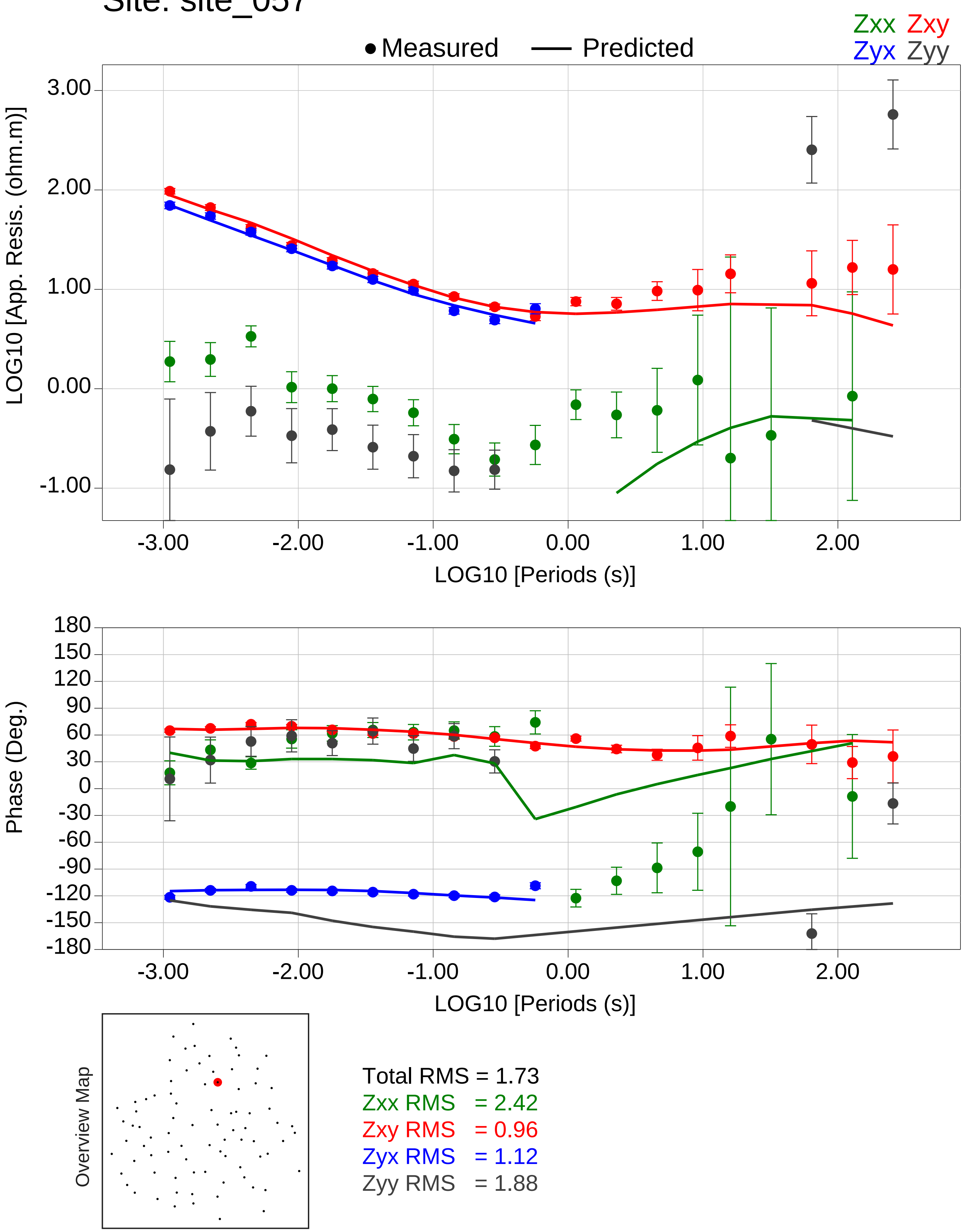

Total RMS = 1.73
Zxx RMS = 2.42
Zxy RMS = 0.96
Zyx RMS = 1.12
Zyy RMS = 1.88

Site: site_058

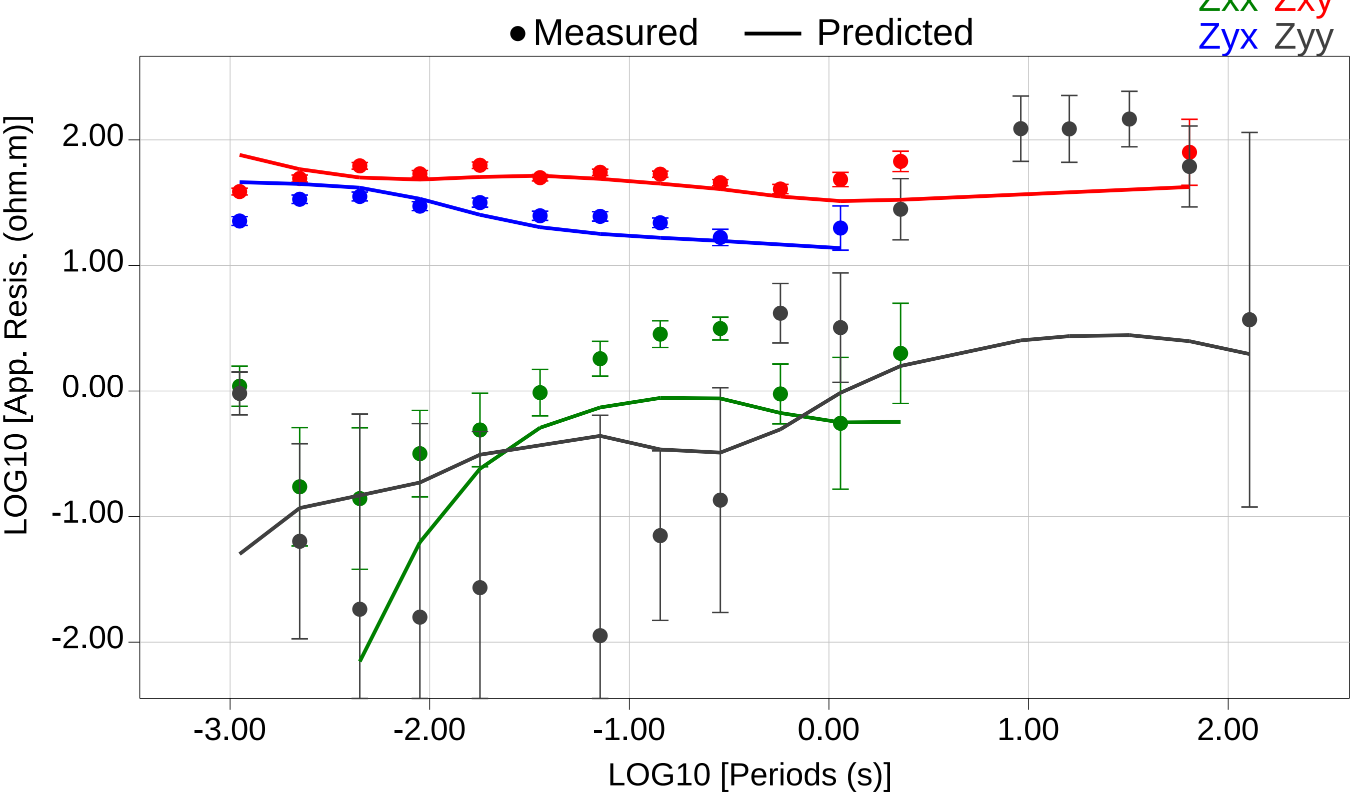

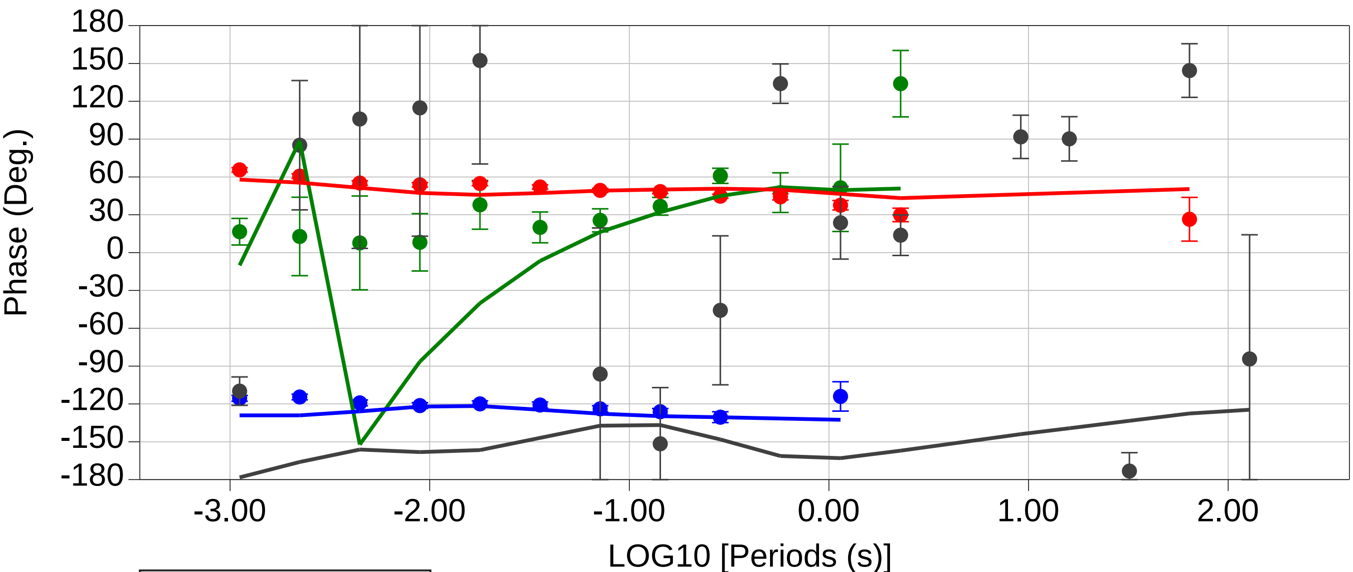

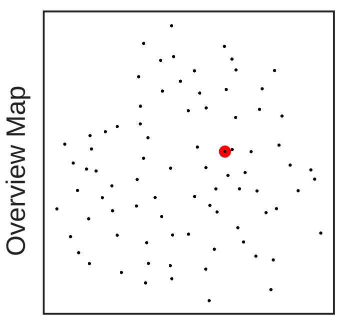

Total RMS = 2.08
Zxx RMS = 1.50
Zxy RMS = 2.60
Zyx RMS = 2.65
Zyy RMS = 1.47

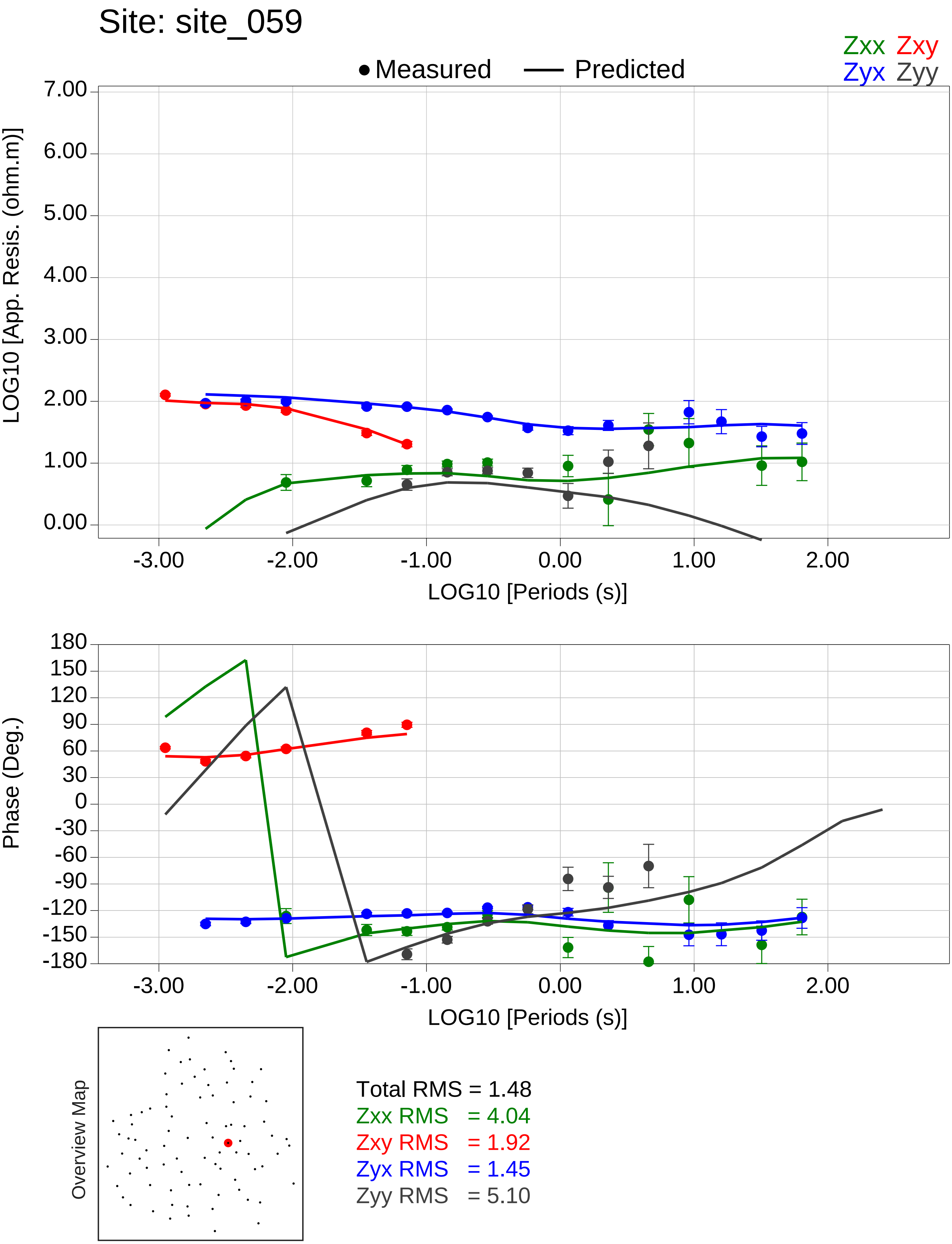

Total RMS = 1.48
Zxx RMS = 4.04
Zxy RMS = 1.92
Zyx RMS = 1.45
Zyy RMS = 5.10

Site: site_060

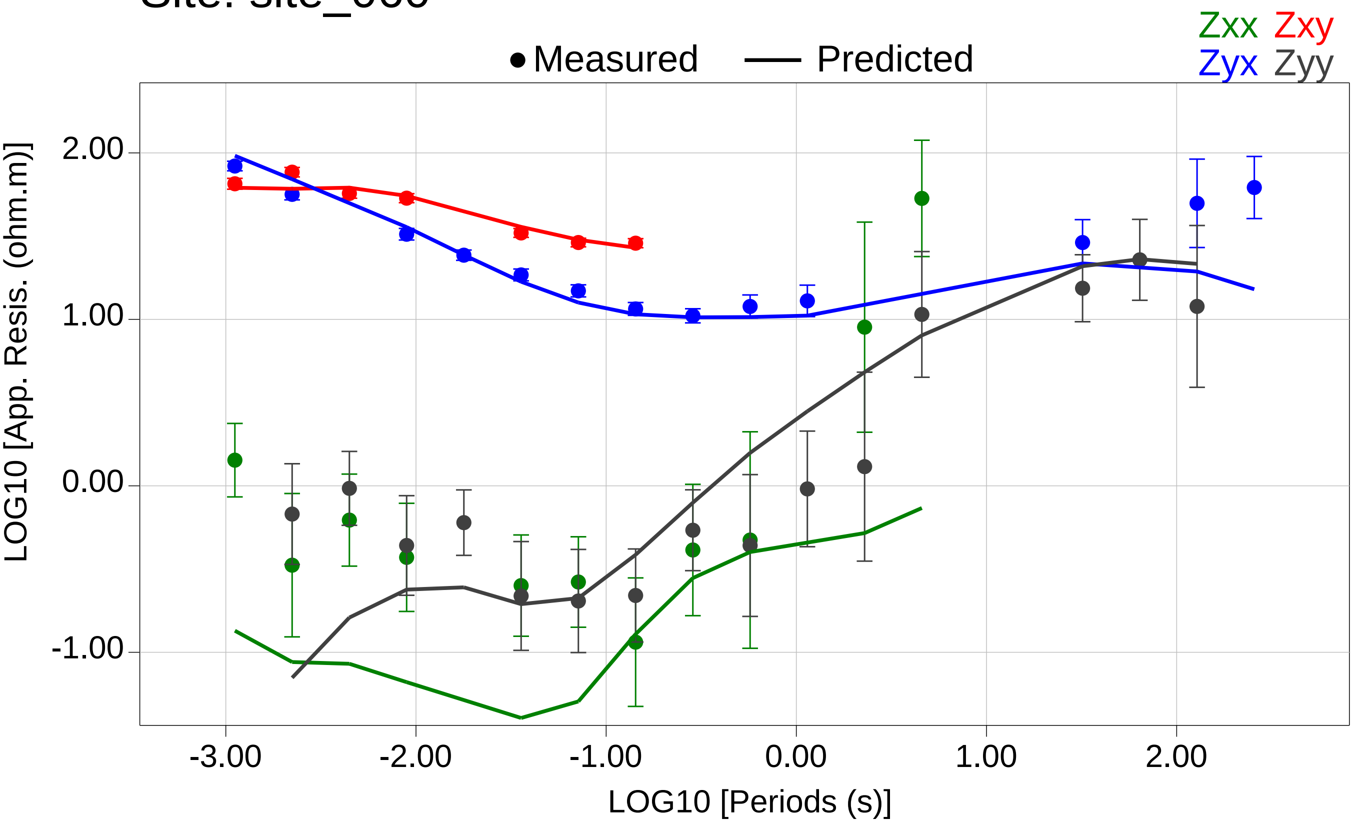

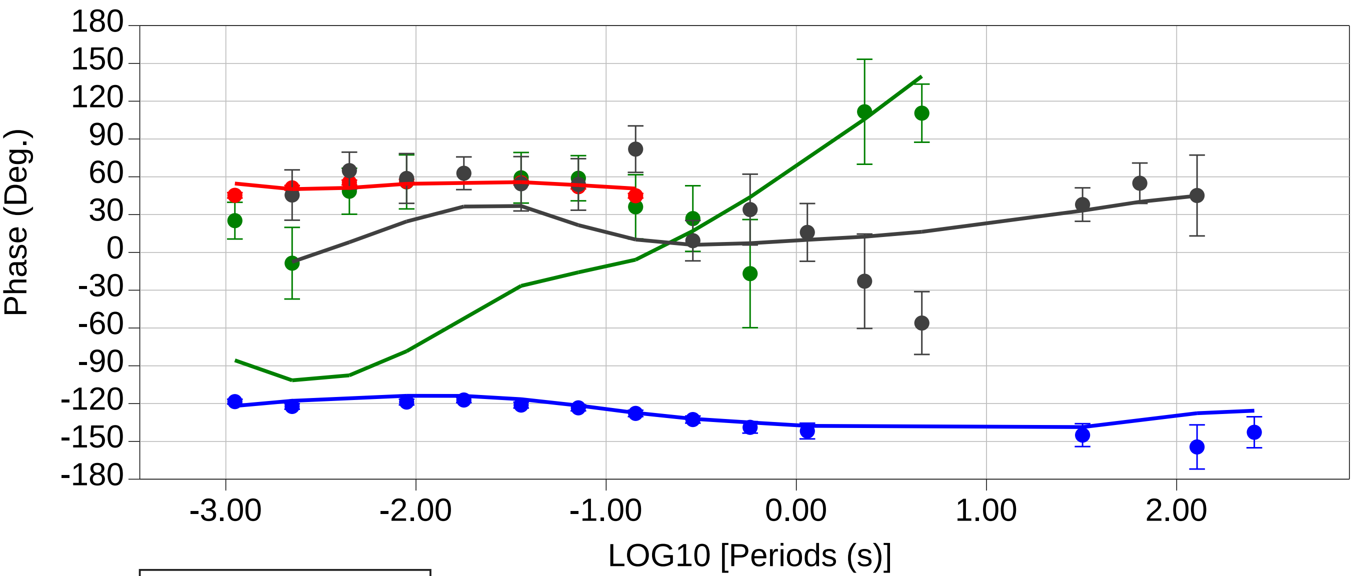

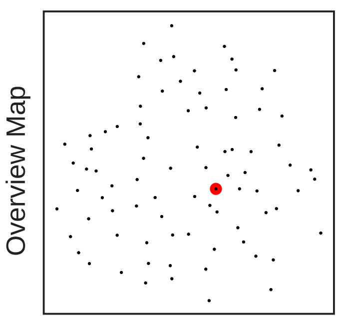

Total RMS = 1.18
Zxx RMS = 1.39
Zxy RMS = 1.36
Zyx RMS = 1.01
Zyy RMS = 1.06

Site: site_061

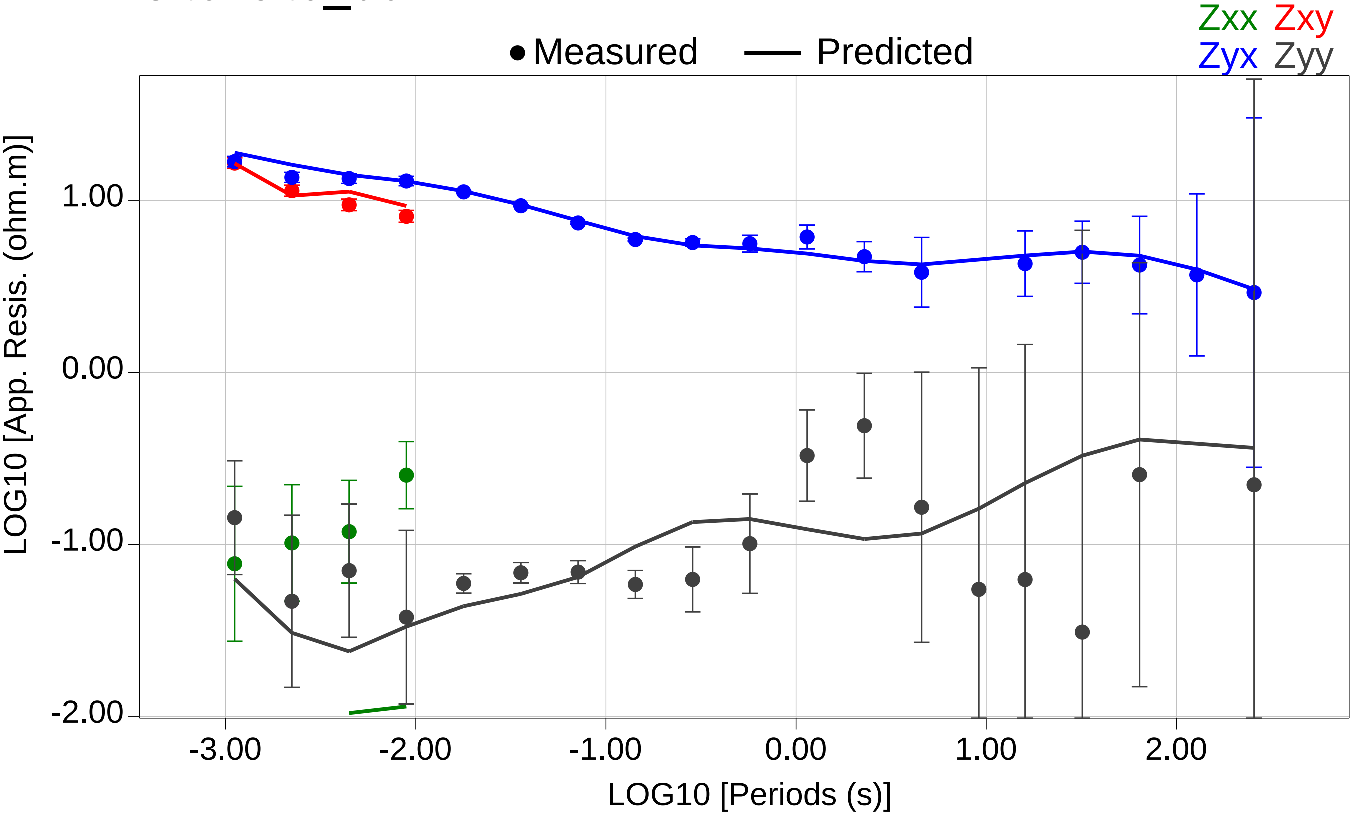

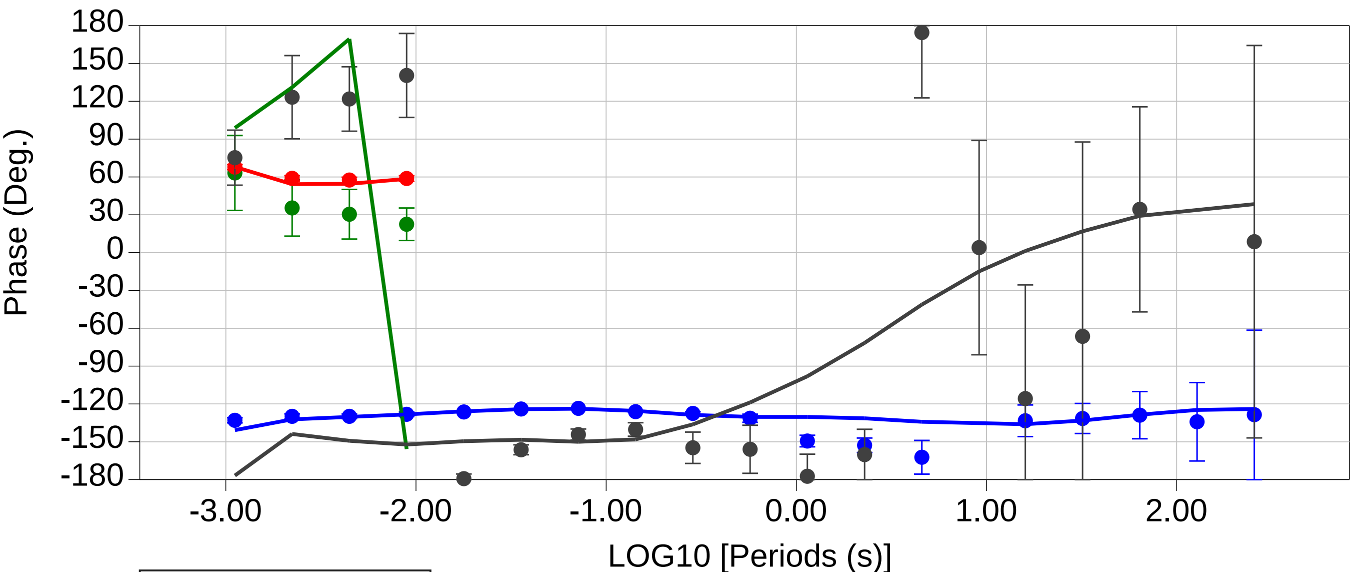

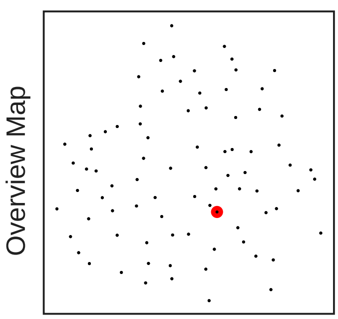

Total RMS = 1.31
Zxx RMS = 1.80
Zxy RMS = 1.01
Zyx RMS = 1.08
Zyy RMS = 1.45

Site: site_063

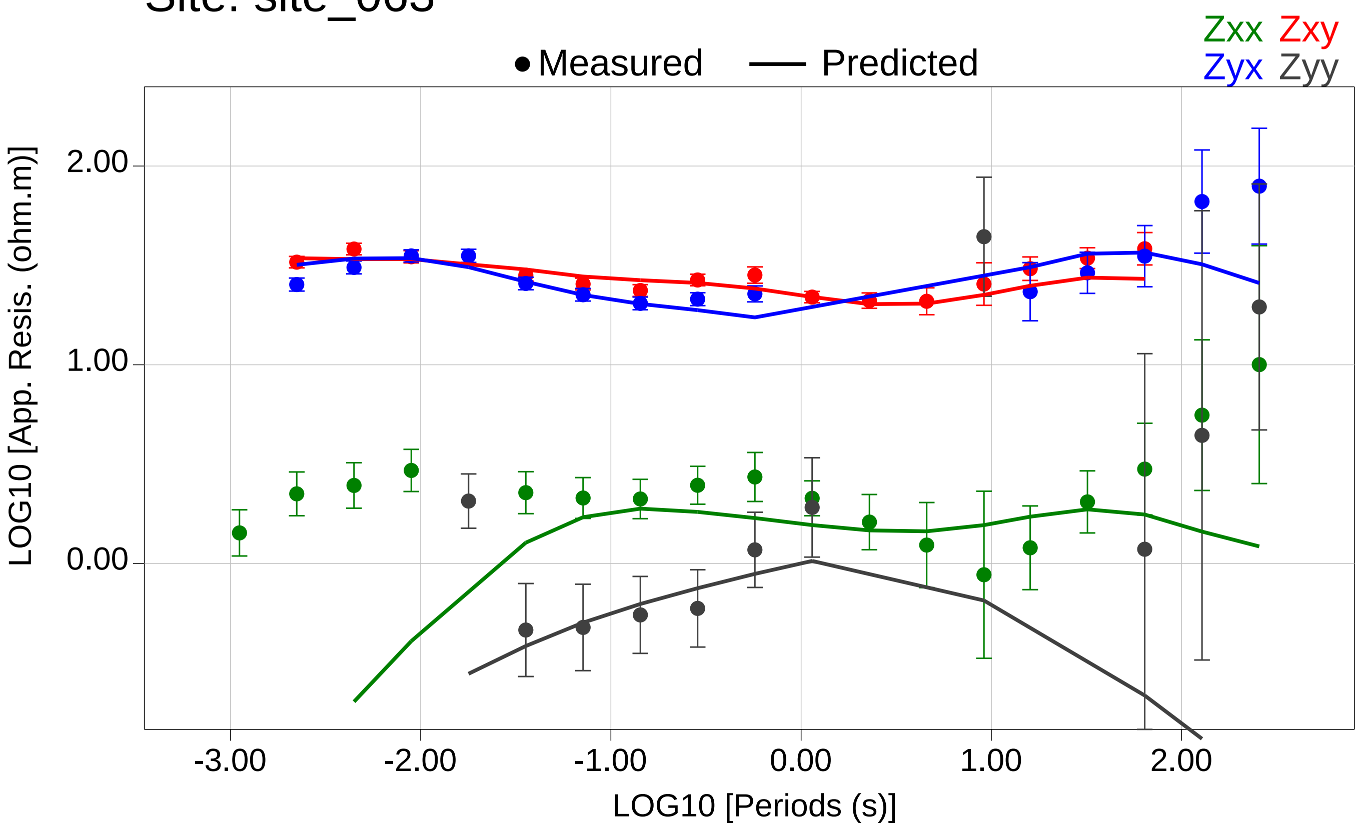

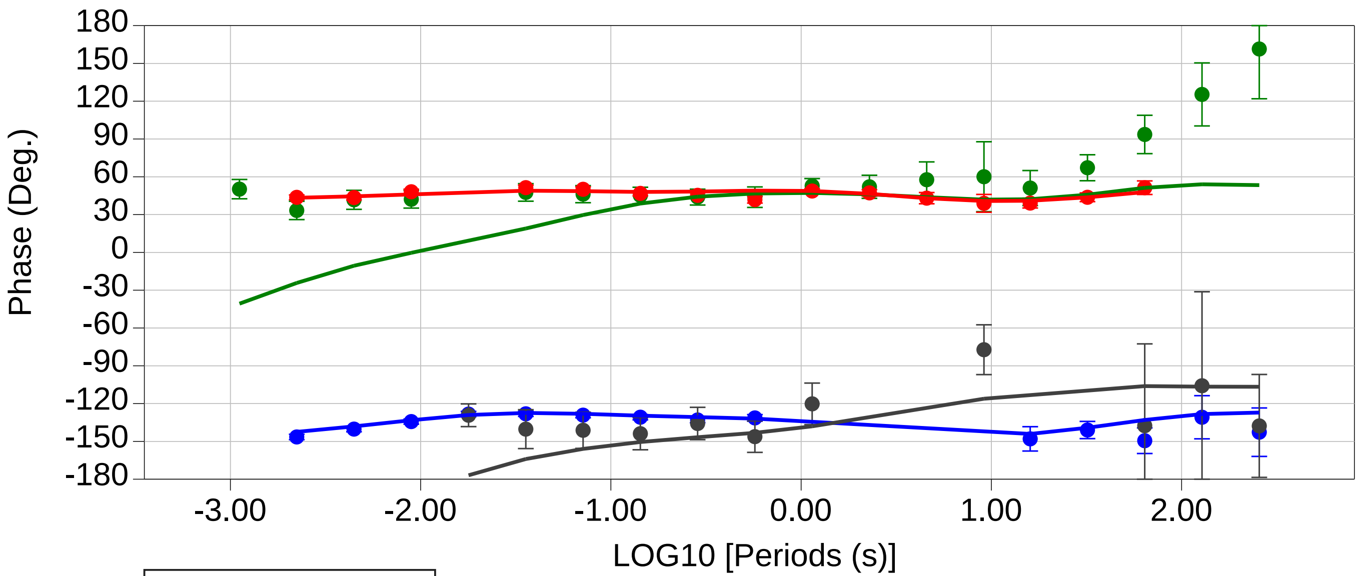

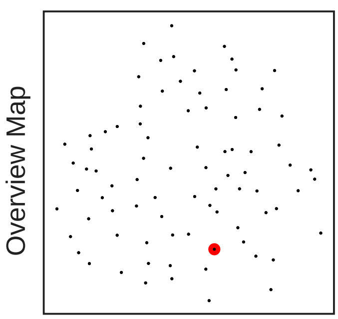

Total RMS = 1.25
Zxx RMS = 1.84
Zxy RMS = 0.75
Zyx RMS = 0.85
Zyy RMS = 0.98

Site: site_064

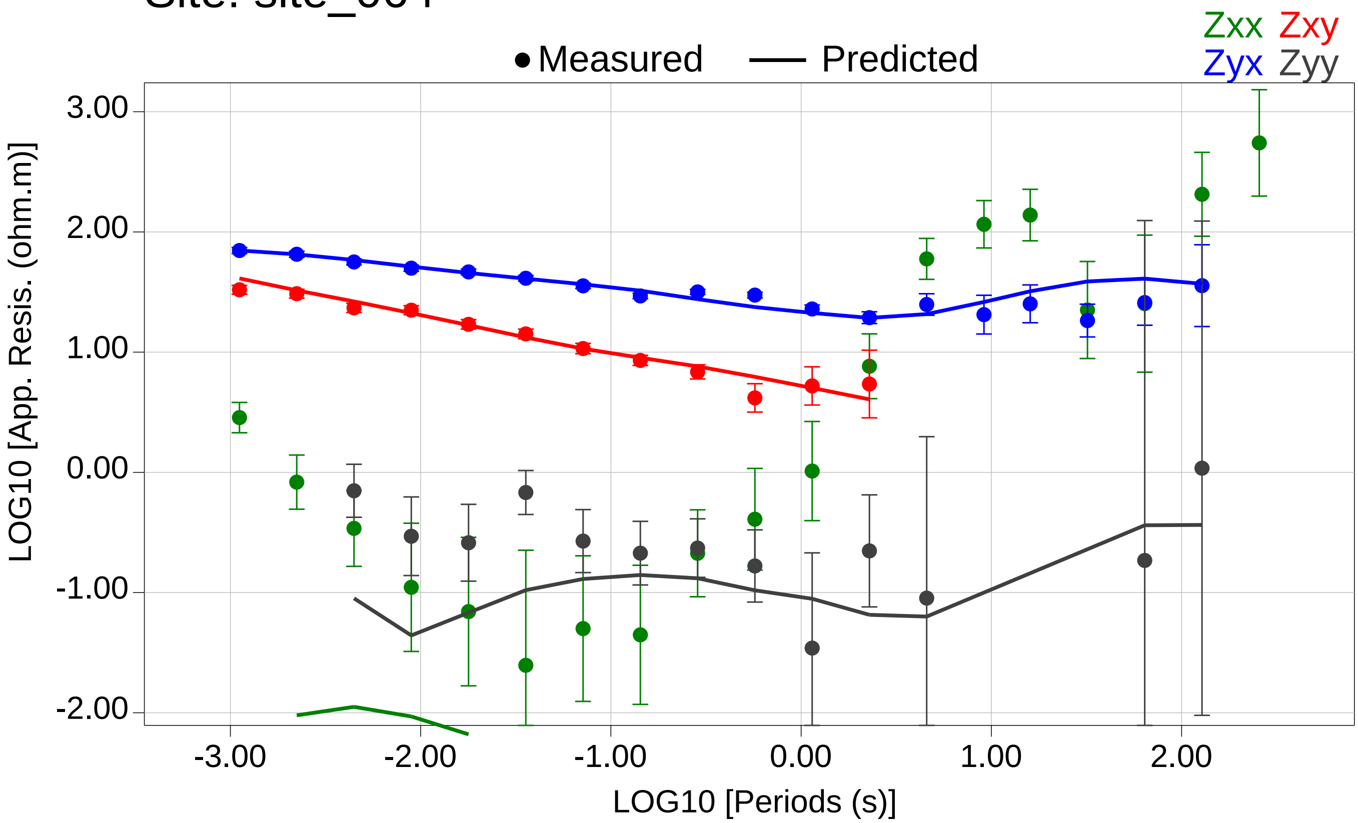

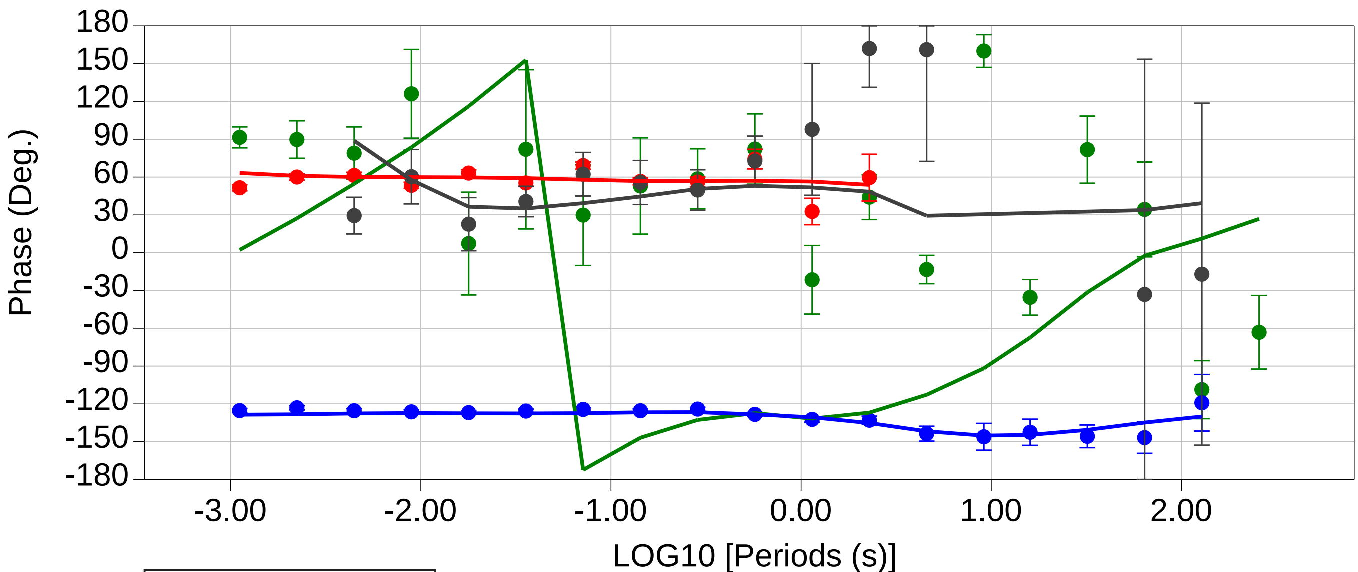

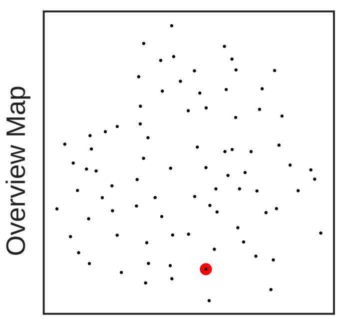

Total RMS = 1.22
Zxx RMS = 1.56
Zxy RMS = 1.27
Zyx RMS = 0.97
Zyy RMS = 0.86

Site: site_065

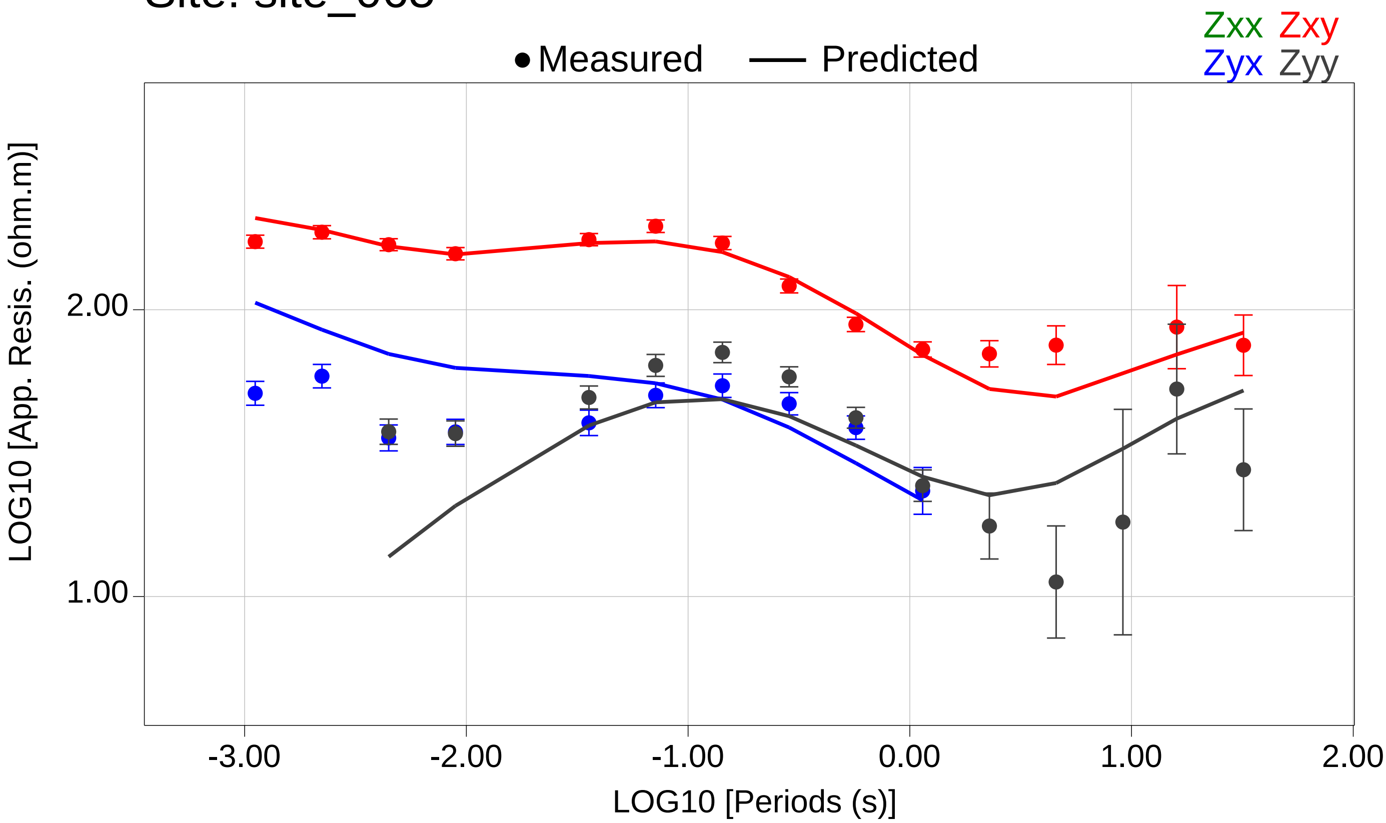

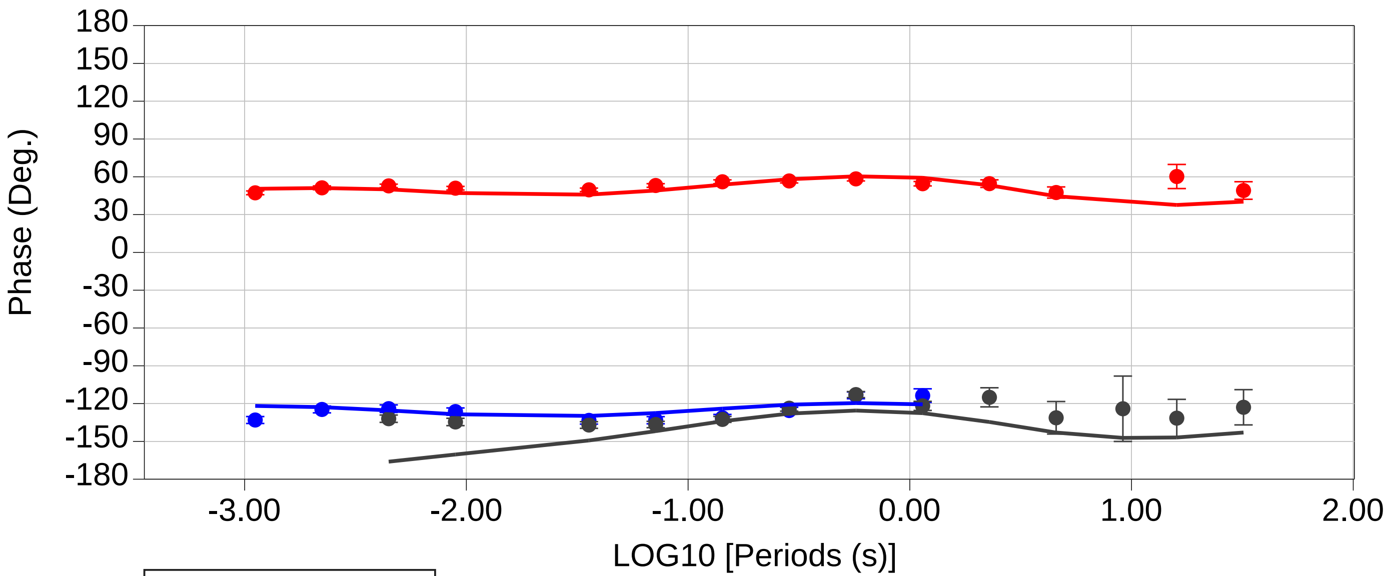

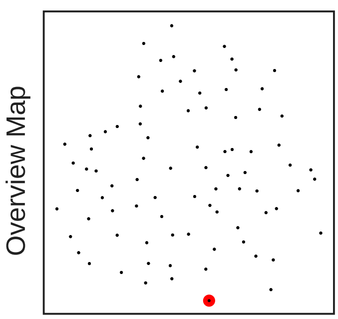

Total RMS = 2.20
Zxx RMS = 0.00
Zxy RMS = 1.26
Zyx RMS = 2.62
Zyy RMS = 2.60

Site: site_066

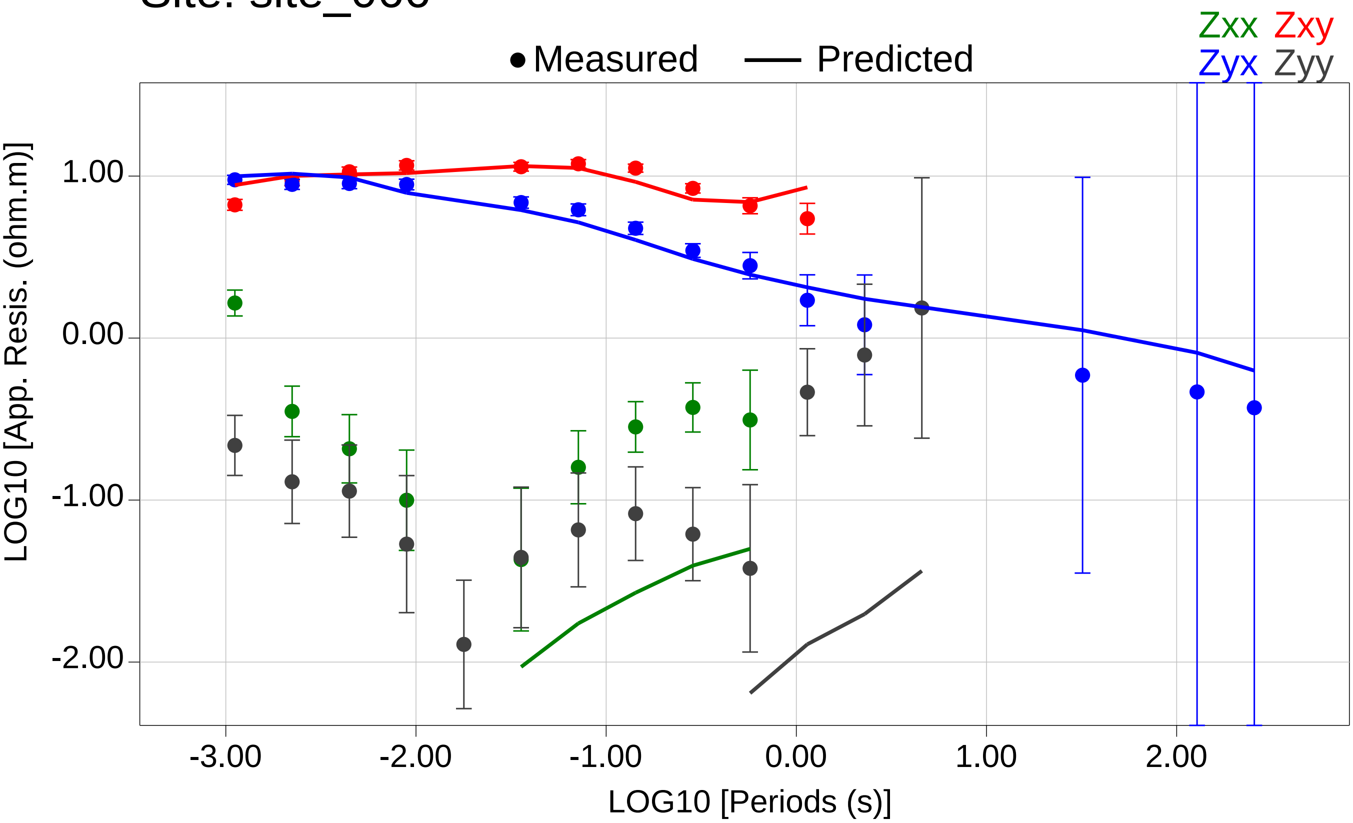

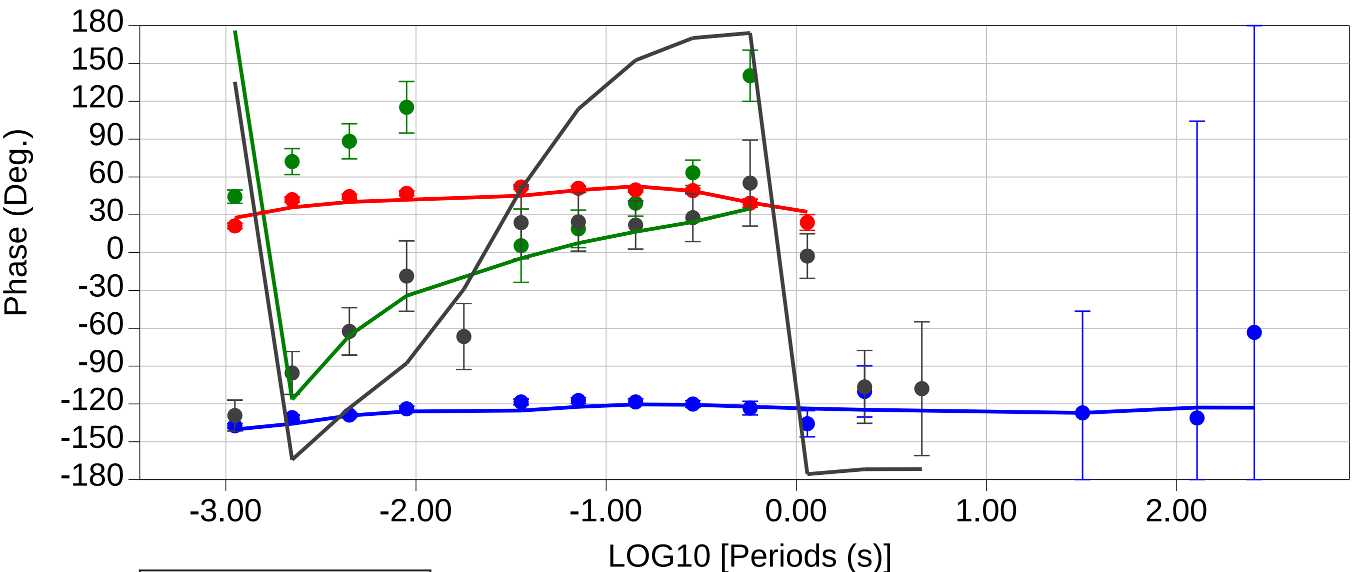

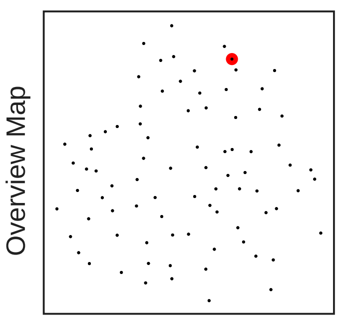

Total RMS = 1.62
Zxx RMS = 2.56
Zxy RMS = 1.53
Zyx RMS = 0.90
Zyy RMS = 1.44

Site: site_067

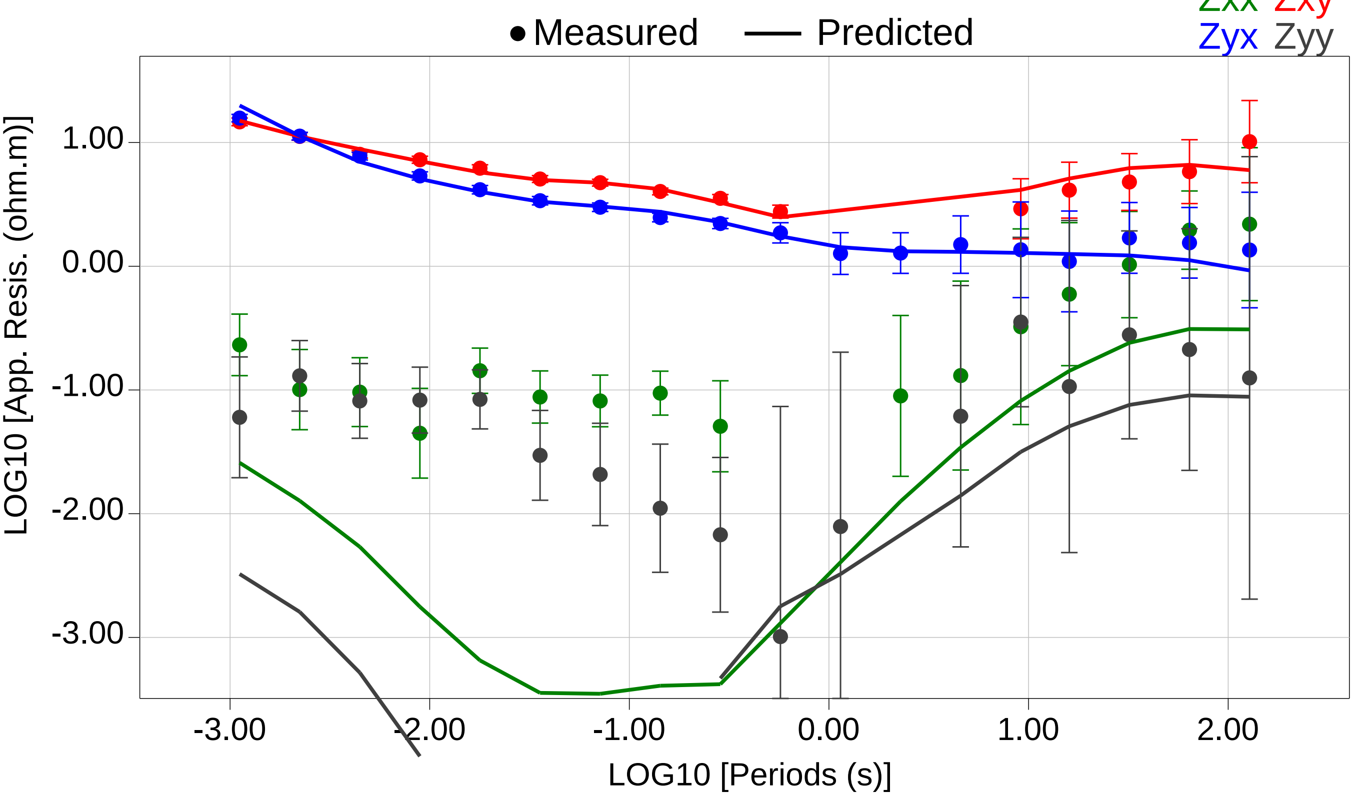

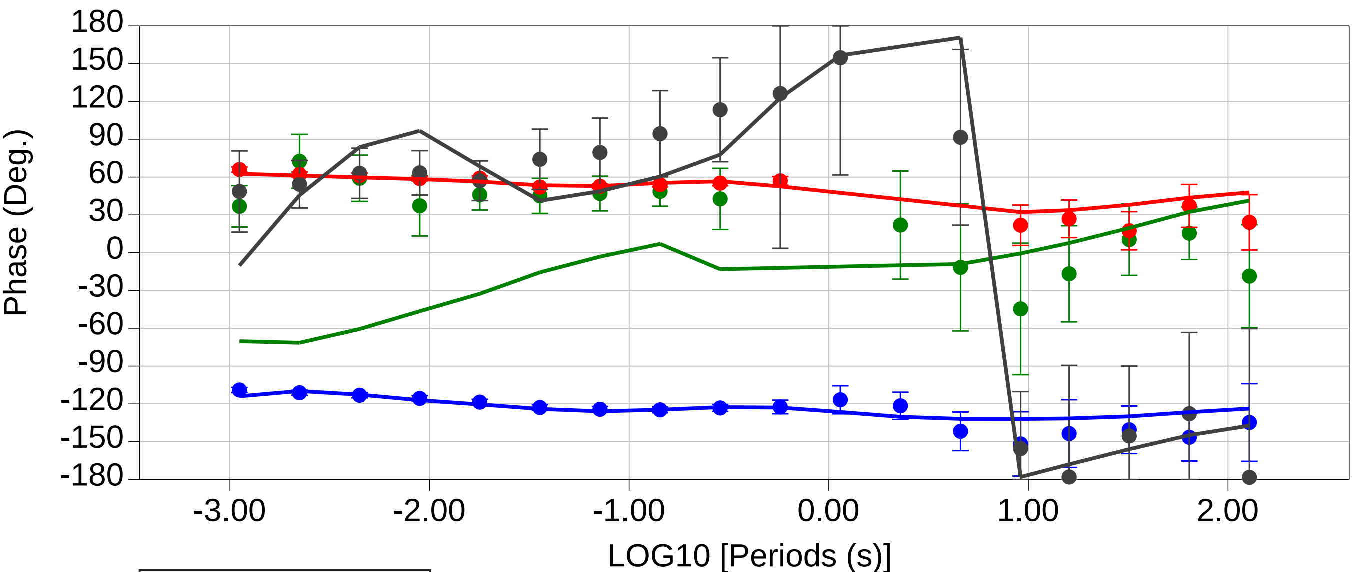

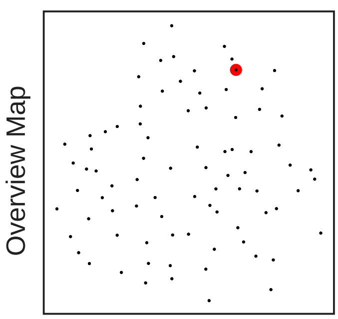

Total RMS = 0.96
Zxx RMS = 1.45
Zxy RMS = 0.58
Zyx RMS = 0.67
Zyy RMS = 0.90

Site: site_068

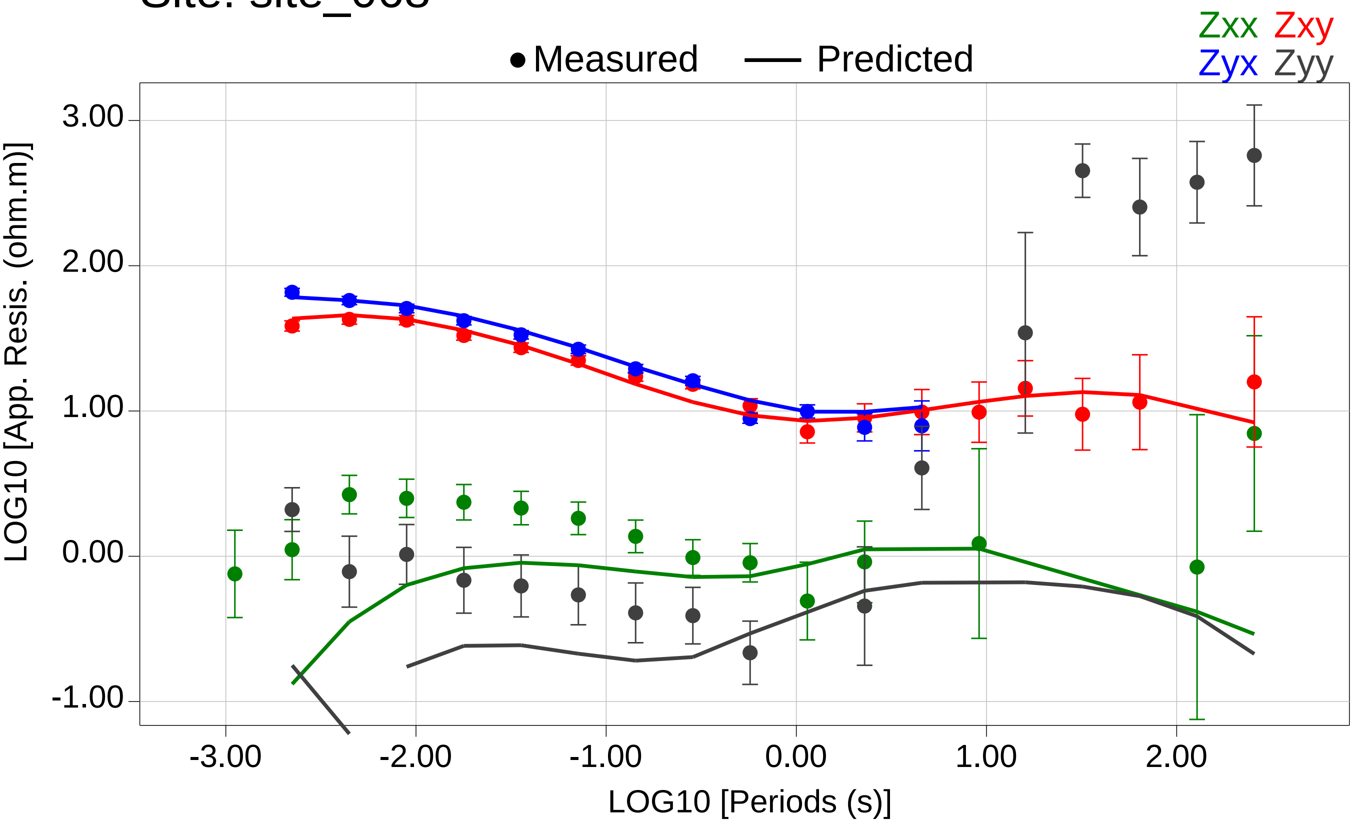

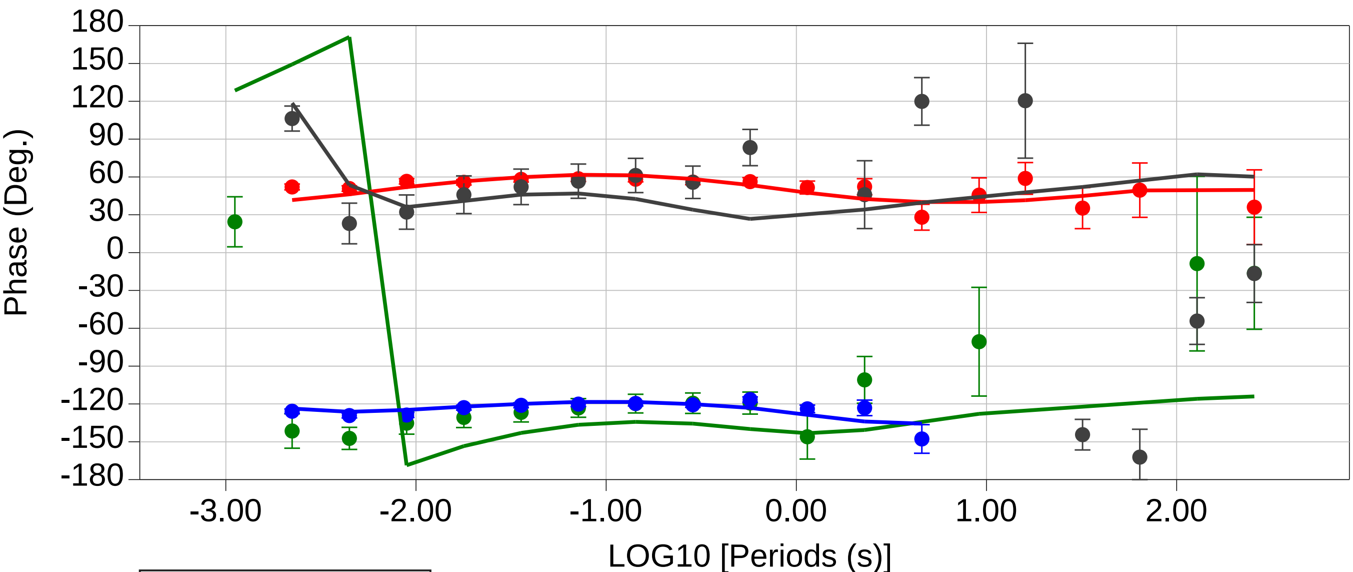

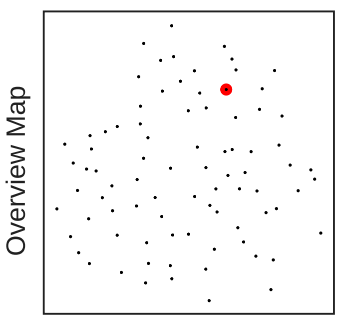

Total RMS = 1.24
Zxx RMS = 1.45
Zxy RMS = 1.01
Zyx RMS = 1.05
Zyy RMS = 1.37

Site: site_069

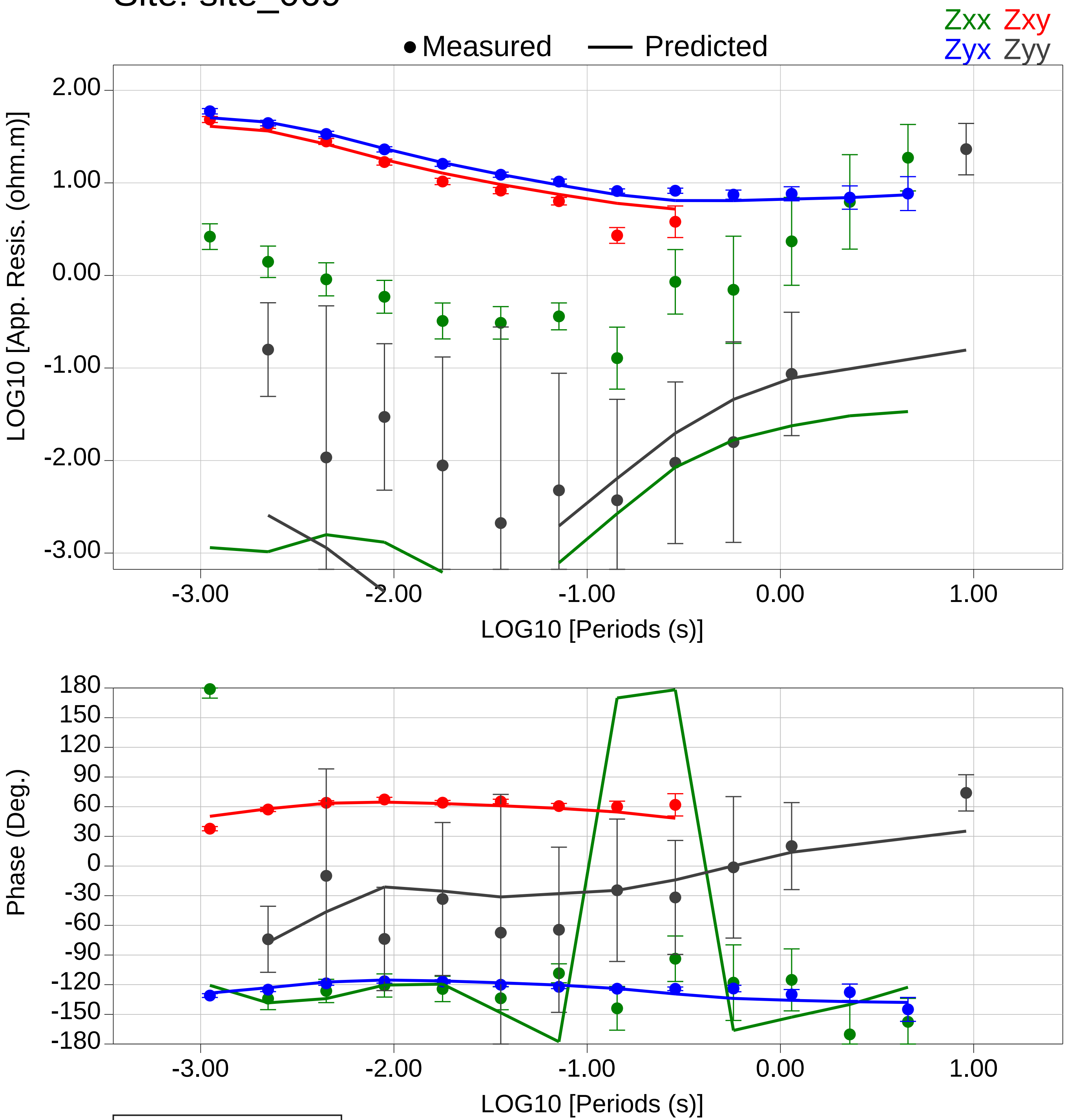

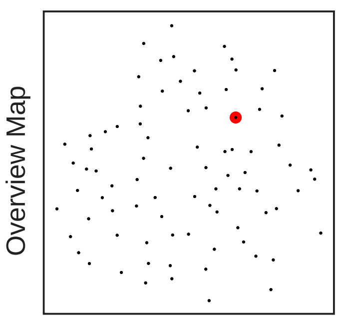

Total RMS = 1.40
Zxx RMS = 1.99
Zxy RMS = 1.60
Zyx RMS = 0.98
Zyy RMS = 0.55

Site: site_070

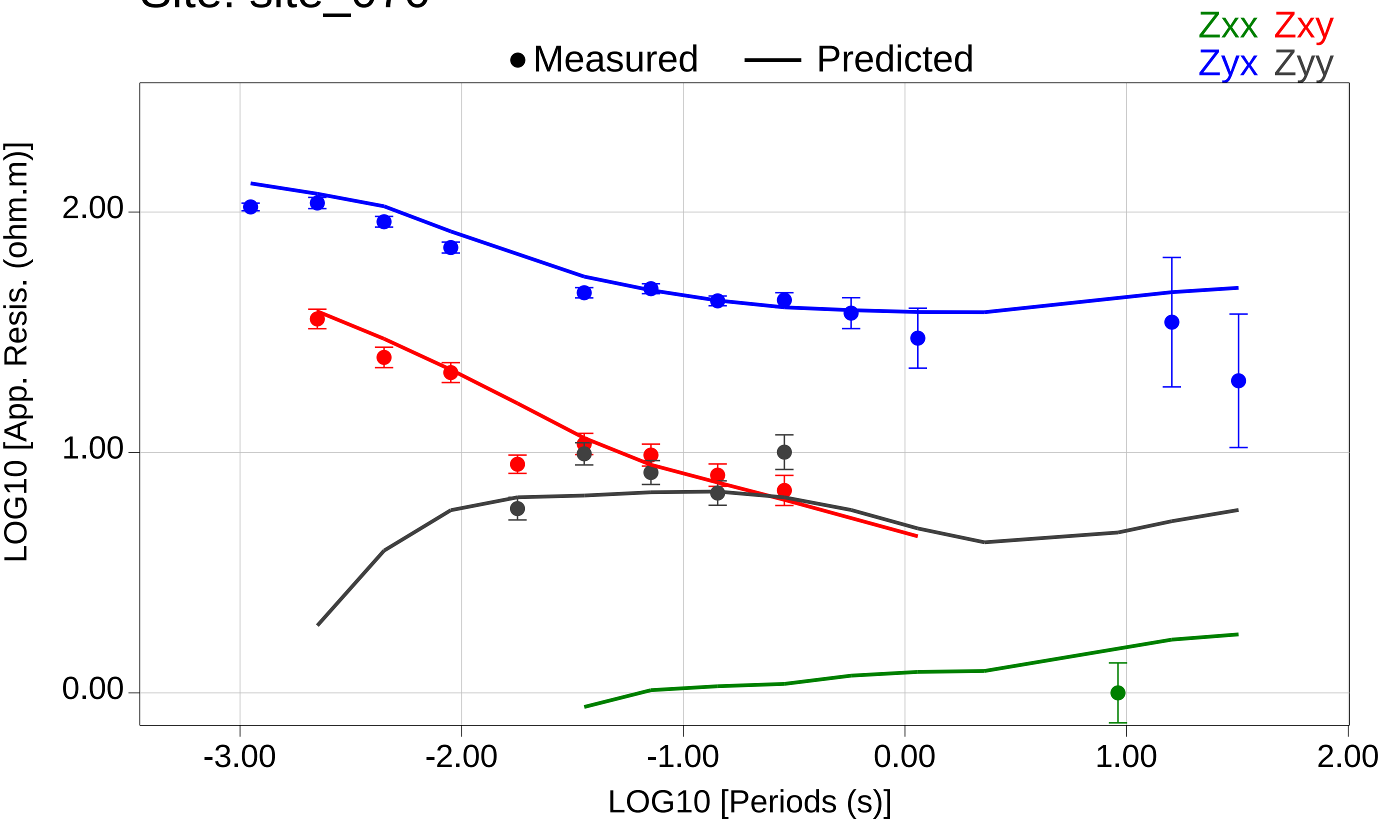

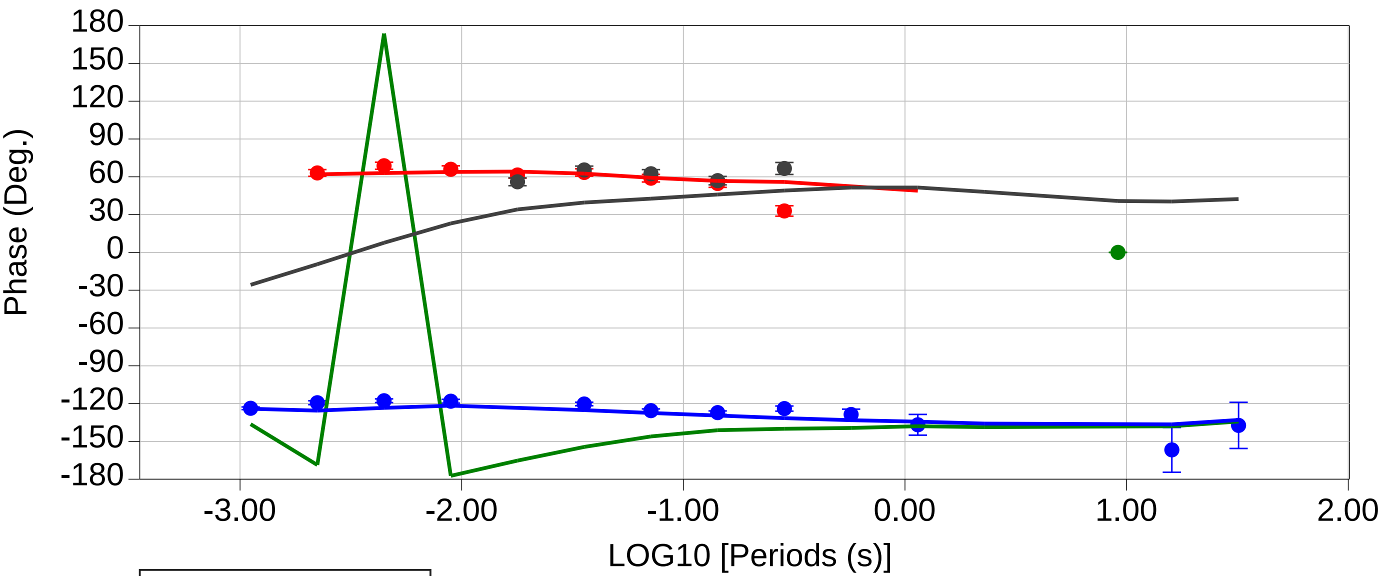

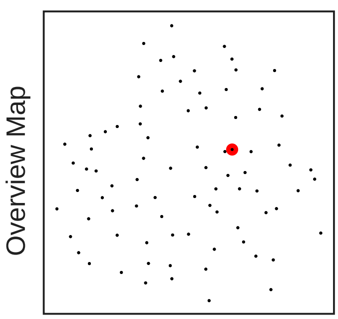

Total RMS = 2.10
Zxx RMS = 5.39
Zxy RMS = 1.72
Zyx RMS = 1.91
Zyy RMS = 5.56

Site: site_071

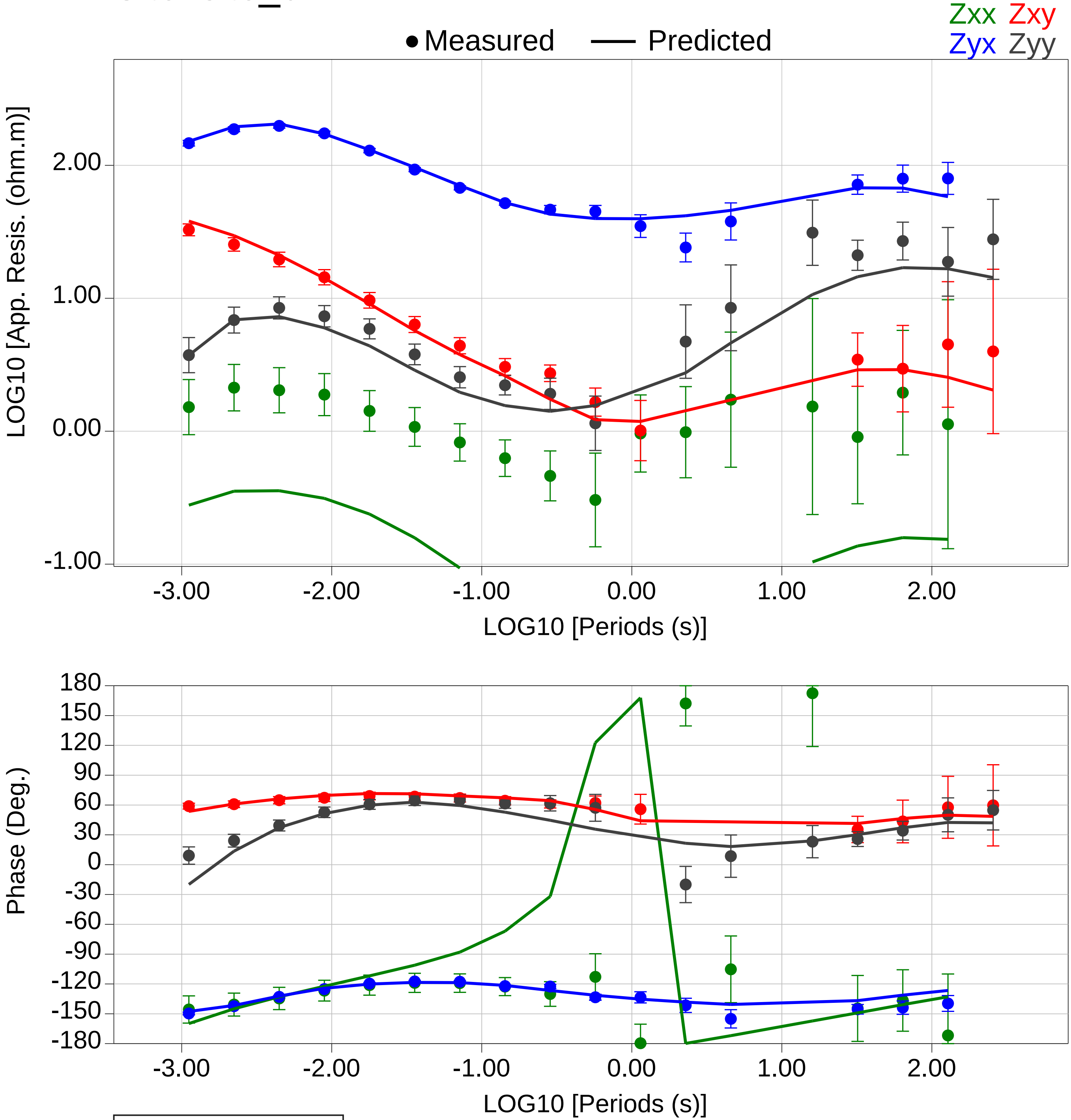

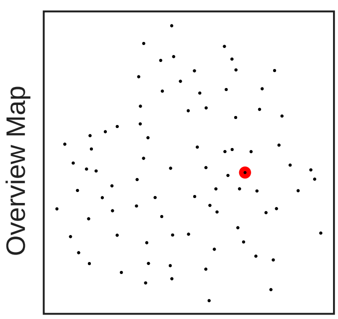

Total RMS = 1.02

Zxx RMS = 1.53

Zxy RMS = 0.65

Zyx RMS = 0.77

Zyy RMS = 0.86

Site: site_072

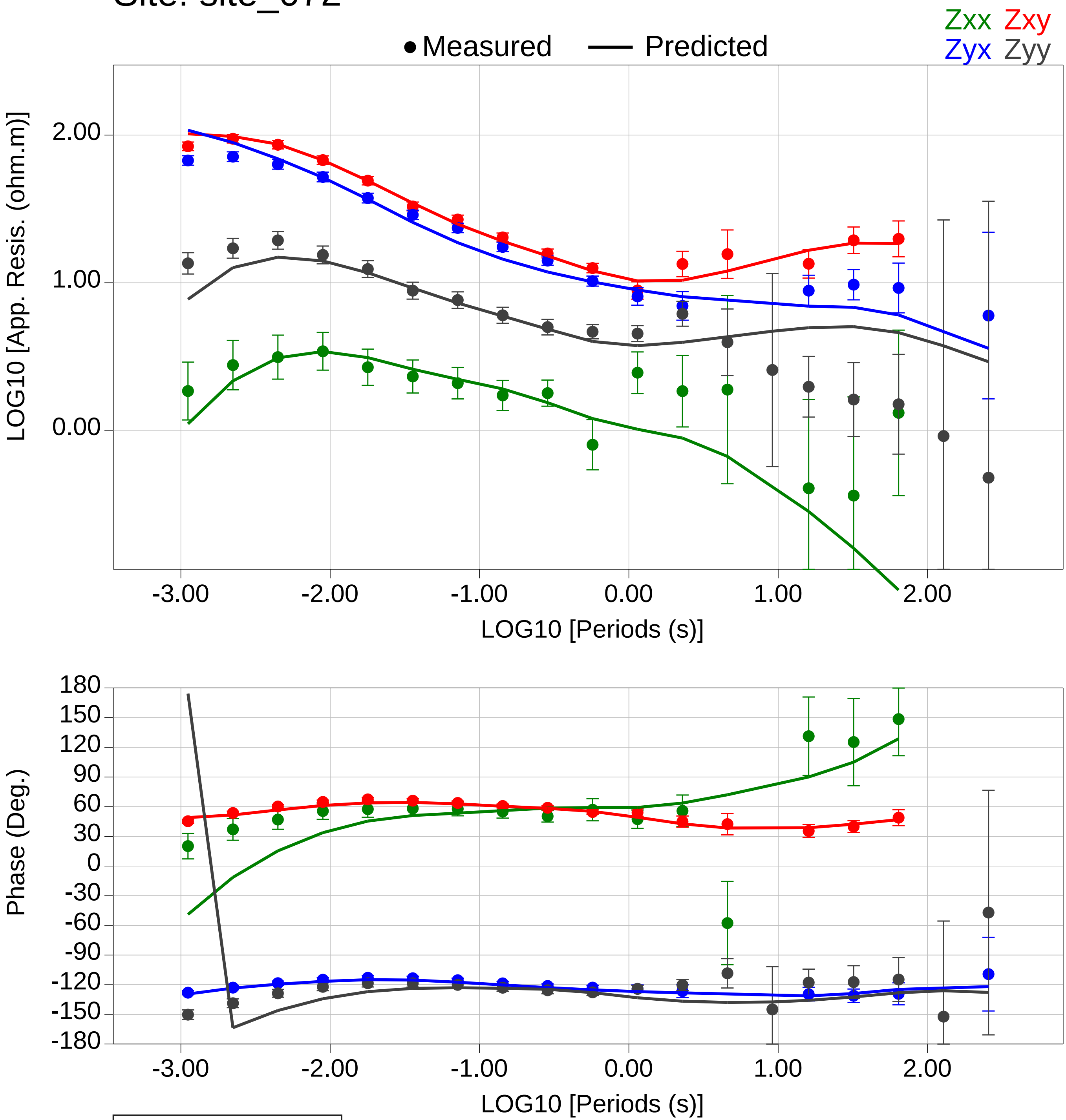

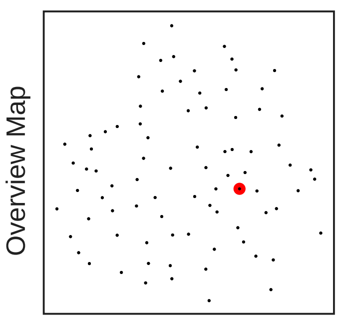

Total RMS = 1.18
Zxx RMS = 1.09
Zxy RMS = 0.75
Zyx RMS = 1.23
Zyy RMS = 1.47

Site: site_073

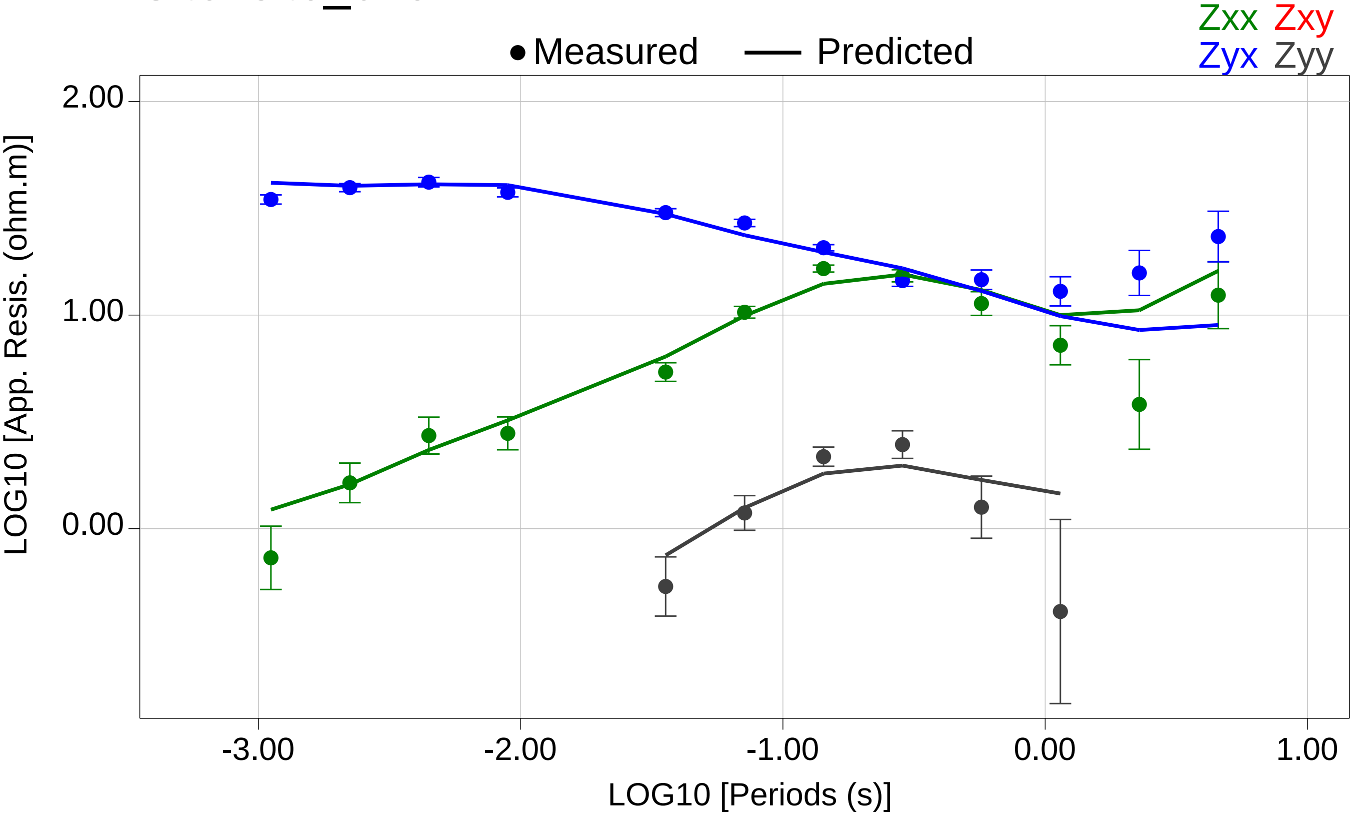

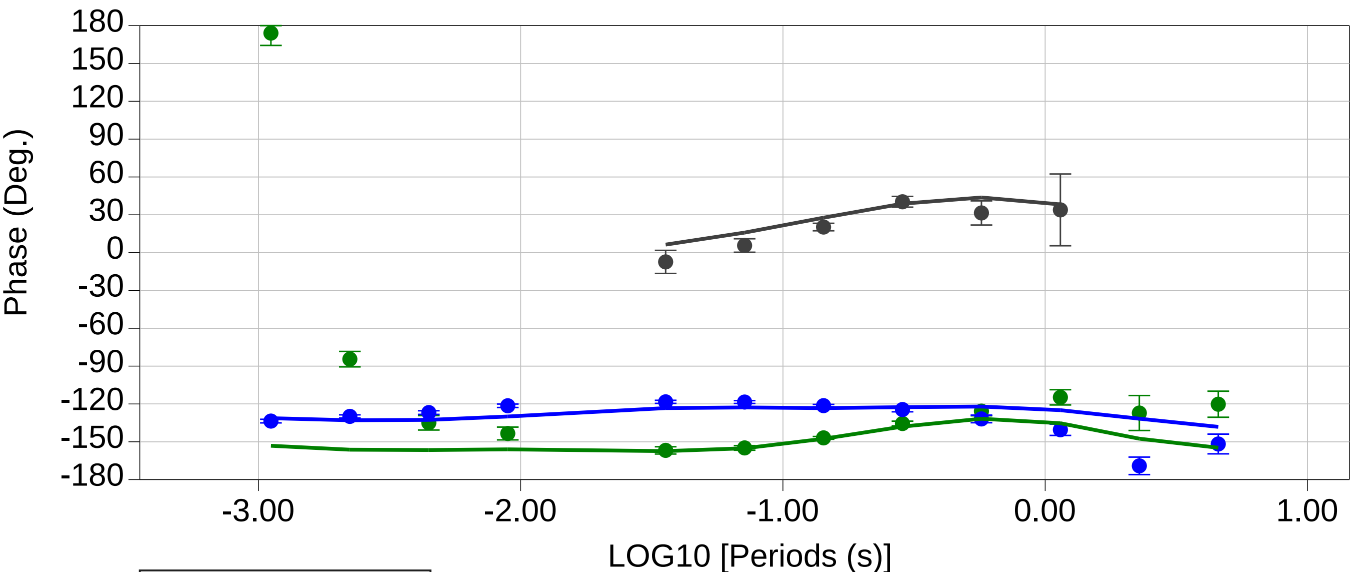

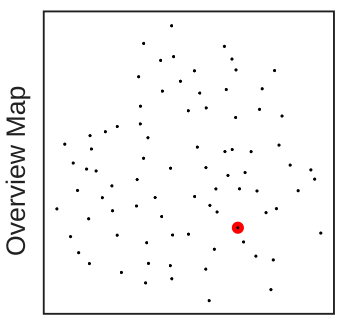

Total RMS = 1.92
Zxx RMS = 2.17
Zxy RMS = 0.00
Zyx RMS = 2.01
Zyy RMS = 1.01

Site: site_074

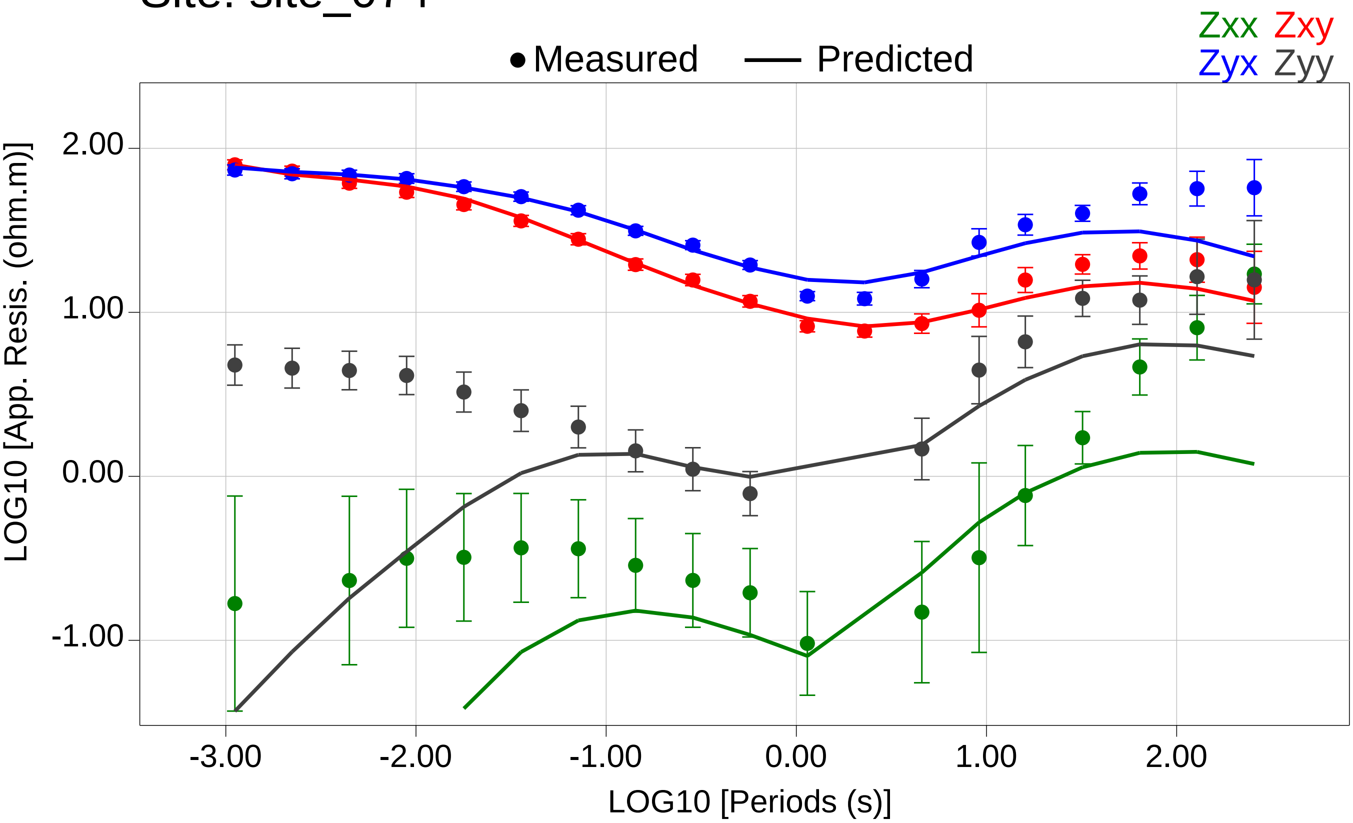

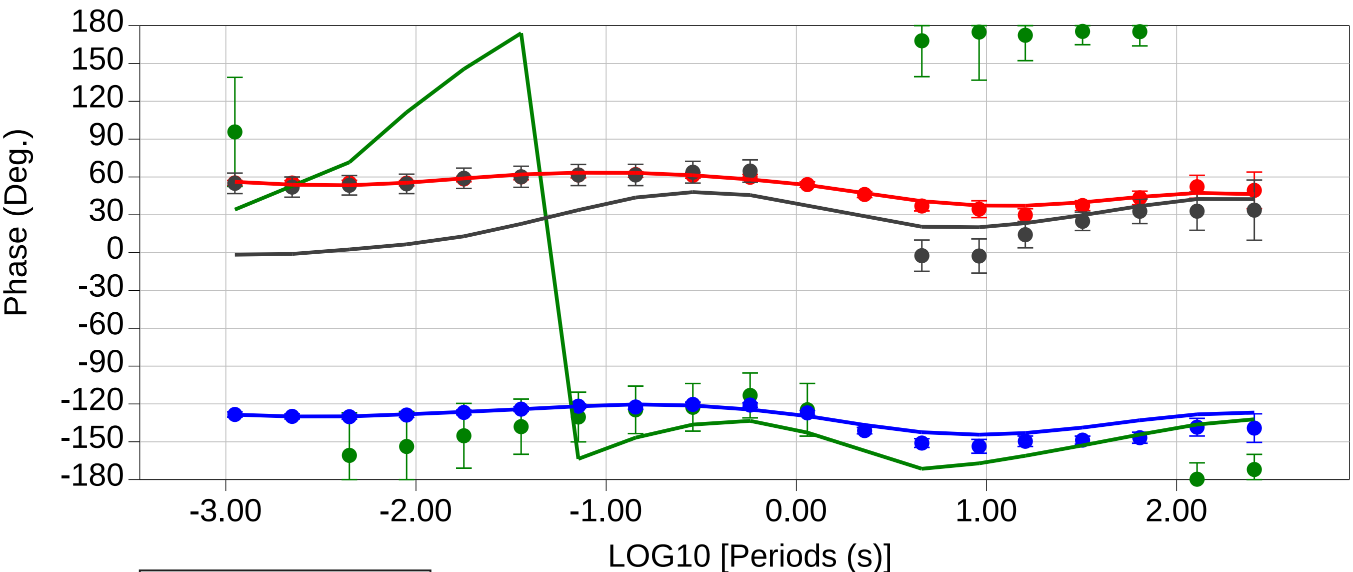

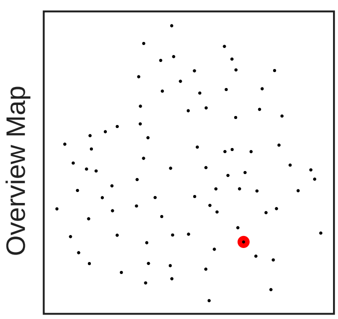

Total RMS = 1.26
Zxx RMS = 1.05
Zxy RMS = 0.59
Zyx RMS = 1.11
Zyy RMS = 1.97

Site: site_079

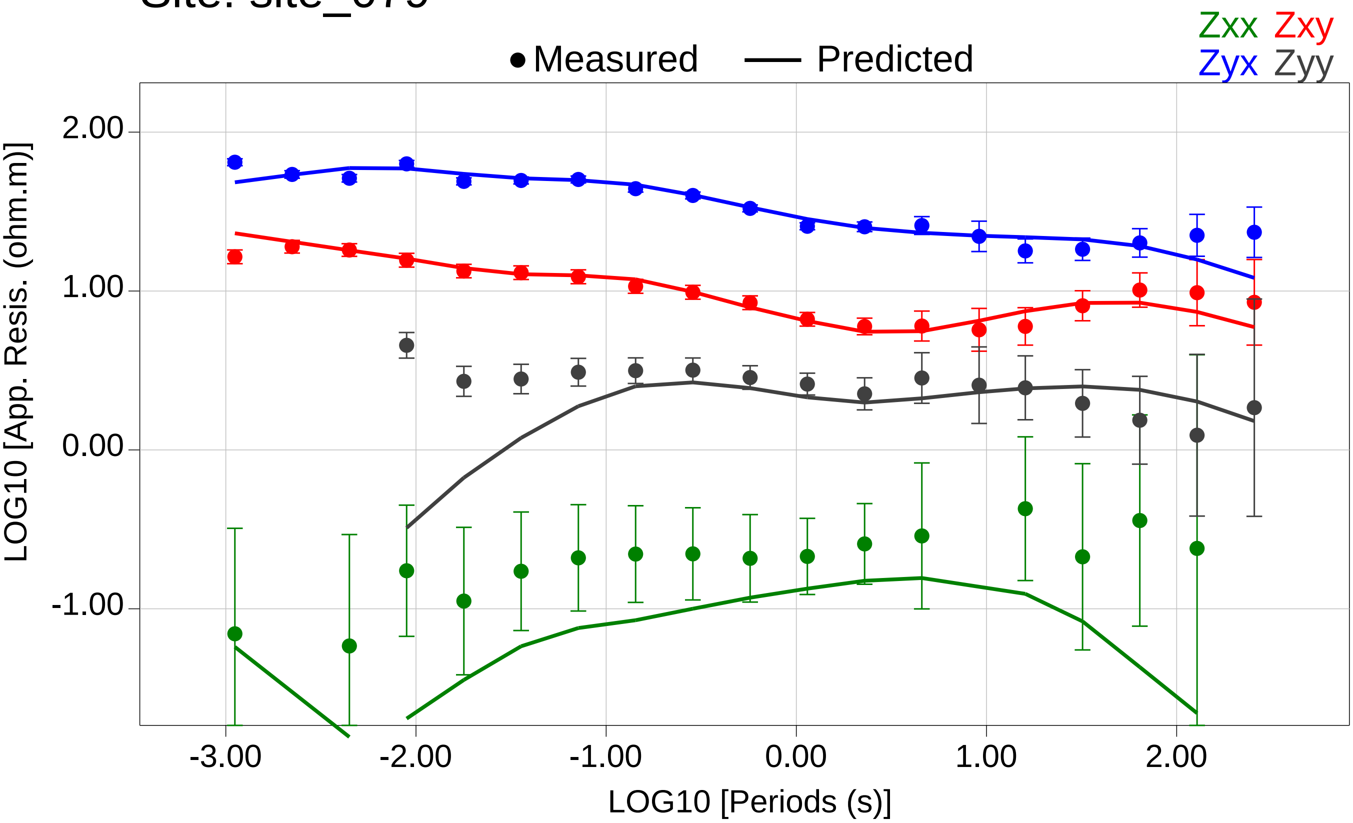

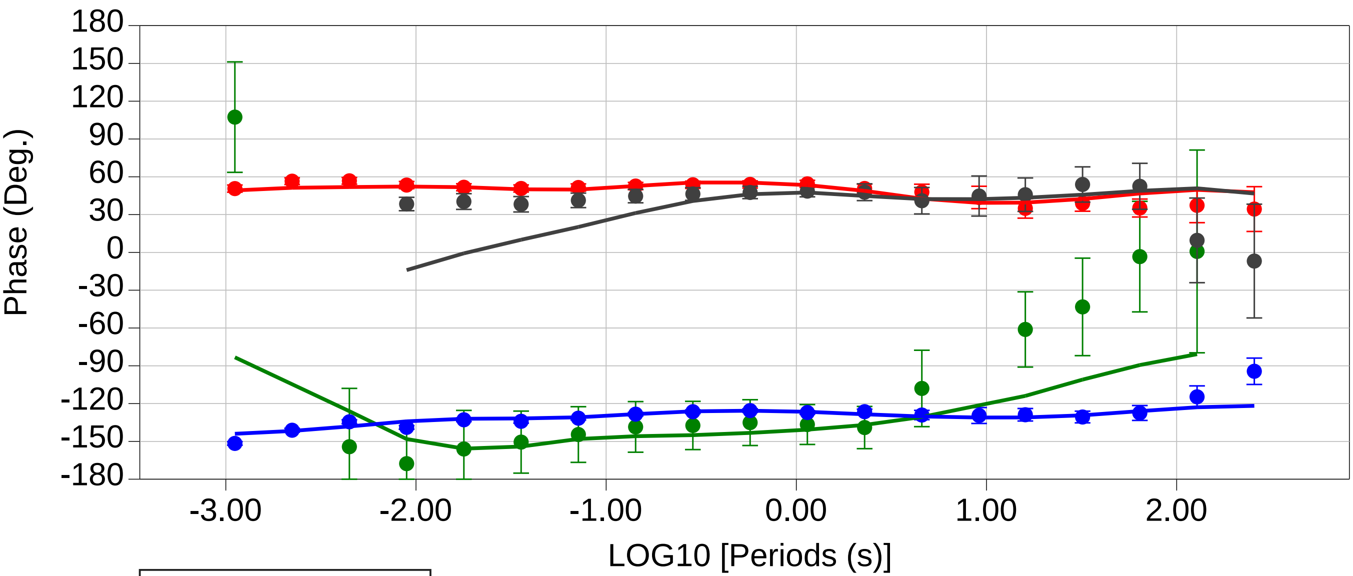

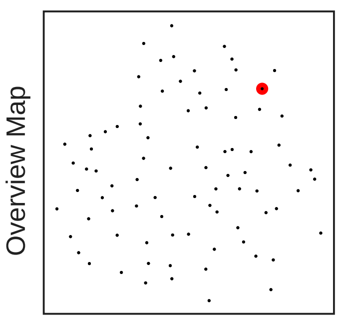

Total RMS = 1.12
Zxx RMS = 0.60
Zxy RMS = 0.67
Zyx RMS = 1.19
Zyy RMS = 1.70

Site: site_080

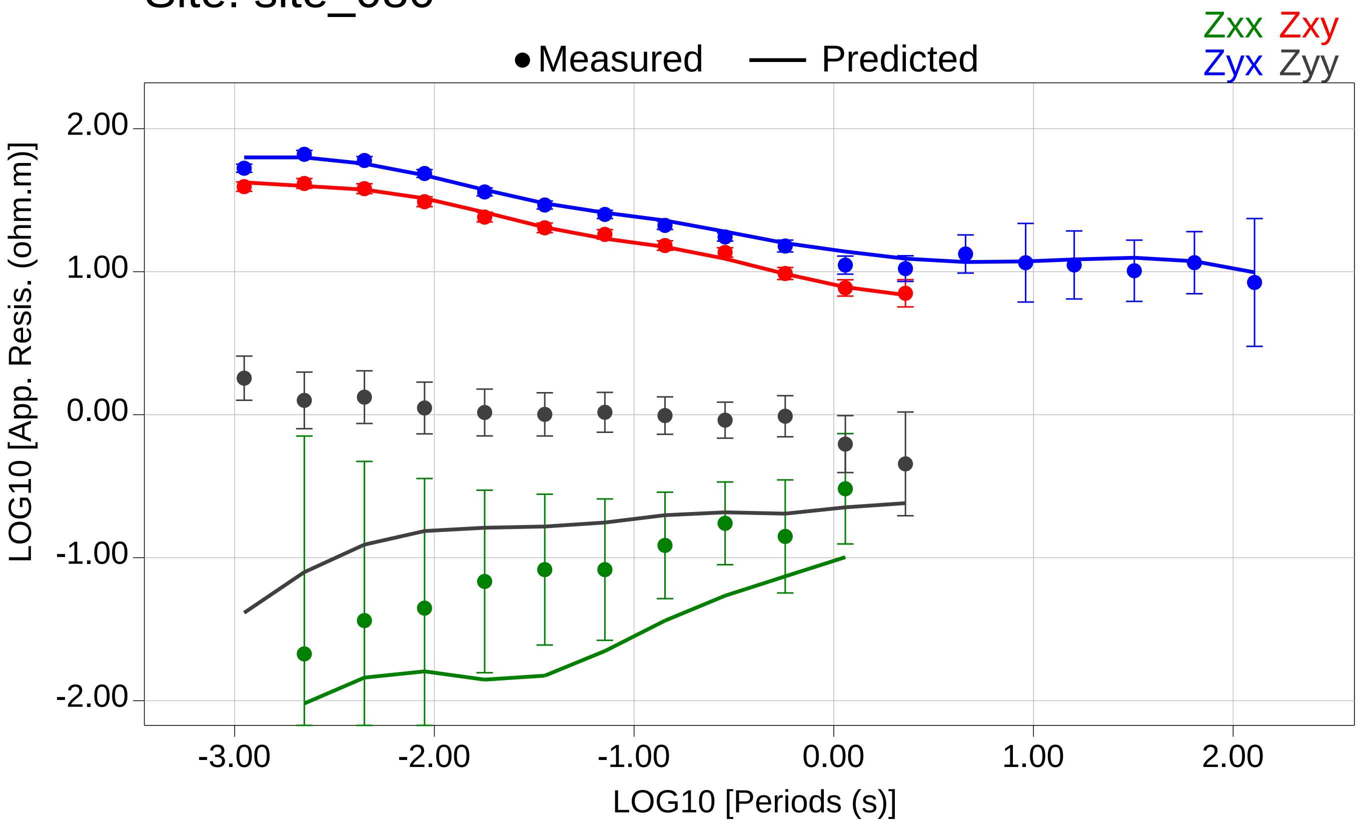

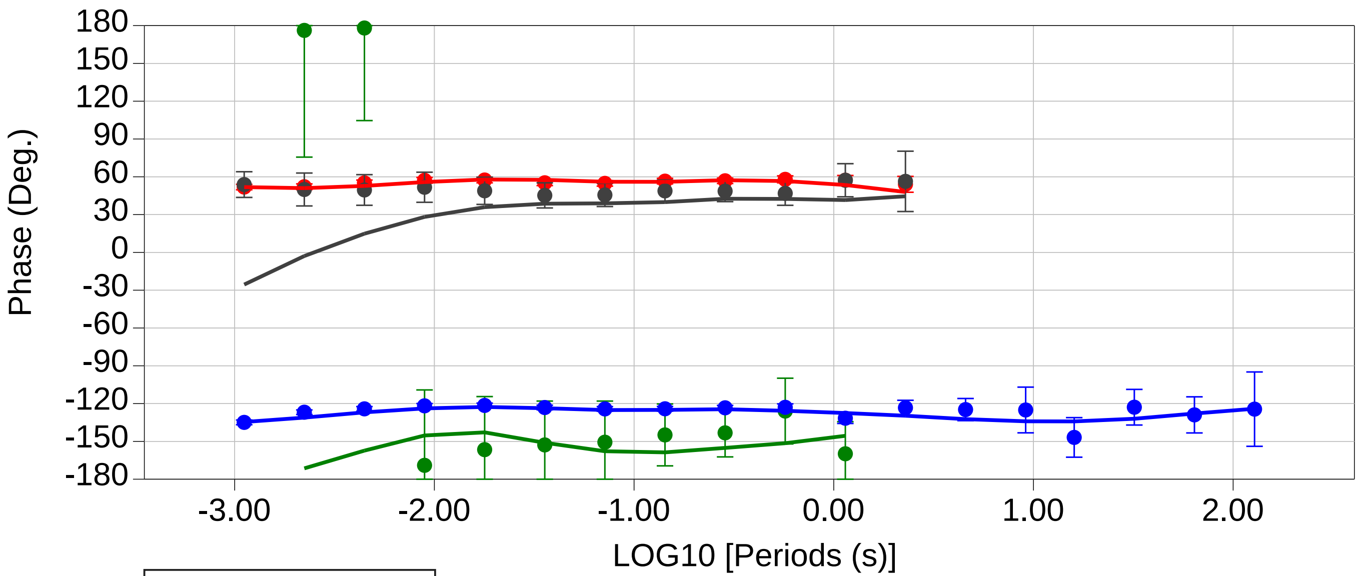

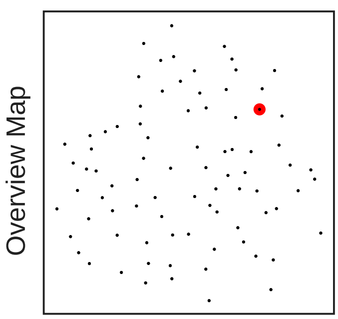

Total RMS = 0.98
Zxx RMS = 0.45
Zxy RMS = 0.47
Zyx RMS = 0.67
Zyy RMS = 1.75

Site: site_081

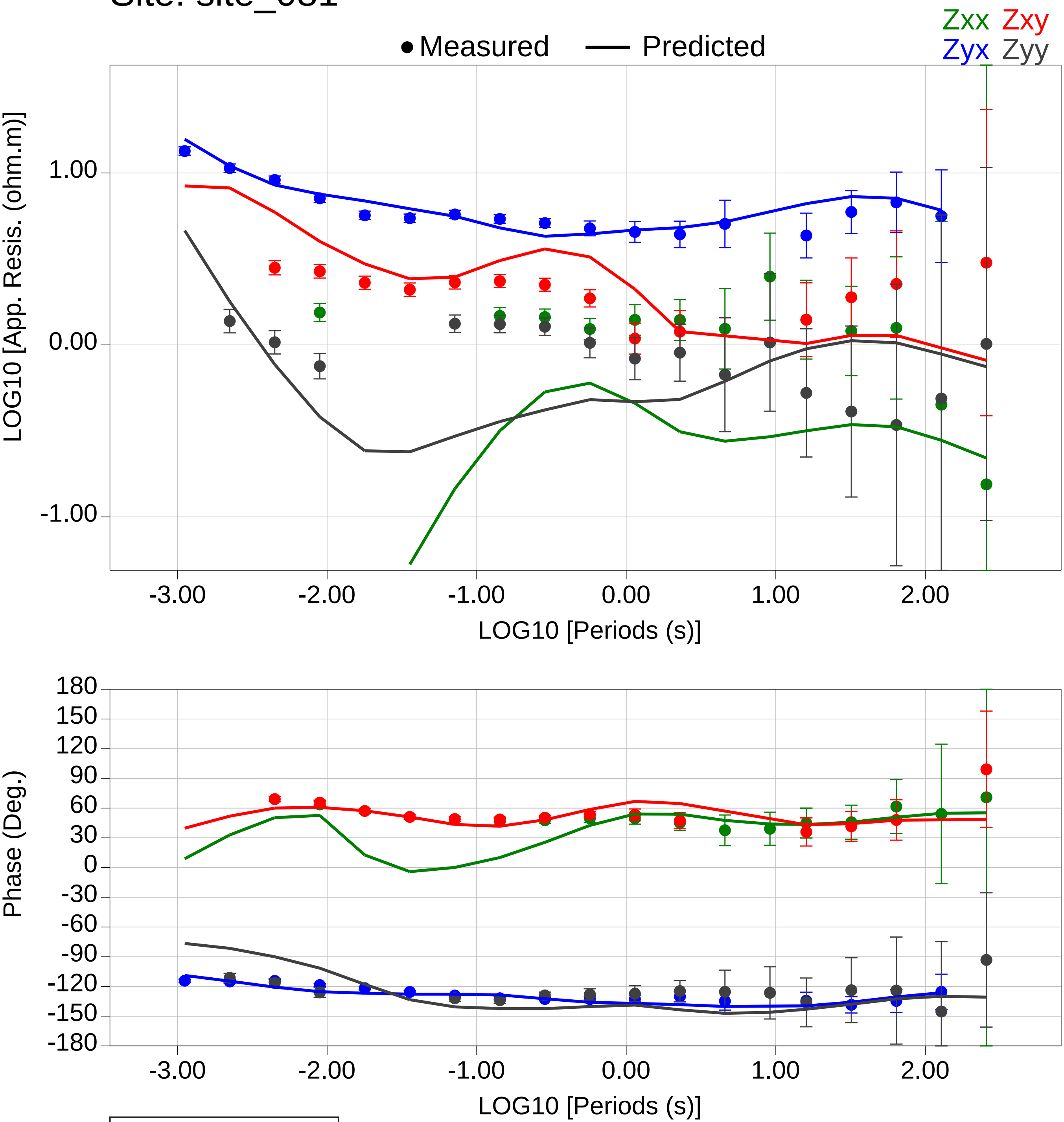

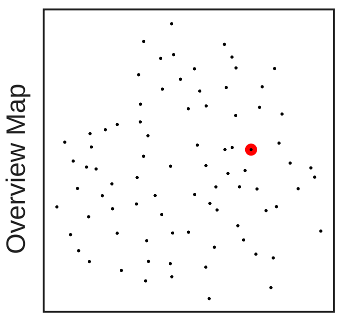

Total RMS = 2.31
Zxx RMS = 5.02
Zxy RMS = 3.30
Zyx RMS = 1.31
Zyy RMS = 3.03

Site: site_083

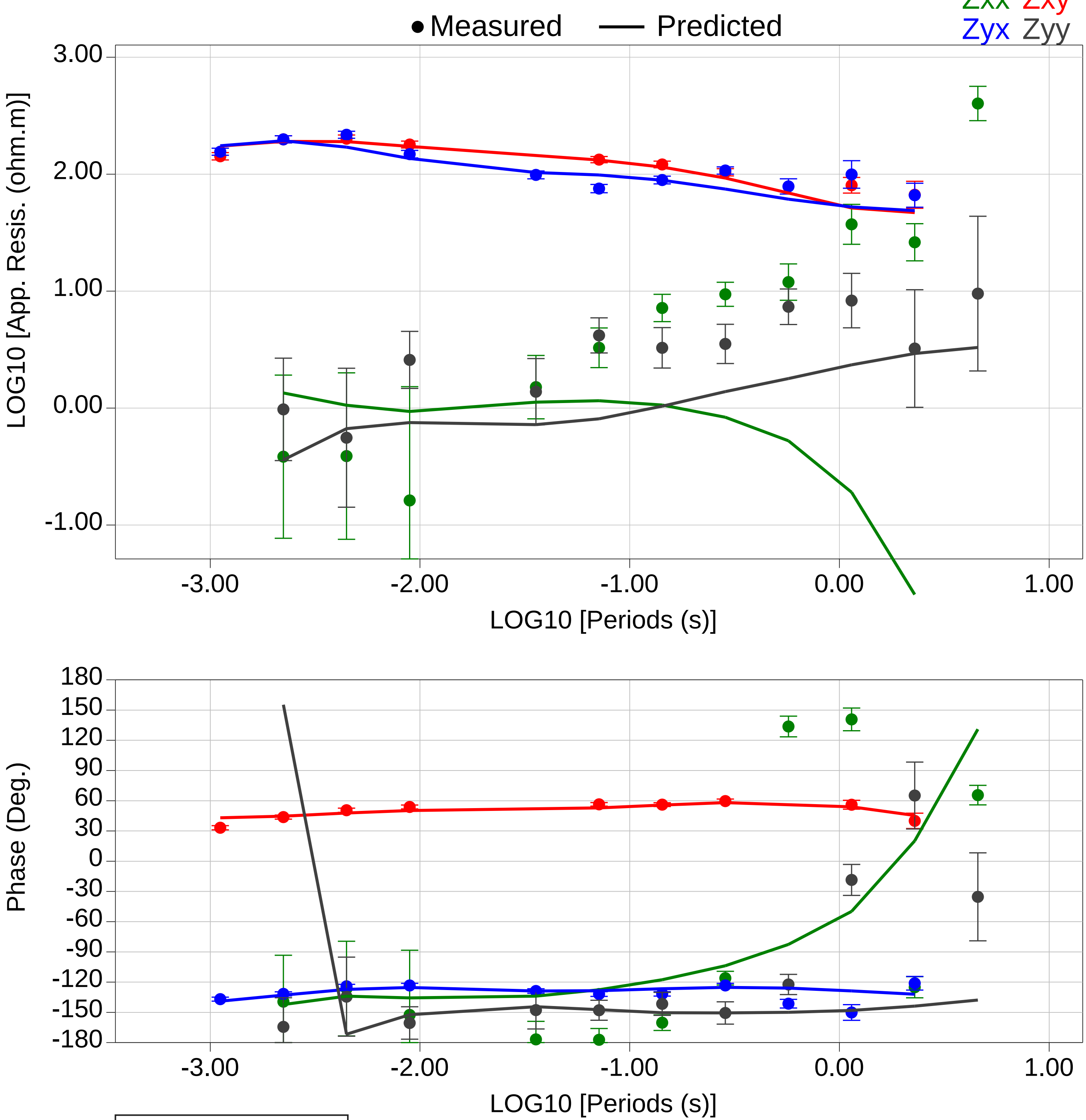

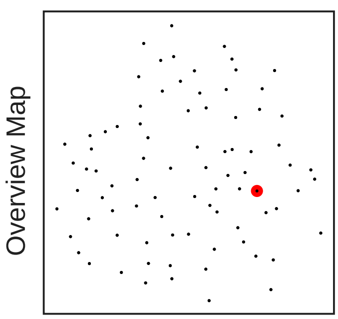

Total RMS = 1.65
Zxx RMS = 2.29
Zxy RMS = 1.25
Zyx RMS = 1.43
Zyy RMS = 1.33

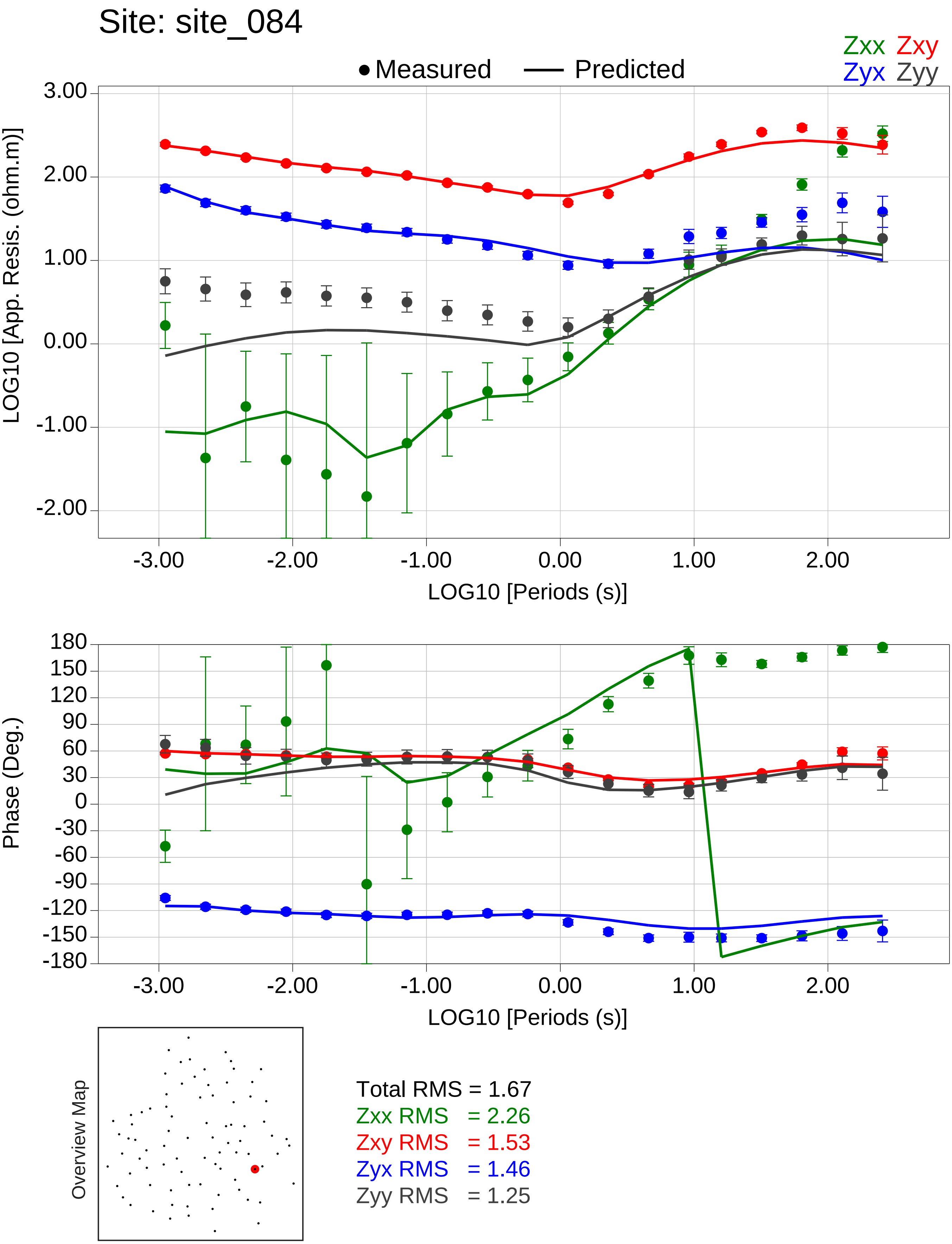

Site: site_084
Measured
Predicted
Zxx Zxy
Zyx Zyy
LOG10 [App. Resis. (ohm.m)]
LOG10 [Periods (s)]
Phase (Deg.)
LOG10 [Periods (s)]
Overview Map
Total RMS = 1.67
Zxx RMS = 2.26
Zxy RMS = 1.53
Zyx RMS = 1.46
Zyy RMS = 1.25

Site: site_086

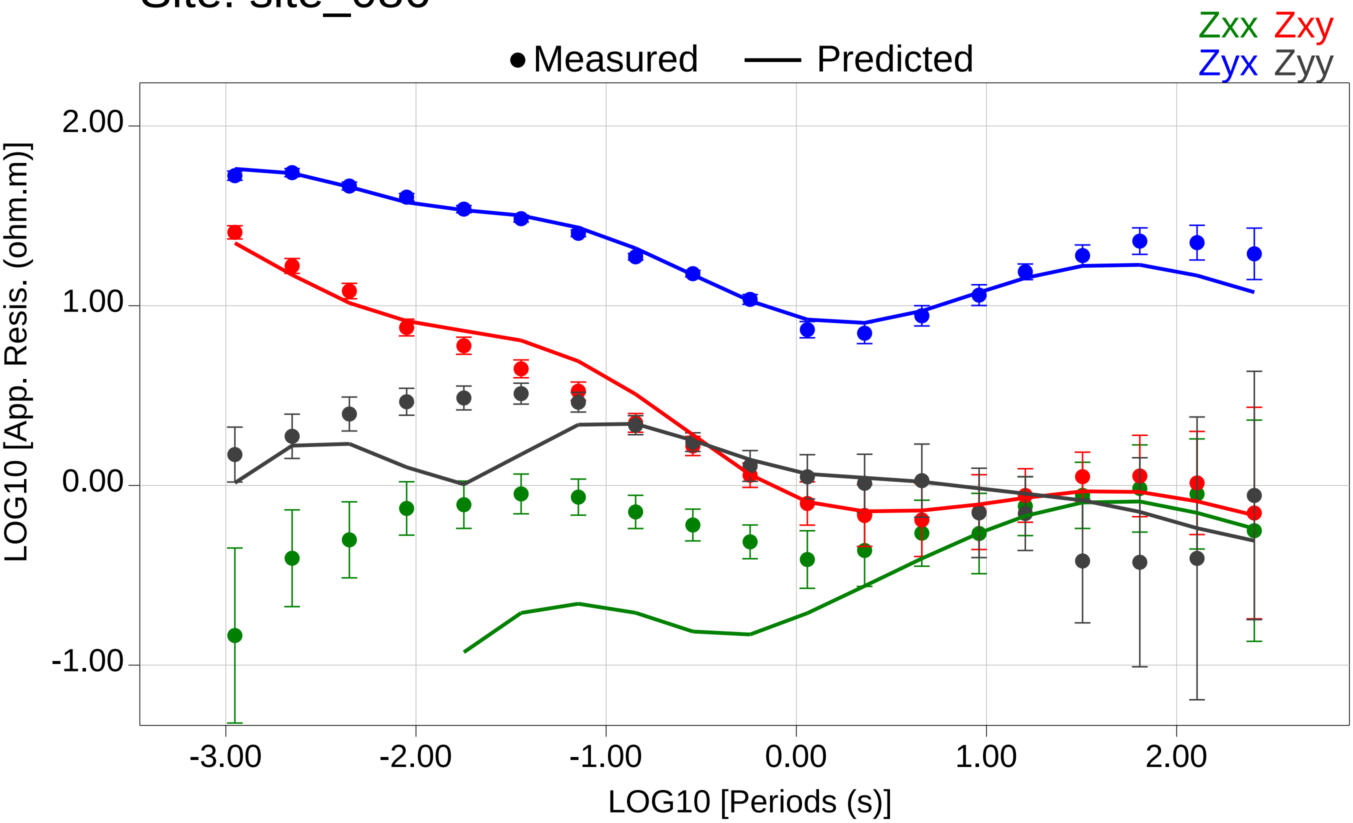

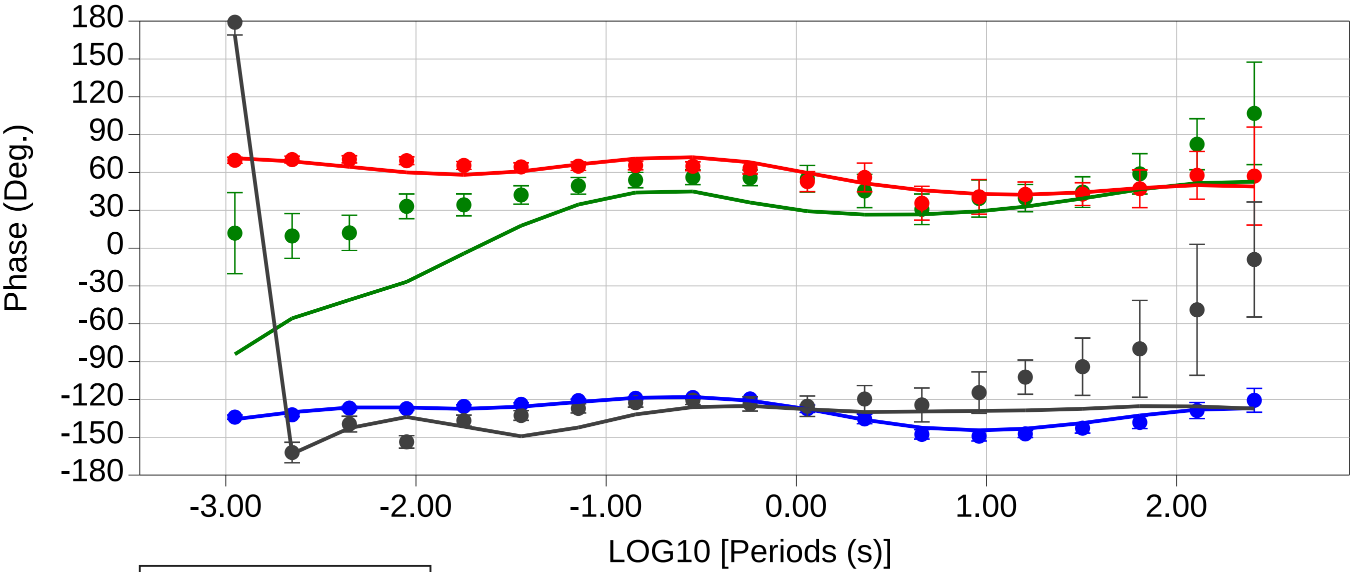

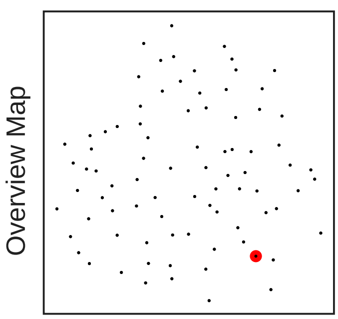

Total RMS = 1.26
Zxx RMS = 1.65
Zxy RMS = 1.03
Zyx RMS = 0.77
Zyy RMS = 1.39

Site: site_087

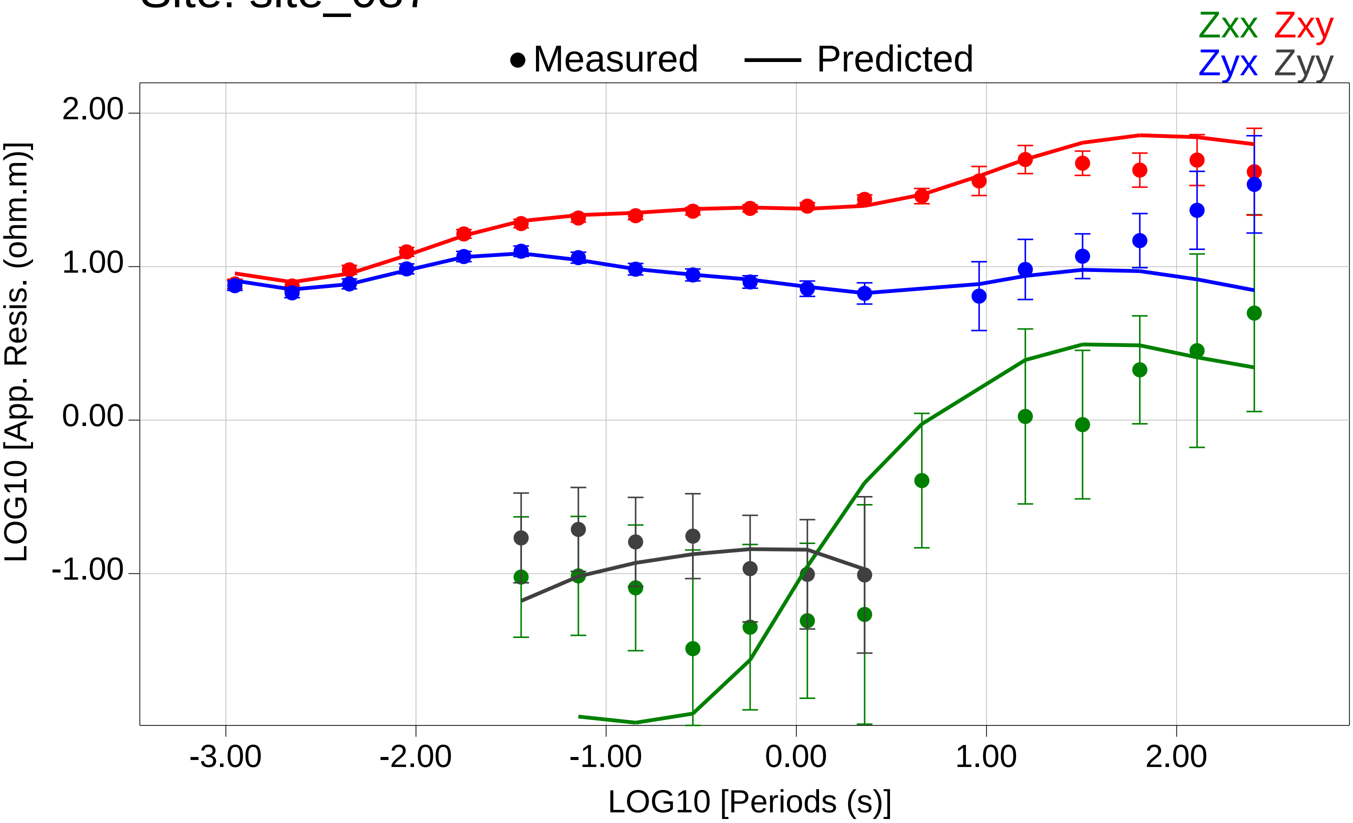

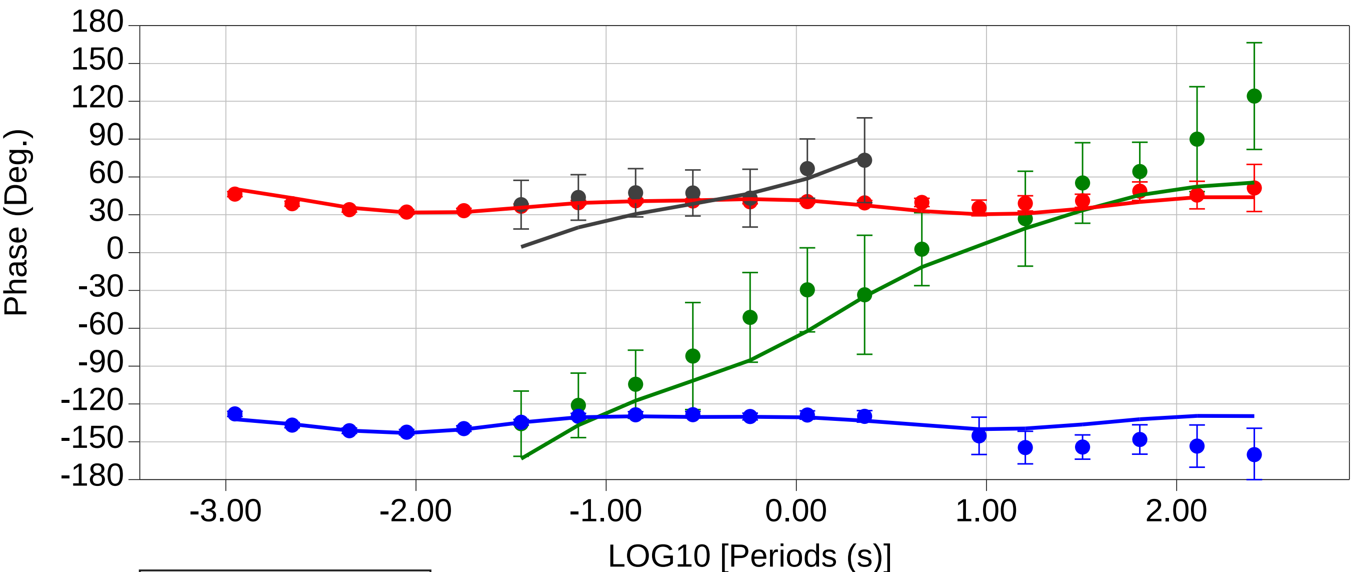

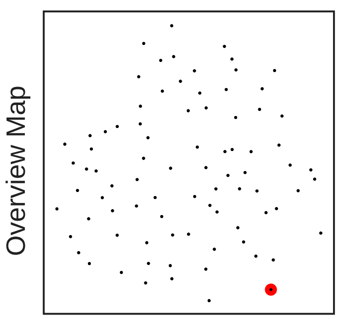

Total RMS = 0.66
Zxx RMS = 0.67
Zxy RMS = 0.79
Zyx RMS = 0.56
Zyy RMS = 0.50

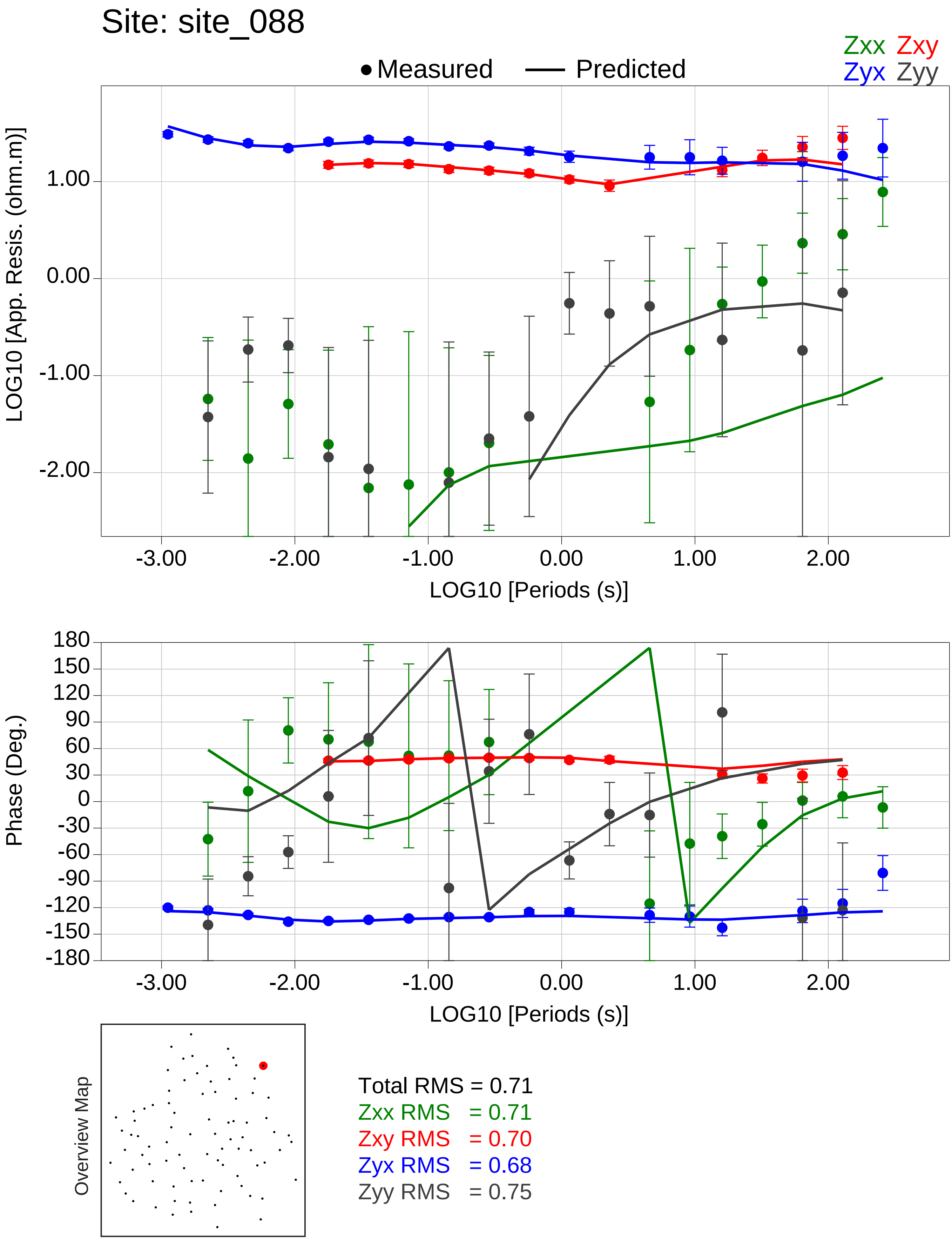

Site: site_088
Measured
Predicted
Zxx Zxy
Zyx Zyy
LOG10 [App. Resis. (ohm.m)]
1.00
0.00
-1.00
-2.00
-3.00
-2.00
-1.00
0.00
1.00
2.00
LOG10 [Periods (s)]
Phase (Deg.)
180
150
120
90
60
30
0
-30
-60
-90
-120
-150
-180
-3.00
-2.00
-1.00
0.00
1.00
2.00
LOG10 [Periods (s)]
Overview Map
Total RMS = 0.71
Zxx RMS = 0.71
Zxy RMS = 0.70
Zyx RMS = 0.68
Zyy RMS = 0.75

Site: site_090

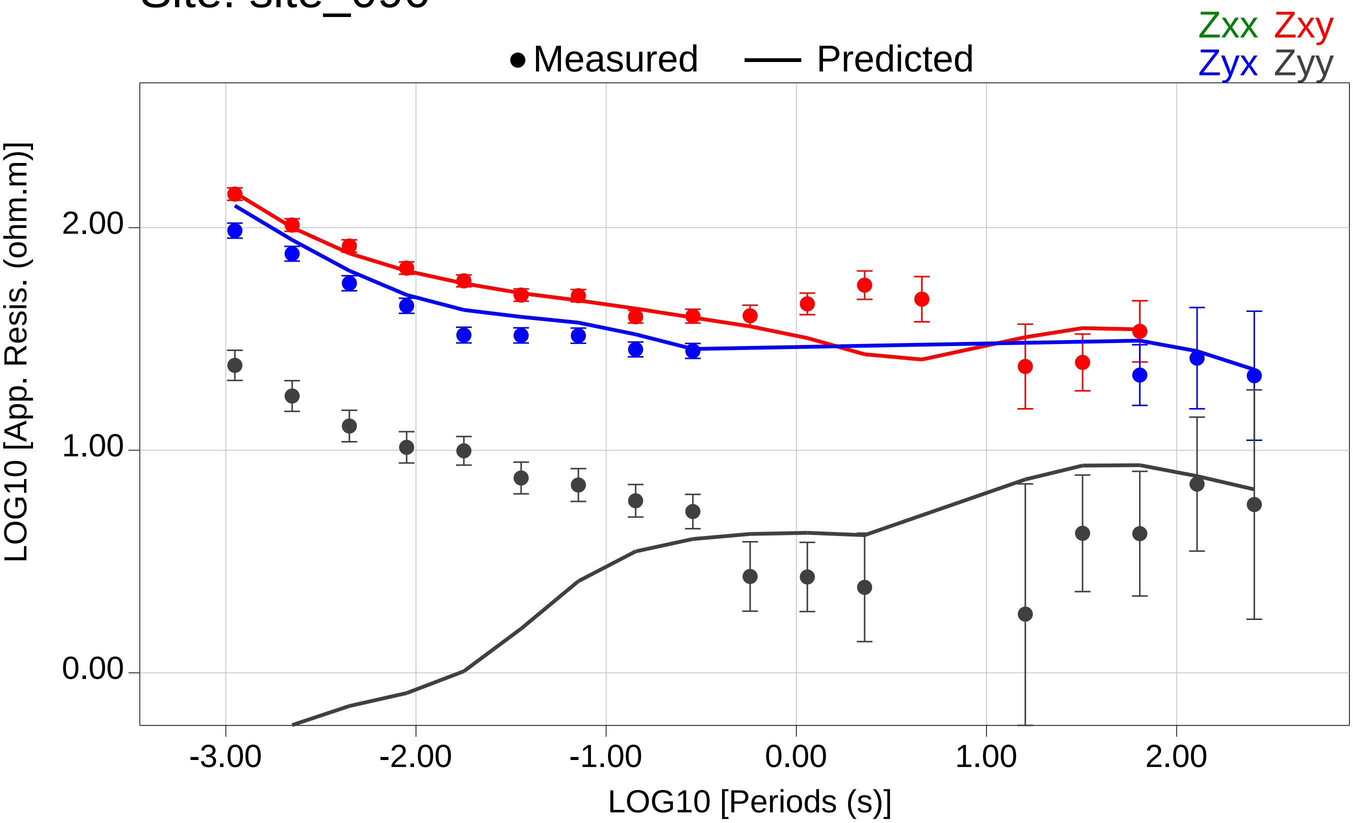

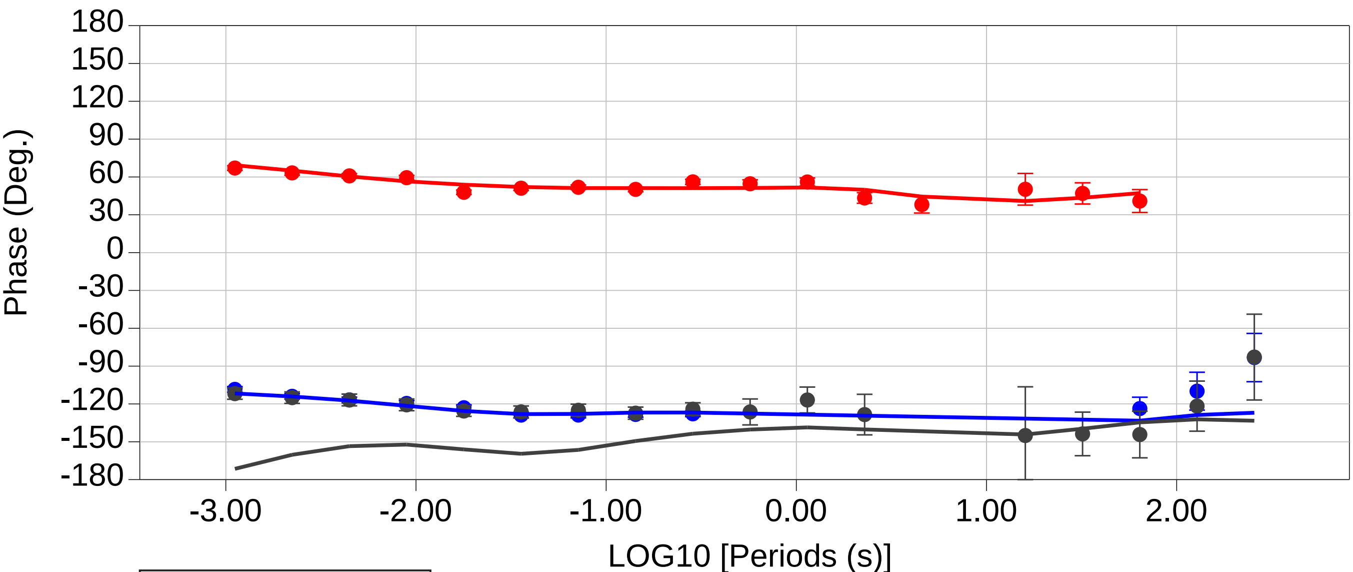

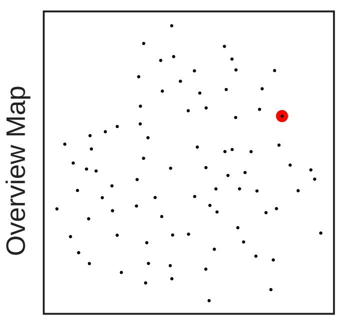

Total RMS = 2.19
Zxx RMS = 0.00
Zxy RMS = 1.03
Zyx RMS = 1.14
Zyy RMS = 3.29

Site: site_091

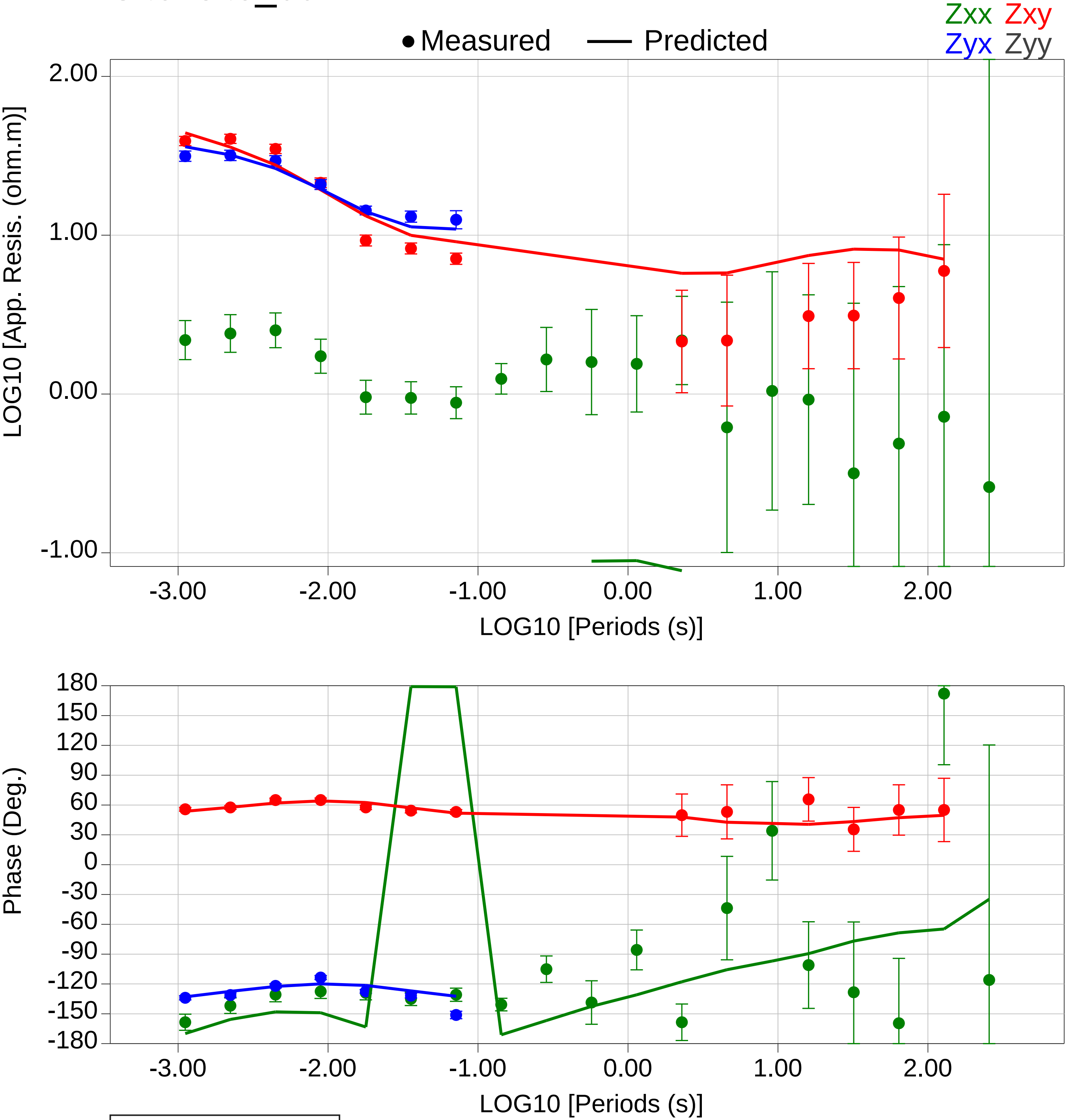

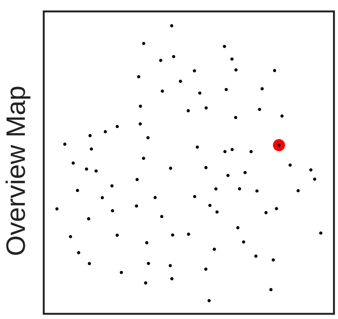

Total RMS = 2.03
Zxx RMS = 2.56
Zxy RMS = 1.27
Zyx RMS = 1.48
Zyy RMS = 0.00

Site: site_092

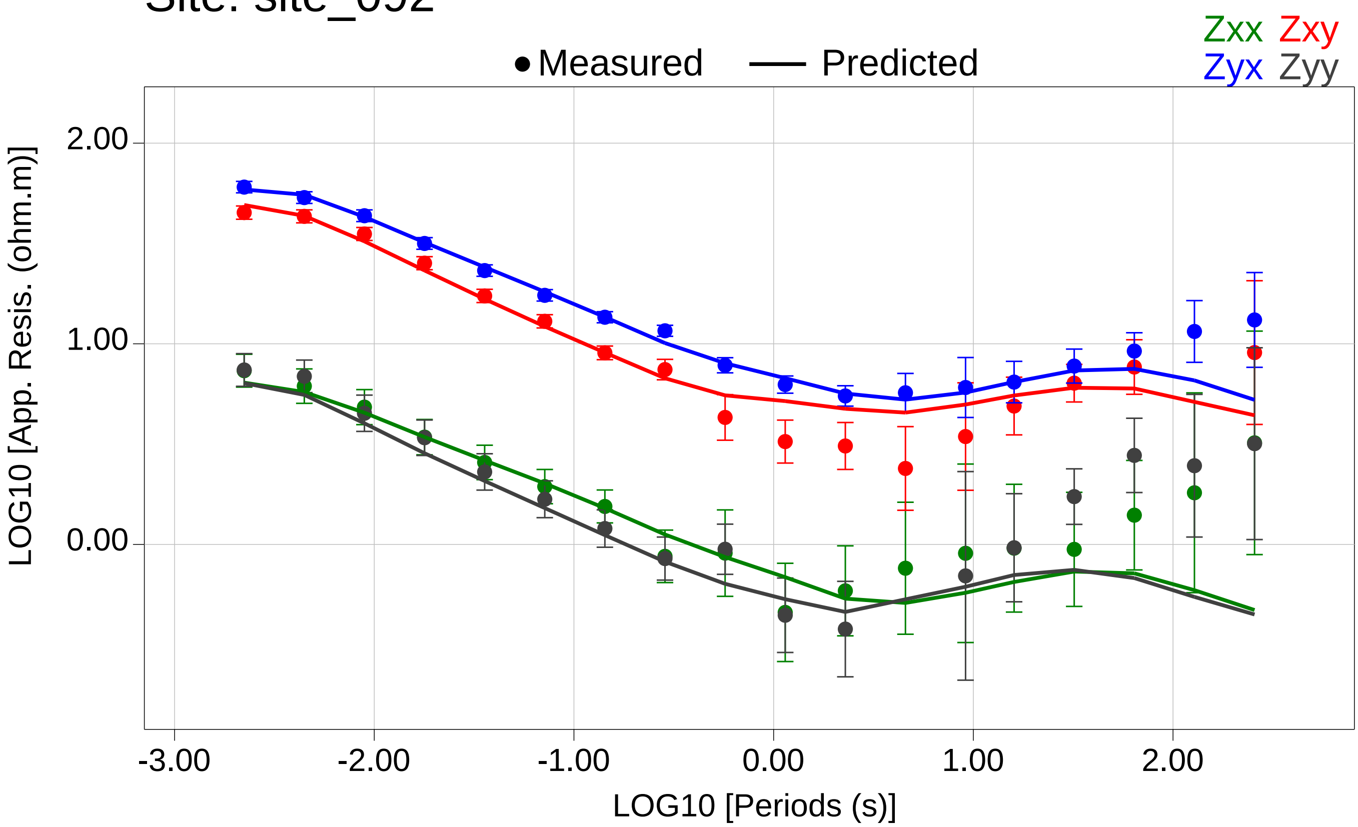

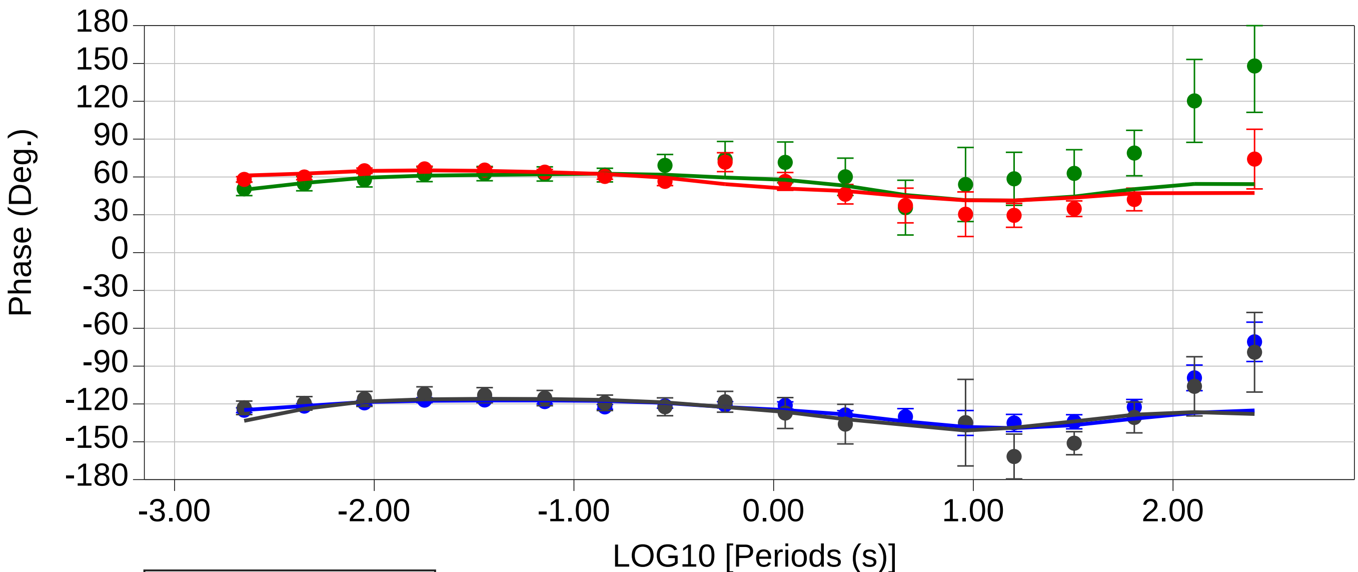

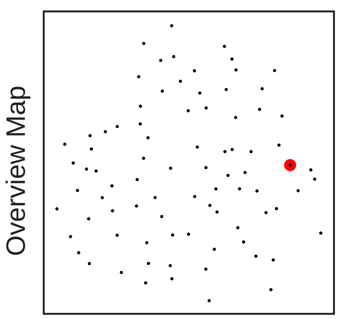

Total RMS = 0.65
Zxx RMS = 0.47
Zxy RMS = 0.73
Zyx RMS = 0.73
Zyy RMS = 0.65

Site: site_093

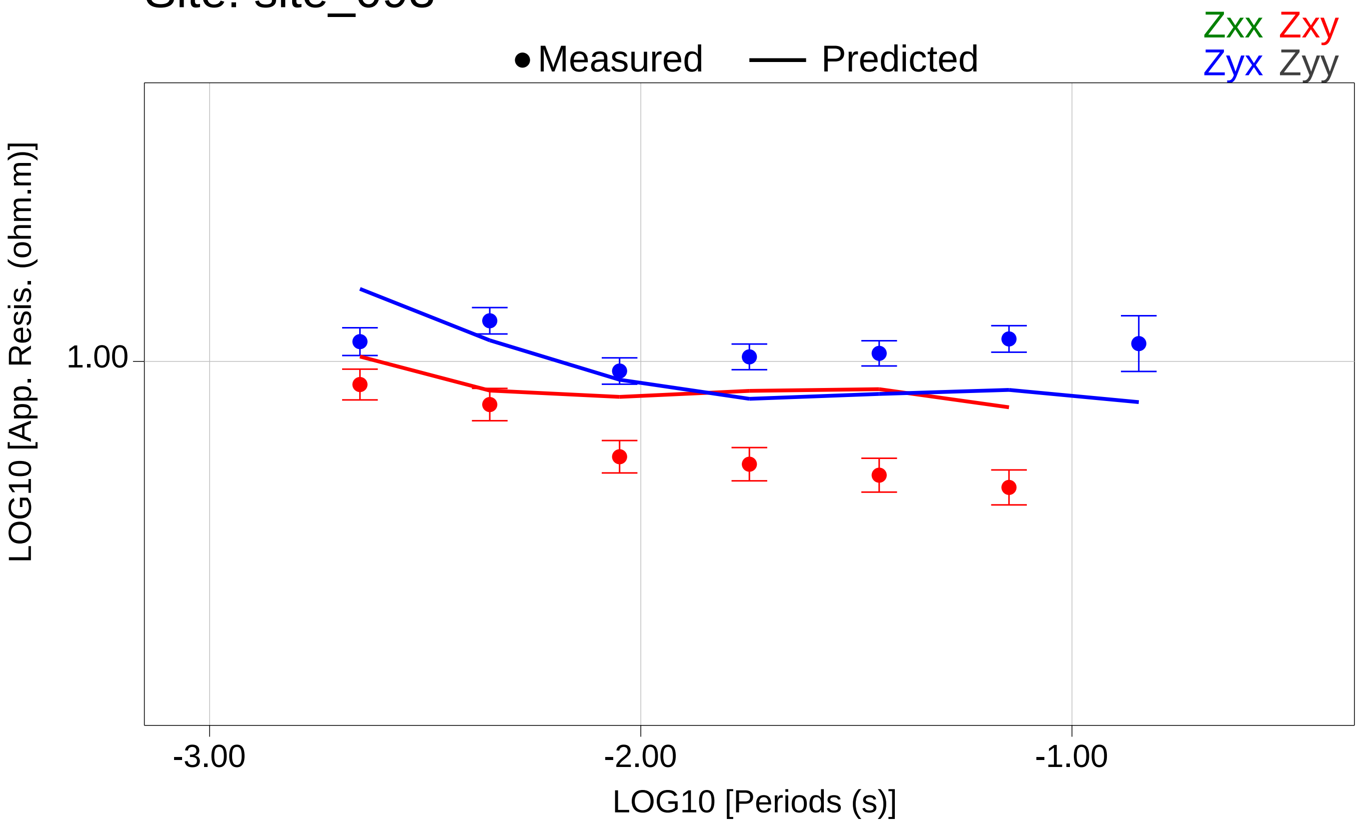

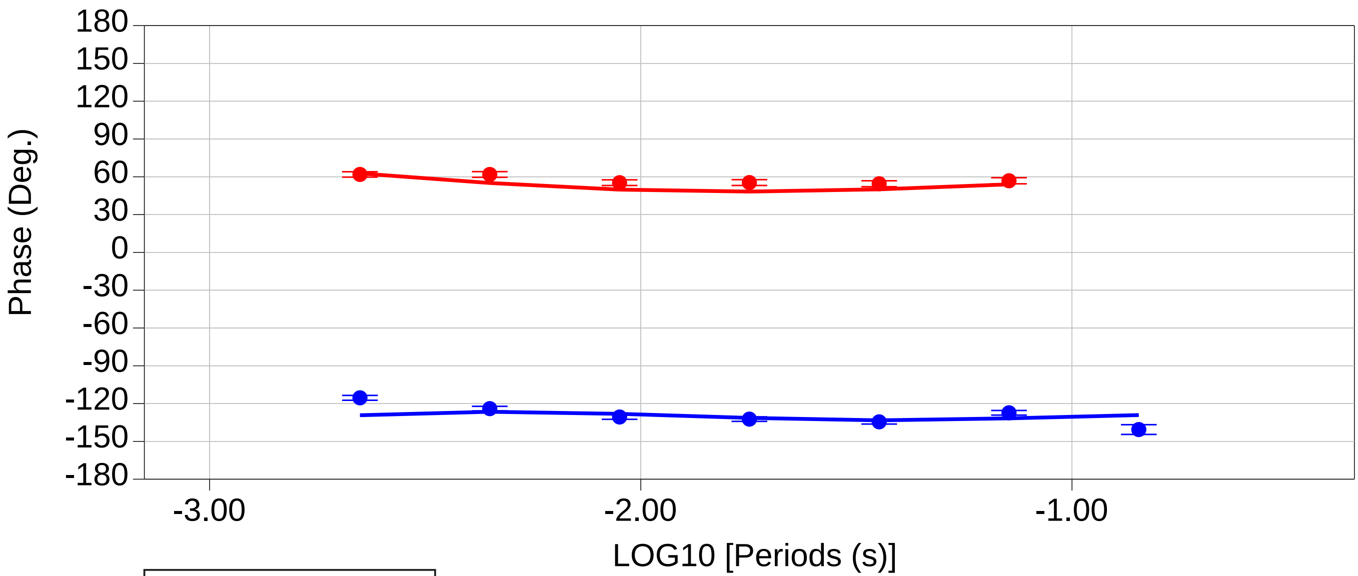

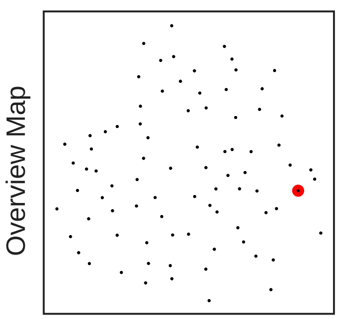

Total RMS = 2.26
Zxx RMS = 0.00
Zxy RMS = 2.37
Zyx RMS = 2.16
Zyy RMS = 0.00

Site: site_094

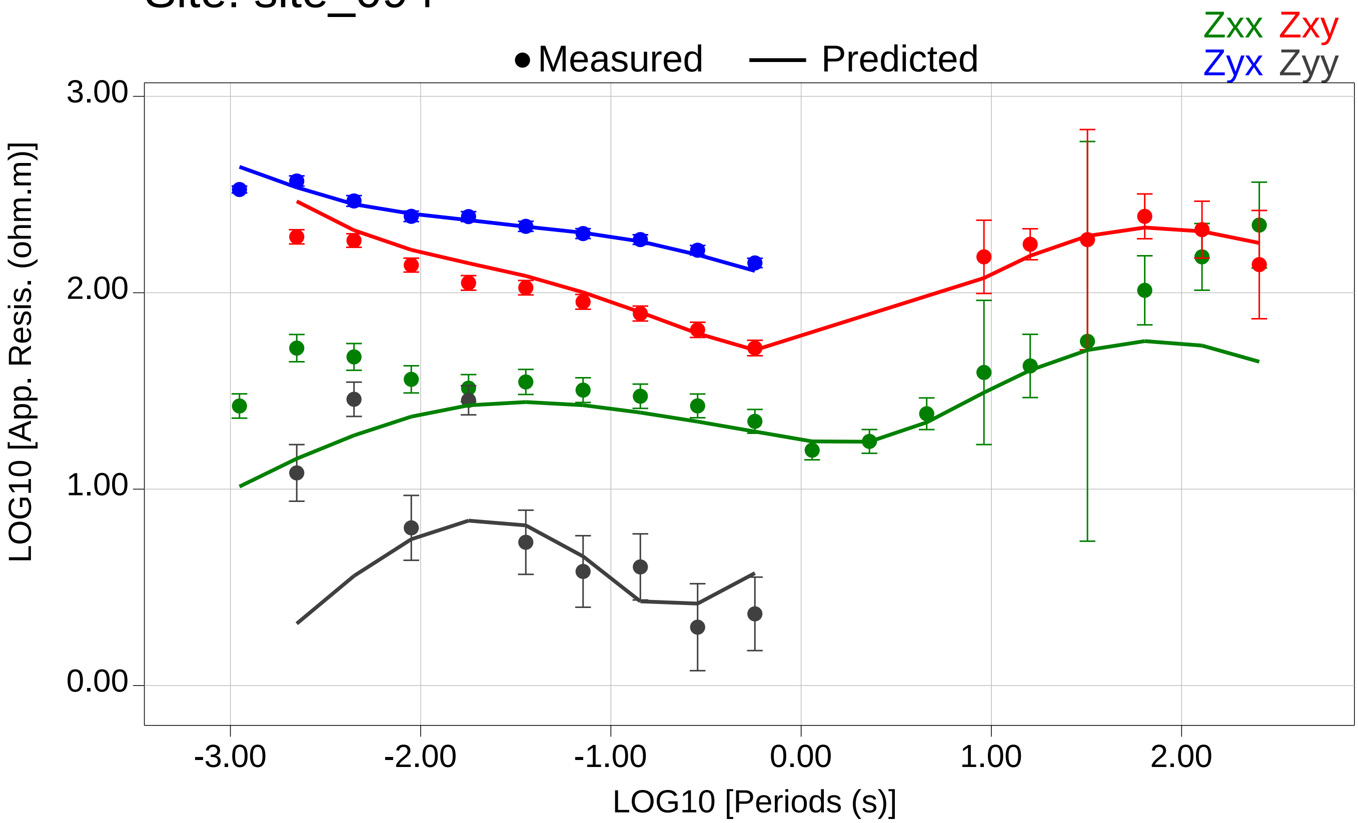

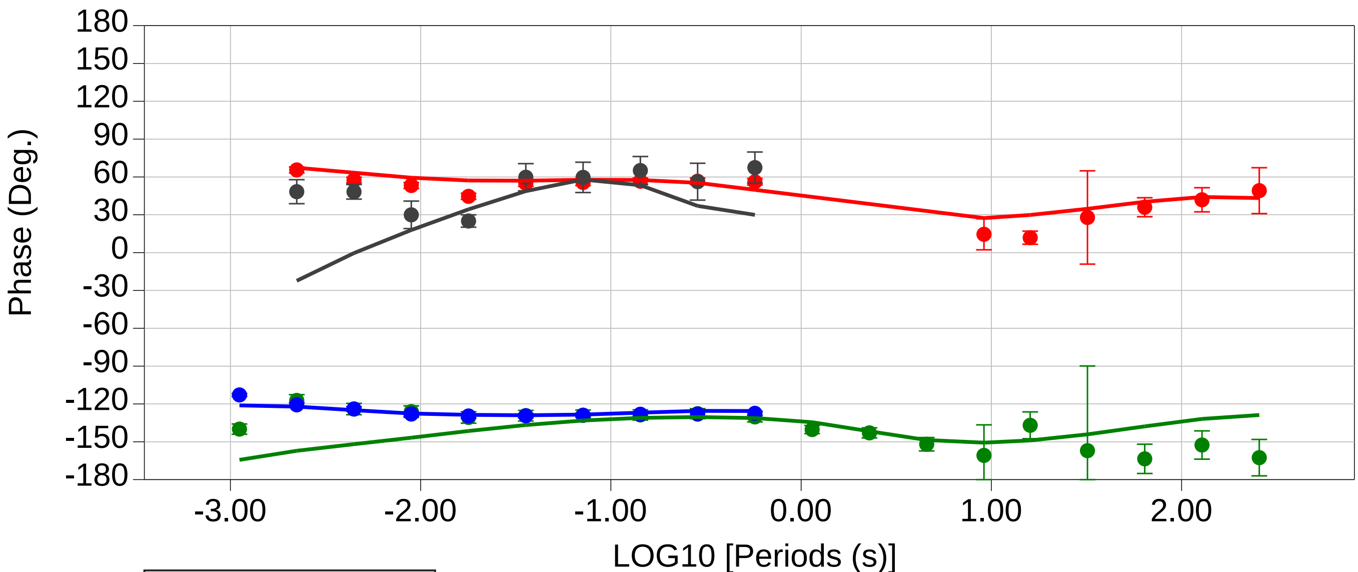

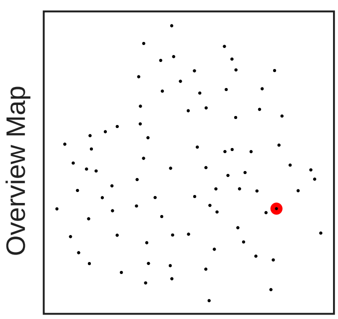

Total RMS = 1.72
Zxx RMS = 1.76
Zxy RMS = 1.40
Zyx RMS = 1.74
Zyy RMS = 2.07

Site: site_097

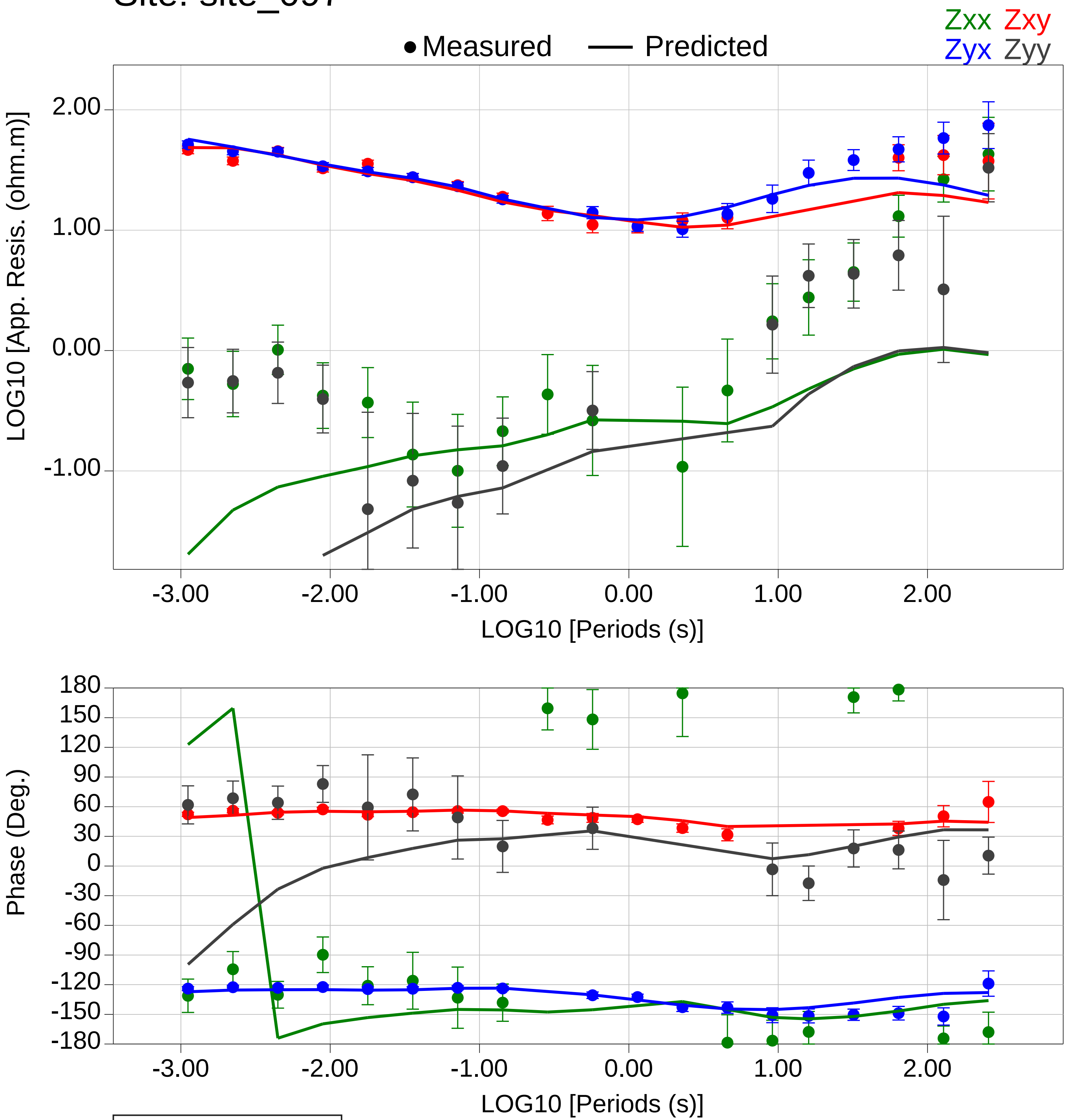

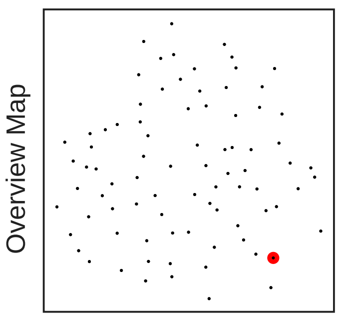

Total RMS = 1.05
Zxx RMS = 1.25
Zxy RMS = 0.97
Zyx RMS = 0.85
Zyy RMS = 1.08

Site: site_099

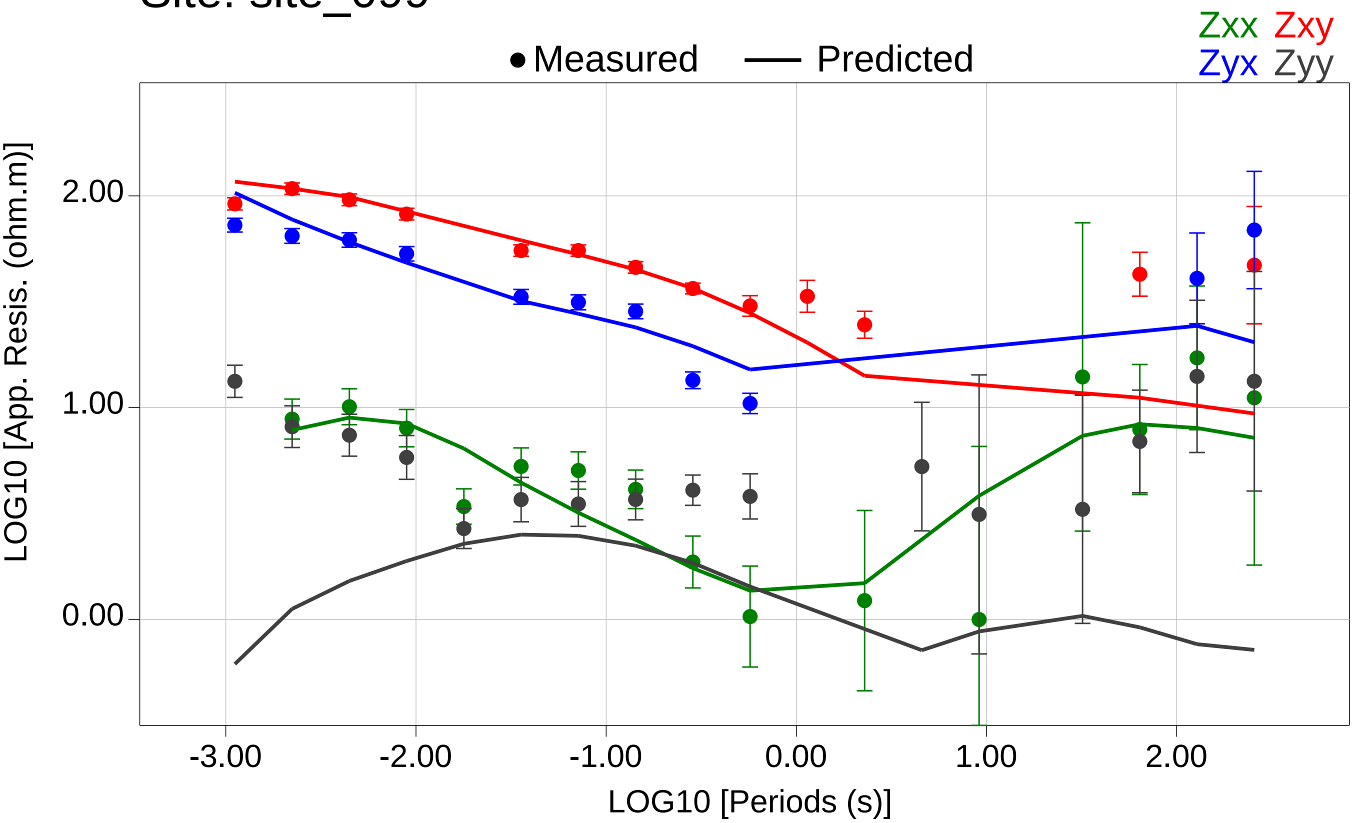

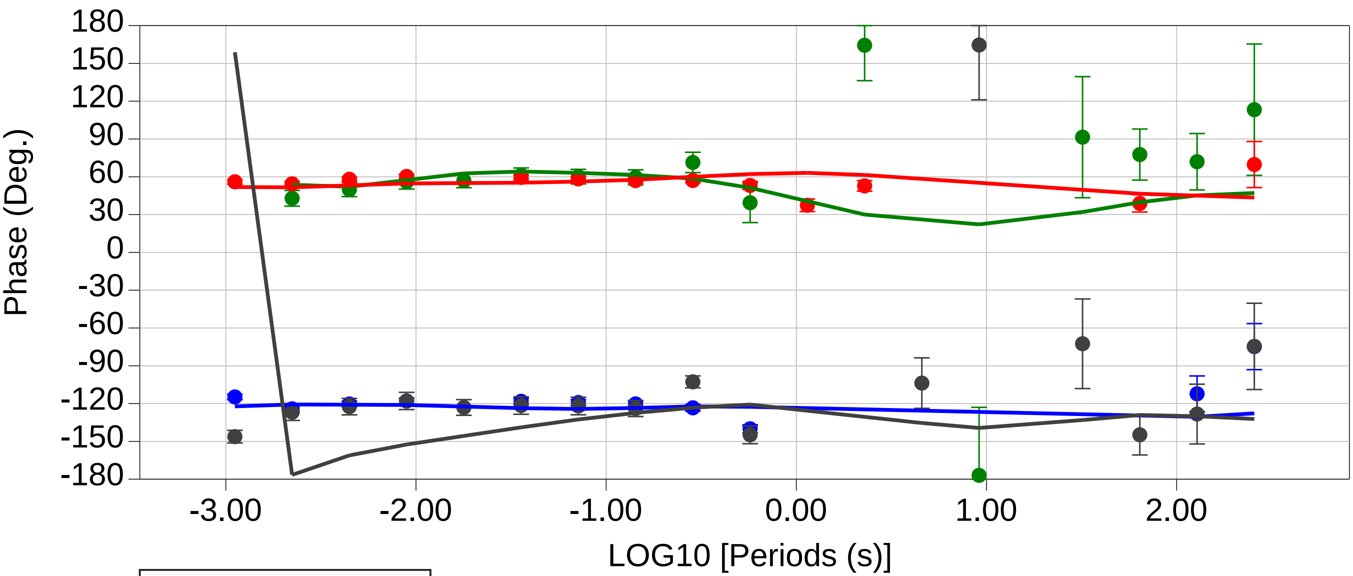

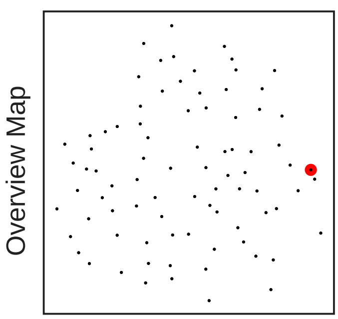

Total RMS = 1.72
Zxx RMS = 1.05
Zxy RMS = 1.55
Zyx RMS = 1.84
Zyy RMS = 2.21

Site: site_100

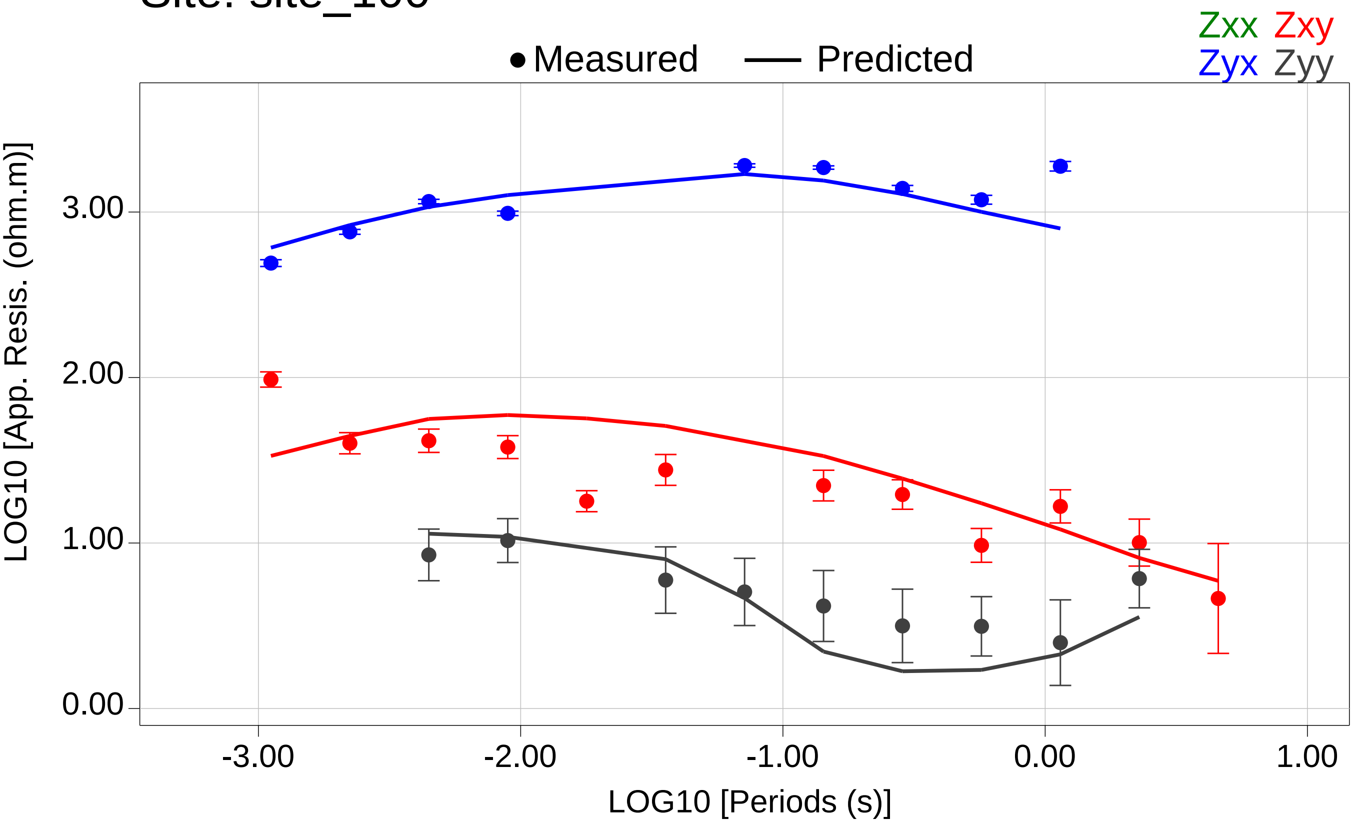

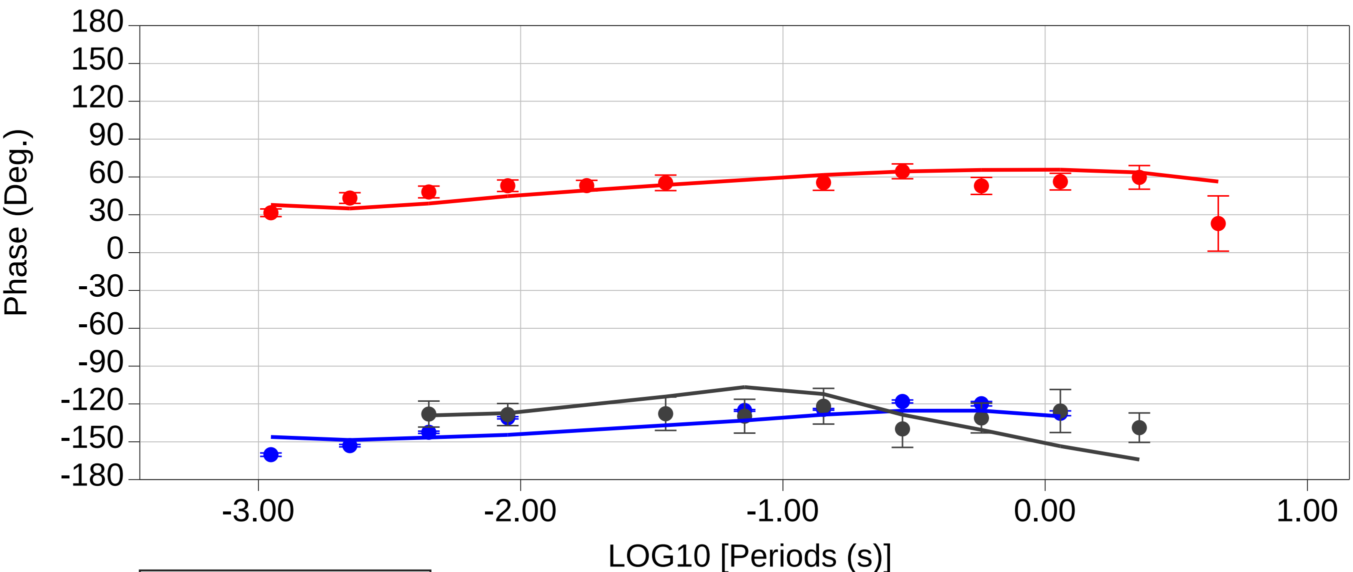

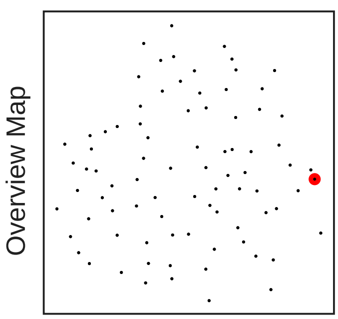

Total RMS = 3.16
Zxx RMS = 0.00
Zxy RMS = 2.25
Zyx RMS = 5.11
Zyy RMS = 0.70

Site: site_102

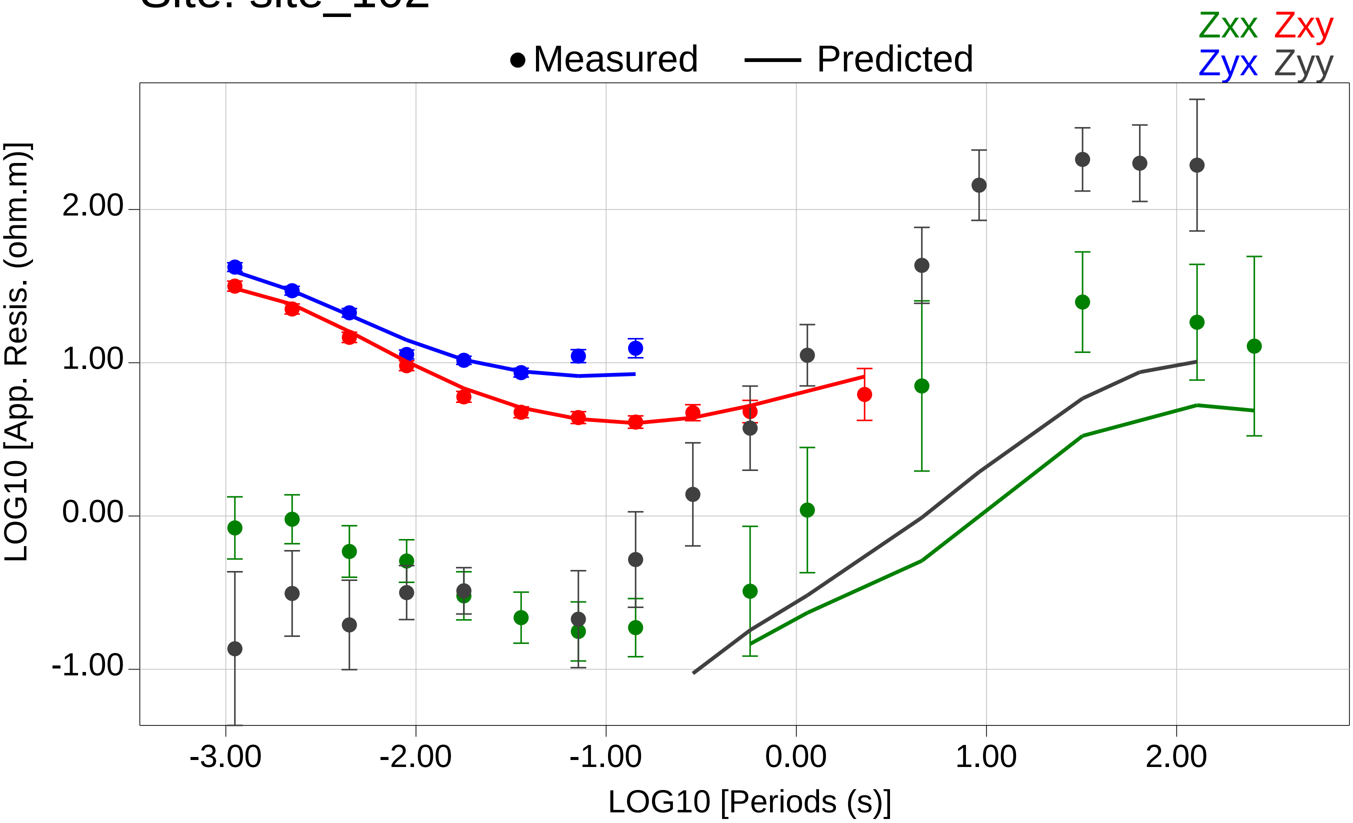

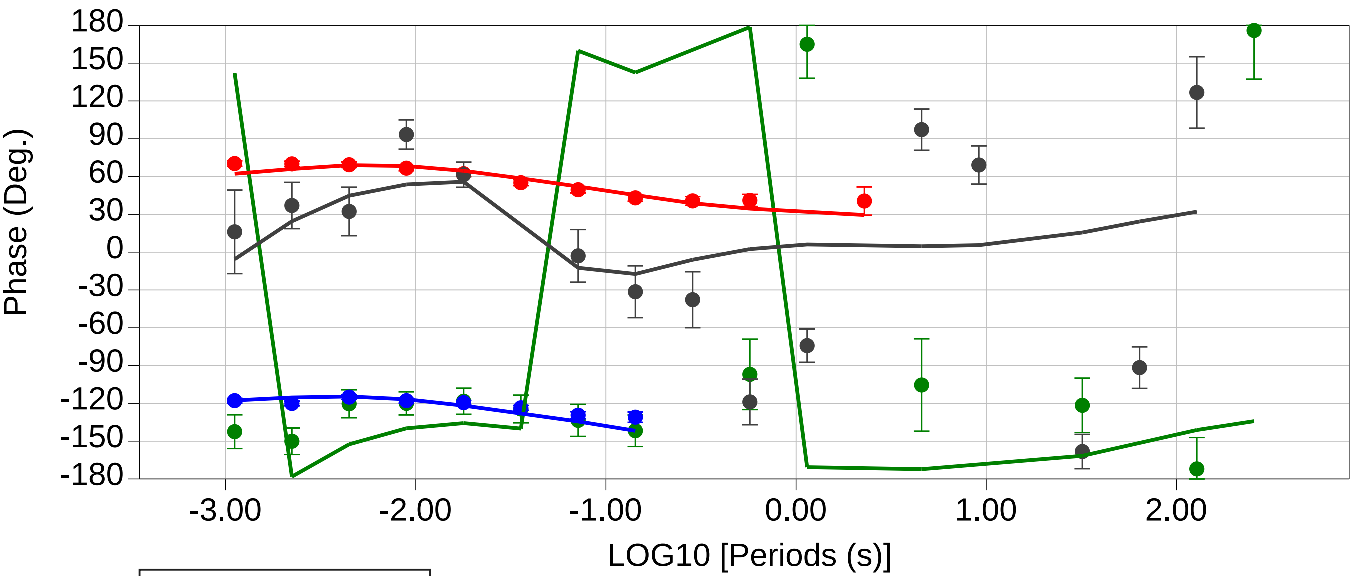

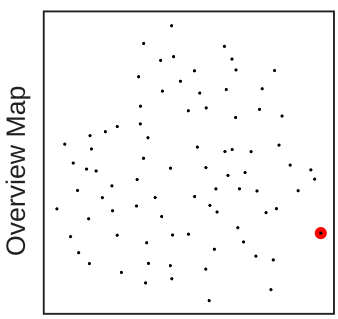

Total RMS = 1.54
Zxx RMS = 1.92
Zxy RMS = 0.88
Zyx RMS = 1.24
Zyy RMS = 1.67

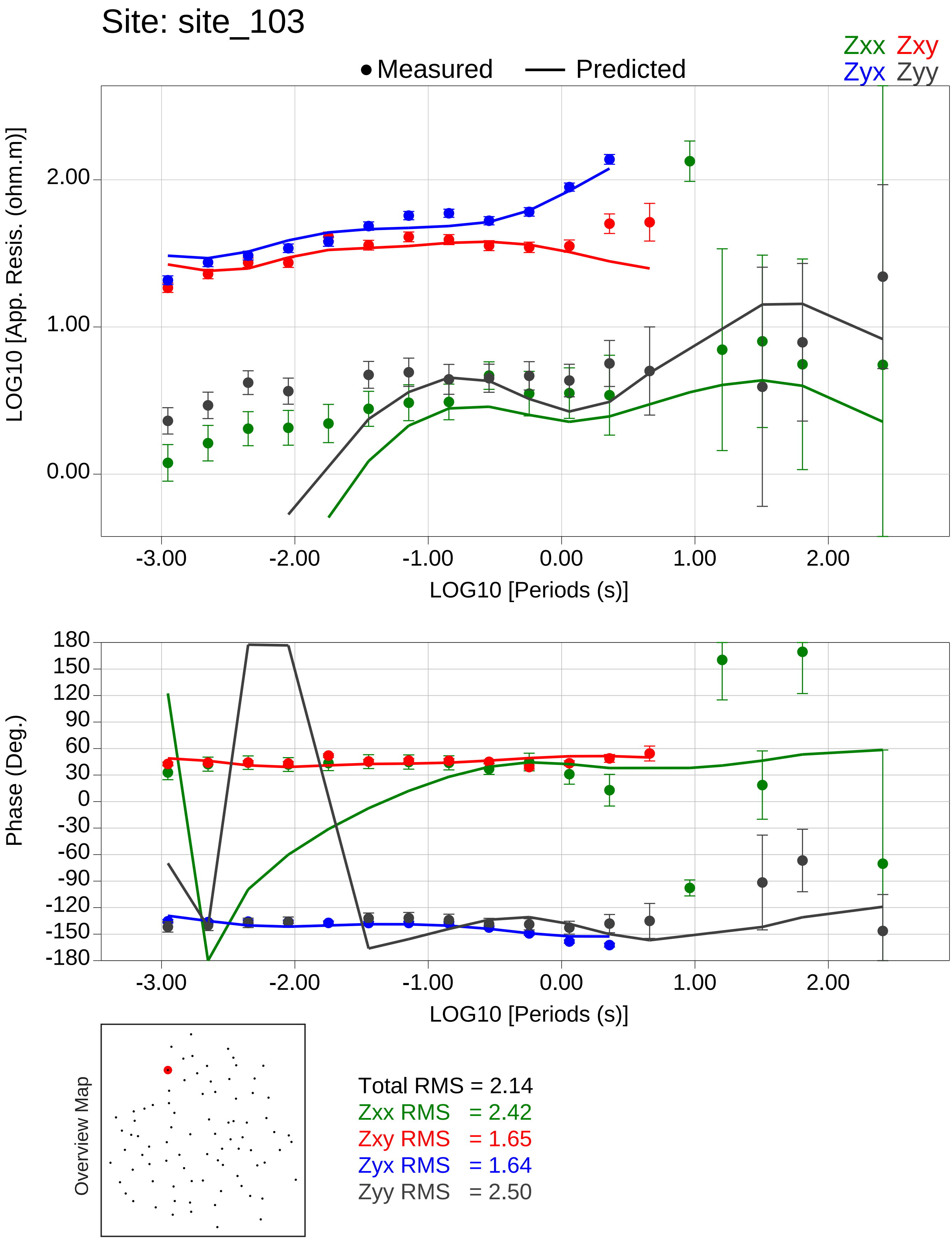
Site: site_103
Measured
Predicted
Zxx Zxy
Zyx Zyy
LOG10 [App. Resis. (ohm.m)]
2.00
1.00
0.00
-3.00
-2.00
-1.00
0.00
1.00
2.00
LOG10 [Periods (s)]
Phase (Deg.)
180
150
120
90
60
30
0
-30
-60
-90
-120
-150
-180
-3.00
-2.00
-1.00
0.00
1.00
2.00
LOG10 [Periods (s)]
Overview Map
Total RMS = 2.14
Zxx RMS = 2.42
Zxy RMS = 1.65
Zyx RMS = 1.64
Zyy RMS = 2.50

Site: site_105

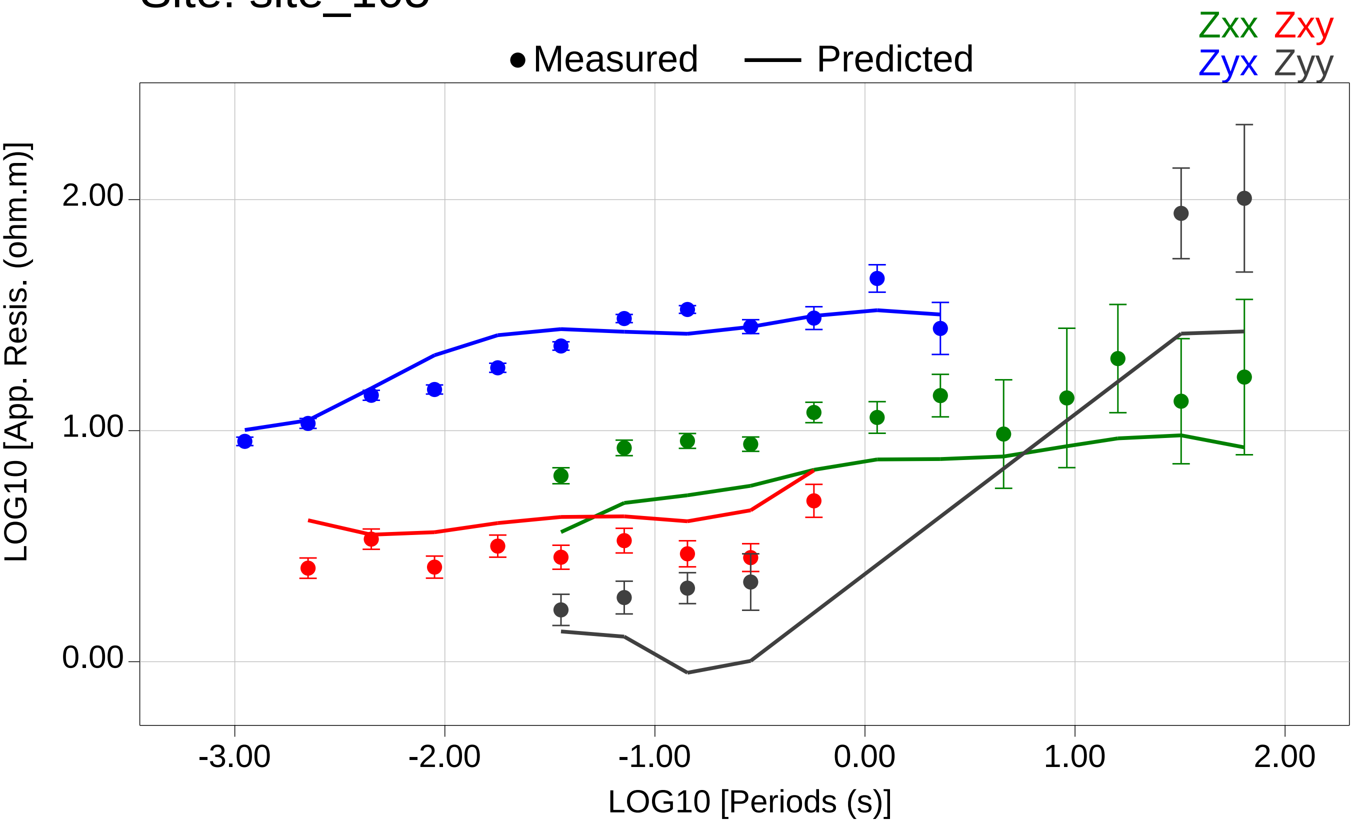

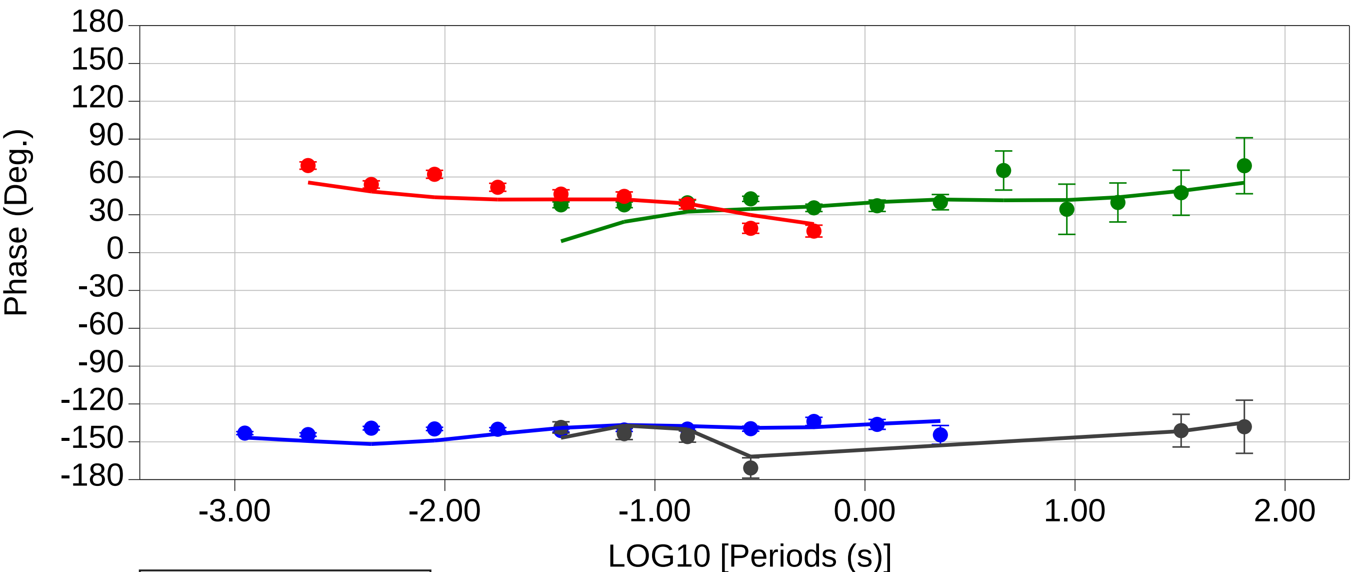

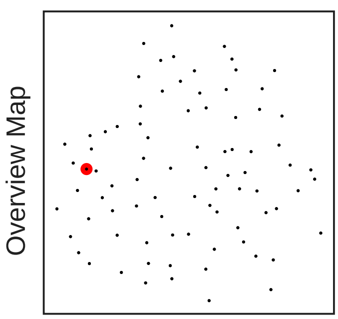

Total RMS = 2.51
Zxx RMS = 2.71
Zxy RMS = 2.25
Zyx RMS = 2.89
Zyy RMS = 1.35